5-10-2017

Determining the Mass of the Supermassive Black Hole in NGC 6814

Emily Rachel Manne-Nicholas
Georgia State University

DETERMINING THE MASS OF THE SUPERMASSIVE BLACK HOLE IN NGC 6814

by

EMILY R. MANNE-NICHOLAS

Under the Direction of Misty C. Bentz

ABSTRACT

Supermassive black holes (SMBH) are now thought to exist at the center nearly all massive galaxies. Not only are they thought to be ubiquitous, but it was also discovered nearly two decades ago that the mass of these SMBHs correlate strongly with properties of their host galaxies including bulge stellar velocity dispersion (M_{BH}-$\sigma_\star$) and bulge luminosity (M_{BH}-L_{bulge}). This correlation was not expected due to the tiny size of the SMBH gravitational sphere of influence compared to the size of the host galaxy, and imply a connection between the two, but this connection is still not well-understood. One step toward understanding this connection is to accurately measure the masses of these black holes. Two of the most common direct SMBH mass measurement techniques are stellar dynamical modeling (SDM), which generally only applies to quiescent galaxies, and reverberation mapping (RM), which can only be applied to active galactic nuclei (AGN) that exhibit broadened emission lines. Due to the unknown geometry of the region that produces these broad lines, the whole RM

sample of black hole masses generally needs to be multiplied by a constant called the f-factor to bring it into agreement with the SDM sample on the M_{BH}-$\sigma_\star$ relation. It is unknown how well this f-factor, being a population average, applies to individual RM masses. It would therefore be useful to measure an SMBH mass with both methods simultaneously to test whether they produce the same black hole mass. However, because the RM and SDM techniques usually apply to galaxies that are not possible for both, this has only been attempted twice before (NGC 3227 and NGC 4151).

The purpose of this dissertation is to apply SDM to the SMBH at the center of NGC 6814 for which there already exists an RM mass. This makes it only the third broad-lined AGN for which an SDM mass has been derived. In order to perform SDM accurately, the distance to the galaxy needs to be well-constrained as the error in the SDM mass scales linearly with distance. Because no adequate distance measurements already exist, the first half of this dissertation is devoted to deriving a Cepheid distance to NGC 6814 from V- and I-band HST WFC3 time series photometry. We measure the distance to NGC 6814 to be $17.54^{+1.44}_{-1.33}$ Mpc. In the second half, we incorporate that distance measurement into our stellar dynamical modeling on Gemini NIFS+Altair IFU data of NGC 6814's central 1.55"×1.55". We derive a mass of $1.19^{+37.57}_{-1.17} \times 10^8$ $M_\odot$ and best fit mass-to-light ratio of $0.948^{+0.032}_{-0.208}$ $M_\odot/L_\odot$. This mass is nearly an order of magnitude larger than the RM mass but has a 3σ range spanning nearly three orders of magnitude. We describe possible reasons for our larger-than-expected mass value, such as the existence of a bar, which would not be well-modeled by an axisymmetric dynamical code. Finally, we describe future steps that may be taken to better constrain the mass, such as creating more models to further explore parameter space.

INDEX WORDS: Supermassive Black Holes, Galaxy Evolution, Active Galactic Nuclei, Cepheids, Stellar Dynamical Modeling

DETERMINING THE MASS OF THE SUPERMASSIVE BLACK HOLE IN NGC 6814

by

EMILY R. MANNE-NICHOLAS

A Dissertation Submitted in Partial Fulfillment of Requirements for the Degree of

Doctor of Philosophy

in the College of Arts and Sciences

Georgia State University
2017

DETERMINING THE MASS OF THE SUPERMASSIVE BLACK HOLE IN NGC 6814

by

EMILY R. MANNE-NICHOLAS

Committee Chair:	Misty C. Bentz
Committee:	D. Michael Crenshaw
	Rachel Kuzio de Naray
	Vadym Apalkov
	Christopher Onken

Electronic Version Approved:

Office of Graduate Studies

College of Arts & Sciences

Georgia State University

May 2017

DEDICATION

This dissertation is dedicated to my parents who raised me to value education. Someday I hope to be as wise as they are.

ACKNOWLEDGMENTS

First and foremost, I thank my advisor, Dr. Misty Bentz. Her countless hours of guidance and her enormous skill as an astronomer have made my dissertation possible. Many thanks also go to our brilliant collaborators: Dr.s Monica Valluri, Chris Onken, and Laura Ferrarese. Their expertise has proven invaluable, and their hospitality during my visits was above and beyond. My committee members, Dr.s Mike Crenshaw (who sent me to AGN summer school, which accelerated my learning), Rachel Kuzio de Naray, and Vadym Apalkov, who have generously given their time and constructive criticisms to make my dissertation better, have my deep gratitude. I would like to acknowledge the help of our research group's post-doctoral researcher, Dr. Merida Batiste, whose guidance on the use of pPXF and the Gemini reduction pipeline softwares saved me many hours of work. Finally, I wish to thank my friends and family (including my cats). Without their unwavering moral support this work could not have been accomplished.

TABLE OF CONTENTS

LIST OF TABLES

LIST OF FIGURES

– 1 –

Introduction

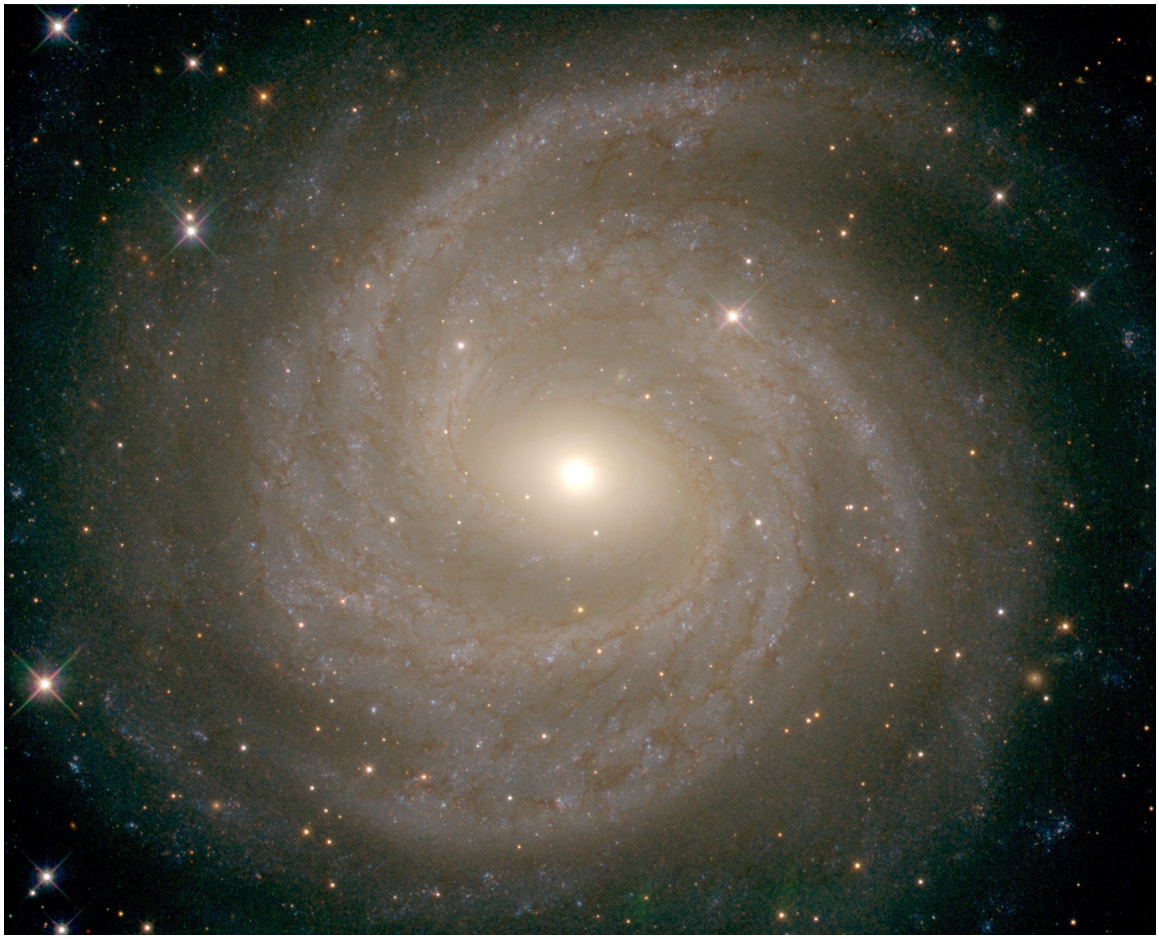

Figure 1.1: Stacked HST WFPC3 image centered on NGC6814. The image orientation is North up and East to the right. The stacked frames were taken in filters F555W, F814W, and F160W.

1.1 Background

Astronomers have known since the 1970s that the central regions of many galaxies host extremely luminous point-sources of highly redshifted light. Their resemblance to a star led them to be called Quasi Stellar Objects (QSOs) (Schmidt 1963), but they turned out to be part of a broader class of objects called Active Galactic Nuclei (AGN). Characterized

by bright emission across nearly the full electromagnetic spectrum, their enormous power output puzzled astronomers. How could so much energy be produced in such a compact region at the center of galaxies? In 1974, Sir Martin Rees hypothesized that black holes, objects of such extreme density that even light cannot escape, might be the engines at the center of these QSOs. He proposed that matter falling under the influence of gravity toward a central black hole could produce the extreme luminosities necessary to power the QSOs. That same year, Balick and Brown discovered a point source of radio emission at the center of our Milky Way galaxy in the direction of the constellation Sagittarius. They named it Sagittarius A*, and quickly drew a connection between it and the QSOs being found in other galaxies.

Sure enough, when astronomers became capable of observing Sagittarius A* at infrared wavelengths, they noticed that the stars, gas, and dust were moving much faster than expected (5 000 km/s) (Schödel et al. 2002). The gravitational attraction necessary to cause these motions could only be produced by an object (or objects) millions of times more massive than the Sun. However, because the region could not be resolved at the time due to instrumental limitations, nobody knew what type of object it could be. Many models were put forth to explain what that compact dark mass might be including a cluster of evolved low-mass stars (Becklin & Neugebauer 1968), neutron stars Becklin & Neugebauer (1968), a cluster of supermassive stars with heavy accretion disk (Kundt 1990), a ball of heavy neutrinos supported by degeneracy pressure (Tsiklauri & Viollier 1998), a ball of bosons (Torres et al. 2000), or a black hole of a mass millions of times that of our Sun, aptly called a supermassive black hole (SMBH) (Salpeter 1964; Zel'dovich 1964). Each of these types of objects have a minimum volume that they can realistically occupy and not collapse or

disperse. The only way to rule out these models was to better resolve the motions of objects closer and closer to the dark mass. If matter is observed to be orbiting at a radius smaller than the minimum radius required for that object to exist, then that model got ruled out.

As telescope resolutions improved, gas and individual stars in Keplerian orbit around the dark mass were observed to pass by the dark mass at shorter and shorter distances. One by one, each model put forth to explain the dark mass was excluded by observations that showed matter orbiting at radii smaller than the density of those models would allow. 2002 marked the year that proved the unseen mass must be a supermassive black hole. Schödel et al. (2002) had been tracking the movements of stars near the central mass for 10 years, and had measured the orbit of one of the stars (S2) to pass within 17 light hours of the massive object. The only object that could hold that much mass in that small of a volume was a black hole!

Similar studies have been conducted on the spatially resolved central regions of other nearby galaxies. The Hubble Space Telescope's incredible resolving power has made a supermassive black hole the only plausible explanation for the observed dynamics of gas and stars in the centers of these galaxies. Dynamical studies combined with theory used to explain the power and emission characteristics of AGN has led to the current paradigm that most every massive galaxy in the Universe hosts a supermassive black hole (Magorrian et al. 1998; Kormendy 2004).

The very ubiquity of SMBHs implies that they are formed quite readily during the lifetime of a galaxy. If they form readily, then that begs the question of how they formed in the first place. Does the black hole form first and then the galaxy forms around it, or vice versa? Perhaps they co-evolve? Evidence for co-evolution can be found in the existence of what are

called scaling relationships, which are correlations between the mass of the black hole and certain properties of the host galaxy. One would not necessarily expect the black hole to have much of an effect on its host galaxy because the size of the gravitational sphere of influence of an SMBH is quite tiny compared to its galaxy. It is not intuitive, therefore, why the mass of an SMBH correlates tightly with characteristics of the host galaxy. It should be noted that these correlations seem to be tightests between the SMBH and the spheroidal component of its host galaxy, though this is still a matter of debate. (For elliptical galaxies, the spheroidal component is the whole galaxy; for spiral galaxies, the spheroidal component would be the bulge.) Spheroidal characteristics that correlate tightly with the mass of the black hole include bulge stellar mass (e.g., Magorrian et al. 1998; Marconi & Hunt 2003; Häring & Rix 2004; Hu 2009; Sani et al. 2011), bulge stellar velocity dispersion (e.g, Ferrarese & Merritt 2000; Gebhardt et al. 2000; Tremaine et al. 2002; Hu 2008; Gültekin et al. 2009; Schulze & Gebhardt 2011; Graham et al. 2011; Beifiori et al. 2012), shape of the luminosity profile of the bulge (e.g., Graham et al. 2001; Graham & Driver 2007; Beifiori et al. 2012), and bulge luminosity (e.g., Kormendy & Gebhardt 2001; Kormendy et al. 2011; Beifiori et al. 2012). For these correlations to exist, the black hole and the much larger galaxy need a way to "communicate" with one another besides through gravity. So how can the bulge of the galaxy "communicate" with the SMBH?

It is hypothesized that AGN provide the link between the SMBH and its host galaxy via a feedback mechanism. AGN occur when material from the host galaxy such as dust and gas loses angular momentum and falls toward the center of the galaxy and into the gravitational sphere of influence of the SMBH. Some of this matter orbits the SMBH at speeds of hundreds to thousands of kilometers per second and forms what are called the

narrow line region (NLR) and the broad line region (BLR) (see Figure 1.2). Encircling the BLR and partially obscuring it is what is called the dusty torus. Some material falls even closer to the SMBH and as it does, it heats up and flattens out forming the accretion disk. Finally, some of the material will actually make it quite close to the black hole and either cross the event horizon and add to the mass of the black hole (a.k.a. feeding), or it will be ejected at high speeds back out into the galaxy either via magnetic field gradients that twist and form a jet and/or by outflows in the form of winds. This ejected material can then, in a process known as feedback, collide with and heat up the intergalactic medium, thus shutting down star formation and also decreasing the likelihood that more material will fall toward the center to feed the AGN. This is the leading hypothesis for how SMBHs are connected to and shape the evolution of their host galaxies (see reviews by e.g., Fabian 2012; Kormendy & Ho 2013; Heckman & Best 2014).

In order to test this hypothesis, we must make some important measurements. One of the most fundamental, yet challenging measurements we can make is the mass of the SMBH. To date, only about 100 direct measurements of black hole masses have been made. The time and effort required to make these direct measurements is costly, and yet it is important to make that investment. Tens of thousands of SMBH mass measurements have been made using indirect methods (Shen et al. 2011) that rely upon and are calibrated by the smaller sample of directly measured ones. These indirect measurements are used to constrain modeling of host galaxy and black hole co-evolution over cosmic time. Without a supermassive black hole, models of galaxy evolution tend to result in too much star formation (e.g., Katz et al. 1996; Balogh et al. 2001; Kereš et al. 2005; Oppenheimer & Davé 2006). Direct black hole

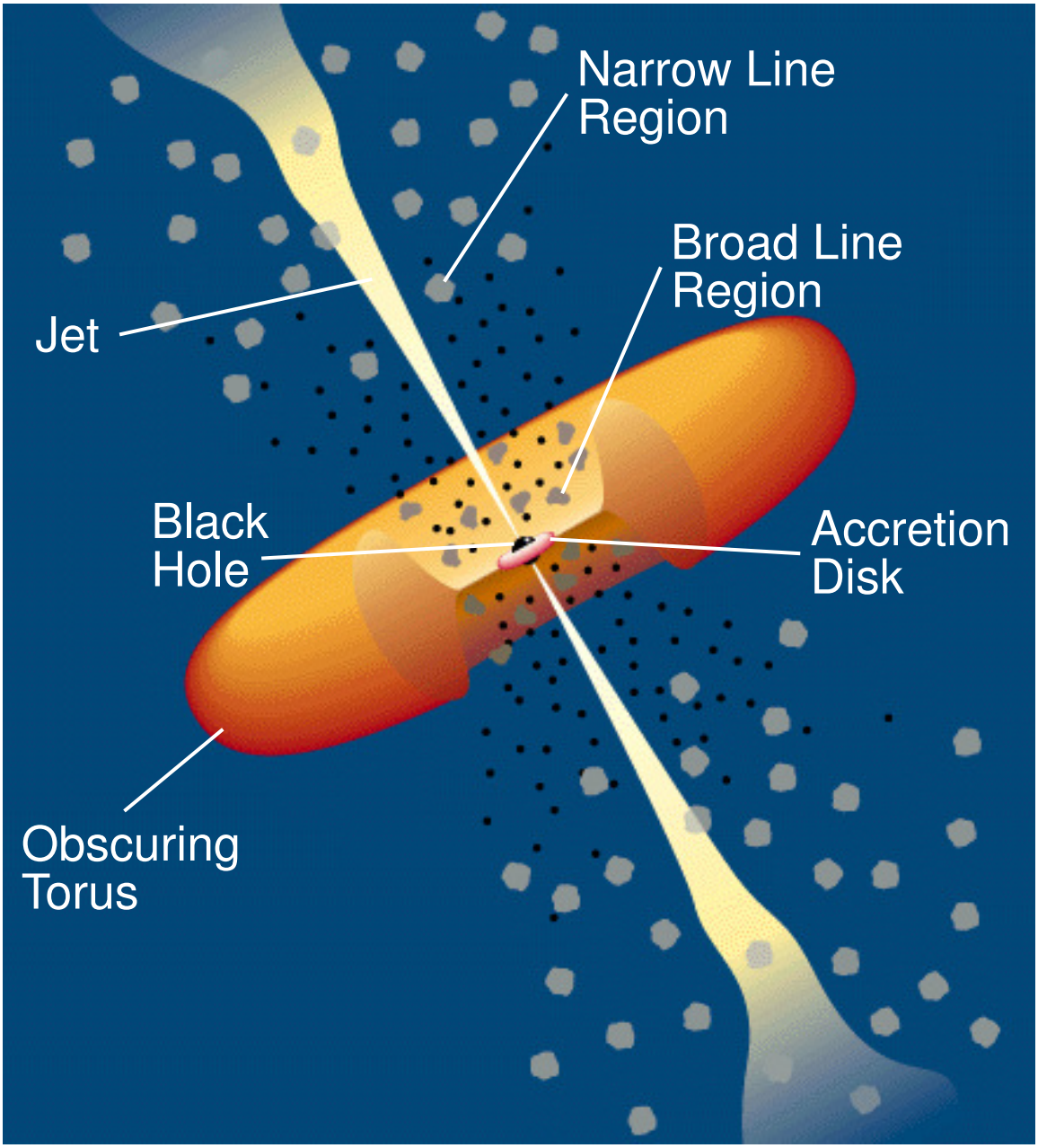

Figure 1.2: Diagram illustrating structure of an AGN from Urry & Padovani (1995)

measurements are therefore needed to calibrate indirect measurements, which are in turn needed to constrain models of galaxy evolution.

Because our understanding of galaxy evolution depends on our knowledge of SMBH masses, a lot of effort has been put into increasing the number of directly measured masses.

The likelihood of being able to directly measure the mass of any given SMBH is very low. However, for about 100 SMBHs, all the necessary conditions are met to enable direct measurements. There are two main methods of directly measuring SMBH masses: reverberation mapping (RM) and stellar dynamical modeling (SDM). Which method one uses depends on the proximity, type and orientation of galaxy in which the SMBH resides. Typically, if the galaxy is quiescent, nearby (less than 100 Mpc), and has an unobscured central region, then one can attempt SDM. If, however, the galaxy is active and shows emission from the BLR, then RM is used. These methods both have their own unique challenges, but to understand them, one must first understand how SDM and RM work.

1.2 Stellar Dynamical Modeling

Stellar dynamical modeling has been used to measure over 50 SMBH masses to date (McConnell & Ma 2013). Like its name suggests, SDM involves modeling the motions of the stars within the gravitational sphere of influence of the SMBH. It uses the orbit superposition technique (Schwarzschild 1979) whereby one builds a library of possible orbits, and then superposes them, seeking to find the comination of orbits that best matches the observed kinematics. The models assume the stars form a collisionless system. The accuracy of mass measurements via SDM are dependent upon the validity of such an assumption and several others, as well as our ability to model such a system.

The observations required to constrain these models must spatially resolve (or nearly spatially resolve) the sphere of influence of the black hole as well as contain spectroscopic information about as much of that region as possible. The somewhat recent advent of Integral Field Spectroscopy is ideal for these types of observations because it provides spectroscopic

information for every spatial element, thereby allowing for brightness and dynamical measurements simultaneously. Resolving the sphere of influence of a black hole with spectrophotometric data is therefore limited by our instrumental resolving power. Said in another way, the SDM sample size is limited by the number of galaxies with unobscured central regions that are nearby enough for us to spatially resolve them.

In addition to resolving power, SDM requires knowledge of the distance to the host galaxy; the error associated with the mass scales linearly with the error in the distance. Because our resolving power limitations require that the host galaxy be relatively nearby, and the motions of nearby galaxies are not dominated by the Hubble flow, we cannot simply use the redshift as an indicator of distance and therefore must calculate the distance to the galaxy in some other way. Essentially, getting an accurate SDM mass of a black hole requires a two-step process. The first step is carefully measuring the distance to that galaxy. The second step is actually performing the SDM itself with distance as an input parameter.

Distance measurements in astronomy are as important as they are challenging. Without knowledge of an object's distance, it is difficult to accurately study its intrinsic properties such as brightness, size, etc. Astronomers are continuously developing and refining distance measuring techniques that are effective for different ranges of distances and types celestial objects. Because no one method is applicable to all objects at all distances, distance methods with overlapping ranges must be compared to one another, and the one that is considered more reliable is used to calibrate its neighbor. As is illustrated in Figure 1.3, these techniques form what is commonly referred to as the "Cosmic Distance Ladder". Like the rungs of a ladder that must be climbed in succession to reach greater heights, so too must astronomers use shorter-distance methods to calibrate longer-distance methods, which are in turn used to

calibrate even longer-distance methods, and so forth. This bootstrapping way of measuring distances makes the accuracy and precision of final measurements dependent upon proper calibration of all lower rungs. These calibrations will become important in later chapters.

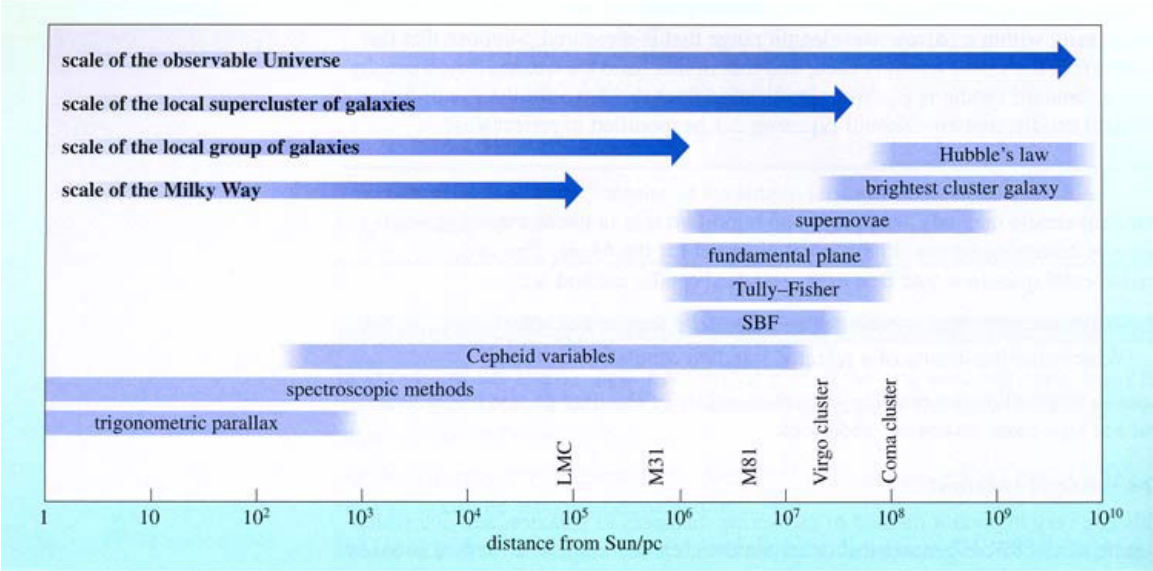

Figure 1.3: Illustration of interdependence of distance measuring techniques used in astronomy. No single technique can be used at all distances, so nearer methods are used to calibrate farther ones, which are in turn used to calibrate even farther ones and so forth. Each method's range is illustrated by a horizontal blue bar. Blue bars are stacked vertically and with overlapping ranges to show the interdependence of the technicques.

Because our goal is to accurately measure the distance to NGC 6814, we had to justify an observationally expensive Cepheid study by ruling out all other possible extragalactic distance measurement techniques. For example, the Surface Brightness Fluctuations (SBF) technique (Tonry et al. 1997), which relies on measuring the amount of granulation in the surface brightness profile of a galaxy caused by resolving individual stars, works best for elliptical galaxies because they lack the dust and substructure that would affect the amount of granulation observed. The Tully-Fisher technique (TF) (Tully & Fisher 1977) involves measuring the width of the molecular hydrogen spin-flip transition line. Indeed, there al-

ready exists a T-F measurement to NGC 6814 of $22.8^{+4.6}_{-3.8}$ Mpc (Tully 1988). However, due to its large uncertainty most likely caused by NGC 6814's nearly face-on orientation, as well as the high systematic uncertainties that plague this technique in general (e.g., Bradford et al. (2016)), we must pursue a more secure measurement. The Cepheid Period-Luminosity relation (Leavitt 1908) is our only feasible option for obtaining an accurate distance measurement to NGC 6814.

1.3 Reverberation Mapping

The distance limitations of SDM require one to use a different technique if one wants to directly measure the black hole masses of very distant galaxies. It is for this very situation that reverberation mapping becomes necessary.

AGN are powerful tools with which to study the Universe. They are one of natures most energetic processes, rivaling the luminosity of their host galaxies, and as such can be observed at cosmic distances. Their emission varies across almost all wavelengths and on timescales of minutes to years, and that variation itself conveys information about the size, shape, and physics of its substructures. The reverberation mapping method takes advantage of the fact that AGN are bright and variable, and uses those traits to measure the mass of the SMBH.

As stated before, the BLR is made of fast-moving material that is located within light days of the black hole. This region absorbs a continuum of photons emitted from hotter regions closer to the black hole called the accretion disk, and then re-emits them in broadened emission lines. If the AGN is in the correct orientation (see Figure 1.2), we can actually observe the change in the continuum flux, and then, light days later, we see a corresponding

change in flux from the broad lines (see Figure 1.4) (Blandford & McKee 1982; Peterson 1993). In other words, as regions close to the SMBH change in brightness, this change can be seen reverberating in broadened emission lines. The lag in the reverberation tells us information about the size of the BLR. If we assume the BLR is symmetric and that the motions in the BLR are dominated by the SMBH's gravity (i.e. there is no significant radiation pressure) (these assumptions have been verified in several cases such as Peterson & Wandel (1999), 2000, Onken & Peterson (2002); Kollatschny (2003)), then by invoking the Virial theorem we can derive the mass of the SMBH via the equation:

$$M_{BH} = f\frac{r\Delta V^2}{G}$$

Where r is the characteristic radius of the BLR, ΔV^2 is the velocity dispersion of the broadened emission line, and f is a constant that carries information about the shape of the BLR. (More on the f-factor later.)

The main advantage of RM is that it is not distance dependent. It is not only not dependent on being able to spatially resolve the often angularly tiny sphere of influence of the SMBH, but it is not even dependent upon knowing the distance to the galaxy itself. RM essentially trades spatial resolution requirements for temporal. Therefore, RM can be used on much more distant SMBHs. This means that our entire understanding of SMBHs at cosmic distances depends on the accuracy of the RM sample of SMBHs.

However, RM has some limitations too. Firstly, AGN in the local universe are rare, and AGN that exhibit broad-line emission even rarer, so RM is impossible to apply to the majority of SMBHs. Secondly, in order to precisely measure time lags, one must have the ability to monitor these objects with high temporal coverage over a time span of days to

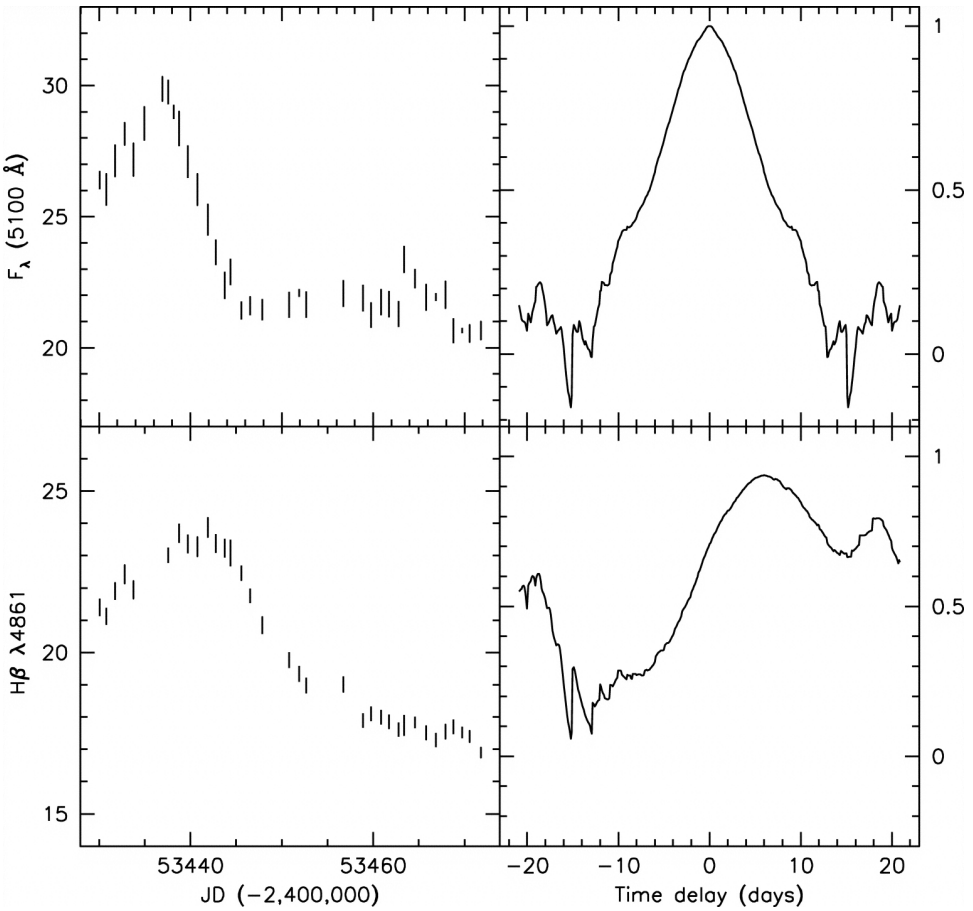

Figure 1.4: From Bentz et al. 2006. Light curves and time delay curves for Seyfert 1 galaxy, NGC 4151, in 5100 Å continuum and broadened Hβ λ4861 light. Left panels: the rise in Hβ flux is delayed with respect to the rise continuum emission. This delay is quantified in the right-hand panels.

months, and monitoring campaigns can be observationally expensive, especially if the AGN happens to be in a more quiescent phase. The other main limitations, as alluded to above, are the assumptions that RM requires, namely the symmetry and shape of the BLR and the lack of importance of radiation pressure. Because we have not yet fully characterized the detailed structure of the BLR for most AGN (though studies are currently underway to determine this such as Grier et al. (2013)), the RM sample requires an average correction

factor to bring it into agreement with the SDM sample. This dependence on the SDM sample makes RM a secondary mass measurement technique.

How is this average correction factor, $\langle f \rangle$, determined? As mentioned above, SMBH masses correlate tightly with host galaxy properties, and we call these correlations "scaling relationships". One particularly tight scaling relationship, the $M_{BH} - \sigma_\star$ relation (Ferrarese & Merritt 2000; Gebhardt et al. 2000), is used to calibrate the RM sample. (It should be noted that yet another assumption is being made here that the RM and SDM sample of black hole share the same correlation between mass and stellar velocity dispersion of the spheroidal component of the host galaxy.) As Figure 1.5 from Park et al. (2012) shows, the average f-factor is the number that brings best-fit line of the RM sample into agreement with the best-fit line for the SDM sample. The f-factor in this case is a population average, but may vary for individual galaxies.

Calculating the f-factor is by no means a trivial task with results ranging from 2.8 ± 0.6 (Graham et al. 2011) to 5.5 ± 1.8 (Onken et al. 2004). It would, therefore, be quite informative to use both RM and SDM on the same SMBH and see, on an individual basis, what f-factor would be needed to make both masses the same. Would the f-factor be similar to the sample average? If it is, then perhaps the size and shape of the BLR is similar for most AGN, and individual measurements of SMBH masses made with RM can be trusted to be accurate. If not, then on an individual basis, RM might only be accurate if one can know the size and structure of the BLR a priori. Regardless of the outcome, understanding the f-factor and how SDM and RM compare is essential to our understanding of SMBH masses at cosmic distances, and therefore our understanding of the role the SMBH plays in host galaxy evolution over cosmic time.

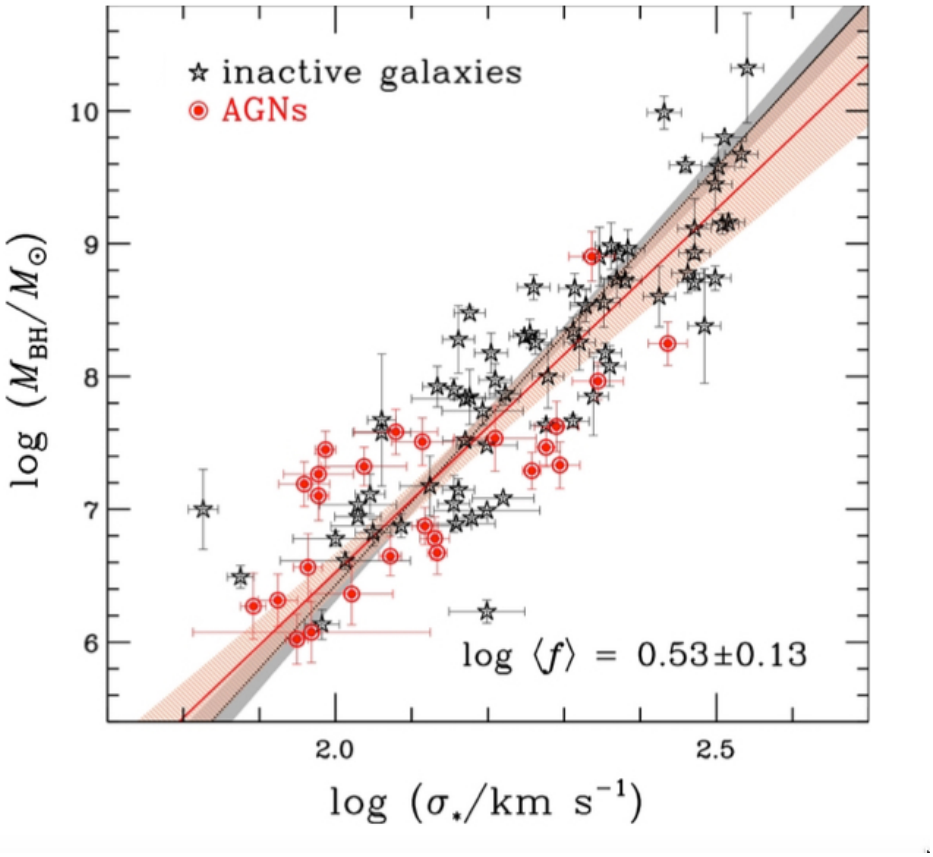

Figure 1.5: Figure from Park et al. (2012) illustrating the derivation of the f-factor by bringing the RM sample (red) onto the same line as the SDM sample (black). Shaded regions represent 1σ confidence intervals of the best fit lines. SDM sample is from McConnell et al. (2011).

1.4 The Role of NGC 6814

As Figures 1.6 and 1.7 illustrate, there exist only a handful of reverberation-mapped AGN to which SDM can be applied. This is because broad-lined AGN are not often nearby enough to be able to resolve the gravitational sphere of influence of the black hole. The possible exceptions occupy the area of Figure 1.6 that is upwards from and to the left of the solid line that represents ourl observational resolution limit of 0.1 arcseconds. NGC 4151's black has already had both its stellar-dynamical mass (Onken et al. 2014) and reverberation mass

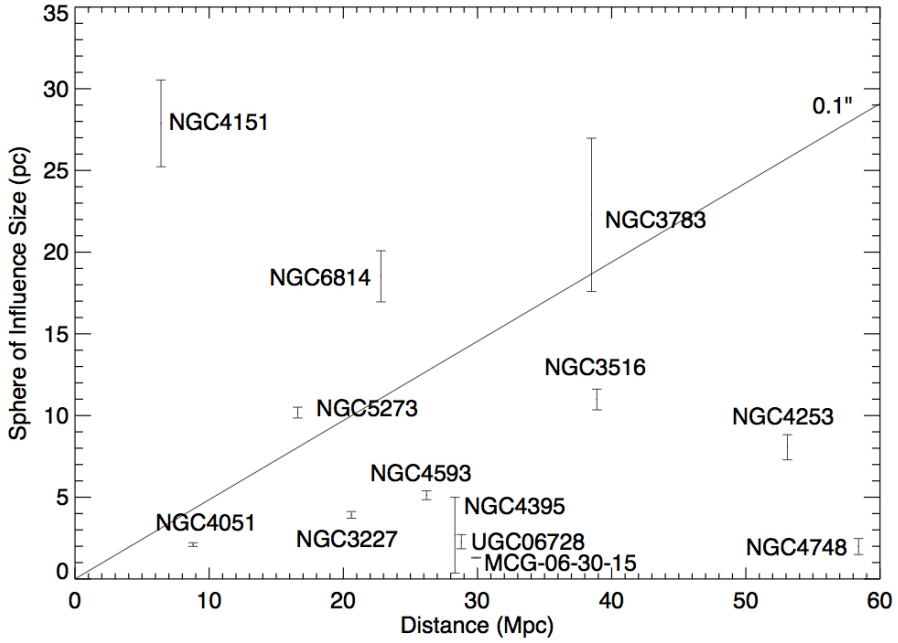

Figure 1.6: Plot of distance versus size of the SMBH's gravitationaly sphere of influence for reverberation-mapped AGN. Solid line represents a typical current spatial resolution limit. Generally, objects above and to the left of line are resolvable, and thus eligible for stellar dynamical mass measurements; objects below and to the right of the solid line are not currently, or for the forseeable future, resolvable. Note that NGC 6814 falls well inside the resolvable region, as does NGC 4151. It should also be noted that distance values do not have error bars because most of these are redshift distances, and so horizontal error bars would add very little information to the plot.

(Bentz et al. 2006) measured. NGC 3227's black hole has also had a marginal SDM mass measurement made Davies et al. (2006) as well as an RM mass measurement (Denney et al. 2010). NGC 5273 and NGC 3783 are within reach, and will be the topic of future SDM studies.

The purpose of this dissertation research is to perform SDM on NGC 6814 for the first time, and to compare both the SDM and RM masses of the SMBH. NGC 6814 will be only the third Seyfert 1 on which SDM will have been performed. The RM mass has already been measured to be $1.44^{+0.271}_{-0.275} \times 10^7$ $M_\odot$ (Bentz & Katz 2015). The Cepheid Period-Luminosity

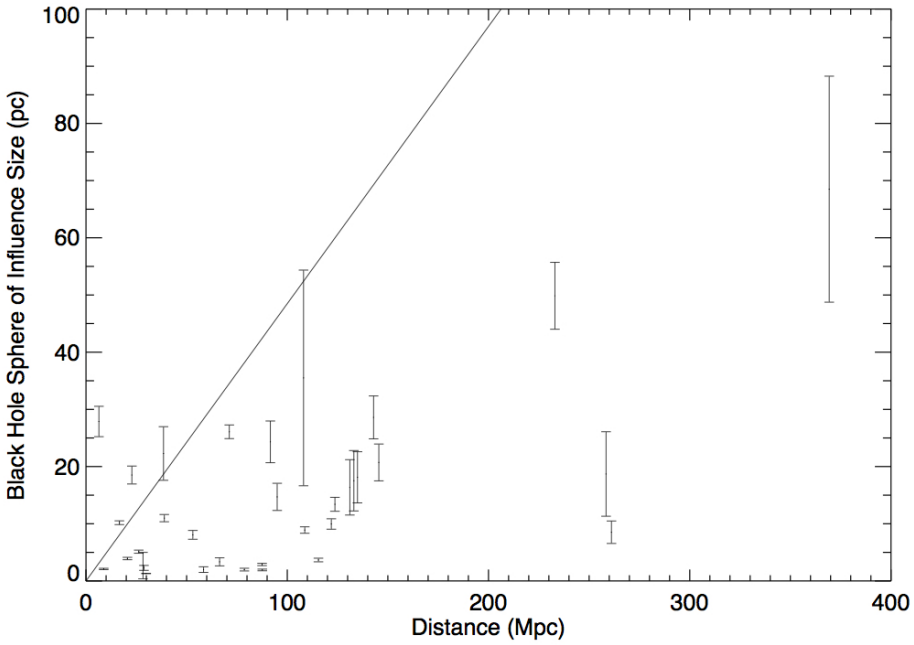

Figure 1.7: Same as previous plot except zoomed out to show all of the RM sample of black hole masses for which there also exists a sphere of influence size estimate. Here it is even more apparent how far out of reach most RM supermassive black holes are from being able to be studied with SDM.

method will be employed to measure the most precise distance to NGC 6814 to date. Once this number is known, then it will be incorporated into the determination of the stellar dynamical mass of the SMBH in NGC 6814.

In Chapter 2 we describe the Cepheid observations and data reduction, and in Chapter 3 we detail our work on defining the Cepheid P-L relationship for NGC 6814. Chapter 4 describes our Gemini observations of the nuclear stellar dynamics, and Chapter 5 reveals the results of the stellar-dynamical modeling. Finally, in Chapter 6 we discuss the implications of our results as well as the future work that could be done to further this area of research.

– 2 –

Cepheid Observations and Measurements

2.1 Background

Cepheid variable stars are incredibly important in astronomy and have profoundly influenced our understanding of the nature of the Universe. They were first discovered by Henrietta Leavitt at the Harvard College Observatory in the early 1900s. While she was studying photographic plates of the Small Magellanic Cloud and Large Magellanic Cloud, she noticed that some of the stars were periodically varying in brightness. Further, she noticed that the brighter the star, the longer the period of the variation. Her research led directly to the discovery of the Cepheid Period-Luminosity relation, also know as The Leavitt Law (Leavitt & Pickering 1912) that states that the distance to a Cepheid can be derived by measuring its period of pulsation and its average apparent magnitude, and then comparing its brightness to Cepheids of known distance. Cepheids became newly established standard candles and ten years later were used by Edwin Hubble to settle the famous Shapley-Curtis debate (Hubble 1922); by identifying a Cepheid in the Andromeda galaxy he proved that "spiral nebulae" were really other galaxies that exist outside of our own galaxy and therefore our Universe is much larger than the Milky Way. Since their discovery, Cepheids have continued to play an indispensible role in cosmic distance measurements.

"Classical" or "Type I" Cepheid variable stars are population I giants/supergiants of spectral class F6-K2 with masses between 4 and 20 solar masses and luminosities between 500 and 30,000 solar luminosities ($-5 < M_v < -2$). Because they are so massive, they are by definition young and found in areas of recent star formation like the spiral arms of late-type galaxies. After they have evolved off the Main Sequence, these giant stars

become Cepheids when they briefly (and sometimes multiple times) cross whats called the "instability strip", where the star's outer layers become unstable and expand and contract periodically (Eddington 1917). The current accepted driver of this instability is changes in the ionization state of helium in its atmosphere. Doubly ionized helium is more opaque to outgoing radiation, and so the stars atmosphere experiences more radiation pressure and expands. As the atmosphere expands, it cools and the doubly ionized helium starts to recombine to form singly ionized helium thereby decreasing the opacity, which in turn decreases the radiation pressure. The force of gravity then causes the atmosphere to contract, and the cycle repeats. All stars experience some form of pulsations, though they are usually damped. Cepheids, however, experience extreme pulsations because their partially ionized zone of helium occurs at the exact depth to cause a resonance (Hofmeister et al. 1964).

The expansion and contraction of the star's atmosphere leads to a typical relative change of 5% in radius and 10% percent in area as well as surface temperature changes of around 1 000 K. These size and temperature changes lead to extremely regular changes in luminosity with time–as regularly as the rotation of the Earth. A Cepheid's light curve can range from a few tenths to two magnitude in amplitude, and it exhibits a characteristic shape that deviates substantially from a sinusoid; the luminosity increases steeply toward maximum, then decreases more gradually toward minimum–like a backward sawtooth wave. The longer the period, the higher average luminosity the Cepheid. The high average luminosity, the large changes in luminosity over time, the characteristic saw-tooth shape of these changes, and the tightness in correlation between luminosity and period are all characteristics that make Cepheids great standard candles for distances up to about 30 Mpc.

Probably the Cepheid P-L relation's most important function has been calibrating another type of standard candle called Type Ia supernovae (Sne Ia). Sne Ia are even more luminous standard candles than Cepheids with absolute magnitudes reaching -19 magnitudes. Their incredible brightnesses allow them to be observed at even greater distances (up to z=1), and so have been used to measure the age, size, and expansion rate of the Universe. The two billion dollar Hubble Space Telescope (HST) was launched in 1990 with one of its main goals being to better constrain H_0 using Cepheid calibrations of secondary distance indicators such as Sn Ia, surface brightness fluctuations, and the Tully-Fisher relation (Freedman et al. 2001). Before the launch, ground-based Cepheid light curves had led to estimates of Ho, the Hubble constant, of anywhere from 50 to 100 km/s/Mpc. depending on the method used. HST, therefore, had the express goal of measuring H_0 to within a 10% uncertainty. The Hubble Key Project, as it was called, led to the discovery of new Cepheids in the 18-galaxy sample. The recalibration of the Sn Ia's distance ladder led to a much more constrained value for H_0 of 72 $\pm$ 8 km/s/Mpc. It also led to the discovery in 1998 that the Universe was not only expanding, but it was accelerating. Cepheid variable stars have played a prominent role in shaping humankind's conception of the Universe's fundamental properties.

2.2 Observations

The very first step toward finding a Cepheid distance to NGC 6814 is to take pictures of it at different times. Thanks to the hard work of Dr. Misty C. Bentz and her Co-Investigators, we were able to collect the necessary HST data. Much of our observing strategy is guided by previous studies such as Riess et al. (2005), and Riess et al. (2009), who have already clearly

demonstrated that HST is uniquely suitable for detecting Cepheids at up to 30 Mpc. Previous studies used the Wide Field Pixel Camera 2 (WFPC2), the Near-Infrared Camera and Multi-Object Spectrograph (NICMOS), or the Advanced Camera for Surveys (ACS), whereas we chose to use the Wide Field Camera 3 (WFC3) for several reasons. Firstly, the UVIS and IR detectors have a relatively small plate scale (0.04″x0.04″) for UVIS and 0.13″x0.13″ for IR), which is important for decreasing the effects of crowding from the many other stars in the galaxy field as well as from background sources. Secondly, WFC3 has the large field of view (162″x162″ for UVIS and 136″x123″ for IR) necessary to capture the majority of the galaxy in a single exposure, thereby increasing the observing efficiency. Thirdly, the V-band F555W filter that we used for the majority of our exposures happily coincides with the maximum throughput of WFC3-UVIS. Lastly, and most importantly, WFC3 is a relatively new instrument, and so has not yet been degraded by the harsh environment of space.

The timing of our observations followed Freedman et al. 1994 who showed that in order to maximize detection efficiency and reduce aliasing, it is best to image the galaxy with a power law spacing between epochs. The range of epochs chosen is designed to be most sensitive to Cepheids with periods between 20 and 60 days, which represents an apparent magnitude range of $m_V \approx$ 25.2 – 27.4 for an assumed distance of 22 Mpc. While it is true that the longer the period, the brighter the Cepheid and the more likely we are to detect it, there is a practical limit to how long we can monitor an object. In order to adequately sample the light curve on a very long-period Cepheid, one would have to implement a very long observing campaign. However, based on similar studies, we expected to detect enough Cepheids at high enough signal to noise to be able to constrain the distance to NGC 6814 without going after the very long period Cepheids. Therefore, the observations span a period

of 69.1 days total beginning 2013-08-10 and ending 2013-10-08, and contain thirteen visits with power-law spacing. This limit for total campaign length was set by the largest time period in which we could hold the orientation of the spacecraft fixed for all the visits — making all the stars fall on the same parts of the chip in every image.

Our choice of filters also follows the well-established strategy of Freedman et al. (1994). The filter which was used during 12 of the visits was the UVIS detector's V-band F555W filter (λ_c = 530.8 nm, $\Delta\lambda$ = 156.2 nm). Even though Cepheid light curves are known to display the largest amplitudes of variation at shorter wavelengths, the reddening and extinction combined with diminished throughput at these wavelengths counteracts this advantage Freedman et al. (1994). Therefore, the V-band is a good compromise between variability amplitude and extinction/reddening. Each of the V-band epochs spans most of the 56-minute visibility of NGC 6814 during a single 96-minute orbit of HST, and are composed of four 600-second exposures in a four-point dither pattern to decrease the effects of systematic errors of individual pixels and increase the sampling of the point spread functions (PSFs). The total on-source time for the V-band was 28.8 ks.

The high variability of the Cepheids in the F555W filter is ideal for locating them and measuring their periods of pulsation, but because we also needed their mean apparent magnitudes, five of the twelve visits also included UVIS I-band F814W (λ_c = 802.4 nm, $\Delta\lambda$ = 153.6 nm) observations. Cepheids' mean apparent magnitudes vary less in the I-band, so fewer epochs are needed than in the V-band. The I-band visits, each consisting of four 630-second exposures in a four point dither pattern, occurred at visits 1, 3, 7, 10, and 12 on the orbit directly after the V-band's orbit. These individual I-band exposures are slightly longer than the V-band ones because the I-band fields will contain more stars and thus be more crowded.

A longer exposure time will increase the S/N and hopefully make up for the increased crowding. The total I-band on-source time is 12.6 ks. The I-band and V-band observations were taken as close together in time as possible so that the I-band variability, though smaller in amplitude, can be used to corroborate the variability in the V-band.

Table 2.1: HST Observations

Visit:Orbit	**Setup**	**Middle MJD**	**Days after Visit 1** (days)	**Exp. Time** (s)
1:1	UVIS/F555W	56514.54296	0.0	2400.00
1:2	UVIS/F814W	56514.60735	0.1	2520.00
2:1	UVIS/F555W	56525.08347	12.2	2400.00
3:1	UVIS/F555W	56531.55688	19.7	2400.00
3:2	UVIS/F814W	56531.61996	19.8	2500.00
4:1	UVIS/F555W	56535.60736	24.4	2400.00
5:1	UVIS/F555W	56541.04396	30.7	2400.00
6:1	UVIS/F555W	56543.20700	33.2	2400.00
7:1	UVIS/F555W	56545.09639	35.4	2400.00
7:2	UVIS/F814W	56545.20650	35.5	2520.00
8:1	UVIS/F555W	56546.66917	37.2	2400.00
9:1	UVIS/F555W	56554.16888	45.9	2400.00
10:1	UVIS/F555W	56560.12535	52.8	2400.00
10:2	UVIS/F814W	56560.18920	52.8	2520.00
11:1	UVIS/F555W	56567.87078	61.7	2400.00
12:1	UVIS/F555W	56574.27629	69.1	2400.00
12:2	UVIS/F814W	56574.33932	69.2	2520.00
13:1-2	IR/F160W	56518.79585	5.0	5041.57
			Total F555W	**28800.00**
			Total F814W	**12600.00**
			Total F160W	**5041.57**

(See Table 2.1 for an overview of the observations.) If a Cepheid candidate shows the same pattern of brightness changes in both bands, then we can be more certain that we have found a true variable star as opposed to noise.

Finally, H-band observations using the WFC3-IR detector and the F160W filter (λ_c = 1536.9 nm, $\Delta\lambda$ = 268.3 nm) were taken on the thirteenth visit over the course of two orbits

for a total exposure time of 5.04157 ks. These data are taken for three purposes: first, to further counter the effects of extinction and reddening by factor of 5 over the V-band (Riess et al. 2011); second, to ensure that there are no zeropoint errors when tying our work to the Sne Ia calibration of Cepheids of Riess et al. (2011); and third, because metallicity affects the Cepheid P-L relation less at longer wavelengths (Marconi et al. 2005).

2.3 Data Processing: Tweakreg and Astrodrizzle

One of the many perks of working with HST WFC3 data is that they can be downloaded from the Multimission Archive at Space Telescope (MAST) both in raw form and in calibrated form. If no special initial processing is needed, which is the case for our data, then they can be downloaded having already been through a standard image processing pipeline called "calwf3:. This pipeline treats the UVIS and IR data slightly differently, but in the end outputs images in the same stage of preliminary processing that carry the suffix "flt.fits".

The basic UVIS pipeline processing begins with a module called "wf3ccd", which creates a ERR (error) and DQ (data quality) fits extension by computing the error for each pixel and flagging known bad pixels. It then subtracts the bias and trims the overscan regions. Next, "wf3rej" is called to reject cosmic rays and combine the images from the two chips into one. Lastly, the images are run through "wf32d" to be dark-subtracted and flat-fielded.

Because IR detectors are different from CCDs in that all the pixels are independently sampled and can be read out non-destructively, the IR pipeline is slightly different. The first module called "wf3ir" flags bad pixels, subtracts the zeroth read, attaches ERR and DQ extensions, corrects for non-linearity, subtracts the dark current (very important in the IR), and flat fields the images. Lastly, the data are sent through wf3rej, which is the

same as for the UVIS cosmic ray rejection. All of these steps can be done even before the data are downloaded from the MAST archive because they are standard steps that usually do not require customization. The next steps including aligning, correcting for geometric distortions, and stacking the images all require the user-modified input parameters, so the data are downloaded and run through another pipeline package called Drizzlepac.

Our first post-download step was to run the data through a task called TweakReg in order to very precisely align the images. Because the goal of our science is to identify the sames stars in images taken across several epochs, it is very important to align our images as accurately as possible. Though the headers of the fits files contain WCS information that can be used to align the images taken within the same visit, TweakReg is needed to account for slight pointing errors that occur between visits and correct these WCS files to within 0.1 pixel accuracy (4 mas for UVIS, 10 mas for IR) (Gilliland 2005). One cause of these pointing errors is that HST experiences periodic thermal expansion and contraction, or 'breathing', as it orbits the Earth. As the telescope breathes, the focus changes, thereby changing the shape and centroid location of the point spread function (PSF) [1]. This change in focus affects the telescope's Fine Guidance Sensors' ability to track guide stars (see Drizzelpac Handbook Appendices for more info).

Another source of error that affects the alignment of images is geometric distortions. HST's WFC3 images suffer from a few different sources of geometric distortions, the most obvious of which is tilt of the focal surface as it reaches the detectors. This is due to the limited amount of space each instrument's optical bench can occupy and to the desire to

[1] A point spread function is the distribution of flux on the detector that is created by a point source of light

reduce the number of reflections in the light path in order to preserve throughput. The UVIS detector is tilted approximately 21° with respect to one of its diagonals, whereas the IR detector is slanted at approximately 10° about its x-axis. This causes the UVIS field of view (FOV), when projected on the sky, to take the shape of a rhombus, and the IR FOV to resemble a rectangle. These tilts are not difficult to correct. What is difficult to correct is the change in plate scale across the UVIS and IR detectors. The slight change in plate scale leads to change in area-per-pixel of 7% across the diagonal of the UVIS chip and 4% across the IR chip.

To counteract breathing and geometric distortions to achieve sub-pixel image registration, TweakReg uses an algorithm similar to DAOFIND to identify point sources from each image. It then creates a catalog of source positions for each image and applies a distortion model that is stored in each image's .fits header. Next, it matches these undistorted source positions to a user specified reference. In our case, we used the default reference image, which is the one that has the most sources in common with all the other images. To make sure cosmic rays or faint sources do not affect the alignment correction, tweakreg allows the user to specify a lower and upper pixel value threshold, which we chose 400 for our lower threshold and 50 000 for our maximum (below the full well depths of the IR and UVIS detectors). After all undistorted offsets between frames are calculated, they are used to update the WCS coordinates of each image's header.

With the shifts stored in the image headers, the data were then stacked using the task Astrodrizzle. Astrodrizzle (short for astrometric drizzle) uses a technique known as drizzling (Fruchter & Hook 1997) formally referred to as variable-pixel linear reconstruction, the goal of which is to reconstruct the spatial information in a stacked image without altering the

signal-to-noise ratio. On a basic level, it works by combining two separate image reconstruction methods into one: interlacing and shift and add. Interlacing, which really only works if dithers are integer pixel values away from one another, is just matching up de-shifted, corresponding pixels values and adding them together. The other method, shift-and-add, involves resampling the pixels onto a finer grid, then de-shifting them by the dither amount, and finally adding them to the output image. This method still ends up convolving the images by the original pixel shape, thus blurring the final output image. Because our images are a combination of integer and non-integer dithers, astrodrizzles combination of shift-and-add and interlacing is key to reducing correlated noise while increasing final resolution.

So, using astrodrizzle we first we stacked all of the V-band images (48 images total, 4 per visit for 12 visits) to create one "deep" frame. Then, using the V-band deep frame as the reference image to which all other frames were aligned, each of the individual visits for the V- and I-bands were combined yielding 12 V-band images and 5 I-band images. Next, all of the I-band images (20 images total, 4 per visit for 5 visits) were drizzled together to create an I-band deep frame, but once again using the V-band deep frame as a reference. Finally, all of the H-band data was combined, also using the V-band deep frame as a reference. Once the exposures for each orbit are combined and all visits are all drizzled to a common reference, then it was finally time to perform photometry.

2.4 Measurements

2.4.1 DoPHOT

Our photometry software of choice is a Fortran code called DoPHOT (Mateo & Schechter 1989). DoPHOT is an automated code designed to iteratively search for objects in images

and output their brightness, positions, and classification. Our main reason for choosing DoPHOT over the several other photometry packages available is, as the manual states: "The particular application for which DoPHOT was designed...involved large numbers of poorly sampled, low signal-to-noise images for which a fast, hands-off approach seemed desirable." These attributes describe our needs quite well. There are tens of thousands of very crowded point sources in our images. Another reason we chose to use DoPHOT is that our collaborator, Laura Ferrarese, was already quite familiar with it; she used it when she was working the Hubble Key Project. Not only did this mean we had excellent mentoring during the learning-how-to-use-it process, but our results can be tied in with the many important previous studies that used this same software to perform Cepheid photometry. Furthermore, DoPHOT's capabilities are already well-studied and have been refined over the more than 20 years since its first release.

Conceptually, DoPHOT works by creating a model for different types of object that may be found in the image. For example, DoPHOT uses an elliptical gaussian to model stars, a more extended elliptical gaussian to model background galaxies, two elliptical gaussians to model stars with double stars or stars whose PSFs overlap, etc. Dophot scans an image and fits models to the sources of emission, and then outputs their classifications as well as their shape, brightness, and positional data. The user guides DoPHOT toward appropriate classifications and accurate apparent magnitudes by modifying an input parameter file. This parameter file allows the user to specify among other things information about the expected size of the PSF, the sky value, the noise properties of the image, the upper and lower pixel value threshold for object identification, and desired significance of the identifications. DoPHOT takes this information and first creates a psf model by searching for the brightest

objects in the image that have roughly the same FWHM as the user specified. Next, it averages the shape of those PSFs together to get an average PSF shape. Starting at the upper threshold, it searches for objects whose flux is above that value and classifies them according to how they compare to the PSF shape. DoPHOT then subtracts those objects from the image, lowers the threshold, creates a new average PSF model, adds back in and re-fits the brighter objects using the new PSF model, subtracts them again, identifies fainter objects and subtracts these too, and repeats the process iteratively until the lower threshold is reached. By remaking the PSF model for every iteration, the PSF shape should get more and more accurate. It should also be noted that DoPHOT creates a noise model for the image. Every time a model PSF is subtracted from the image, the program runs the risk of falsely identifying the residuals as a new source. To avoid this problem DoPHOT adds noise to the image after every PSF subtraction, which by default is 30% of the brightness of the subtracted object.

Another useful feature of DoPHOT is that it allows for "warmstarts". A warmstart is a way the user can use information from an image with higher S/N (e.g. a deep frame) to force identifications in lower S/N images. For example, if a star is detected in a stacked deep frame but is only marginally detected in a single visit frame, then DoPHOT will perform the fit in the single frame even if it does not meet the original threshold criteria for that fit. It should be noted that DoPHOT's model magnitudes are calculated by fitting a model to the PSF and then using information about the height of that model rather than integrating the flux under it.

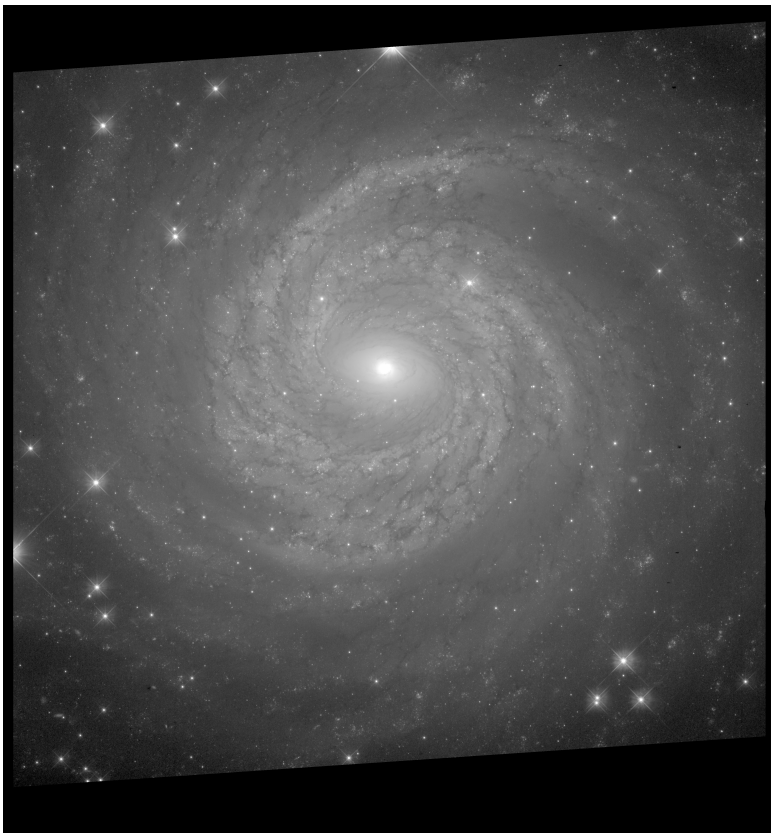

Figure 2.1: HST WFC3 image of NGC 6814 using the V-band, F555W filter. This image was formed by aligning and stacking all 12 visits to form a "deep" frame.

2.4.2 Data Processing

DoPHOT requires input images to be in a very specific format down to the length of the header. To prepare our data for DoPHOT, we first multiplied by the summed exposure time to get the images in units of electrons, rather than electrons per second, the default unit for pipeline-processed HST data. Next, because the sky background flux had been subtracted during drizzling, we added back in the sum of the sky backgrounds for each of the stacked images. Because DoPHOT requires data to be of integer type, we multiplied our images by a factor of four to maintain precision, and then converted our data to integers. We also made the minimum pixel value -100 electrons and the maximum 32 000 electrons using the

IRAF routine called "imarith". Lastly, we masked out (set to zero) areas of the image that carry no photometric information such as the first and last several columns as well as two triangular, wedge-shaped areas on top and bottom created by the distortion correction of the FOV. This procedure was performed on all of the twelve V-band visit images, the 5 I-band images, the H-band image, and also the deep frames. Figure 2.1 shows our resultant V-band deep frame. With all of our images in the proper format, we tuned the parameter files and ran DoPHOT on all of our images.

DoPHOT classifies objects by comparing their shape to its working PSF model. The objects are given a number designation from 1 to 9. Stars, which are what we are after, are labeled type 1s and 7s and have FWHMs very similar to the averaged PSF model. Whether a star is a 1 or a 7 depends on its signal-to-noise. Stars with higher signal-to-noise, or type 1s, and are fit with the full 7-parameter model that consists of x- and y-position (in pixels), apparent magnitude, x- and y- FWHM, tilt, underlying sky value, and all associated errors. The lower signal-to-noise Type 7s are only fit with a 4-parameter fit: x- and y-position, apparent magnitude, and sky value. DoPHOT classifies other object types too, but these are of little interest to us, except they tell us that these are not stars.

In order to check that our fits were finding all the stars and not fitting too much noise, we made a color-coded region file to plot in ds9 on top of the image that was fit. This allowed us to check the identifications by eye and see if all the likely star candidates were being fit. As can seen in Figure 2.2, green circles are stars with the full 7-parameter fit, and yellow circles are stars with only enough signal-to-noise to perform a 4-parameter fit (only sky level, x- and y-position, and central intensity). On average, about 80 000 objects were fit and classified per image.

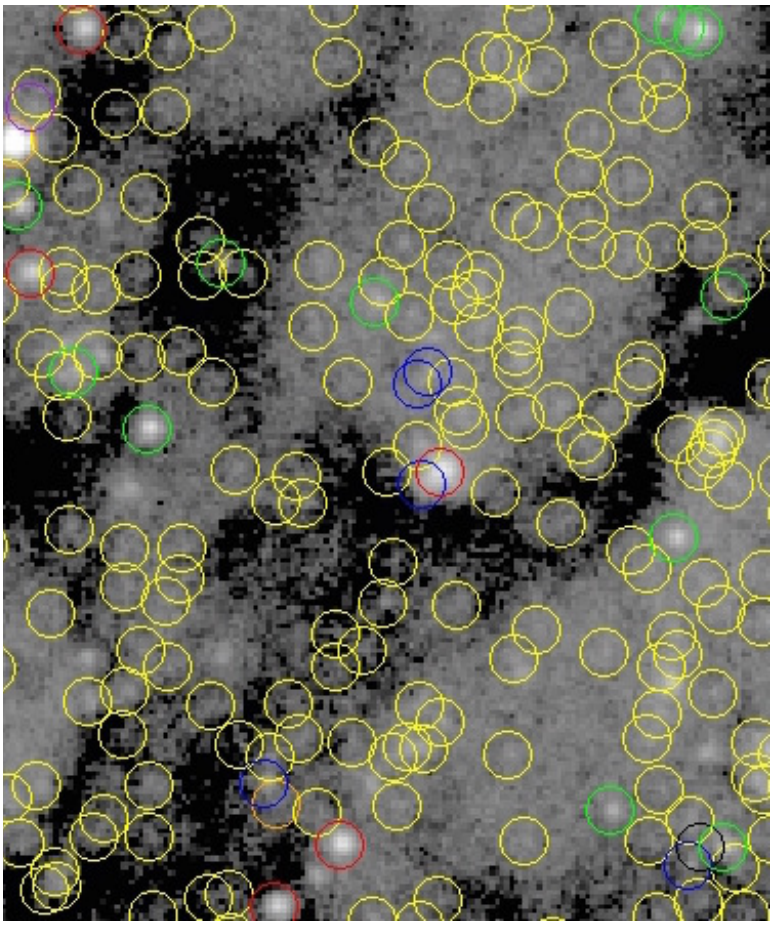

Figure 2.2: Zoomed-in section of V-band image of NGC 6814 with region file overlay showing DoPHOT's identifications. Green circles are point sources with enough S/N to perform a 7-parameter fit. Yellow circles represent lower SNR point source identification yielding only a 4-parameter fit. Red designates an object that is not as peaked as a star and is possibly a background galaxy. Blue is also not as peaked as a single star, but probably a double star, and black cirlces are too low S/N for even a 4-parameter fit.

With all of our images run through DoPHOT, we then performed DoPHOT warmstarts using the higher signal-to-noise deep frame identifications as inputs to the individual visits fits. A few thousand more objects were found in the individual visits after performing these warmstarts.

2.4.3 Aperture Corrections

Astronomers have been developing ways to accurately measure the brightness of stars in crowded fields using digital detectors for decades. (An in depth review of crowded field photometry is beyond the scope of this work. However, a few basic concepts will be reviewed here for the sake of understanding the next step in our data analysis.) A simplistic approach to flux measurement is aperture photometry whereby a circle, or "aperture", is drawn around the light source and the flux inside this circle is integrated. An annulus is then drawn around that circle to measure the sky background flux, which is then subtracted from the source flux. When performing aperture photometry, it is best to limit the aperture radius to a size that balances the goal of capturing as much light as possible from the source while simultaneously minimizing contamination from shot noise, background flux variations, and neighboring sources. This method works well in sparser fields in which it can capture most of the light in the PSF, including the extended emission in the wings. Aperture photometry cannot be used alone in our case because our NGC 6814 field is extremely crowded.

Not only does DoPHOT measure and output aperture fluxes, but it also (as described above) outputs fluxes measured via PSF fitting. Photometry derived from PSF fitting has the advantage of being able to be used in crowded fields because it can separate the light of nearby sources from each other. However, the PSF models can only be fit to a small region around the PSF, but are assumed to be smooth, so they might not account for all the light that is contained in the extended wings of the profile. This means that there could exist a systematic underestimation of the brightness of the sources. Not only could there be missing flux from the PSF fits, but that amount of missing flux could vary as a function of position

in the FOV. This is because the PSF shape can change as a function of position on the chip. In fact, the PSF also varies with the waveband of the image, so the amount of missing flux would differ between filters as well.

A way of compensating for the missing flux of the model PSF fits is to perform what are called aperture corrections. Aperture corrections entail utilizing a sparse, uniformly distributed field of point sources to measure the difference between the fluxes measured with PSF fitting and that measured with aperture photometry. This difference is a measurement of the missing flux in the PSF fits, and is called the aperture correction. To characterize the aperture correction across the NGC 6814 FOV, we turned to Hubble Archive images.

Omega Centauri is a well-known globular cluster of stars (largest in the Milky Way) that has been imaged extensively, and in all of the same filters we are using. The field is evenly populated with stars, but not nearly as crowded as that of NGC 6814, and has been a popular choice for aperture corrections of other studies. For our aperture photometry measurements, we chose to use a radius of 10 pixels for two reasons. First, trial and error suggested that as radii were made larger than 10 pixels the aperture fluxes were no longer increasing monotonically. This indicates that most of the flux was being captured inside that radius. Secondly, WFC3 has already had its zeropoint calibrations calculated at 10-pixel aperture, so that any missing flux outside of that radius would be corrected during our zeropoint corrections. After running these Omega Centauri images through DoPHOT we measured the difference between model and PSF magnitudes at different locations on the chip. Once we had these aperture corrections as a function of position on the image, we experimented with fitting analytical functions to these differences. After experimenting with different orders of polynomials, we discovered that a slightly tilted plane (see blue surface in

Figures 2.3, 2.4, and 2.5) best characterized the changing aperture corrections (red points) across the image. Higher order terms added no useful information.

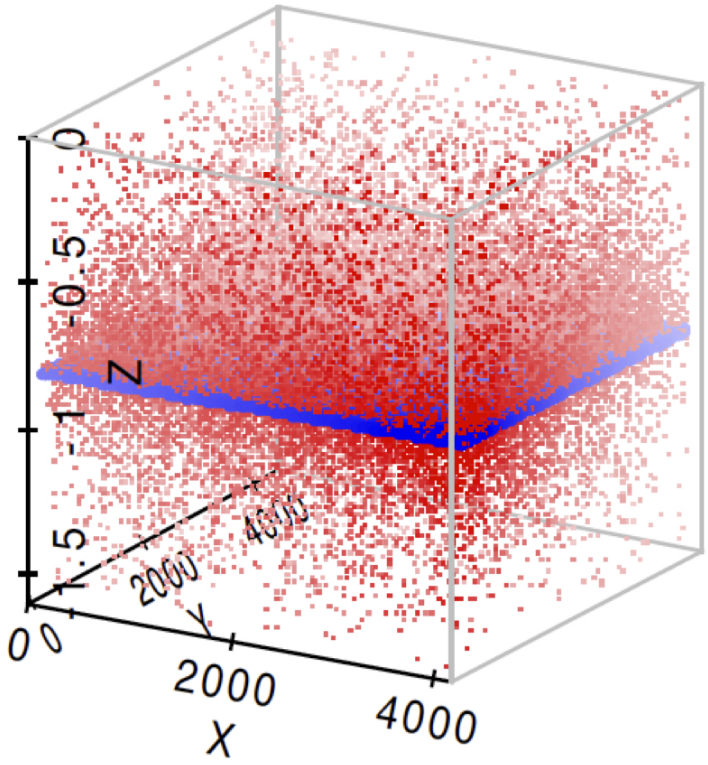

Figure 2.3: Aperture correction measured from Omega Centauri V-band frame plotted as a function of position on the chip. Red points represent the difference (in magnitudes) between PSF model and 10-pixel aperture flux. Blue surface traces the best-fit, slightly tilted plane that was fit to the red points.

As can be seen in Figures 2.3, 2.4, and 2.5, the amount of flux missing from the PSF fits, about 0.7 magnitudes, was not trivial. These aperture correction surfaces were added DoPHOT's PSF fitting brightness measurements of NGC 6814.

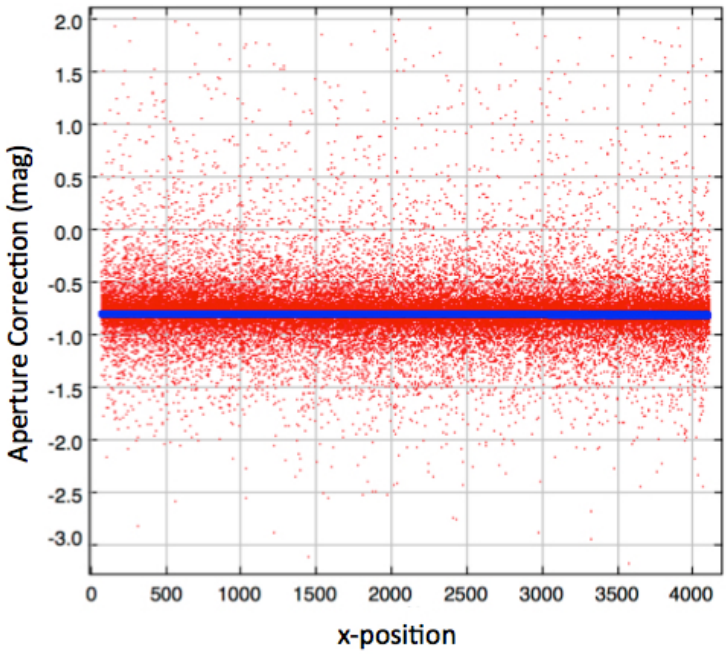

Figure 2.4: Side view (y=0) of same data as Figure 2.3. Note that the tilt of the blue points composing the best-fit plane is very slight, and is almost imperceptible in this image.

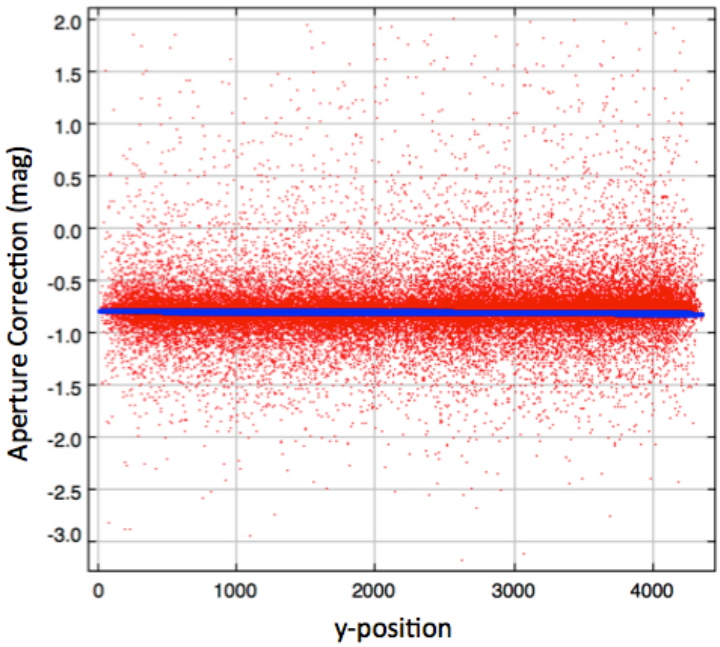

Figure 2.5: Side view (x=0) of same data as Figure 2.3. Note that the tilt of the blue points composing the best-fit plane is very slight, and is almost imperceptible in this image.

2.4.4 Magnitude Calibrations and Corrections

Because our end goal is to compare the average brightness of our Cepheids to a set of known Cepheids, we need to convert the brightness measurements from DoPHOT to the same standardized photometric system as the comparison Cepheids. The three most common standardized photometric systems used by astronomers are the Vega system (see Bohlin & Gilliland (2004)), the ST system (see Koornneef et al. (1986)), and the AB system (see Oke (1964)). The Cepheid P-L relations we employ later are in UBVRI magnitudes, which are based on the Vega system. Luckily, the instruments aboard HST have already been well-characterized (see Sirianni et al. (2005)), and so our calibrations involve just a few quick calculations.

Starting with our DoPHOT photometry, and recalling that our images have been multiplied by 4 to preserve precision, we first converted our data magnitudes back to instrumental counts (in electrons) via the equation:

$$Counts_V = \frac{1}{4} \times 10^{\frac{m_{V,dat}}{-2.5}} \tag{2.1}$$

$$Counts_I = \frac{1}{4} \times 10^{\frac{m_{I,dat}}{-2.5}} \tag{2.2}$$

We then converted from electrons to ST magnitudes using:

$$m_{V,ST} = -2.5 \log(\frac{Counts_V}{t_V}) + zpt_V - Ext_V \tag{2.3}$$

$$m_{I,ST} = -2.5 \log(\frac{Counts_V}{t_I}) + zpt_V - Ext_V \tag{2.4}$$

Where t is the exposure time (2400 s for V, 2520 s for I), zpt is the photometric zeropoint for the ST system, which is calculated by using the header keywords "photflamV" or "photflamI" and the equation:

$$zpt_V = -2.5\log(photflamV) - 21.1 \tag{2.5}$$

$$zpt_I = -2.5\log(photflamI) - 21.1 \tag{2.6}$$

Ext is the extinction due to interstellar absorption and scattering, which was calculated using Schlafly & Finkbeiner (2011)'s recalibration of the absorption coefficients: $A_B = 0.673$ and $A_V = 0.509$. This implies that $E(B-V) = A_B - A_V = 0.673 - 0.509 = 0.164$ magnitudes. To calculate the extinctions, Ext_V and Ext_I, the $E(B-V)$ color was then multiplied by coefficients (3.177 for V and 1.825 for I) taken from Table 14 of Sirianni et al. (2005), which lists extinction ratios in WFC filters for different SEDs. It should be noted that these coefficients depend on the spectral energy distribution of the object that is emitting light, which are Cepheids in our case. Because Cepheids are F-, G-, and K-type giant stars, we assumed a GII-type SED.

Finally, from our extinction-corrected ST magnitudes, we converted to Vega UBVRI magnitudes using the Sirianni et al. (2005) transformations and synthetic photometry coefficients from Sahu et al. (2014):

$$m_{V,UBVRI} = m_{V,ST} - zpt_V + 25.741 - 0.086 \tag{2.7}$$

$$m_{I,UBVRI} = m_{I,ST} - zpt_I + 24.603 - 0.003 \tag{2.8}$$

(Note that we subtracted to ST zeropoint before adding the UBVRI corrections.)

Now that we had our calibrated photometry, it was time to find the Cepheids, which is the subject of the next Chapter.

– 3 –

Cepheid Analysis

In Chapter 2, we described how we performed photometry on our HST imaging of NGC 6814. This photometry resulted in multi-epoch, calibrated V- and I-band magnitudes and magnitude errors for each star-like object at position x,y on the chip. In this chapter, we describe the steps we have taken toward identifying the expected 40 to 60 true Cepheids from our large sample of over 100 000 candidates.

3.1 Sample Selection Cuts

3.1.1 Initial Cuts

A true Cepheid whose period we can measure with a reasonable precision must meet a couple of key requirements. First, its location on the sky will remain the same (within an error tolerance) for all epochs in which it is identified. Therefore, we used a matching algorithm to pick out the stars that were identified to be in the same location between at least two epochs within the same band. To perform the match, we used the software package called Tool for OPerations on Catalogues And Tables, or TOPCAT (Taylor 2005), which is an extremely useful graphical viewer and editor of tabular data. We executed an inclusive, 2D-cartesian match with an radial error tolerance of 1.0 pixel for all 12 V-band epochs and also all 5 I-band epochs. If a DoPHOT identification was due to noise, then it would be unlikely for that same ID to be made for another epoch. This step helped eliminate some of the false IDs that were due to noise. After making this cut, we were left with a catalog of all sources that were identified in at least two epochs within a given waveband. The V-band catalog

containing 124 093 candidates, and I-band catalog containing 123 290 candidates, were still separate at this point.

The next logical cut was that we required a Cepheid candidate to be identified in at least 9 of the 12 V-band epochs and 3 of the 5 I-band epochs. This requirement exists so that we have enough constraints to produce a good fit to a light curve. This cut was again made using TOPCAT. We loaded the catalogs into Topcat, and replaced all the null IDs of a given sources brightness with a very large number, 9 999. Then we wrote an IDL script to loop through each source and throw out ones that had fewer than the requisite number of identifications, which could be identified by having a sum of all of the brightness measurements across all epochs that was greater than $9\,999 \cdot 3 = 32\,000$ and $9\,999 \cdot 2 = 21\,000$ for the V- and I-band respectively. Discarding sources with too few epochs in which they were identified may have eliminated some dimmer Cepheids on the edge of detection, but these Cepheids would have had too few constraints on their light curves to be of any use to us anyway. Our sample size now contained 51 581 V-band candidates and 99 945 I-band candidates. As we try to measure the distance to NGC 6814, we must walk the line between detecting enough Cepheids on the faint end to constrain the slope of the P-L relation, but we also need to include only Cepheids for which we have accurate measurements. One bad Cepheid could contribute more error to our distance measurement than would add statistical significance to our sample.

Finally, we used TOPCAT to match the V-band and I-Band catalogs leaving us with 22 109 candidates. Because all images were drizzled to the same reference image, their alignment is to the nearest 0.1 pixel. This means that the x and y coordinates of a given source should be the same within 0.1 pixel between all epochs and across both wavebands.

Therefore, we required the coordinates of each Cepheid candidate to be matched to within 1 pixel in V and I. Even though we expect the alignment between images to be much better, we make this cut conservatively because there are future cuts that will eliminate false matches.

3.1.2 Variability Index Cut

Our sample at this point only contained sources that had at least 9 V-band brightness measurements and corresponding 3 I-band ones. From our initial sample of over 100 000 sources, we had now excluded all but approximately 22 109. However, this sample was still composed primarily of non-Cepheid bright stars. To try to fit a light curves to all of these sources and weed out the non-Cepheids would take several days of computing time. Therefore, we make one more sample selection cut. Because Cepheids are variable, and their V and I band variability is almost contemporaneous, we required a sources amplitude of variability to be above a certain threshold and to be reflected in both bands simultaneously. This is why we designed our observations so that all five I-band observations have V-band observations taken on adjacent orbits. A quick and common way of characterizing the coherence of the variability of these five V- and I-band brightness measurements is to calculate what is called a variability index.

Our variability index for two-filter photometry calculation is based on the methods described by Welch & Stetson (1993). Dr. Bentz wrote an IDL script which takes as input V-band and I-band light curves and associated uncertainties along with the dates of the observations and outputs a number that reflects each sources degree of variability. We then decide a cutoff threshold for how large this number must be in order to keep it as a Cepheid candidate.

But how is the variability index calculated? First, a mean brightness is calculated for each source in both V and I. Because the uncertainty in brightness for a given source can vary between epochs, each mean brightness is weighted by this error:

$$\sum_{i=1}^{n} \frac{V_i}{\sigma_{V,i}^2} \Bigg/ \sum_{i=1}^{n} \frac{1}{\sigma_{V,i}^2} \tag{3.1}$$

$$\sum_{i=1}^{n} \frac{I_i}{\sigma_{I,i}^2} \Bigg/ \sum_{i=1}^{n} \frac{1}{\sigma_{I,i}^2} \tag{3.2}$$

Next, using this weighted mean, the difference between each individual brightness measurement and that sources mean brightness is calculated, which is called a residual. The residuals are divided, or normalized, by the associated error so that the larger the error, the smaller the residual:

$$\delta V_i = \frac{V_i - \bar{V}}{\sigma_{V,i}^2} \tag{3.3}$$

$$\delta I_i = \frac{I_i - \bar{I}}{\sigma_{I,i}^2} \tag{3.4}$$

Note that the residuals can be either positive or negative depending on whether the source at a given epoch is brighter or dimmer than the weighted mean brightness. The V and I residuals for each epoch are multiplied together and then summed over all epochs, and then normalized by the number of epochs:

$$VariabilityIndex = \sqrt{\frac{n}{n-1}} \frac{1}{n} \sum_{i=1}^{n} (\delta V_i \delta I_i) = \sqrt{\frac{1}{n(n-1)}} \sum_{i=1}^{n} (\delta V_i \delta I_i) \tag{3.5}$$

All of this is performed on each source. Sources with correlated variability will have V and I residuals that are either both positive or both negative at a given epoch. Because multiplying two negative numbers together results in a positive number (and the same with two positive numbers), sources with correlated variability will sum to be a positive number. Sources with random, uncorrelated variability will have residual products with both positive and negative signs, and thus their sum will tend toward zero. As a bonus, sources with correlated and high-amplitude variability will have a higher index than an equally well-correlated but smaller-amplitude varying source.

There are a couple of caveats to using this method to make sample selection cuts. First, this methods sensitivity increases at the number of epochs to the one-half power. Because we have 5 epochs with both V and I observations, this technique is half as sensitive to variability as if we had 25 epochs. This makes sense because one can imagine that in the case of very few epochs, random errors would have a higher probability accidentally being correlated. Random errors, even if accidentally correlated, are unlikely to be high-amplitude. However, if there exists a single very high-amplitude residual for an epoch, which could conceivably be due to a cosmic ray hit or some other anomaly of the detector or reduction process, then the variability index could be artificially high (or highly negative). A way to measure the number of sources with artificially highly positive variability indices is to look at the number of highly negative variability indices. The positive spuriously high indices will be hard to distinguish from the actual variable stars. However, indices that are highly negative must be spurious because they would be anti-correlated, which Cepheids are not. If we assume an equal likelihood that a source has a positive or negative spuriously high residual, then the number of highly negative sources should give us an idea of the number of high ones.

Furthermore, even if we do include a few sources for which their index is artificially high, there will not be enough to dramatically increase the computing time required for the next step, which is actual light curve fitting. In other words, these few spuriously high variability index sources will be excluded during the actual modeling.

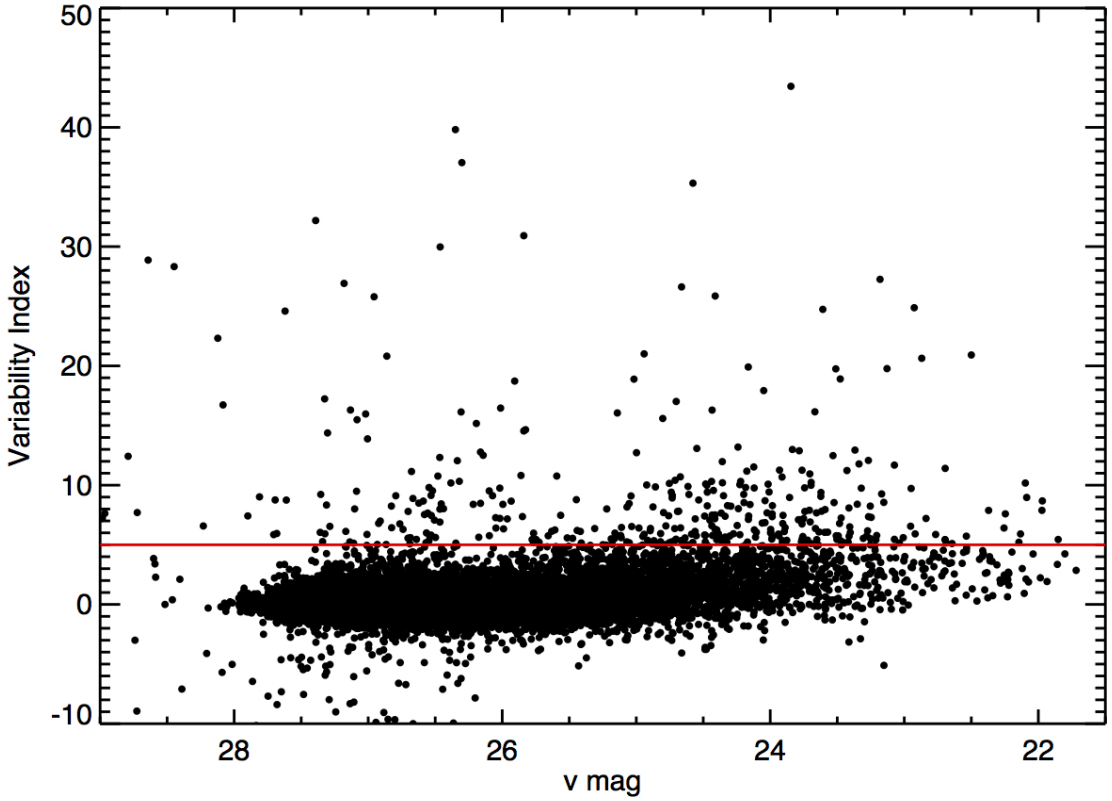

Figure 3.1: Variability index plot.

Figure 3.1 above shows a plot of variability index versus average V-band apparent magnitude. From this plot, one can see that of our 21 109 sources group together in a region near zero variability index and across several orders of magnitude in V. However, there is also a set of sources that extend above this grouping. As is the case with Yoachim et al. (2009), we see a clear and natural division between variable and non-variable sources at around a

variability index of 5. A red line has been drawn at this cutoff, and any source above this red line we keep in our sample of possible Cepheids.

3.1.3 Color Index Selection

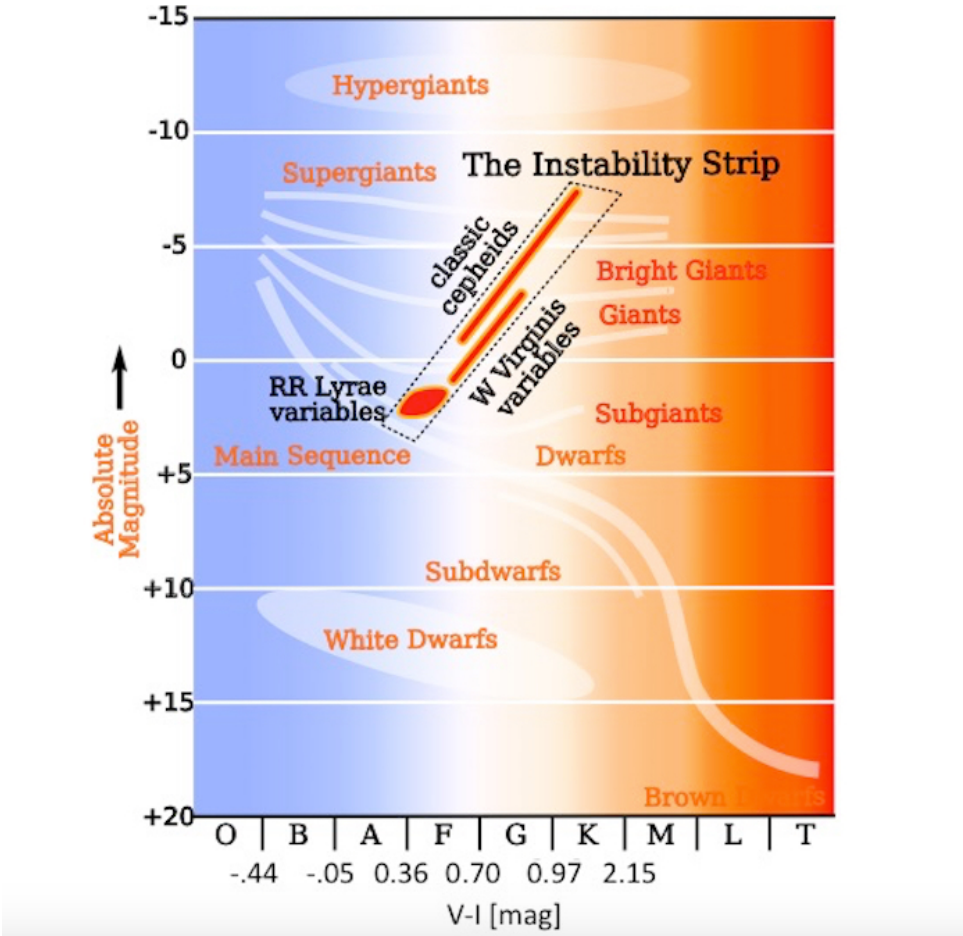

Figure 3.2: Color-Magnitude plot. V-I colors come from Ducati et al. (2001)

Now that we have a sample of stars that probably vary, we also need to make sure they fall in the correct location on a color-magnitude diagram. As was discussed in the introduction, Cepheids are post main-sequence stars that exist on the instability strip (see Figure 3.2. As such, they have V-I magnitudes of between approximately 0.25 and 1.3 magnitudes (Yoachim et al. 2009). We therefore restrict our sample to only stars that fall in this color range. To

do that, we computed the mean V-mag, and the mean I-mag, subtracted them, and then plotted them against the mean I-mag.

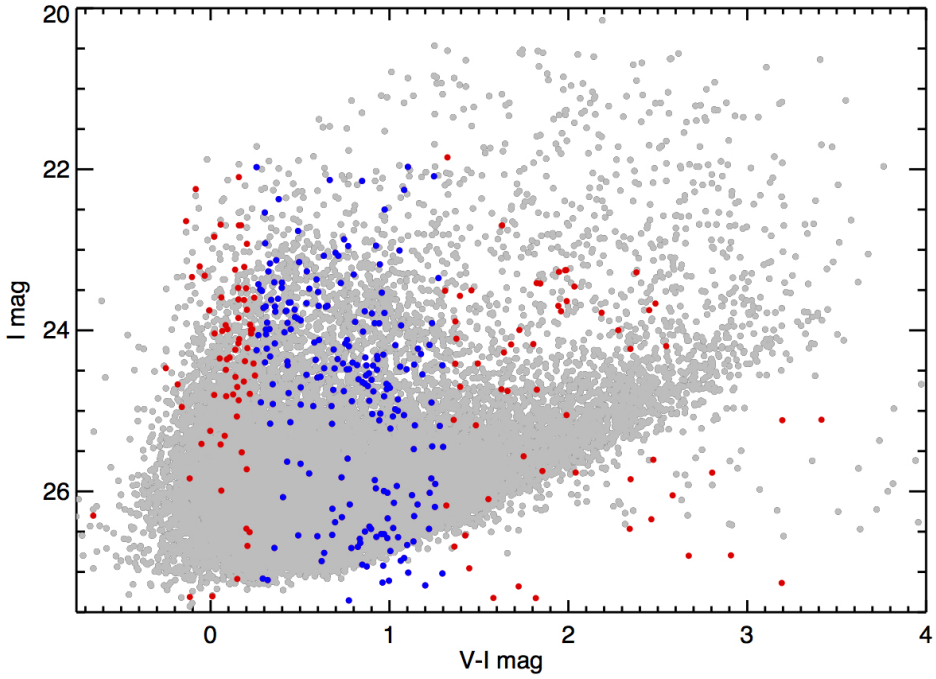

Figure 3.3: V-I color plotted against average I-band apparent magnitude.

Figure 3.3 shows in grey the whole sample before the variability index cut is made. The 406 sources that have a variability index of greater than 5 are plotted in color (both blue and red). The subsample of these within the range of color expected of a true Cepheid is plotted in blue, and there are 220 of these sources. With this color cut made, we now had a small enough sample to begin fitting light curves.

3.2 Light-Curve Fitting

Now that we had a manageable sample of sufficiently varying sources within the correct color, we were finally ready to fit light curves. The goal of fitting light curves is to extract the period of pulsation and mean apparent magnitudes for each Cepheid. Many methods

exist for fitting light curves, but not all of them are created equal. The classic "string length" method of Lafler & Kinman (1965) involves testing trial periods until the one for which the distance connecting each consecutive data point is minimized. This method, while quite effective for cases of well-sampled, high S/N light curves, is not designed to produce optimal fits for Cepheids on the edge of detection, i.e. sparsely and irregularly sampled light curves with significant noise.

An efficient light curve fitting method that is more appropriate for our data quality involves matching our data to libraries of template light curves. These template light curves are model fits to well-sampled, high S/N Cepheid light curves from the SMC, LMC and/or our own Milky Way. They are fit using a technique called Principle Component Analysis (PCA), which was first applied to a large set of Cepheids by Tanvir et al. (2005). PCA is a powerful statistical tool that has the advantage over other techniques of fitting both the V and I band data simultaneously. This allows all of the data to be used in the fit, and takes advantage of the natural correlations between the variations in V and I. The goal of PCA is to take a set of variables that are used to describe the system that may be redundant and dependent on each other and reduce them to a smaller set of linearly independent variables. In our case, the only three variables we need to extract from our Cepheids would be period, phase, and mean apparent magnitude. Additional components are needed to describe the sawtooth shape of the light curve. PCA then ranks components from highest to lowest according to the amount they contribute to the fit of the data. Often only the first few components are needed to describe the majority of the variability of the light curve. These components are stored in arrays as templates, along with polynomial fits to the light curves as a function of period. These polynomial fits help reduce the number of free variables.

In practice, our particular sets of Cepheid templates comes from the PCA analysis of Tanvir et al. (2005) of long-period Cepheids (P $>$ 10 days) from the SMC, LMC and the Milky Way (MW). Yoachim et al. (2009), whose work draws from the techniques in Tanvir et al. (2005), added short-period and first-overtone pulsating Cepheids to the samples. We used nine separate libraries of templates, most of which contain an overlapping group of Cepheids. The only group that had no connection to the others was the first overtone group of templates. The other eight were composed of fundamentals. We had a library that contained every single fundamental mode template available. This group was divided into two separate libraries of all long-period and all short-period templates. These long and short groups were even further divided by source location, i.e. LMC, SMC, or MW. The MW sample was not separated by long and short period, but the LMC and SMC were.

One might reasonably wonder why it is necessary to separate these templates into different populations based on period and location. One reason is that it has been shown that fitting short and long period Cepheids separately yields better overall fits (NEED REFERENCE). Another reason is because the PCA results between the samples are slightly different. Yoachim et al. (2009) find that Cepheids from the SMC have a significantly different percentage of their variability described by the first component of the PCA than does the LMC and MW. There is also some evidence that the metallicity of the sample can affect the slope of the P-L relation (Kennicutt et al. 1998; Sakai et al. 2004; Macri et al. 2006; Saha et al. 2006; Romaniello et al. 2008; Sandage & Tammann 2008). The SMC is known to be of lower metallicity than the LMC and the MW.

3.3 Final Sample Cuts and P-L Relation

After fitting our 220 candidate Cepheid light curves with nine different samples of templates, we then visually inspected the fits to get a sense of the quality and typical χ^2 values of a 'believable' fit. The fits that looked promising seemed to have $\chi^2 < 3$. Figure 3.4 shows one such fit.

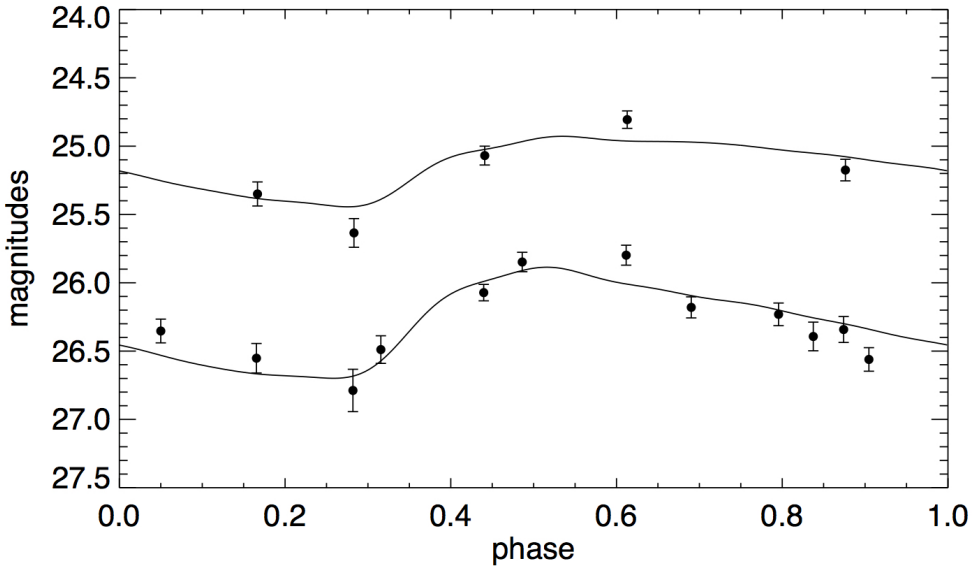

Figure 3.4: I-band (top set of 5 points) and V-band (bottom set of 12 points) Cepheid candidate light curve. Black lines are best-fit Cepheid model light curve. Best fit period is 51.6 ± 3.14 days.

To be conservative, we selected all Cepheid model fits with $\chi^2 < 5$ across all nine sets of templates. Cepheid model fits yielded periods, mean apparent magnitudes in V and I, phases, and associated errors. To determine which of the nine sets was best fitting the data,

we examined which of them was producing the most fits as well as which was producing the lowest χ^2 for a given candidate. As expected, due to the lack of sensitivity to short periods, the short-period templates produced very few reasonable fits. The first-overtone templates produced very few fits also, as expected because first-overtone pulsators are difficult to distinguish from fundamental mode Cepheids (more on this later). Between the SMC, LMC and MW, the LMC long-period templates produced the most fits with the smallest χ^2 values, so these were the ones we used to fit the Cepheids.

After the templates had been chosen, and a sample cut had been made at χ^2 of 5, there were a few more cuts left to make. We required that the best-fit period be between 10 and 70 days. This is a slightly expanded range from what our observational cadence implies we are sensitive to, which was 20 to 60 days. Next, we visually inspected all fits to make sure they looked plausible. Table 3.1 shows the model parameters characterizing 42 Cepheid candidates that have survived all cuts thus far. Light curves for and images of each of these candidates are shown in Appendix A. A V-band image of NGC 6814 is shown in Figure 3.5 with Cepheids locations denoted by green circles.

After culling our sample and discovering 42 probable Cepheids, we formed the V and I P-L relations by plotting $\log P$ versus apparent magnitude (see Figures 3.6 and 3.7). It should be noted that we have not yet performed an extensive error analysis, so not all sources of error are included in these error bars. However, the errors output by the template fitting code should track the true error to first order, and were used in our line fitting.

In order to actually measure a distance modulus from Cepheids of an unknown distance, one must compare them to a population of Cepheids at a known distance. The choice of which known-distance Cepheids against which to calibrate the unknown Cepheids is not a trivial

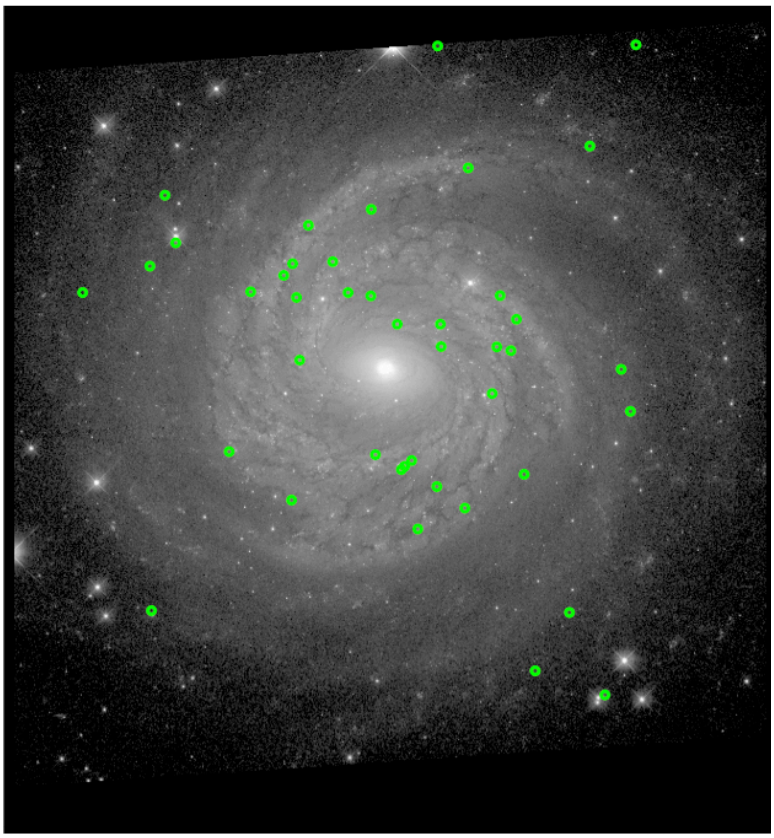

Figure 3.5: V-band image of NGC 6814 with probable Cepheid locations identified in green.

one, for this choice will often be that which introduces a significant source of uncertainty in the final distance measurement (see e.g. Riess et al. (2016) for a recent discussion). Some common choices are MW Cepheids with HST parallax measurements (Benedict et al. 2007; van Leeuwen et al. 2007; Freedman et al. 2012), LMC or Andromeda Cepheids with detached eclipsing binary (DEB) calibrators (Paczynski & Sasselov 1997), and Cepheids in the maser galaxy NGC 4258 (Herrnstein et al. 1999; Humphreys et al. 2013).

For our purposes, we elect to use the P-L relation calibrated using the LMC. We adopt the V-and I-band P-L relation slopes of Udalski et al. (1999), which was derived from the over 3000 LMC and SMC Cepheid light curves analyzed by the OGLE II team. We fit a straight line to our data using an IDL code called mpfitexy.pro, the details of which are described in

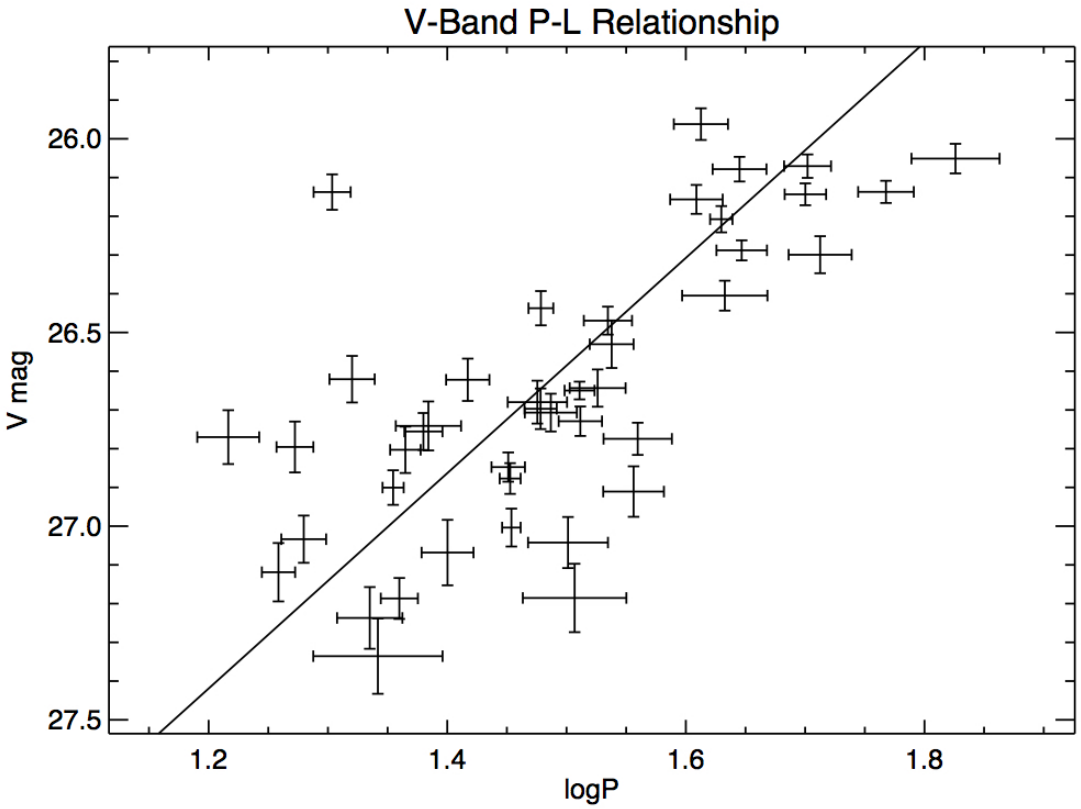

Figure 3.6: V-band P-L Relation.

Section 4 of Williams et al. (2010). This script is an extension of the linear fitting package called mpfit.pro (Markwardt 2009). By holding the slope fixed at the appropriate values below (which are the coefficients of $\log P$ below), we derived the following P-L relations:

$$V_{N6814} = -2.779(31) \log P + 30.755(11)$$

$$I_{N6814} = -2.979(21) \log P + 30.049(13)$$

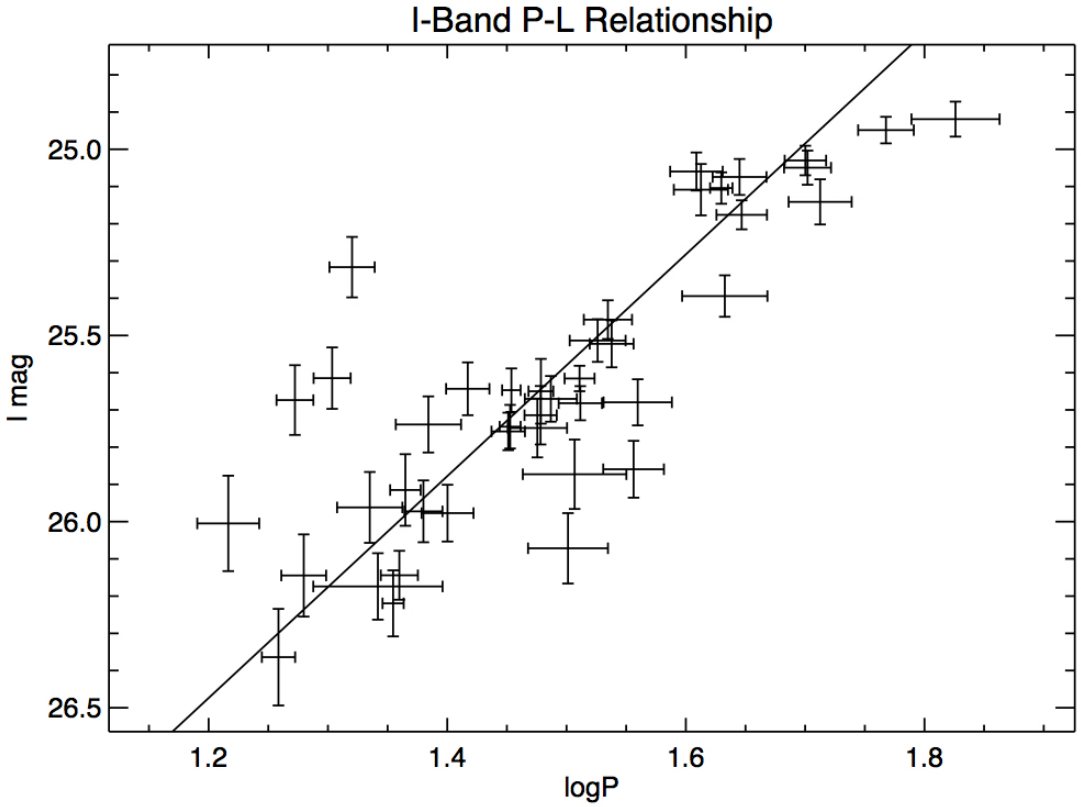

Figure 3.7: I-band P-L Relation.

The OGLE LMC V- and I-band P-L relation are:

$$V_{LMC} = -2.779(31)\log P + 17.066(21)$$

$$I_{LMC} = -2.979(21)\log P + 16.594(14)$$

The distance moduli of NGC 6814 relative to the LMC are then:

$$\Delta\mu_V = 30.755(11) - 17.066(21) = 13.629(24)$$

$$\Delta\mu_I = 30.049(13) - 16.594(14) = 13.411(19)$$

Using the Macri et al. (2006) distance modulus to the LMC of $\Delta\mu_{0,LMC} = 18.41 \pm 0.23$ mag, we derive a distance to NGC 6814 of:

$$\mu_{V,N6814} = 13.689(24) + 18.41(16) = 32.01(17)$$

$$\mu_{I,N6814} = 13.455(19) + 18.41(16) = 31.87(17)$$

Table 3.1: Cepheid Model Fit Parameters

ID#	$\tilde{\chi}^2$	x (pix)	y (pix)	m_i (mag)	$m_{i,err}$ (mag)	m_v (mag)	$m_{v,err}$ (mag)	P (days)	P_{err} (days)	ϕ (days)	ϕ_{err} (days)
163	4.94	1552	1792	25.11	0.069	25.96	0.041	40.99	2.14	0.60	0.51
165	1.82	2675	2894	25.05	0.046	26.07	0.030	50.35	2.28	6.03	2.26
166	2.25	1643	3272	24.95	0.036	26.14	0.029	58.58	3.14	41.29	1.06
167	3.56	1774	3076	24.92	0.047	26.05	0.038	66.99	5.70	52.92	2.05
168	2.18	3325	2497	25.07	0.048	26.08	0.032	44.16	2.29	2.85	2.19
169	2.07	3405	4244	25.03	0.040	26.14	0.028	50.14	2.01	37.84	0.72
170	2.91	427.6	2910	25.61	0.083	26.14	0.046	20.12	0.72	15.21	0.83
171	2.66	3157	3698	25.06	0.051	26.16	0.037	40.63	2.06	0.46	2.19
172	2.98	3375	2270	25.14	0.061	26.30	0.048	51.59	3.14	18.91	2.70
173	2.76	2762	2766	25.10	0.042	26.21	0.034	42.63	0.92	14.42	0.57
174	1.56	929	3178	25.18	0.039	26.29	0.026	44.34	2.16	34.42	0.44
175	4.21	2161	1974	25.65	0.087	26.44	0.044	30.10	0.72	6.25	1.25
177	2.20	790	3052	25.39	0.056	26.40	0.039	42.92	3.53	19.46	3.00
178	2.01	1510	3003	25.46	0.052	26.47	0.036	34.25	1.59	8.34	1.61
180	3.60	2503	3581	25.32	0.081	26.62	0.060	20.90	0.91	0.45	1.00
181	3.25	2732	2598	25.64	0.071	26.62	0.055	26.13	1.09	9.62	1.28
182	2.05	2004	2037	25.71	0.078	26.70	0.052	30.08	0.94	22.94	0.91
183	2.05	2121	2740	25.51	0.057	26.64	0.048	33.58	1.81	21.64	1.82
184	0.69	1856	2910	25.62	0.034	26.65	0.023	32.43	0.94	21.73	0.90
185	1.82	3238	744	25.52	0.063	26.53	0.061	34.50	1.46	15.40	0.68
186	1.94	1558	3065	25.97	0.083	26.76	0.048	23.99	0.88	17.06	1.07
187	2.94	1596	2546	25.74	0.075	26.74	0.063	24.22	1.53	12.14	2.85
188	2.19	2199	2006	25.67	0.094	26.80	0.066	18.72	0.67	4.57	1.19
190	1.40	2863	873	25.67	0.061	26.71	0.049	30.68	1.54	20.95	1.59
193	1.15	2232	1637	25.76	0.050	26.85	0.038	28.26	0.91	23.30	0.39
194	1.18	871	3434	25.68	0.046	26.73	0.038	32.48	1.36	28.09	1.28
196	3.00	1332	2914	25.75	0.079	26.68	0.055	29.89	1.71	28.32	1.71
197	2.57	2334	1865	26.07	0.095	27.04	0.066	31.71	2.45	28.48	2.30
198	1.59	2656	2618	26.22	0.089	26.90	0.045	22.63	0.46	12.77	0.51
199	2.73	2353	2739	26.00	0.128	26.77	0.070	16.46	0.98	12.32	1.95
201	1.60	2357	2619	25.68	0.062	26.77	0.042	36.28	2.39	11.07	2.33
202	1.36	1216	2054	25.75	0.059	26.88	0.040	28.36	0.57	15.04	0.54
203	2.76	3047	1188	25.92	0.096	26.80	0.060	23.17	0.68	21.68	0.84
204	1.90	1979	2891	25.65	0.058	27.00	0.049	28.43	0.51	13.47	0.35
205	2.20	2484	1750	25.86	0.076	26.91	0.065	35.99	2.11	26.49	1.25
208	2.05	799	1198	26.14	0.110	27.03	0.061	19.04	0.82	3.28	1.10
209	2.42	1981	3357	26.36	0.130	27.12	0.075	18.14	0.58	5.93	0.90
210	1.28	2143	1957	25.98	0.076	27.07	0.085	25.13	1.26	1.05	1.70
211	1.21	2338	4237	26.14	0.066	27.19	0.053	22.90	0.82	6.16	1.80
213	2.09	1578	2883	25.96	0.095	27.24	0.080	21.63	1.36	16.98	2.53
215	2.10	2804	1931	26.17	0.089	27.34	0.097	21.97	2.74	12.19	2.97
218	3.23	2632	2366	25.87	0.093	27.19	0.088	32.12	3.21	21.90	3.26

3.4 Reddening Correction

Because dust preferentially scatters blue light, our V-band magnitudes are systematically dimmer than they should be compared to the I-band magnitudes. In order to correct this effect, we will perform a Wesenheit Reddening Correction. From McCommas et al. (2009): "The effect of reddening can be corrected using the "Wesenheit" reddening-free index" (Madore 1982),

$$\mu_W \equiv \mu_V - A_V = \mu_I - A_I$$

For V and I photometry the Wesenheit index is defined as $W = V - R \times (V - I)$. R is taken to be 2.682 based on Schlafly & Finkbeiner (2011). The Wesenheit index then becomes $W = -1.682V + 2.682I$ for purposes of error propagation. Using this we can write new P-L relations for the Wesenheit index:

$$W_{N6814} = -3.269(68) \log P + 28.716(17)$$

$$W_{LMC} = -3.269(68) \log P + 15.910(46)$$

$$\mu_{W,N6814} = 28.716(17) - 15.910(46) + 18.41(16) = 31.22(17)$$

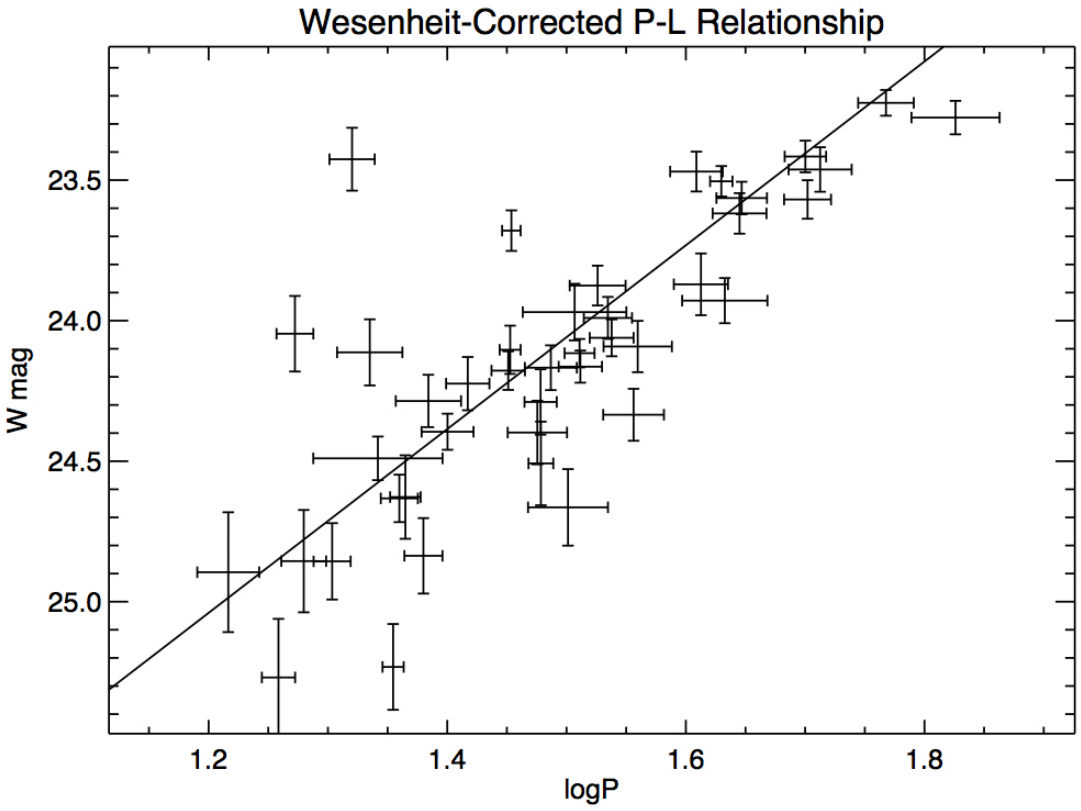

Figure 3.8: Wesenheit P-L Relation.

3.5 Metallicity Correction

Cepheids with higher metallicities are thought to be intrinsically brighter than lower metallicity Cepheids of the same period according to e.g. Macri et al. (2006). Some galaxies have been shown to exhibit a metallicity gradient, which means that the distance modulus one measures might depend on the radial distance from the galactic center. To counteract this effect, one can attempt to characterize the metallicity (log[O/H]) as a function of radius for the particular galaxy being studied.

In our case, the metallicity gradient of NGC 6814 has already been measured by Shaheen Iqbal and Stuart Ryder of Australian National University. Her findings show a flat gradient, which implies that a metallicity correction is not necessary for our Cepheids.

In the future we wish to confirm these results with our own B- and I-band IFU data collected using the Australian National University's 2.3-meter telescope and the WiFeS instrument. However, for now we apply no metallicity gradient correction.

3.6 Uncertainty and Comparison to Previous Distance Measurements

We find a Wesenheit-reddening corrected distance modulus of $\mu_{W,N6814} = 31.22 \pm 0.17$ magnitudes. This corresponds to a distance of $17.54^{+1.44}_{-1.33}$ Mpc, which corresponds to an 8% error in distance. The dominant source of uncertainty, as is the case with many Cepheid studies, is introduced with our choice of calibration Cepheids in the LMC. Indeed, our measurement error associated with the distance of NGC 6814 *relative to the LMC* is less than 3%. Though an 8% total error in distance is not trivial, it is by far most precise measurement of the distance to NGC 6814 to date. This is because previous distance measurements have been performed with methods that are known to be inaccurate for galaxies such this one.

For example, assuming a ΛCDM cosmology of $\Omega_M = 0.27$, $\Omega_\Lambda = 0.73$, and $H_0 = 73.0 \pm 5$ km/s/Mpc, then the galactocentric redshift distance to NGC 6814 was measured to be 23±1.6 Mpc (de Vaucouleurs et al. 1991). Tully et al. (2013) find that peculiar velocities can introduce a significant amount of error on redshift distances measured for galaxies within 50 Mpc or with recessional velocities less than 4 000 km/s. Because NGC 6814 is well within this threshold, its redshift distance cannot be trusted. As a sanity check, we compare our Cepheid distance measurement to the redhsift distance and find an implied peculiar velocity of 380 km/s (derived via Hubble's Law; $v = H_0 d$). Data from the *Cosmicflows* 2 survey of distances and peculiar velocities for over 8 000 galaxies Tully et al. (2013) shows that 380 km/s is a fairly typical value for a galaxy like NGC 6814.

A Tully-Fisher distance to NGC 6814 of 22.8 Mpc is also reported in the Nearby Galaxies Catalog (Tully 1988). However, this distance measurement, which combines a B-band brightness measurement from the RC3 Catalog with an HI 21-cm line width from (Shostak 1978), has many issues. First, the B-band photometry measurement did not account for, and subtract out, the light from the AGN. This could cause the galaxy to appear brighter (especially in the B-band) and therefore closer. Second, a single HI width is generally less accurate for determining a rotation curve than a full rotation curve. Not only were the measurements not ideal, but it has been shown that T-F distances become unreliable at galaxy disk inclinations as high as 45° (Tully & Pierce 2000). Because NGC 6814 is nearly face-on, this T-F distance is essentially meaningless.

Our Cepheid study is now the most carefully measured and meaningful distance to NGC 6814 to date. This number can now be used to measure the SMBH mass at the center of NGC 6814, the accuracy of which depends linearly on the distance. This is the subject of the next two Chapters.

– 4 –

Stellar Dynamical Modeling

4.1 Background

On its most basic level, stellar dynamical modeling involves taking spectra of unresolved stellar populations, measuring their brightness distribution and Doppler motions, and then comparing these motions to a model in order to glean information about the gravitational potential in which the stars are moving. This process has often been applied to elliptical galaxies, but can also be applied to the spheroidal component of late-type galaxies as well as rotation-dominated systems. The principles governing current stellar dynamical modeling were first put forth by Dr. Martin Schwarzchild in 1979 when he described the first triaxial orbital superposition method. As the quality of stellar spectra has improved, the number of constraints available for the modeling has increased, thus allowing the models to fit more free parameters and become more generalized.

4.2 Observations

Our observations were taken using the Near-Infrared integral Field Spectrometer (NIFS) + ALTAIR instrument on the Gemini-North 8.1-m telescope located on Hawaiis Mauna Kea. NIFS is a near-IR Integral Field Unit (IFU) that uses a mirrored image slicer to split the image into different slices, and then reflect those slices to a set of slits, which then disperses each slice into a spectrum that is then incident upon a detector. Images are reconstructed from these spectra using the NIFS pipeline. IFUs gather simultaneous spectral and spatial information yielding a data product is called a 3D datacube. Datacubes have two spatial dimensions, x and y, and one wavelength dimension, λ. This means that for every position

in the FOV there is corresponding spectral data. The NIFS field of view is 2.99"x2.97" and the scale across the slices is 0.103" (determined by the width of the slits) and 0.04" along slices (determined by the pixel size).

Table 4.1: Gemini NIFS Observations

UTC (yyyy-mm-dd)	**MJD Start** (s)	**Exp. Time** (sec)	**AO Corr.** (arcsec)
2013-09-30	56565.214888	3840	0.41
2013-10-01	56566.311241	960	0.64
2013-10-31	56596.210446	1680	0.55
2013-11-01	56597.200297	960	0.62
2014-05-20	56797.581917	960	0.49
2014-08-05	56874.408050	3360	0.50
2014-08-06	56875.340674	3000	0.54
2014-08-23	56892.311151	3120	0.48
2014-08-24	56893.280767	3840	0.31
2014-08-25	56894.381605	600	0.71
2014-08-26	56895.345714	1920	0.46
2014-08-30	56899.273722	3840	0.46
2014-09-01	56901.351564	2160	0.37
		Total 30240	**Avg 0.50**

The cumulative time spent staring at the central region of NGC 6814 (after all bad frames were removed) was 248 exposures of 120 seconds each for a total of 29 760 s (see Table 4.1). These observations were taken between the dates of October 1, 2013 and Sept 1, 2014 (GN-2013B-Q-52, PI Bentz) via queue observing, meaning that they were executed by a staff observer during imaging blocks that were fit into Gemini's overall observing schedule whenever possible. The Altair adaptive optics (AO) system was used in order to maximize image spatial resolution. Our median AO correction, which is the ratio between peak intensity of a wavefront distorted by turbulence in the atmosphere to the peak intensity of a perfectly spherical wavefront, was 0.45. Fortuitously, NGC 6814's central AGN point source

was bright enough to be used as a guide star for the AO system. This meant the AO was correcting for atmospheric distortions as close to the region of interest as possible. It also added flexibility to the scheduling of our observations because the laser guide star system (only available 7-14 nights out of the month and must be scheduled well in advance) was not needed. We used the H-K filter with the K-grating centered at 2.25 μm with a spectral range of 1.99 to 2.40 μm, a spectral resolution of about 5 290, and a velocity resolution of about 56.7 km/s.

The structure of our typical observing blocks are as follows. First, exposures of a spectroscopic standard A0V star called HD172904 were taken. This type of star was chosen because Vacca et al. (2003) has developed an IDL code that uses a high-resolution model of the spectrum of Vega (also an A0V star) to remove stellar absorption features, thus producing a pure telluric spectrum. Next, our science target, NGC 6814, was imaged several times for 120 seconds per exposure and was alternated with skyflat offset exposures of the same length. A dither pattern was employed in order to better sample the image with the detector. Xe-Ar lamp spectra were taken each night. This calibration is useful because if the grating has been changed between imaging blocks, the spectra can be displaced on the detector by 1 to 2 pixels, so a new lamp exposure should be taken at every science pointing to be sure the wavelength calibration is accurate. Then, if the science exposures took longer than 1.5 hours, images of another spectrophotometric A0V standard star, called HD193689, were taken. During the reductions process, nights for which two telluric standards were imaged meant that the first half of the science frames were calibrated with the first standard, and the next half of the science frames were calibrated with the last standard.

The morning after the observing block, daytime calibrations were collected. Flatfields were taken with both an open shutter and closed shutter. The closed shutter flats are subtracted from the open shutter flats in order to get rid of thermal emission from the telescope (important for IR observations) itself as well as dark current and hot pixels, a step that is especially important in the infrared. Once the dark flats are subtracted, then the open shutter flats are used in the traditional way of characterizing the detector response across the chip. Dark frames are also taken for the same duration as the science and other calibration images. Lastly, a few "Ronchi" calibration mask frames are taken, which is when a straight wire is placed across the slit and is projected onto the chip in order to help with spatial rectification. Otherwise the curve in the slice spectra caused by the optics of the telescope would be more difficult to characterize.

Due to time constraints, sometimes not all necessary calibrations could be taken for every observing block. For example, on the night of 20131005, no daytime calibrations were taken. In these cases we used the calibrations from the previous date or next date depending on which date was closest. The daytime calibrations from 20131001 were used on the data from 20131005. The same situation occurred for 20140901 for which daycals from 20140830 were used. Also, the nights for which the science exposures took less than 1.5 hours to collect only had one spectro-photometric standard star observed. In that case, all of the science frames for that night could be and necessarily were calibrated with that one star.

4.3 Data Processing: NIFS Pipeline

The IRAF-based NIFS pipeline consists of three separate modules: baseline calibrations, science data reduction, and telluric correction, which need to be performed on each night

of data separately. Each module has a wrapper script that requires the user to edit certain parameters such as image lists and directory names, and then it is recommended to copy and paste smaller subsections of this script into a command line. A few of the tasks are recommended to be run in interactive mode, which allows the user to monitor the results and check for errors. It should be noted that all NIFS raw images are formatted as Multi-Extension Fits (MEF) files with two extensions: [0] for the Primary Header Unit (PHU) that contains metadata about the exposure, and [1] for the data read from the array. The goal of the pipeline is to take a 2D science frame that has all the spectra from the 29 image slices stacked side-by-side and reconstruct a calibrated 3D data cube with two spatial and one spectral dimensions.

The baseline calibrations begin by carving out the 29 slices of the lamp on and lamp off flats and assigning each to a separate image extension. Also created are a data quality (DQ) and a variance (VAR) extension for each of the 29 slices for a total of 87 image extensions. The flats are normalized and a bad pixel mask is created in order to account for dead or hot pixels. Once the flats are created, then the same image slice separation procedure is done for the arcs, arc darks, and Ronchi calibration frames, and all of those are dark subtracted and flatfielded using the flatfield frames created earlier. In the wavelength calibration step, while working with the arc lamp spectra, the user is advised to interact with the automated line identification task in order to make sure emission lines are identified at the proper wavelengths, and to delete any line identifications that have low signal to noise and would therefore add uncertainty to the overall wavelength calibration. The last step in these baseline calibrations involves the Ronchi mask images. Here again, the user is asked to verify or correct interactively the identified peaks in emission across all 29 Ronchi mask

science extensions so that the code knows where the spectra for each slit fall on the image for each slice. The Ronchi mask is then used to calibrate the spatial mapping for the image slices.

With the baseline calibrations done, the science data reduction is run next. It begins in a similar way to the baseline calibrations in that it takes the science frames and their associated darks, separates the slices, and adds DQ and VAR extensions. Next, the science frames are dark corrected, wavelength calibrated using the arcs created in the baseline calibrations, and then bad pixel corrected. Using the spatial mapping information measured from the Ronchi flats, and also the wavelength calibration information, a final mapping scheme is created to rectify the 87 extensions into a 3D data cube. Lastly, the science data is resampled spatially and spectrally so that the resolution will be consistent throughout the 3D cube when it is created in the next module.

The third and final module utilizes the spectrophotometric standard stars to perform telluric corrections. This step needs to be repeated for every set of science frames and their closest in time telluric stars frames. If two telluric standards were imaged during that image block, then this module needs to be run twice for that night. This module mostly repeats the steps done to the science frames, and initially treats the standard star the same as the science object. Once the standard stars image has been sliced up, dark-corrected, flatfielded, wavelength-calibrated, bad pixel corrected and transformed into a 3D data cube, then a 1D spectrum of the telluric standard is extracted. During this step, the user interactively places an aperture over the star in order to guide the code to where to make the extraction, i.e. at the centroid of the light profile within the aperture.

Before the telluric corrections can actually be applied, we decided to modify the telluric spectrum and remove the black body shape so that the sky lines are the only features left in the spectrum. We also needed to remove a stellar absorption line that A-stars in the K-band exhibit at 21 700 Å, and that we did not want to affect in our telluric corrections. The black body shape and absorption line removal were performed in IRAF using the "splot" function. We created a model 1D black body spectrum using the mk1dspec task and an input temperature of 10 000K, which is close to the typical black body temperature of an A0V star. We then used IRAF's splot task in "etch-a-sketch" mode to interpolate over the absorption lines. Finally, we divided the 1D telluric spectrum by the model black body in order to get a normalized telluric spectrum.

Once the 1D spectrum of the telluric star was normalized, then the science frames were corrected for telluric lines, and the final products are one calibrated 3D science data cube for each science observation taken, or 248 data cubes.

Before making any dynamical measurements, the 248 separate data cubes needed to be aligned and stacked to maximize the signal-to-noise ratio. To do that we selected a prominent broadened emission line, the Brackett gamma line at 2.1655 μm. We make use of the knowledge that the AGN is an unresolved point source, so we use it's broad line emission to isolate it from the rest of the galaxy light, and then align all the images using it as a reference. We then sliced the 3D cubes along the wavelength axis at the peak of this emission line so that the AGN was at its brightest in comparison with the rest of NGC 6814. Next we measured the centroid of the AGN at that wavelength for each of the cubes using the "a" function of the IRAF task called imexamine. Once the position of the AGN was known for all cubes, then the x- and y-offsets between the cubes were calculated. The

final cube was created by inputting this list of offsets to IRAF's imcombine task. During the combining process, all cubes were first trimmed in all three dimensions in order to get rid of noisy spaxels. The cube was trimmed such that the spatial dimensions, which were originally 53×53 spaxels, were now 31×31 spaxels with the AGN in the central spaxel. The cubes were then median combined with three sigma clipping, but keeping a minimum of two thirds of the total 248, or 164 cubes.

Our final data product is a 31x31x1840 data cube covering a wavelength range of 20 184.6 Å to 24 109.3 Å that has been spatially and spectrally linearized. Each spaxel is 0.05" ×0.05", and has an average spectral FWHM of 3.3 Å.

4.4 Measurements

4.4.1 PPXF

Now that our data cube is fully calibrated, we employ a powerful spectral fitting software called Penalized PiXel Fitting, or pPXF (Cappellari & Emsellem 2004), that can measure dynamical quantities such as velocity and velocity dispersion from each spaxel of our data cube. pPXF is a well-tested stellar dynamical modeling tool that has been used in such important projects as the Atlas3D Project (Cappellari et al. 2011), the aim of which was to study local galaxy evolution by characterizing the global dynamics of 260 early-type galaxies contained within a 42-Mpc volume.

pPXF characterizes line profiles shapes with Gauss-Hermite polynomials, which is a slightly more sophisticated method for modeling line profiles than the more common and simple method of superposing multiple Gaussian curves. It has been shown that Gauss-Hermite polynomials preserve information contained in asymmetries the line profiles better

than regular Gaussian superposition (e.g.,Barbosa et al. 2009; Riffel et al. 2010). Figure 4.1 from Figure 1 of Riffel (2010) illustrates how varying the Gauss-Hermite moments is reflected in the shape of the line profile. The redshift and blueshift asymmetries in the wings are reflected in h_3, and h_4 controls the peakiness of the shape.

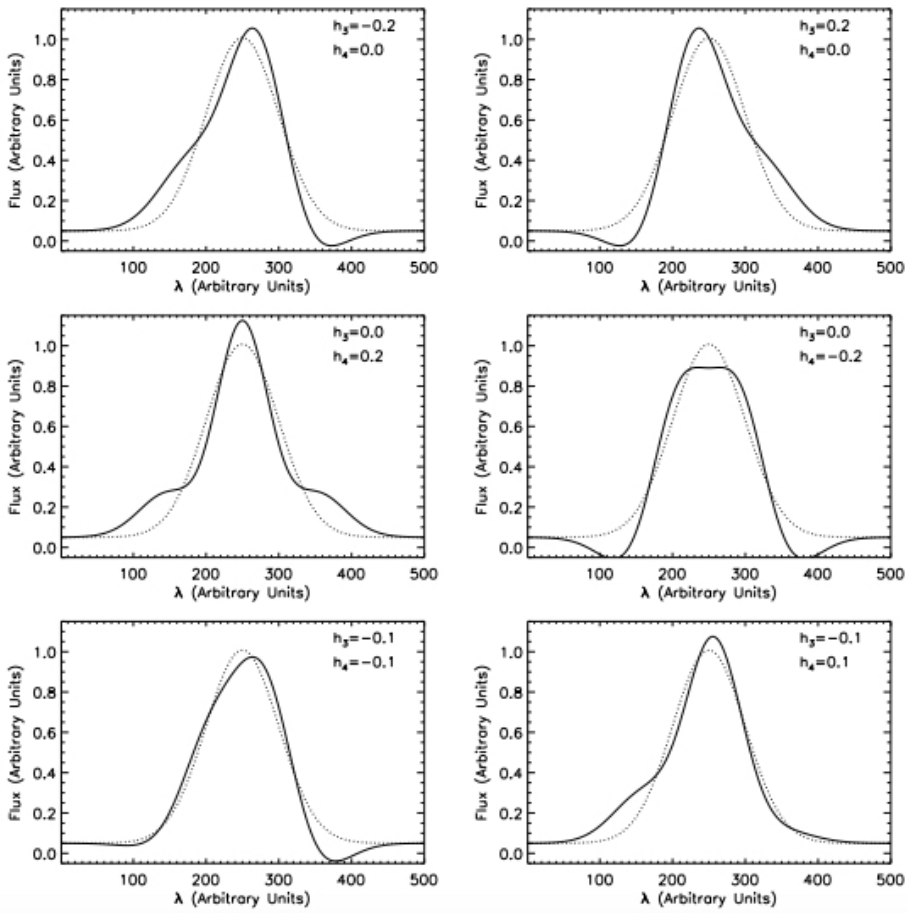

Figure 4.1: Reproduction of Figure 1 from Riffel (2010) comparing Gaussian superposition (dotted lines) to Gauss-Hermite series (solid lines) for varying values of h_3 and h_4 while holding amplitude, h_1 (central wavelength), and h_2 (line width) fixed to the same values for both lines.

This software makes use of the fact that galaxies can be approximated as purely a collection of stars, and that the light we observe is a luminosity weighted composite spectrum of several different spectral types. Therefore, in order to accurately measure absorption line

widths and shapes of a galaxy, from which can be derived quantities like velocity and velocity dispersion, one needs to choose a representative set of stellar templates of different spectral types that can be strategically combined to model the observed galaxy spectra.

pPXF convolves these stellar templates with the line-of-sight velocity dispersion (LOSVD) moments that are parametrized in pixel space. The galaxy spectrum is then fit by using the nonlinear least squares method of chi-squared minimization. What is especially useful is that pPXF also accounts for the varying signal-to-noise of the observed spectra. The noisier and/or more poorly sampled an absorption line, the less information it contains about the higher order moments of the LOSVD. Therefore, pPXF only tries to reproduce a detailed line fit when the S/N is high, and then tends toward a simple Gaussian when the S/N is low, which is achieved using the maximum penalized likelihood method (e.g., Merritt 1997). This helps the model reproduce the detailed information contained in the high S/N lines, but keeps the model from reproducing low S/N lines too precisely and allowing noise to masquerade as higher order moments of the LOSVD. The amount of penalization can be tuned by the user. pPXF also attempts to report an error for each of the moments as well, but this error measurement has little to no physical meaning and is only derived from the χ^2 minimization.

We used pPXF to measure stellar kinematics from NGC 6814's NIFS data cube in the following way: First we downloaded a library of H-band GNIRS stellar template spectra from the Gemini Observatory website[1]. These Winge et al. (2009) spectra span a range of 2.18-2.43 μm, have a spectral resolution FWHM of 3.2 Å, and a velocity resolution and spectral resolution of 19 km/s and 6 600 respectively. We chose a representative subset of 12

[1]http://www.gemini.edu/sciops/instruments/nearir-resources/spectral-templates

stars that span different spectral types (see Table 4.2). As you can see from the table, they were K or M giants which are thought to be the greatest contributor to the luminosity to our composite galaxy spectrum.

Table 4.2: Spectral Templates

ID	**Spectral Type**
BD -01 3097	M2III
HD 108164	K2III
HD 121447	K4III
HD 201065	K5I
VES 145	M0I
BD +09 4750	M1III
BD +44 337	K5I
HD 118290	K5III
HD 139195	K0III
HD 166229	K2.5III
HD 181596	K5 D
HD 613	K4III

Besides data and template spectra, pPXF has several input parameters that must be supplied by the user. One of the first choices was what wavelength range to fit. As can seen from Figure 4.2, our fits were to the CO bandheads at around 2.3 μm, so we restricted our range to 22 635.6-24 085.9 Å. We also supplied the redshift of z = 0.005214, the FWHM of the galaxy spectra 3.3 Å, the FWHM of the stellar templates 3.2 Å (both measured with IRAF's splot). After tuning all of these parameters and using all 12 candidate spectral templates, we ran pPXF in a loop on the 31×31 grid of spaxels for a total of 961 runs. For each run, pPXF models the position and shape of the CO-bandhead absorption lines each spaxel. pPXF then outputs the first six Gauss-Hermite moments which are called h_1 (hereafter, velocity (v)),

h_2 (hereafter, velocity dispersion ($\sigma_\star$), h_3 (akin to skewness), h_4 (curtosis), h_5, and h_6[2]. Our pPXF fitting results are presented in Appendix B.

We opt to perform our own error measurements in the following way: In addition to dynamical parameters, pPXF outputs weighting information for all twelve stellar templates. The stellar templates that more accurately fit the data are weighted more heavily and are often used in a higher fraction of the fits. Typical weights ranged from 0-30%. We performed statistics on each template to see the frequency with which that template was used by pPXF and by how much it was weighted on average. Templates that were used less than approximately 50% of the time or were on average weighted less than 10% were discarded. The top five most weighted and most frequently used templates were selected. We then reran pPXF using these best five templates as well as with each of them individually. We used the dispersion in the results between the individual runs in order to characterize the error on the results when all five templates were used. A typical fit is shown for your visual inspection pleasure in Figure 4.2, and as can be seen, the galaxy spectrum is well-reproduced by the model.

When all of the fits from all of the spaxels are plotted together, a clearer picture of the overall stellar dynamics is seen. In Figure 4.3 the velocity (v), velocity dispersion ($\sigma_\star$), h_3 and h_4 fits are plotted as a function of position on the sky with the associated error maps plotted directly underneath. The velocity map shows a clear rotation axis and, given this is the spheroidal component of a face on galaxy, the small magnitude of the rotation makes sense. The velocity dispersion map shows some interesting structure. The velocity dispersion

[2]These last two higher order moments, h_5 and h_6, were not used in our analysis, and can hereafter be ignored

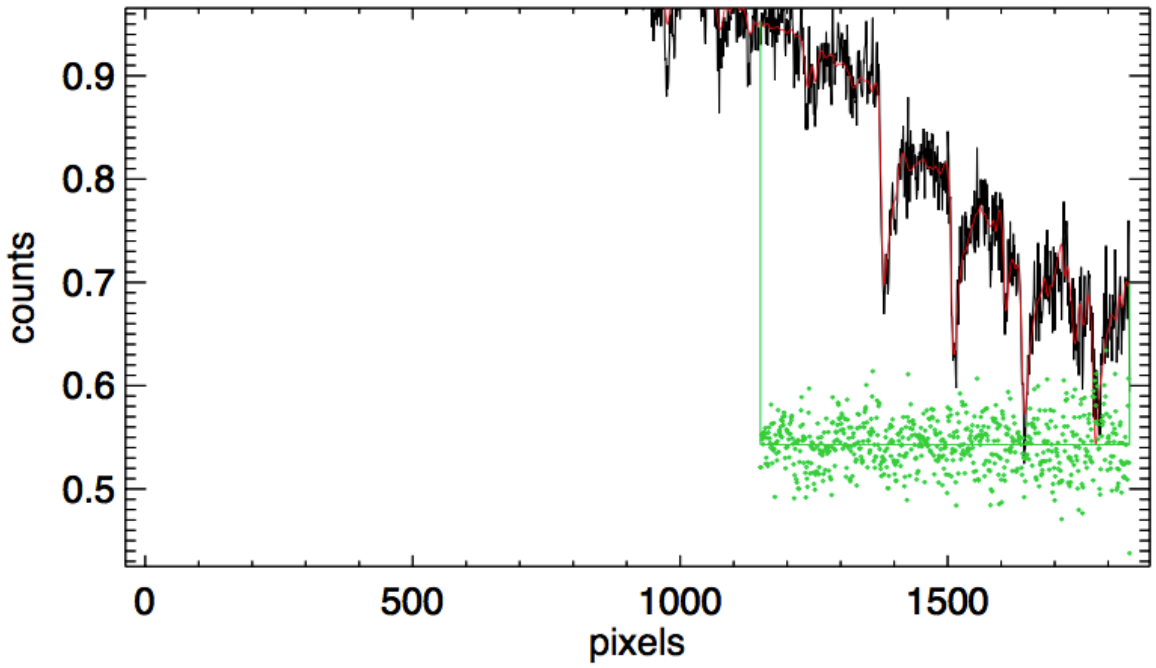

Figure 4.2: pPXF model fit to spaxel at x,y = 7,7. Black line is spectral data. Red line is model fit. Green dots are data minus model residuals.

seems to show a ring shape depression and then increases toward the outer edges. This may relate to NGC 6814's identification as a so-called "sigma-drop" galaxy (Márquez et al. 2003, 2004) (see Chapter 5 for further discussion). There is also a peak in the very center where the black hole's sphere of influence should be, but also where the AGN contamination is greatest. Whether this central increase in velocity dispersion is a dynamical signature of NGC 6814's SMBH, or whether the AGN has obscured it beyond resolution is the subject of the next chapter. For now, we will concentrate on the next steps needed to prepare these

measurements for input into the next code–the code that is used to model these dynamics and output the mass of the SMBH.

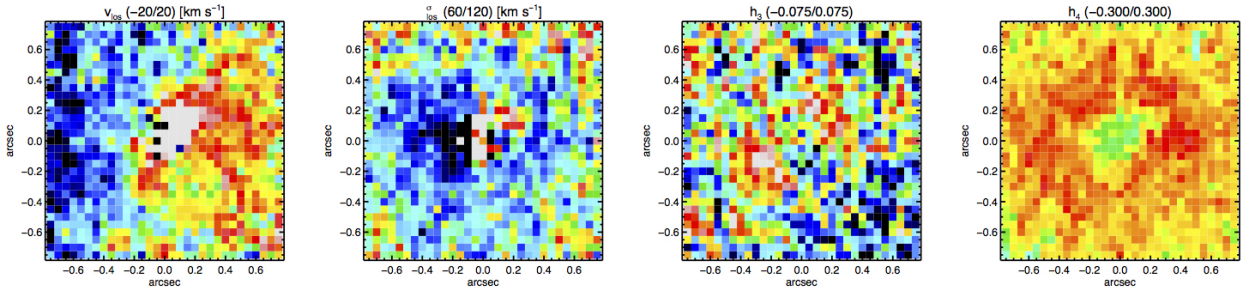

Figure 4.3: Dynamical Maps of NGC 6814 resulting from pPXF fitting of NIFS spectra. From left to right: velocity (v), velocity dispersion ($\sigma_\star$), h_3 and h_4. Red corresponds to positive values, blue to negative.

4.4.2 Voronoi Binning, Bisymmetrization, and Fitting the Kinematic PA

In order to prepare the data to be used as constraints in the stellar dynamical modeling code, there are a couple of processing steps that need to be taken. The first step is to fit the kinematic position angle (PA) of the velocity distribution. Luckily, an IDL code already exists called "fitkinematicpa.pro", which can be downloaded from Michele Cappellaris website. (This code was developed using the technique presented in Krajnović et al. (2006)). The code takes as input x and y positions, velocity at those positions, and an initial guess of the systemic velocity. It then outputs the position angle measured clockwise with respect to the positive y-axis, its associated error, and the calculated systemic velocity of NGC 6814. Our PA was +9.4 degrees with respect to the positive y-axis, and systemic velocity was 1 510 km/s. We subtracted the systemic velocity from our pPXF fit velocities so that the magnitude of the velocity errors could be considered in relation to the rotation residuals.

The second step is called Voronoi binning, which is a way to rebin the data so that each bin has equivalent signal to noise. This helps reduce the number of bins to a manageable number for the dynamical modeling code to handle. It also helps increase the signal to noise in each bin. The Voronoi binning code allows the user to specify the target S/N for each bin, but the question then becomes: how many bins do we want to end up with? If there are too many bins, then the code takes too long to run. If there are too few bins, then the sphere of influence of the SMBH will not be resolvable. Practically speaking, too few bins leads to a paucity of model constraints, which in turn leads to degeneracies in the fits. A good compromise between resolution and computing time seemed to be to aim to collapse our 961 data points into about 300 bins. We ended up with 242 and a S/N of 600. The Voronoi-binned maps are shown in Figure 4.4. The bins get larger radially outward from the center because the surface brightness of the galaxy decreases radially and therefore larger bins are needed to maintain the same S/N.

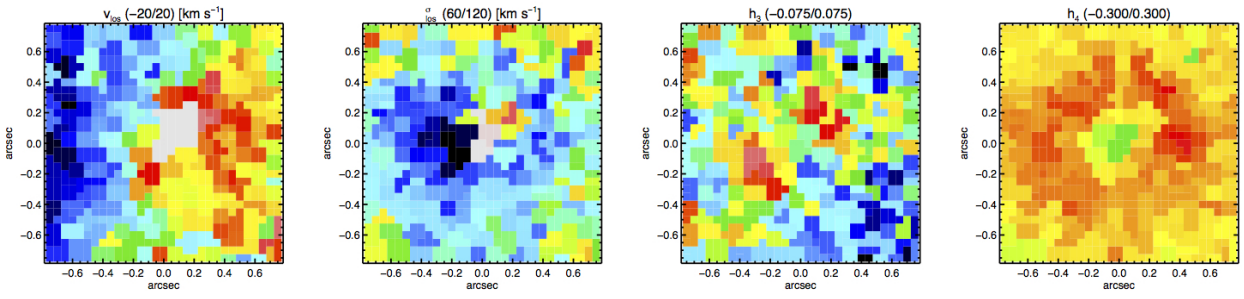

Figure 4.4: Voronoi-binned NIFS dynamical maps of NGC 6814.

The next step exploits the assumption that the distribution of the stars in the galaxy is symmetric about the kinematic rotation axis of the velocity distribution, which we already measured to be 9.4 degrees. Each velocity, sigma, h_3, and h_4 bins was averaged with its corresponding reflected bin across the axis (see Figure 4.5. This process of bisymmetrization

was completed using another of Michele Cappellaris IDL codes called symmetrizevelfield.pro, which is part of the JAM package. By exploiting symmetry and averaging information about the axis of symmetry, one is decreasing noise and simultaneously making future stellar dynamical modelling easier.

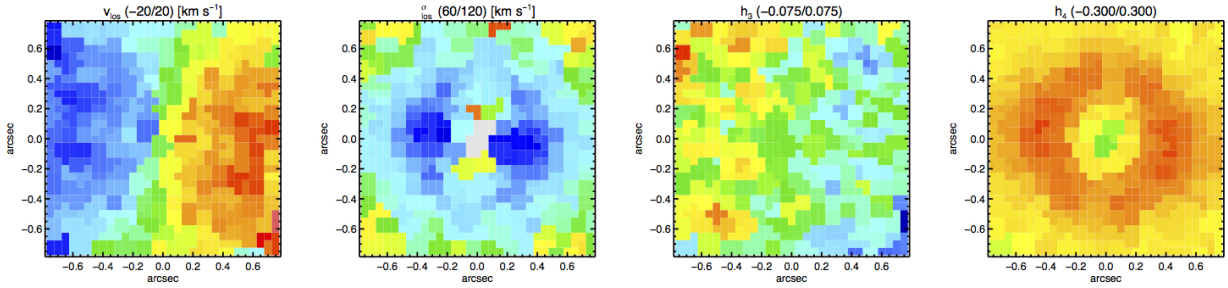

Figure 4.5: Voronoi-binned and bisymmetrized NIFS dynamical maps of NGC 6814.

Finally, after fitting the spectra with pPXF, fitting the kinematic PA of the velocity profile, Voronoi binning the data, and then bisymmetrizing it, we are ready to determine the mass of the SMBH. This is the subject of the next chapter.

– 5 –

Dynamical Modeling Analysis

5.1 SOSA and SOLPA

We employ Dr. Monica Valluri's stellar dynamical modeling algorithm (Valluri et al. 2004, 2005) to constrain the mass of NGC 6814's SMBH (M_{BH}). Generally speaking, this algorithm takes as input our kinematic measurements of the LOSVD, $\sigma_\star$, h_3 and h_4 (see previous chapter) as well as the shape of the luminosity distribution of stars. The user supplies a testable (M_{BH}) and mass-to-light (Υ) ratio. Next, the code uses the Schwarzchild Orbit Superposition principle (Schwarzschild 1979) and creates a library of possible orbits of stars, and then superposes these orbits to find the model distribution of stars and that best reproduces these observed quantities. It compares the model to the data and outputs a χ^2 value for each M_{BH} and Υ. The code is run on a grid of M_{BH}s and Υs and the χ^2s are compared to each other until a minimum is found that points to an optimal M_{BH} and Υ.

Because this type of stellar dynamical modeling can suffer from degeneracies, assumptions are made in order to constrain the models. Though there exists evidence that many elliptical galaxies and galaxy bulges are somewhat triaxial (Contopoulos 1956), this modeling software assumes an axisymmetric distribution of stellar orbits of known inclination of the symmetry axis. (In the previous chapter, we used a program called fitkinematicpa.pro to fit this symmetry axis and found it to be 9.4°.) These stellar orbits are assumed to be in steady state, and as such are obeying three integrals of motion: total energy, angular momentum in the direction of the symmetry axis, and a third integral which confines each orbit to a finite number of intersections between the meridional plane and the zero-velocity curve (ZVC). This curve traces the outer limits of an orbit of a given energy.

Under these assumptions and for each given M_{BH} and Υ value, orbit libraries, or collections of possible orbits of groups of stars, are created. Because the goal is to reproduce the data as closely as possible, the model orbits are convolved with the datas measured PSF and line spread function (LSF). The orbits are "launched" from the ZVC and allowed to complete many cycles. The stars are "observed" at 100 equal time steps for 200 total orbits, and information about the star's position and velocity are stored in grids. Because we observe the kinematics as a 2D projection on the sky, the orbital information is stored in 2D projected coordinates. The frequency with which an orbit is observed in a specific bin is also stored and used as a weight for that bin when calculating the mass distribution of the galaxy's inner region.

A non-negative least-squares optimization is performed to determine which combination of possible set of orbits, weighted and linearly superposed, yields the best model with the smallest χ^2 value. The whole code is run on a grid of black hole masses and stellar mass-to-light ratios. Each combination of M_{BH} and Υ results in its own χ^2 value and velocity maps, which are then compared to each other to see which M_{BH} and Υ pair produced the best fit.

5.2 Inputs and Outputs

The Valluri stellar dynamical modeling algorithm is divided into two parts: SOSA and SOLPA (Schwarzchild Orbit superposition (Linear Programming) Algorithm). SOSA and SOLPA are written in Fortran and make use of the Numerical Algorithms Group, or NAG mathematical library. The first part, SOSA, creates the orbit libraries; the second part, SOLPA, optimizes the orbit superposition.

Before the code can begin to model the dynamics of the galaxy, the user must provide the code with measurements directly from the data including size of the PSF, the shape and size of the 2D surface brightness profile of the bulge, and an initial estimate of the most likely mass-to-light ratio. We describe how we measured these quantities below. Next, we describe how we used these measurements in our models as well as which parameters we varied in our pursuit of the best fitting model.

5.2.1 PSF Fitting Using GALFIT

In order to characterize the PSF shape of the NIFS observations for input into the stellar dynamical modeling code, we used a 2D surface brightness fitting program called GALFIT (Peng et al. 2002, 2010), which is an algorithm that fits 2D analytical functions directly to imaging data. In order to fit a 2D function to the PSF, we first needed to isolate the unresolved AGN point source from the rest of the host galaxy emission. To do this, we again selected a frame from the data cube that contains broadline emission, and then subtracted an average of two frames that only contain continuum emission on either side of the broadline frame, thereby isolating the emission from the point source AGN which serves to characterize the PSF. Next, we input that image into GALFIT, and used multiple gaussian components to fit the image. GALFIT outputs a model image and a residual image representing the difference between the model and the data (see Figure 5.1). Looking at the residual image can give the user an idea of the goodness of fit. If the residuals are close to zero and very little of the PSF's structure is left over, then that means the model is matching the data well. We achieved a clean residuals image with a PSF model containing three gaussian components of different FWHMs and brightnesses. These components are summarized in Table **??**. This

PSF information is fed into the stellar dynamical code, which uses it to convolve with its model to reproduce spatial information in the observations.

Table 5.1: PSF Gaussian Component Fit Parameters

Component #	σ	**Weight**
1	0.05”	0.212
2	0.13”	0.266
3	0.26”	0.522

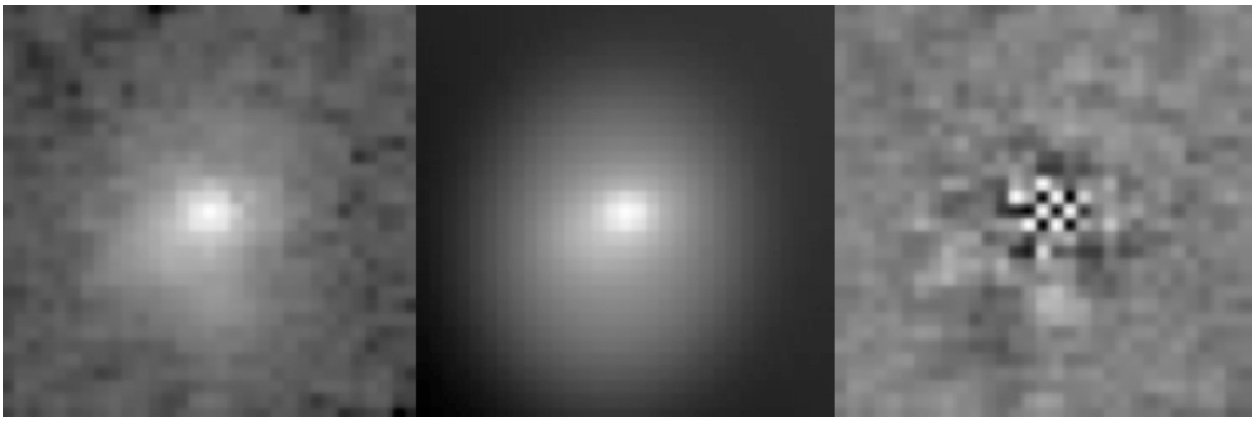

Figure 5.1: Left: PSF image; Center: PSF model; Right: Residual image

5.2.2 Multi-Gaussian Expansion

The Valluri stellar dynamical modeling code requires the user to input information about how the light (which traces the mass) in NGC 6814's bulge is distributed. The code uses the light distribution of the galaxy to form an axisymmetric mass density profile. However, because the NIFS FOV is so small (recall 2.99”×2.97”) in comparison to the angular size of the bulge, which is approximately 15” in radius, we had to use wider FOV imaging that we already had from other research. The large FOV image we used came from H-band data I took using the WIYN High-Resolution Infrared Camera (WHIRC) instrument on the WIYN

3.5-m telescope located on Kitt Peak in Arizona. WIYN's FOV of 3.3 square arcminutes allowed us to fully image the bulge and even most of the disk. [1]

Using the WHIRC/WIYN H-band image of NGC 6814, Dr. Bentz used a fitting algorithm called Multi-Gaussian Expansion (MGE) by Emsellem et al. (1994) to characterize the 2D distribution of light. As its name suggests, this technique assumes that the luminosity distribution can be well-approximated by a summation of concentric gaussian profiles that are convolved with the image's PSF shape. The MGE code outputs the integrated counts under each gaussian as well as their respective $\sigma_\star$ and axial ratios (see Table 5.2). We chose to use only the inner three gaussians because the outer two are related to the disk and not the bulge.

Table 5.2: MGE Code Output

Total Flux (counts)	σ (pix)	**Axial Ratio** (b/a)
3.358×10^6	4.538	0.574
6.032×10^6	38.628	0.827
3.517×10^6	123.987	0.320
1.636×10^7	144.784	1.000
5.603×10^6	525.370	1.000

Before these quantities can be put into the SDM code, they must then be converted from instrumental units of counts and pixels to physical units of $L_\odot/pc^2$ and arcsec. The process for doing that is as follows. First, the total counts under each gaussian were converted to peak surface brightness (C_0) in units of counts/pixel via Equation (1) of Cappellari (2002):

[1] Our median-combined 28×120-second images (3 360 seconds of total exposure time) of NGC 6814 were taken on the 20^{th} of September, 2011. Images were put through standard pre-processing: linearity-corrected, flat-fielded, dark-subtracted, bad-pixel masked. The fringing created by OH night sky lines were also removed by creating a template from sky offset images and then scaling and subtract that template from the science image. Finally, the sky value was removed via GALFIT modeling.

$$C_0 = \frac{TotalCounts}{2\pi\sigma_{pix}^2 q}$$

Where q and σ_{pix} are the axial ratio and width of the gaussian component respectively. C_0 can then be converted to an H-band surface brightness in mag/arcsec^2 (μ_H) using:

$$\mu_H = 22.7 + 5\log(SCALE) + 2.5\log(t_{exp}) - 2.5\log C_0 - A_H$$

$SCALE$, here, is the pixel scale of WHIRC, which is 0.097"/pix. 22.7 (mag) is the photometric zeropoint, and was calculated using two field stars highlighted in Figure 5.2. These stars were calibrated using the 2MASS Point Source Catalog. The extinction correction, $A_H = 0.083$ mag, was drawn from the Schlafly & Finkbeiner (2011) recalibration of the Schlegel et al. (1998) dust maps of the Milky Way. The exposure time, t_{exp}, was 120 seconds (the images were median combined). Next the surface brightnesses were converted to distance-independent surface brightness density, H', in units of $M_\odot$/pc^2 using:

$$H' = \left(\frac{64\,800}{\pi}\right)^2 10^{0.4(M_{\odot,H}-\mu_H)}$$

Where $M_{\odot,H}$ is the surface brightness of the Sun at a distance such that 1 pc^2 subtends 1 arcsec^2, which is the definition of absolute H-band magnitude. We used the Binney & Merrifield (1998) absolute H-band magnitude of 3.32 $\pm$ 0.03 mag to derive $\mu_H = 22.98$ mag/arcsec^2.

The final unit-corrected MGE results are shown in Table 5.3. We chose to use only the inner three gaussians because the outer two are related to the disk and not the bulge.

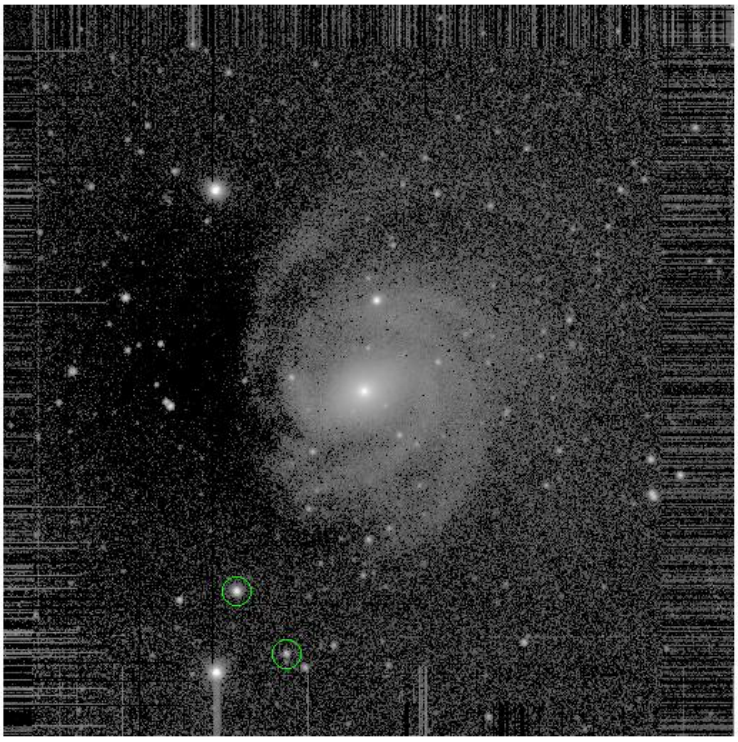

Figure 5.2: Stars marked with green circles that were used to calibrate our MGE components. Brighter star is 2MASXJ19424441-1018504 with $m_H = 12.808 \pm 0.028$ mag. Fainter star is 2MASXJ19424561-1019039 with $m_H = 14.756 \pm 0.066$ mag. Brightnesses are from the 2MASS Point Source Catalog.

Table 5.3: MGE Parameters

Surface Density ($L_{\odot,H}/pc^2$)	σ (arcsec)	**Axial Ratio** (b/a)
5.152×10^4	0.44	0.57
8.857×10^2	3.75	0.83
1.296×10^2	12.03	0.32
(1.414×10^2)	(14.04)	(1.00)
(3.679×10^0)	(50.96)	(1.00)

The gaussian components are also shown in Figure 5.3 as contours overlaid onto the H-band image of NGC 6814 to check goodness of fit.

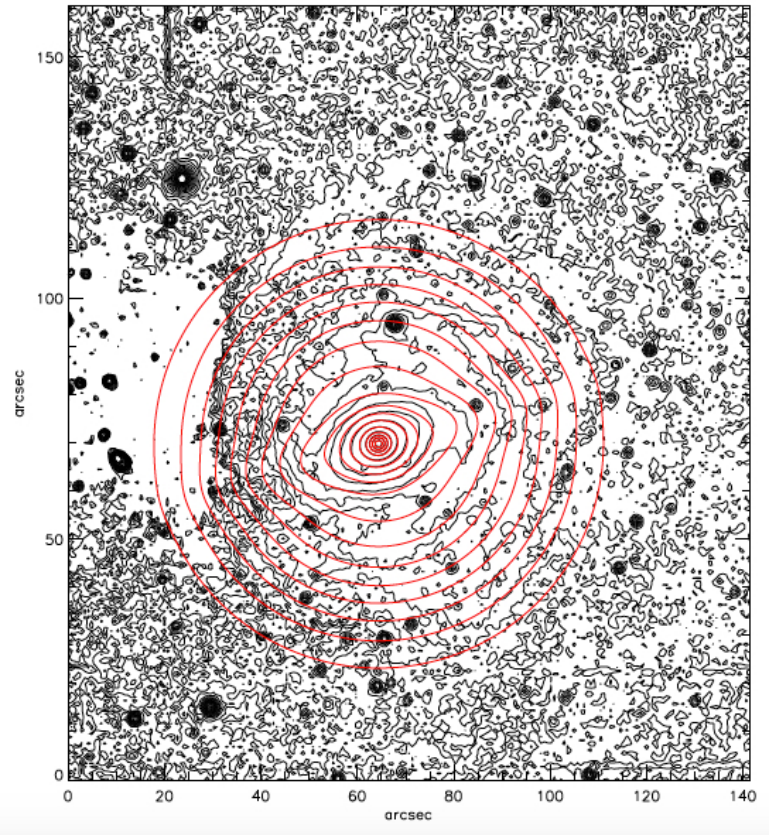

Figure 5.3: MGE contours overlaid onto WHIRC/WIYN H-band image of NGC 6814.

5.2.3 Mass-to-Light Ratio Estimation

First, it should be noted that the Valluri SDM code does allow for radial variation of the mass-to-light ratio (Υ) of the bulge, as there is some evidence that it does vary radially in many galaxies. However, the exact way in which it varies is not very well understood and is an ongoing subject of research (see e.g., van der Kruit & Freeman (2011) for a recent review). Therefore, for now, we choose to assume Υ does not change radially.

Though the Valluri SDM code is run on a whole grid of possible Υs and the best one is chosen from comparing the χ^2 of the models, an a priori estimate of this parameter is

extremely useful for guiding our initial range of testable Υs. A first order estimate can also act as a check for whether the model is fitting this parameter well.

Dr. Bentz estimated Υ to first order by first measuring by eye the B-I, V-I, and R-I colors of NGC 6814's bulge using Figure 5.4 from the Carnegie-Irvine Nearby Galaxy Survey[2]. Because the photometry at small radii are contaminated with AGN light, and the bulge extends out to 15", the colors were measured at a radius between 5" and 15".

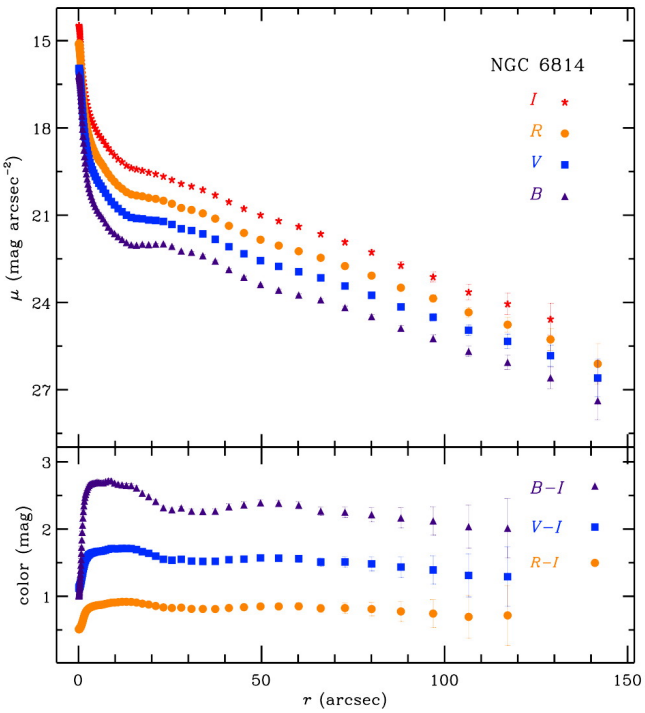

Figure 5.4: Figure from the Carnegie-Irvine Nearby Galaxy Survey showing NGC 6814's color profile in B, V, R, and I.

[2]http\protect\kern+.2222em\relax//cgs.obs.carnegiescience.edu/CGS/data/images/NGC6814_prof.jpg

$$B - I = 2.6 \pm 0.1$$

$$V - I = 1.7 \pm 0.1$$

$$R - I = 0.9 \pm 0.1$$

From these, we can determine the following:

$$B - R = 1.7$$

$$B - V = 0.9$$

Using these colors, Υ can be derived from Bell & de Jong (2001), Table 1:

$$\log \Upsilon = -0.663 + 0.704(B - V) = -0.029 \implies \Upsilon = 0.94$$

$$\log \Upsilon = -0.754 + 0.489(B - R) = 0.077 \implies \Upsilon = 1.19$$

$$\log \Upsilon = -1.030 + 0.870(V - I) = 0.362 \implies \Upsilon = 2.30$$

From Bell et al. (2003), Appendix A2:

$$\log \Upsilon = -0.209 + 0.210(B - V) = -0.020 \implies \Upsilon = 0.95$$

$$\log \Upsilon = -0.262 + 0.180(B - R) = 0.044 \implies \Upsilon = 1.10$$

From Zibetti et al. (2009), Table B1:

$$\log \Upsilon = -1.147 + 1.144(g - r)$$

and from Fukugita et al. (1996):

$$B - R = 1.506(g - r) + 0.370$$

so that

$$\log \Upsilon = -1.428 + 0.760(B - R) = -0.136 \implies \Upsilon = 0.73$$

Finally, these H-band values of Υ were averaged together to yield a final first order estimate of 1.0 $M_\odot/L_\odot$.

5.2.4 Model Setup

Now that we had a PSF shape, a surface brightness profile fit, and an initial guess for the primary Υ, most of the hard work was done. Next, we needed to actually create models and explore parameter space. Many of our parameter choices were guided by our collaborator and the code's author, Dr. Monica Valluri's extensive knowledge of the sensitivity of the models to each choice (Valluri et al. 2004). We also were guided by the work of Dr. Christopher Onken (Onken et al. 2004, 2007, 2014), whose studies on a different galaxy, NGC 4151, bear many parallels to this work.

Besides the values of Υ and M_{BH} that define the grid of models, the code requires the user to tune a few other parameters that are applied to the whole grid. One such tunable quantity is the size of the orbit library that will be used to create the models. Valluri et al. (2004) find that the ideal orbit library size is a little over five times the number of constraints.

Any smaller than that and the error bars will decrease artificially. In our case, we have 242 apertures (or voronoi bins) with four kinematic quantities measured per aperture (v, $\sigma_\star$, h_3, and h_4), as well as mass and surface brightness constraints create a total of about 8000. We opted to use an orbit library size of 8100 orbits. The user must also specify the inclination of the bulge (not to be confused with the inclination of the kinematic major axis). Because the disk is nearly face on, we chose a similar inclination for the bulge of 15°, though this choice will need to be tested. Finally, the code requires a distance to NGC 6814, which we set to 23 Mpc because the results from the Cepheid analysis were not available before we started creating our models. Because the Cepheid analysis yielded a distance that is smaller ($17.54^{+2.05}_{-1.84}$ Mpc), we can simply scale all modeled black hole masses by the ratio of the two numbers, or $17.56/23 = 76\%$[3]

After tuning the parameters above that apply to all models, the two main parameters to test were Υ and M_{BH}. For our first grid of models we chose 10 Υ values and 10 M_{BH}s (see 5.4), which formed a grid of 100 models total. We centered our ranges on the expected values of each. For Υ, our expected value was around 1.0 $M_\odot/L_\odot$ (see Section 5.2.3), so we ran models for a range from 0.4 to 1.3 $M_\odot/L_\odot$ with increments of 0.1 between each value. Our initial black hole mass range was centered on the RM mass of about 2.0×10^7 $M_\odot$, and spanned from 1.0×10^4 to 1.0×10^8 $M_\odot$.

Figure 5.5 shows the best-fitting model dynamical maps produced from our first grid of 100 models (bottom four panels). The data maps are reproduced for comparison (top panels). The model map very much over-estimates $\sigma_\star$. Marginalization plots are shown in

[3]We apply this mass scaling only to the final set of models discussed because these were the only ones that constrained the mass properly.

Table 5.4: Modeled black hole masses and mass-to-light ratio values.

$\mathbf{M}_{BH}$ ($M_\odot$)	Υ ($M_\odot/L_\odot$)
1.0E+04	0.4
1.0E+05	0.5
1.0E+06	0.6
5.0E+06	0.7
1.0E+07	0.8
1.5E+07	0.9
2.0E+07	1.0
2.5E+07	1.1
5.0E+07	1.2
1.0E+08	1.3

Figure 5.6. Υ is constrained to 1.0 and respectively only to about 1.5σ confidence. M_{BH} appears as if its best-fit value is 1.0×10^8 $M_\odot$ with about 1.5σ confidence as well. However, that mass value is at the top of the possible range, so the uptick in the χ^2 value at larger values is most likely an effect of smoothing.

Because $\sigma_\star$ is the most important quantity to model accurately (M_{BH} is determined using this quantity), we tried fitting only v and $\sigma_\star$ and not h_3 nor h_4. If our h_3 and h_4 data from pPXF are too noisy, its possible they are not adding any value to the models and could be negatively affecting our fits to v and $\sigma_\star$. The results of restricting our fits to v and $\sigma_\star$ only are shown in Figures 5.7 and 5.8.

Figures 5.7 shows a clear improvement of our fit to v and $\sigma_\star$, thus suggesting that our h_3 and h_4 data might be throwing off our model fits. The marginalization plots are slightly different as well, and suggest that Υ is still about 1.0 $M_\odot/L_\odot$, and the best fit black hole mass is still 1.0×10^8 $M_\odot$, but its upper limit is still not well-constrained.

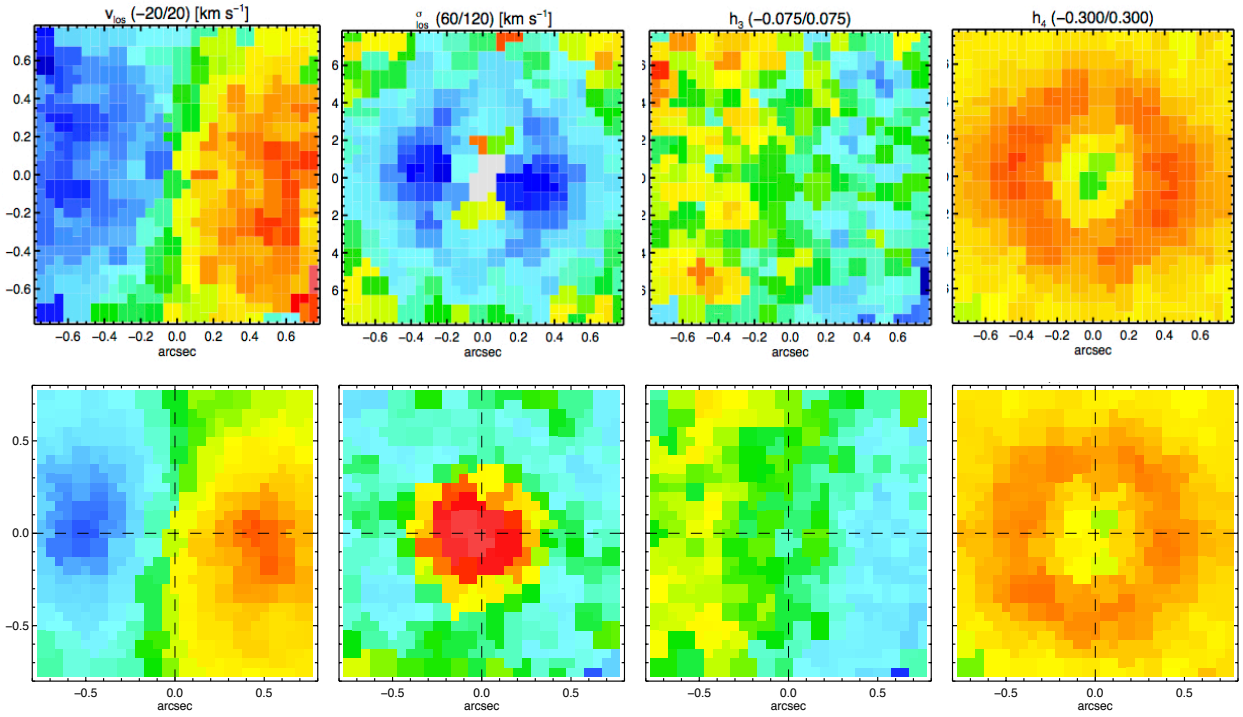

Figure 5.5: Data (top) and model (bottom) dynamical maps. Maps are of (left to right) v, $\sigma_\star$, h_3, and h_4. The model $\sigma_\star$ overestimates the measured $\sigma_\star$.

Though we expected our SDM mass to be close to RM mass, which we recall is $1.44^{+0.271}_{-0.275} \times 10^7$ $M_\odot$ (Bentz & Katz 2015) [4], we were surprised that these models seemed to favor a mass that was almost an order of magnitude larger (though the mass is not well constrained at all). Assuming that perhaps some other input parameters were causing the mass to be artificially high, we kept the same ranges of M_{BH}s and Υs, but we varied inclination angle of the bulge and number of orbits. The inclination angles tested were 10°, 15°, 20°, 50°, and 90° (all of which had orbit library sizes of 8 100 orbits). Holding the inclination angle fixed at 15°, we

[4]This mass is based on the Hβ broad emission line and assumes $< f >$-factor of 4.3.

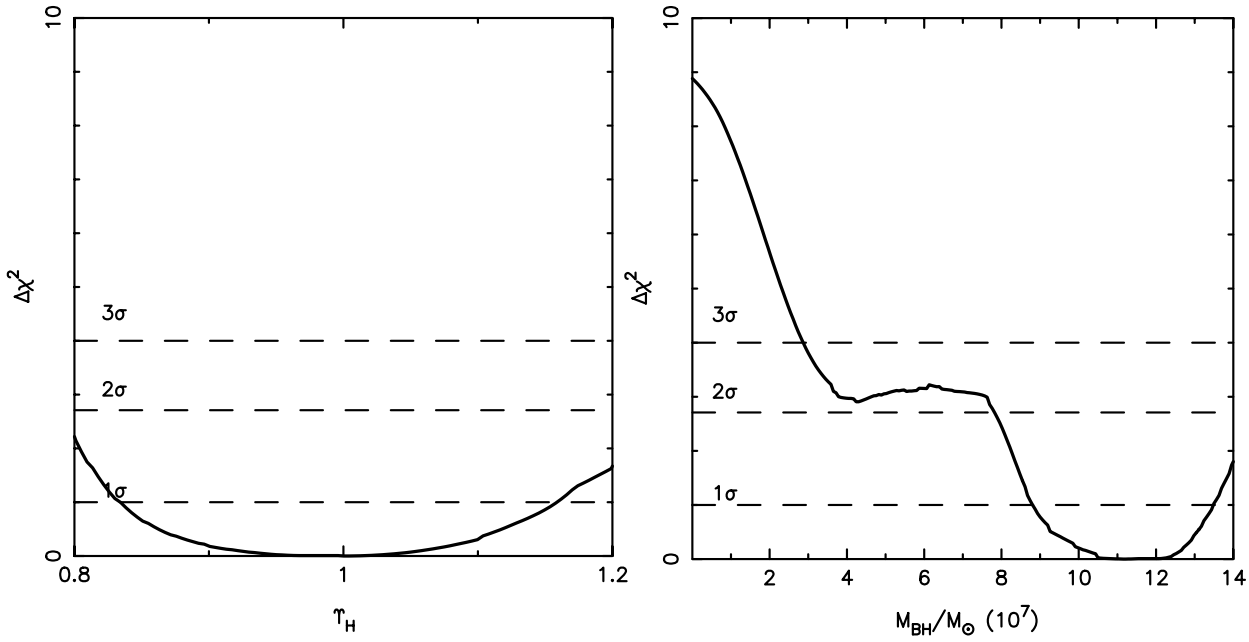

Figure 5.6: Four-parameter fit marginalized χ^2 plots for Υ (left) and M_{BH} (right).

varied the size of the orbit library by decreasing it to 5 400 and increasing it to 16 940. We also experimented with including and excluding h_3 and h_4 in the model fits. In the end, however, we were only able to constrain the upper and lower mass limits by increasing the mass range, which is listed in Table 5.5 along with the values of Υ. The inclination of the bulge was set at 15°, h_3 and h_4 were excluded, and 8 100 orbits were used.

The results of this expanded-range set of models are illustrated in Figures 5.9, 5.10, and Figure 5.11. Figure 5.9 closely resembles the second set of models for which h_3, and h_4 were also excluded. However, both sets still overestimate $\sigma_\star$ at larger radii, and also underestimate

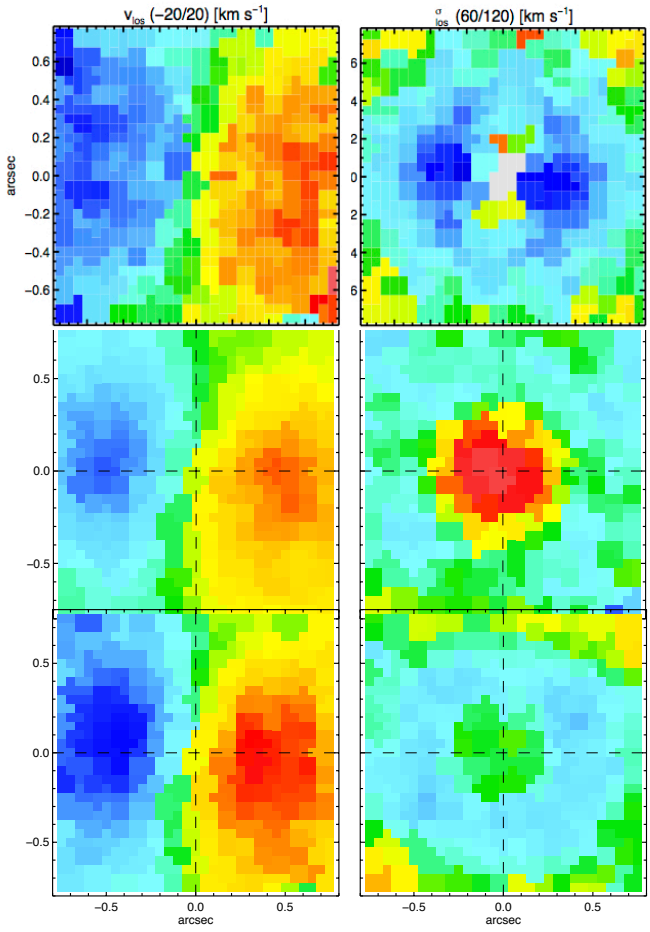

Figure 5.7: Data (top), four-parameter model (middle, same as previous plot except h_3 and h_4 not shown), and two-parameter fit (bottom) dynamical maps of v (left) and $\sigma_\star$ (right). The two-parameter fit on the bottom reproduces the data (especially $\sigma_\star$) better than four-parameter fit in middle.

it at small radii. It is unclear whether the strong positive region at small radii in the data is due to AGN contamination, or whether this is part of the gravitational signature of the SMBH. Regardless, the best fit M_{BH} is 76% of 1.56×10^8 $M_\odot$ or $1.19^{+37.57}_{-1.17} \times 10^8$ $M_\odot$. The 3σ uncertainty spans over three orders of magnitude and are less well-constrained on the lower mass end. The best fit Υ is $0.948^{+0.032}_{-0.208}$ $M_\odot/L_\odot$ (here we quote the 1σ uncertainty because this is thought to be more indicative of the actual error on Υ (M. Valluri, personal communication).

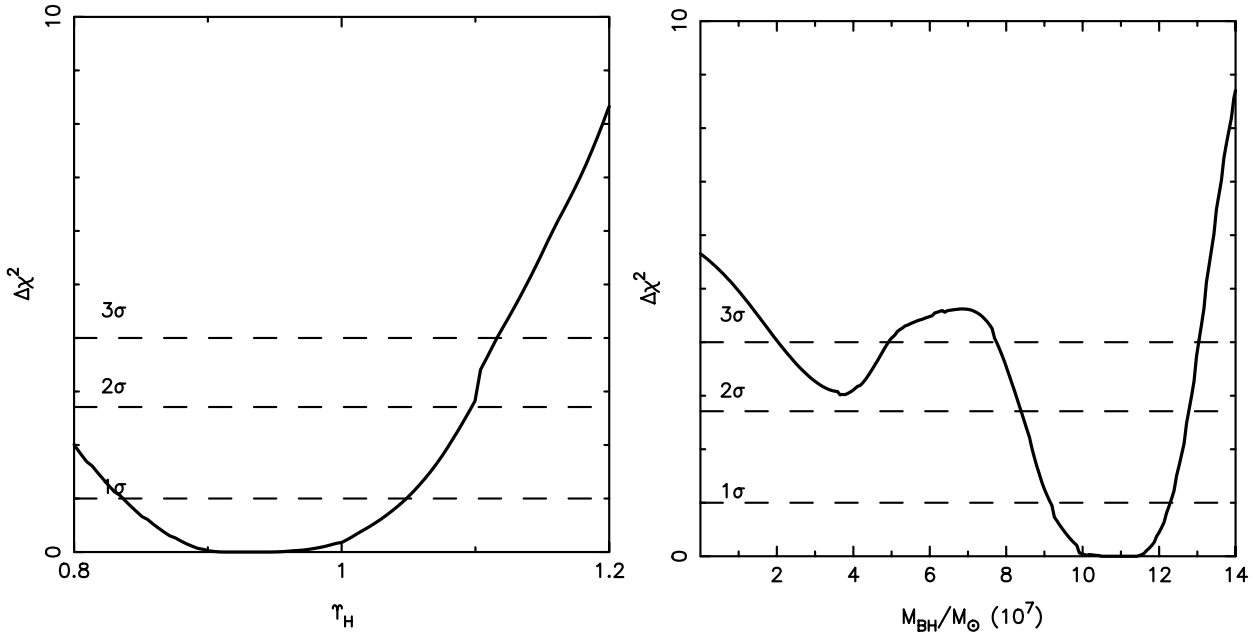

Figure 5.8: Two-parameter fit marginalized χ^2 plots for Υ (left) and M_{BH} (right).

Table 5.5: Modeled black hole masses and mass-to-light ratio values.

$\mathbf{M}_{BH}$ ($M_\odot$)	Υ ($M_\odot/L_\odot$)
1.0E+04	0.3
5.0E+04	0.4
1.0E+05	0.5
5.0E+05	0.6
1.0E+06	0.7
5.0E+06	0.8
1.0E+07	0.9
5.0E+07	1.0
1.0E+08	1.1
5.0E+08	1.2
1.0E+09	1.3
5.0E+09	1.4
1.0E+10	-
5.0E+10	-
1.0E+11	-

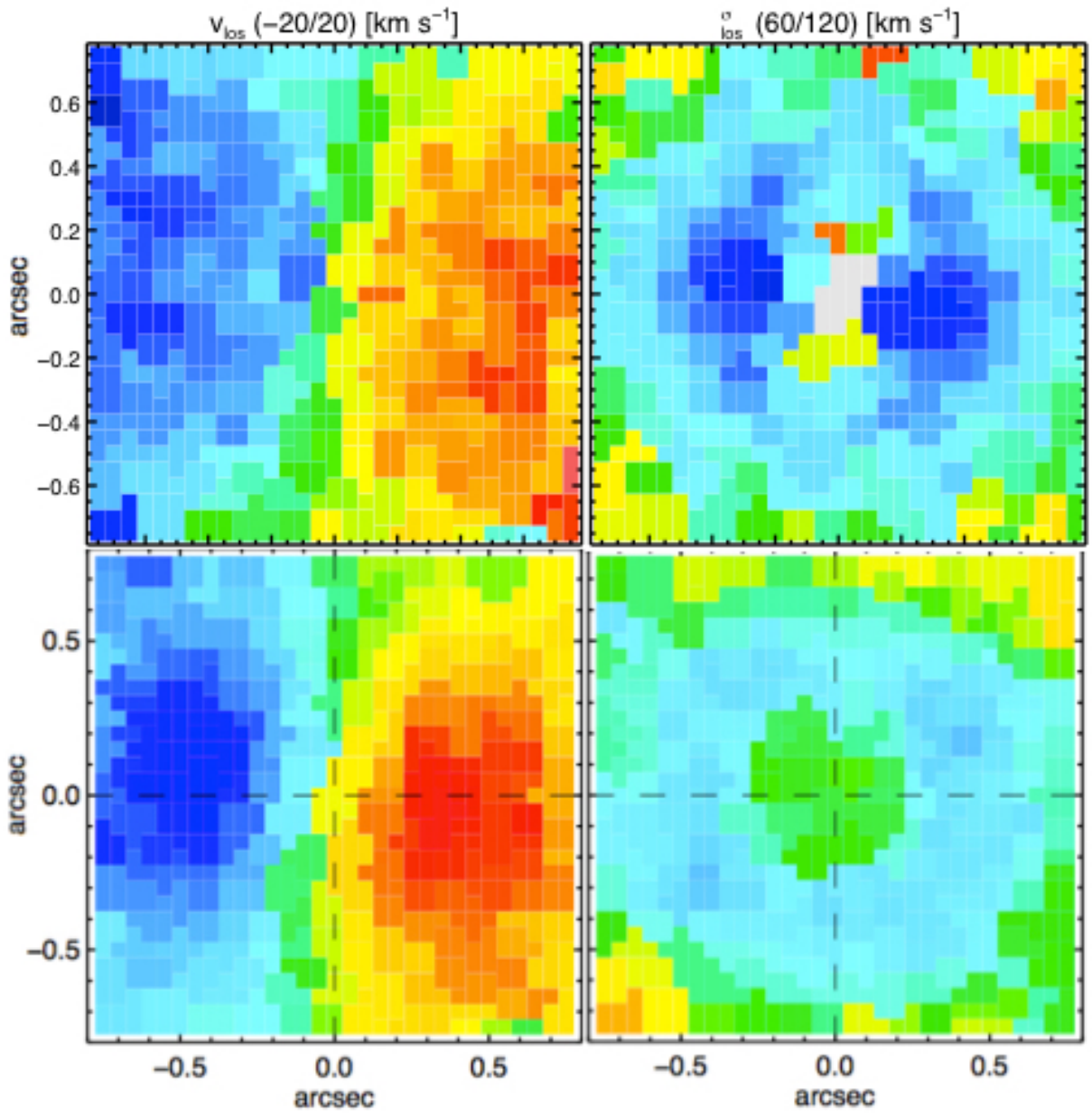

Figure 5.9: Top: data. Bottom: model. Left: v. Right: $\sigma_\star$

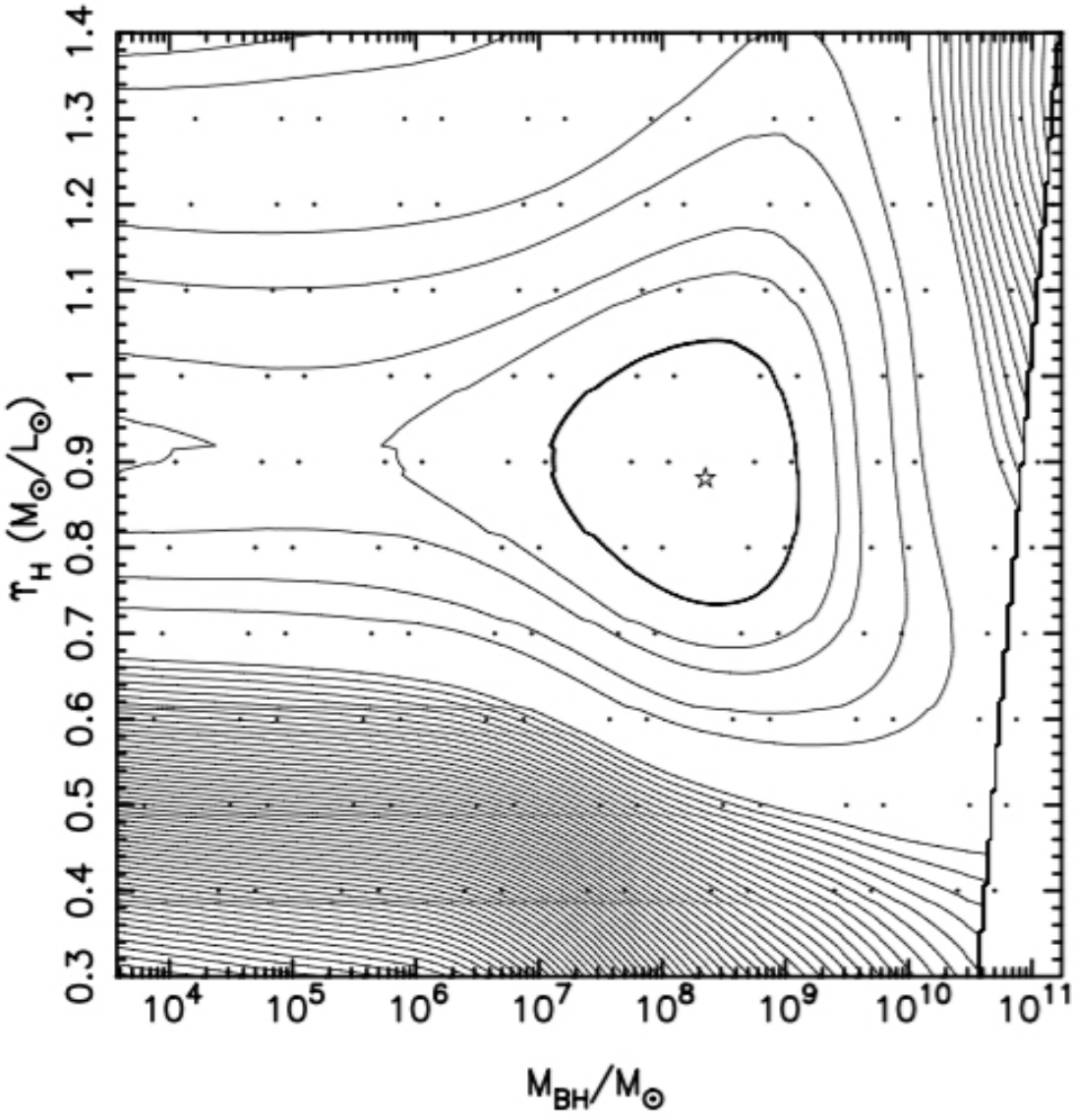

Figure 5.10: Contour plot of expanded-range models of v and $\sigma_\star$. Inclination set to 15° and number of orbits was 8 100. First six contours represent 1σ, 2σ, 3σ, etc. All other contours are equally spaced in χ^2.

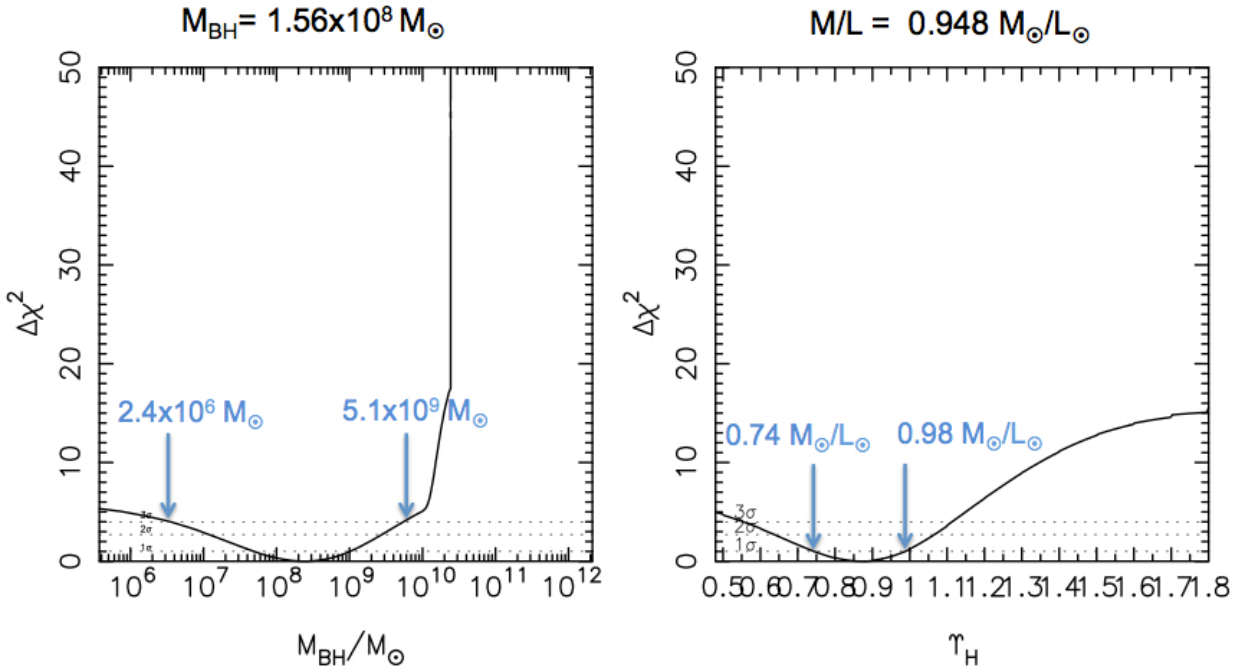

Figure 5.11: Two-parameter fit marginalized χ^2 plots for M_{BH} (left) and Υ (right). Dashed lines represent 1σ, 2σ, 3σ.

5.3 Discussion and Future Work

In the previous section, we derived a best-fit mass for NGC 6814's central black hole of $1.19^{+37.57}_{-1.17} \times 10^8$ $M_\odot$ with a 3σ uncertainty spanning over three orders of magnitude. This poorly constrained best-fit mass is an order of magnitude higher than the RM mass derived from Hβ, and it is almost two orders of magnitude higher than the recent RM modeling mass, $2.63^{+1.94}_{-0.89} \times 10^6$ $M_\odot$ of Pancoast et al. (2014). However, our SDM mass is consistent within 3σ of both of these measurements. This indicates that more models are warranted in order to further constrain the mass and determine whether our measurement remains consistent. Indeed, there remain several regions of parameter space that have yet to be explored.

From our first round of models, we see that when we try to fit all four of v, $\sigma_\star$, h_3, and h_4, the software struggles to reproduce $\sigma_\star$. We therefore try to only fit v and $\sigma_\star$ in our second round of models. We find that our fits improve from just fitting v and $\sigma_\star$. This may mean that there is not be enough signal to noise for our pPXF fits to have produced valuable h_3 and h_4 constraints. However, if we discover that some other minimum in the parameter space exists that produces better fits, then we may try to reincorporate h_3 and h_4 into the models.

Another parameter that warrants further investigation is inclination of the bulge. Though we tested 10°, 15°, 20°, 50°, and 90°, we still need to retest those with a larger mass range. Orbit library size also needs to be retested with the larger mass range.

Additionally, an aspect we have thus far not explored is the effect of how the χ^2 statistic is calculated and what smoothing parameter is used. The SOSA/SOLPA code outputs a few different versions of χ^2 that include different sets of constraints. Though some preliminary testing showed that the version of χ^2 used produced the most sensical results, further testing

is needed. With regard to the smoothing parameter, it is used to regularize the models and penalize any sharp changes in phase space. Realistic galaxies have smooth phase space distributions. However, too much smoothing tends to bias the results. We will test whether changing the smoothing parameter affects the results.

Finally, and perhaps most importantly, we note that NGC 6814's morphology might not be well-suited to the present modeling code's assumptions. SOSA/SOLPA assumes an axisymmetric kinematic distribution. However, NGC 6814 is weakly barred with a de Vaucouleurs classification of SAB(rs)bc, which can be seen clearly in Figure 5.3. Márquez et al. (1999) find that the bar is 12 arcseconds long and is aligned along $+25°$. It has been shown that, if a galaxy is barred, stellar dynamical modeling tend to overestimate the mass of the black hole (Brown et al. 2013). A stellar dynamical modeling code that can account for a bar does not presently exist, but is under development.

– 6 –

Conclusions and Future Work

We have made significant strides toward measuring the mass of the supermassive black hole at the center of NGC 6814. We emphasize that this is only the third AGN for which an SDM mass has been derived. This is also the first time a Cepheid distance has been measured for NGC 6814.

At this point, it might be useful to take a step back and remember how this research is relevant to humankinds understanding of the nature of the Universe. If the Universe contains an estimated 2 trillion galaxies, and most of the massive galaxies are thought to contain a supermassive black hole at its center, then why is one more mass measurement useful? For that matter, why do we care about supermassive black holes at all?

It is important to study SMBHs because they are thought to play an important role in galaxy evolution (Fabian 2012; Kormendy & Ho 2013; Heckman & Best 2014). Any astronomer seeking to model galaxy evolution can use black hole masses to constrain their models. However, using black hole masses to constrain galaxy evolution models requires knowledge of many masses, and masses at large redshifts. Scaling relations, which are the observed tight correlations between the mass of the SMBH and more easily measured observables of the host galaxy, are the only way we can measure most black hole masses. These scaling relations are calibrated by direct black hole measurements, so our ability to accurately measure black hole masses with scaling relations is contingent upon our ability to precisely measure black hole masses nearby. In particular, it is important to reliably calibrate the RM scaling relation, because this can be used for black holes that are farther

away. So that is why we care about supermassive black hole masses, and especially direct measurements of them. But why is NGC 6814 special?

First, and most basically, NGC 6814 is special because its a nearby (z = 0.005214) Seyfert 1.5 AGN, which are rare. Nearby objects are usually more easily studied, especially when it comes to stellar dynamical modeling. There exist only a handful of galaxies for which we can perform both stellar dynamical modeling and reverberation mapping in order to directly measure the SMBHs mass. NGC 6814 is the only the third galaxy (NGC 4151 and NGC 3227 having been the first two) ever to have both methods applied. Furthermore, there exist only a few other galaxies for which this experiment will even be possible for the foreseeable future, and these include NGC 5273, MGC-06-30-15, NGC 3783 and UGC 06728. But why is it important to compare the results of two different methods of direct SMBH mass determination?

The answer relates to this concept of the f-factor. The f-factor is a constant that contains unknown information about the geometry of the broad line region, and is the number required to make the RM sample of black hole masses consistent with the stellar dynamical sample on the M_{BH}-$\sigma_\star$ relation. Because the f-factor represents a population average, and because it is expected that not all broad-line regions are shaped the same, it is therefore useful to see how individual f-factors compare to the population average. By taking the ratio of NGC 6814's RM mass to its SDM mass, we can calculate its individual f-factor. Given the present lack of tight constraints on the SDM mass, we feel this calculation is best left for future investigations, as it would be rather meaningless at the present time. If, in future studies, the SDM mass can be reasonably constrained and the f-factor calculated, then by

comparing its individual f-factor to the population average, we can more insight into how much variation there is between an individual's f-factor and the average f-factor.

It should also be noted that studies are currently underway to model the shape of the BLR using reverberation mapping of different parts of the redshifted and blueshifted wings of the broad lines (e.g., Bentz et al. (2010)). This will allow RM masses to be self-consistent, and will provide an independent check on the accuracy of dynamical modeling masses. Indeed there already exists an RM modeling mass measured for NGC 6814 (Pancoast et al. 2014) as was discussed in Chapter 5. However, direct comparisons of RM and SDM masses, like the one in this work, are still important to perform because we still do not understand if there are any meaningful differences between the AGN and quiescent samples that could affect scaling relations.

The assumption that the dynamical and active samples of black hole masses follow the same M_{BH}-$\sigma_\star$ relation underpins our entire understanding of SMBH masses at cosmic distances. Testing this assumption, as this work has made strides toward doing, is vital to our understanding of the role of SMBHs in galaxy evolution throughout the history of the Universe.

REFERENCES

Balogh, M. L., Pearce, F. R., Bower, R. G., & Kay, S. T. 2001, MNRAS, 326, 1228

Barbosa, F. K. B., Storchi-Bergmann, T., Cid Fernandes, R., Winge, C., & Schmitt, H. 2009, MNRAS, 396, 2

Becklin, E. E., & Neugebauer, G. 1968, ApJ, 151, 145

Beifiori, A., Courteau, S., Corsini, E. M., & Zhu, Y. 2012, MNRAS, 419, 2497

Bell, E. F., & de Jong, R. S. 2001, ApJ, 550, 212

Bell, E. F., McIntosh, D. H., Katz, N., & Weinberg, M. D. 2003, ApJS, 149, 289

Benedict, G. F., McArthur, B. E., Feast, M. W., Barnes, T. G., Harrison, T. E., Patterson, R. J., Menzies, J. W., Bean, J. L., & Freedman, W. L. 2007, AJ, 133, 1810

Bentz, M. C., Denney, K. D., Cackett, E. M., Dietrich, M., Fogel, J. K. J., Ghosh, H., Horne, K., Kuehn, C., Minezaki, T., Onken, C. A., Peterson, B. M., Pogge, R. W., Pronik, V. I., Richstone, D. O., Sergeev, S. G., Vestergaard, M., Walker, M. G., & Yoshii, Y. 2006, ApJ, 651, 775

Bentz, M. C., & Katz, S. 2015, PASP, 127, 67

Bentz, M. C., Walsh, J. L., Barth, A. J., Yoshii, Y., Woo, J.-H., Wang, X., Treu, T., Thornton, C. E., Street, R. A., Steele, T. N., Silverman, J. M., Serduke, F. J. D., Sakata, Y., Minezaki, T., Malkan, M. A., Li, W., Lee, N., Hiner, K. D., Hidas, M. G., Greene, J. E., Gates, E. L., Ganeshalingam, M., Filippenko, A. V., Canalizo, G., Bennert, V. N., & Baliber, N. 2010, ApJ, 716, 993

Binney, J., & Merrifield, M. 1998, Galactic Astronomy

Blandford, R. D., & McKee, C. F. 1982, ApJ, 255, 419

Bohlin, R. C., & Gilliland, R. L. 2004, AJ, 127, 3508

Bradford, J. D., Geha, M. C., & van den Bosch, F. C. 2016, ApJ, 832, 11

Brown, J. S., Valluri, M., Shen, J., & Debattista, V. P. 2013, ApJ, 778, 151

Cappellari, M. 2002, MNRAS, 333, 400

Cappellari, M., & Emsellem, E. 2004, PASP, 116, 138

Cappellari, M., Emsellem, E., Krajnović, D., McDermid, R. M., Scott, N., Verdoes Kleijn, G. A., Young, L. M., Alatalo, K., Bacon, R., Blitz, L., Bois, M., Bournaud, F., Bureau, M., Davies, R. L., Davis, T. A., de Zeeuw, P. T., Duc, P.-A., Khochfar, S., Kuntschner, H., Lablanche, P.-Y., Morganti, R., Naab, T., Oosterloo, T., Sarzi, M., Serra, P., & Weijmans, A.-M. 2011, MNRAS, 413, 813

Contopoulos, G. 1956, ApJ, 124, 643

Davies, R. I., Thomas, J., Genzel, R., Müller Sánchez, F., Tacconi, L. J., Sternberg, A., Eisenhauer, F., Abuter, R., Saglia, R., & Bender, R. 2006, ApJ, 646, 754

de Vaucouleurs, G., de Vaucouleurs, A., Corwin, Jr., H. G., Buta, R. J., Paturel, G., & Fouqué, P. 1991, Third Reference Catalogue of Bright Galaxies. Volume I: Explanations and references. Volume II: Data for galaxies between 0^h and 12^h. Volume III: Data for galaxies between 12^h and 24^h.

Denney, K. D., Peterson, B. M., Pogge, R. W., Adair, A., Atlee, D. W., Au-Yong, K., Bentz, M. C., Bird, J. C., Brokofsky, D. J., Chisholm, E., Comins, M. L., Dietrich, M., Doroshenko, V. T., Eastman, J. D., Efimov, Y. S., Ewald, S., Ferbey, S., Gaskell, C. M., Hedrick, C. H., Jackson, K., Klimanov, S. A., Klimek, E. S., Kruse, A. K., Ladéroute, A., Lamb, J. B., Leighly, K., Minezaki, T., Nazarov, S. V., Onken, C. A., Petersen, E. A., Peterson, P., Poindexter, S., Sakata, Y., Schlesinger, K. J., Sergeev, S. G., Skolski, N.,

Stieglitz, L., Tobin, J. J., Unterborn, C., Vestergaard, M., Watkins, A. E., Watson, L. C., & Yoshii, Y. 2010, ApJ, 721, 715

Ducati, J. R., Bevilacqua, C. M., Rembold, S. B., & Ribeiro, D. 2001, ApJ, 558, 309

Eddington, A. S. 1917, The Observatory, 40, 290

Emsellem, E., Monnet, G., & Bacon, R. 1994, A&A, 285, 723

Fabian, A. C. 2012, ARA&A, 50, 455

Ferrarese, L., & Merritt, D. 2000, ApJ, 539, L9

Freedman, W. L., Hughes, S. M., 2009AJ....137.4707M, B. F., Mould, J. R., Lee, M. G., Stetson, P., Kennicutt, R. C., Turner, A., Ferrarese, L., Ford, H., Graham, J. A., Hill, R., Hoessel, J. G., Huchra, J., & Illingworth, G. D. 1994, ApJ, 427, 628

Freedman, W. L., Madore, B. F., Gibson, B. K., Ferrarese, L., Kelson, D. D., Sakai, S., Mould, J. R., Kennicutt, Jr., R. C., Ford, H. C., Graham, J. A., Huchra, J. P., Hughes, S. M. G., Illingworth, G. D., Macri, L. M., & Stetson, P. B. 2001, ApJ, 553, 47

Freedman, W. L., Madore, B. F., Scowcroft, V., Burns, C., Monson, A., Persson, S. E., Seibert, M., & Rigby, J. 2012, ApJ, 758, 24

Fruchter, A., & Hook, R. N. 1997, in Proc. SPIE, Vol. 3164, Applications of Digital Image Processing XX, ed. A. G. Tescher, 120–125

Fukugita, M., Ichikawa, T., Gunn, J. E., Doi, M., Shimasaku, K., & Schneider, D. P. 1996, AJ, 111, 1748

Gebhardt, K., Bender, R., Bower, G., Dressler, A., Faber, S. M., Filippenko, A. V., Green, R., Grillmair, C., Ho, L. C., Kormendy, J., Lauer, T. R., Magorrian, J., Pinkney, J., Richstone, D., & Tremaine, S. 2000, ApJ, 539, L13

Gilliland, R. L. 2005, Guiding Errors in 3-Gyro: Experience from WF/PC, WFPC2, STIS,

NICMOS and ACS, Tech. rep.

Graham, A. W., & Driver, S. P. 2007, ApJ, 655, 77

Graham, A. W., Erwin, P., Caon, N., & Trujillo, I. 2001, ApJ, 563, L11

Graham, A. W., Onken, C. A., Athanassoula, E., & Combes, F. 2011, MNRAS, 412, 2211

Grier, C. J., Peterson, B. M., Horne, K., Bentz, M. C., Pogge, R. W., Denney, K. D., De Rosa, G., Martini, P., Kochanek, C. S., Zu, Y., Shappee, B., Siverd, R., Beatty, T. G., Sergeev, S. G., Kaspi, S., Araya Salvo, C., Bird, J. C., Bord, D. J., Borman, G. A., Che, X., Chen, C., Cohen, S. A., Dietrich, M., Doroshenko, V. T., Efimov, Y. S., Free, N., Ginsburg, I., Henderson, C. B., King, A. L., Mogren, K., Molina, M., Mosquera, A. M., Nazarov, S. V., Okhmat, D. N., Pejcha, O., Rafter, S., Shields, J. C., Skowron, J., Szczygiel, D. M., Valluri, M., & van Saders, J. L. 2013, ApJ, 764, 47

Gültekin, K., Richstone, D. O., Gebhardt, K., Lauer, T. R., Tremaine, S., Aller, M. C., Bender, R., Dressler, A., Faber, S. M., Filippenko, A. V., Green, R., Ho, L. C., Kormendy, J., Magorrian, J., Pinkney, J., & Siopis, C. 2009, ApJ, 698, 198

Häring, N., & Rix, H.-W. 2004, ApJ, 604, L89

Heckman, T. M., & Best, P. N. 2014, ARA&A, 52, 589

Herrnstein, J. R., Moran, J. M., Greenhill, L. J., Diamond, P. J., Inoue, M., Nakai, N., Miyoshi, M., Henkel, C., & Riess, A. 1999, Nature, 400, 539

Hofmeister, E., Kippenhahn, R., & Weigert, A. 1964, ZAp, 60, 57

Hu, J. 2008, MNRAS, 386, 2242

—. 2009, ArXiv e-prints

Hubble, E. P. 1922, ApJ, 56

Humphreys, E. M. L., Reid, M. J., Moran, J. M., Greenhill, L. J., & Argon, A. L. 2013, ApJ, 775, 13

Katz, N., Weinberg, D. H., & Hernquist, L. 1996, ApJS, 105, 19

Kennicutt, Jr., R. C., Stetson, P. B., Saha, A., Kelson, D., Rawson, D. M., Sakai, S., Madore, B. F., Mould, J. R., Freedman, W. L., Bresolin, F., Ferrarese, L., Ford, H., Gibson, B. K., Graham, J. A., Han, M., Harding, P., Hoessel, J. G., Huchra, J. P., Hughes, S. M. G., Illingworth, G. D., Macri, L. M., Phelps, R. L., Silbermann, N. A., Turner, A. M., & Wood, P. R. 1998, ApJ, 498, 181

Kereš, D., Katz, N., Weinberg, D. H., & Davé, R. 2005, MNRAS, 363, 2

Kollatschny, W. 2003, A&A, 407, 461

Koornneef, J., Bohlin, R., Buser, R., Horne, K., & Turnshek, D. 1986, Highlights of Astronomy, 7, 833

Kormendy, J. 2004, Coevolution of Black Holes and Galaxies, 1

Kormendy, J., Bender, R., & Cornell, M. E. 2011, Nature, 469, 374

Kormendy, J., & Gebhardt, K. 2001, in American Institute of Physics Conference Series, Vol. 586, 20th Texas Symposium on relativistic astrophysics, ed. J. C. Wheeler & H. Martel, 363–381

Kormendy, J., & Ho, L. C. 2013, ARA&A, 51, 511

Krajnović, D., Cappellari, M., de Zeeuw, P. T., & Copin, Y. 2006, MNRAS, 366, 787

Kundt, W. 1990, Ap&SS, 172, 109

Lafler, J., & Kinman, T. D. 1965, ApJS, 11, 216

Leavitt, H. S. 1908, Annals of Harvard College Observatory, 60, 87

Leavitt, H. S., & Pickering, E. C. 1912, Harvard College Observatory Circular, 173, 1

Macri, L. M., Stanek, K. Z., Bersier, D., Greenhill, L. J., & Reid, M. J. 2006, ApJ, 652, 1133

Madore, B. F. 1982, ApJ, 253, 575

Magorrian, J., Tremaine, S., Richstone, D., Bender, R., Bower, G., Dressler, A., Faber, S. M., Gebhardt, K., Green, R., Grillmair, C., Kormendy, J., & Lauer, T. 1998, AJ, 115, 2285

Marconi, A., & Hunt, L. K. 2003, ApJ, 589, L21

Marconi, M., Musella, I., & Fiorentino, G. 2005, ApJ, 632, 590

Markwardt, C. B. 2009, in Astronomical Society of the Pacific Conference Series, Vol. 411, Astronomical Data Analysis Software and Systems XVIII, ed. D. A. Bohlender, D. Durand, & P. Dowler, 251

Márquez, I., Durret, F., González Delgado, R. M., Marrero, I., Masegosa, J., Maza, J., Moles, M., Pérez, E., & Roth, M. 1999, A&AS, 140, 1

Márquez, I., Durret, F., Masegosa, J., Moles, M., Varela, J., González Delgado, R. M., Maza, J., Pérez, E., & Roth, M. 2004, A&A, 416, 475

Márquez, I., Masegosa, J., Durret, F., González Delgado, R. M., Moles, M., Maza, J., Pérez, E., & Roth, M. 2003, A&A, 409, 459

Mateo, M., & Schechter, P. L. 1989, in European Southern Observatory Conference and Workshop Proceedings, Vol. 31, ESO/ST-ECF Data Analysis Workshop, ed. P. J. Grosbøl, F. Murtagh, & R. H. Warmels, 69–83

McCommas, L. P., Yoachim, P., Williams, B. F., Dalcanton, J. J., Davis, M. R., & Dolphin, A. E. 2009, AJ, 137, 4707

McConnell, N. J., & Ma, C.-P. 2013, ApJ, 764, 184

McConnell, N. J., Ma, C.-P., Gebhardt, K., Wright, S. A., Murphy, J. D., Lauer, T. R., Graham, J. R., & Richstone, D. O. 2011, Nature, 480, 215

Oke, J. B. 1964, ApJ, 140, 689

Onken, C. A., Ferrarese, L., Merritt, D., Peterson, B. M., Pogge, R. W., Vestergaard, M., & Wandel, A. 2004, ApJ, 615, 645

Onken, C. A., & Peterson, B. M. 2002, ApJ, 572, 746

Onken, C. A., Valluri, M., Brown, J. S., McGregor, P. J., Peterson, B. M., Bentz, M. C., Ferrarese, L., Pogge, R. W., Vestergaard, M., Storchi-Bergmann, T., & Riffel, R. A. 2014, ApJ, 791, 37

Onken, C. A., Valluri, M., Peterson, B. M., Pogge, R. W., Bentz, M. C., Ferrarese, L., Vestergaard, M., Crenshaw, D. M., Sergeev, S. G., McHardy, I. M., Merritt, D., Bower, G. A., Heckman, T. M., & Wandel, A. 2007, ApJ, 670, 105

Oppenheimer, B. D., & Davé, R. 2006, MNRAS, 373, 1265

Paczynski, B., & Sasselov, D. 1997, in Variables Stars and the Astrophysical Returns of the Microlensing Surveys, ed. R. Ferlet, J.-P. Maillard, & B. Raban, 309

Pancoast, A., Brewer, B. J., Treu, T., Park, D., Barth, A. J., Bentz, M. C., & Woo, J.-H. 2014, MNRAS, 445, 3073

Park, D., Kelly, B. C., Woo, J.-H., & Treu, T. 2012, ApJS, 203, 6

Peng, C. Y., Ho, L. C., Impey, C. D., & Rix, H.-W. 2002, AJ, 124, 266

—. 2010, AJ, 139, 2097

Peterson, B. M. 1993, PASP, 105, 247

Peterson, B. M., & Wandel, A. 1999, ApJ, 521, L95

Riess, A. G., Li, W., Stetson, P. B., Filippenko, A. V., Jha, S., Kirshner, R. P., Challis, P. M., Garnavich, P. M., & Chornock, R. 2005, ApJ, 627, 579

Riess, A. G., Macri, L., Casertano, S., Lampeitl, H., Ferguson, H. C., Filippenko, A. V., Jha, S. W., Li, W., & Chornock, R. 2011, ApJ, 730, 119

Riess, A. G., Macri, L., Casertano, S., Sosey, M., Lampeitl, H., Ferguson, H. C., Filippenko, A. V., Jha, S. W., Li, W., Chornock, R., & Sarkar, D. 2009, ApJ, 699, 539

Riess, A. G., Macri, L. M., Hoffmann, S. L., Scolnic, D., Casertano, S., Filippenko, A. V., Tucker, B. E., Reid, M. J., Jones, D. O., Silverman, J. M., Chornock, R., Challis, P., Yuan, W., Brown, P. J., & Foley, R. J. 2016, ApJ, 826, 56

Riffel, R. A. 2010, Ap&SS, 327, 239

Riffel, R. A., Storchi-Bergmann, T., & Nagar, N. M. 2010, MNRAS, 404, 166

Romaniello, M., Primas, F., Mottini, M., Pedicelli, S., Lemasle, B., Bono, G., François, P., Groenewegen, M. A. T., & Laney, C. D. 2008, A&A, 488, 731

Saha, A., Thim, F., Tammann, G. A., Reindl, B., & Sandage, A. 2006, ApJS, 165, 108

Sahu, K., Deustua, S., & Sabbi, E. 2014, WFC3/UVIS Photometric Transformations, Tech. rep.

Sakai, S., Ferrarese, L., Kennicutt, Jr., R. C., & Saha, A. 2004, ApJ, 608, 42

Salpeter, E. E. 1964, ApJ, 140, 796

Sandage, A., & Tammann, G. A. 2008, ApJ, 686, 779

Sani, E., Marconi, A., Hunt, L. K., & Risaliti, G. 2011, MNRAS, 413, 1479

Schlafly, E. F., & Finkbeiner, D. P. 2011, ApJ, 737, 103

Schlegel, D. J., Finkbeiner, D. P., & Davis, M. 1998, ApJ, 500, 525

Schmidt, M. 1963, Nature, 197, 1040

Schödel, R., Ott, T., Genzel, R., Hofmann, R., Lehnert, M., Eckart, A., Mouawad, N., Alexander, T., Reid, M. J., Lenzen, R., Hartung, M., Lacombe, F., Rouan, D., Gendron, E., Rousset, G., Lagrange, A.-M., Brandner, W., Ageorges, N., Lidman, C., Moorwood, A. F. M., Spyromilio, J., Hubin, N., & Menten, K. M. 2002, Nature, 419, 694

Schulze, A., & Gebhardt, K. 2011, ApJ, 729, 21

Schwarzschild, M. 1979, ApJ, 232, 236

Shen, Y., Richards, G. T., Strauss, M. A., Hall, P. B., Schneider, D. P., Snedden, S., Bizyaev, D., Brewington, H., Malanushenko, V., Malanushenko, E., Oravetz, D., Pan, K., & Simmons, A. 2011, ApJS, 194, 45

Shostak, G. S. 1978, A&A, 68, 321

Sirianni, M., Jee, M. J., Benítez, N., Blakeslee, J. P., Martel, A. R., Meurer, G., Clampin, M., De Marchi, G., Ford, H. C., Gilliland, R., Hartig, G. F., Illingworth, G. D., Mack, J., & McCann, W. J. 2005, PASP, 117, 1049

Tanvir, N. R., Hendry, M. A., Watkins, A., Kanbur, S. M., Berdnikov, L. N., & Ngeow, C. C. 2005, MNRAS, 363, 749

Taylor, M. B. 2005, in Astronomical Society of the Pacific Conference Series, Vol. 347, Astronomical Data Analysis Software and Systems XIV, ed. P. Shopbell, M. Britton, & R. Ebert, 29

Tonry, J. L., Blakeslee, J. P., Ajhar, E. A., & Dressler, A. 1997, ApJ, 475, 399

Torres, D. F., Capozziello, S., & Lambiase, G. 2000, Phys. Rev. D, 62, 104012

Tremaine, S., Gebhardt, K., Bender, R., Bower, G., Dressler, A., Faber, S. M., Filippenko, A. V., Green, R., Grillmair, C., Ho, L. C., Kormendy, J., Lauer, T. R., Magorrian, J., Pinkney, J., & Richstone, D. 2002, ApJ, 574, 740

Tsiklauri, D., & Viollier, R. D. 1998, ApJ, 501, 486

Tully, R. B. 1988, Nearby galaxies catalog

Tully, R. B., Courtois, H. M., Dolphin, A. E., Fisher, J. R., Héraudeau, P., Jacobs, B. A., Karachentsev, I. D., Makarov, D., Makarova, L., Mitronova, S., Rizzi, L., Shaya, E. J., Sorce, J. G., & Wu, P.-F. 2013, AJ, 146, 86

Tully, R. B., & Fisher, J. R. 1977, A&A, 54, 661

Tully, R. B., & Pierce, M. J. 2000, ApJ, 533, 744

Udalski, A., Szymanski, M., Kubiak, M., Pietrzynski, G., Soszynski, I., Wozniak, P., & Zebrun, K. 1999, Acta Astron., 49, 201

Urry, C. M., & Padovani, P. 1995, PASP, 107, 803

Vacca, W. D., Cushing, M. C., & Rayner, J. T. 2003, PASP, 115, 389

Valluri, M., Ferrarese, L., Merritt, D., & Joseph, C. L. 2005, ApJ, 628, 137

Valluri, M., Merritt, D., & Emsellem, E. 2004, ApJ, 602, 66

van der Kruit, P. C., & Freeman, K. C. 2011, ARA&A, 49, 301

van Leeuwen, F., Feast, M. W., Whitelock, P. A., & Laney, C. D. 2007, MNRAS, 379, 723

Welch, D. L., & Stetson, P. B. 1993, AJ, 105, 1813

Williams, M. J., Bureau, M., & Cappellari, M. 2010, MNRAS, 409, 1330

Winge, C., Riffel, R. A., & Storchi-Bergmann, T. 2009, ApJS, 185, 186

Yoachim, P., McCommas, L. P., Dalcanton, J. J., & Williams, B. F. 2009, AJ, 137, 4697

Zel'dovich, Y. B. 1964, Soviet Physics Doklady, 9, 195

Zibetti, S., Charlot, S., & Rix, H.-W. 2009, MNRAS, 400, 1181

Appendices

– A –

Appendix A

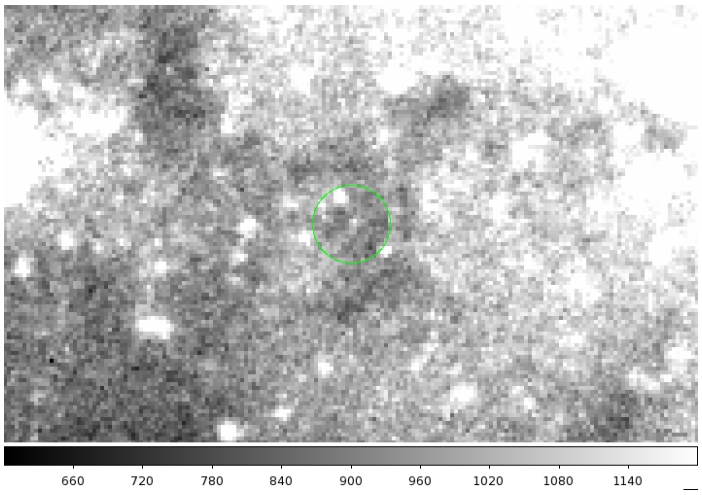

Figure A.1: Cepheid 163 image.

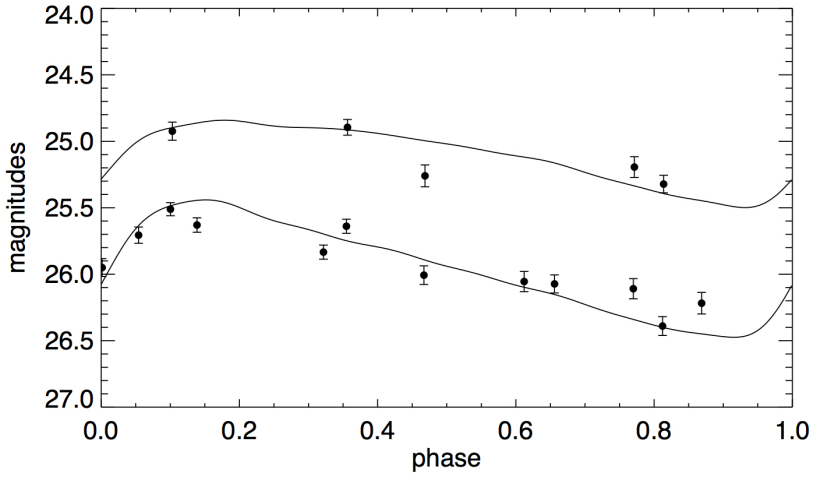

Figure A.2: Cepheid 163 light curve. I-band (top set of points) and V-band (bottom set of points) Cepheid candidate light curve. Black lines are best-fit Cepheid model light curves.

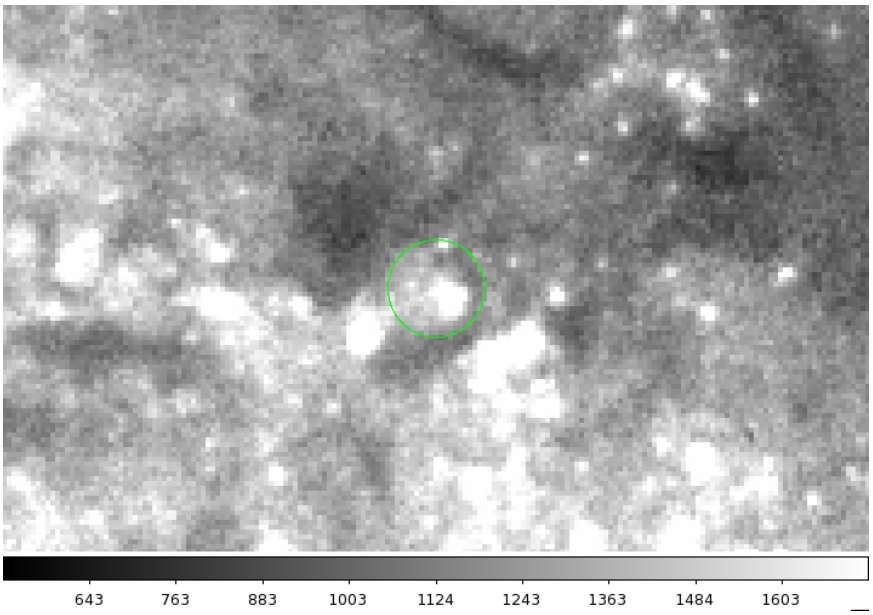

Figure A.3: Cepheid 165 image.

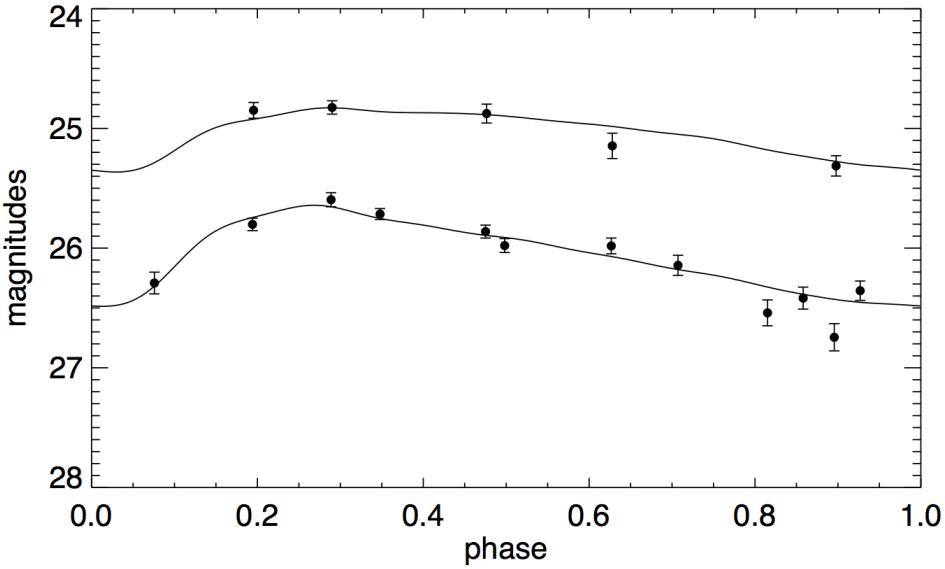

Figure A.4: Cepheid 165 light curve. I-band (top set of points) and V-band (bottom set of points) Cepheid candidate light curve. Black lines are best-fit Cepheid model light curves.

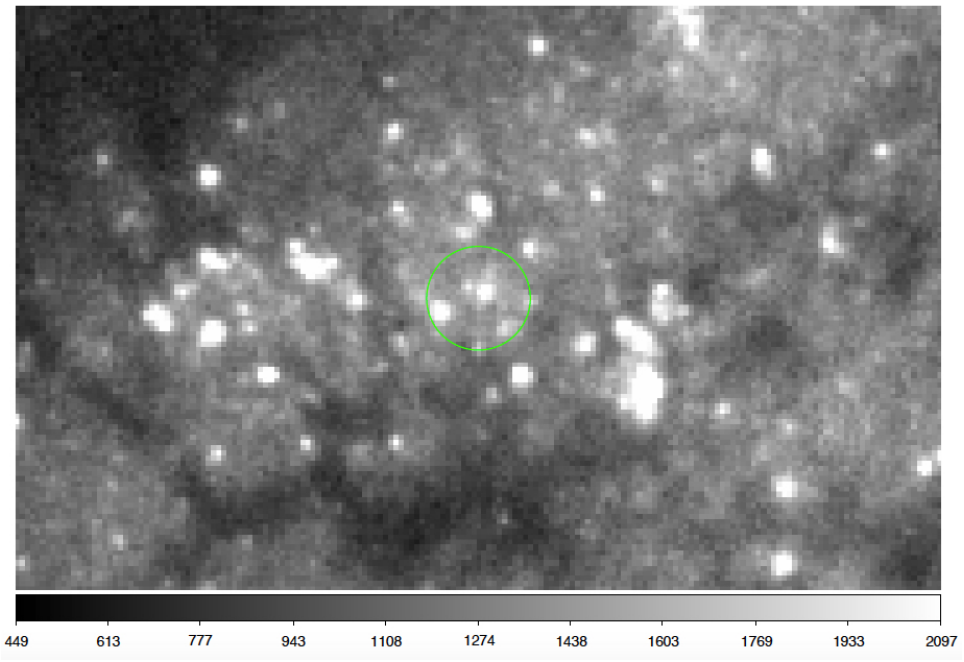

Figure A.5: Cepheid 166 image.

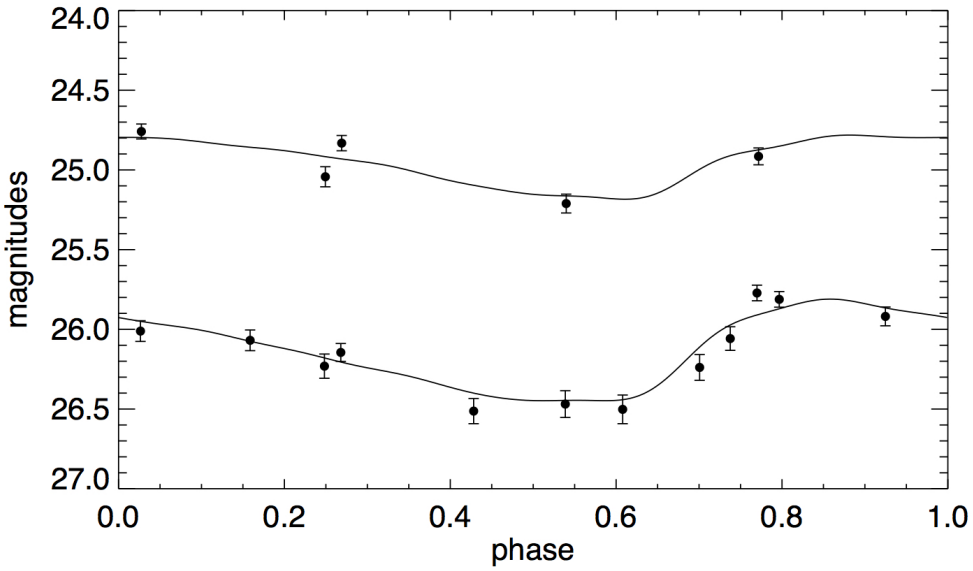

Figure A.6: Cepheid 166 light curve. I-band (top set of points) and V-band (bottom set of points) Cepheid candidate light curve. Black lines are best-fit Cepheid model light curves.

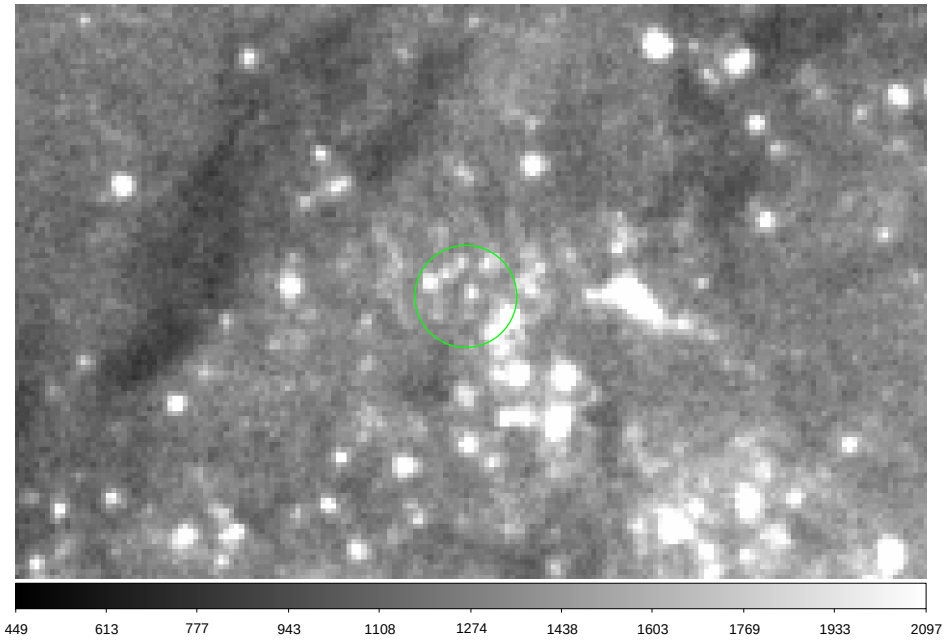

Figure A.7: Cepheid 167 image.

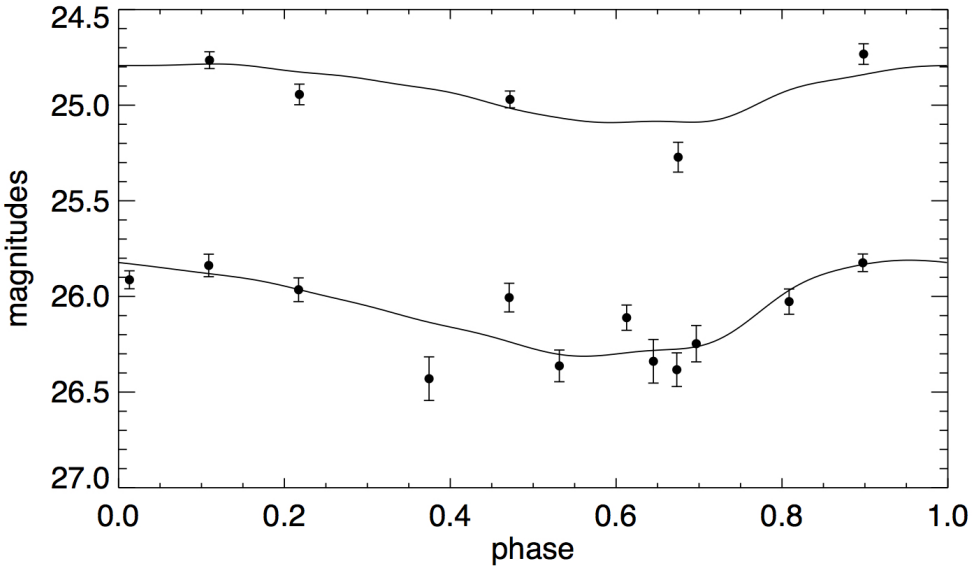

Figure A.8: Cepheid 167 light curve. I-band (top set of points) and V-band (bottom set of points) Cepheid candidate light curve. Black lines are best-fit Cepheid model light curves.

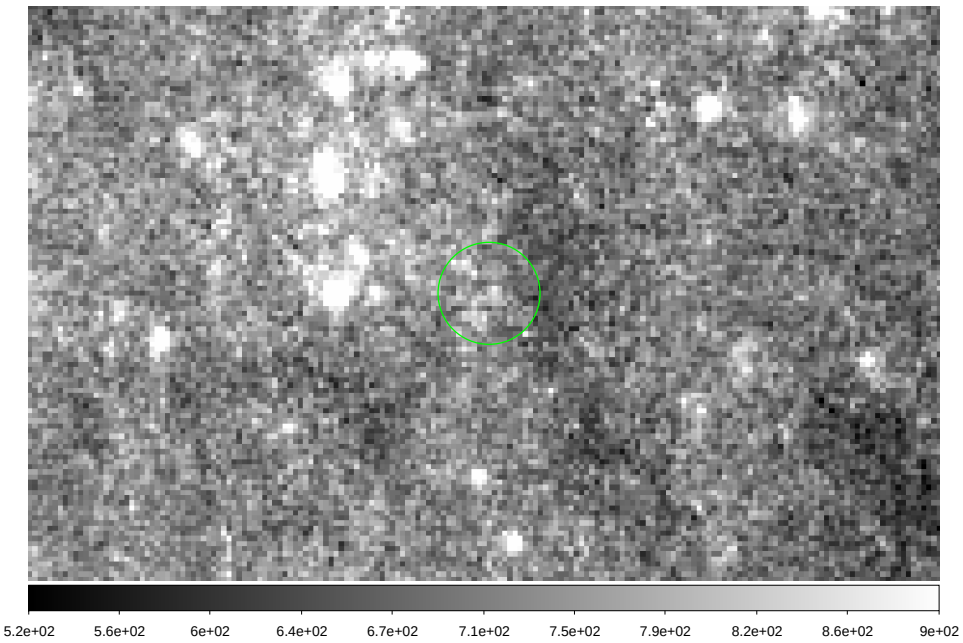

Figure A.9: Cepheid 168 image.

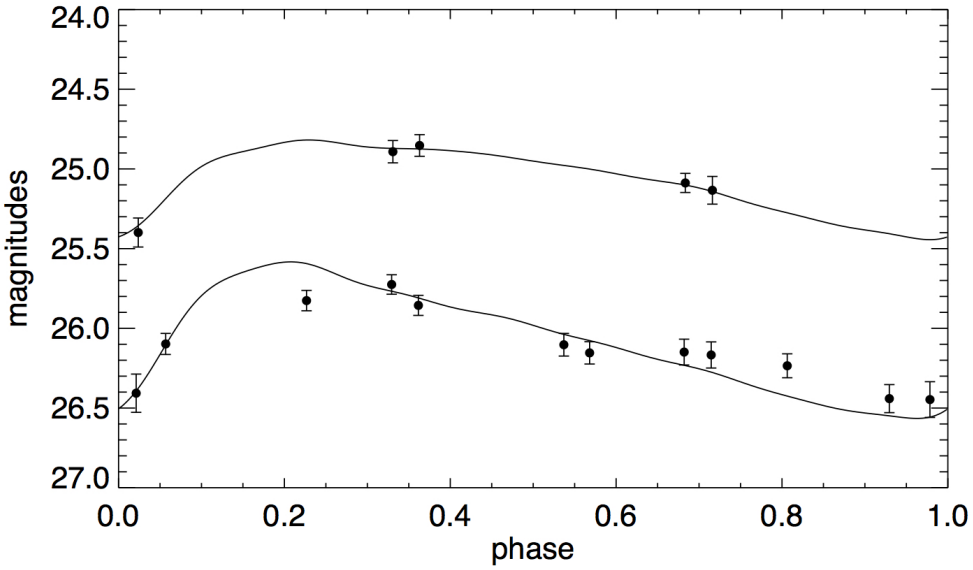

Figure A.10: Cepheid 168 light curve. I-band (top set of points) and V-band (bottom set of points) Cepheid candidate light curve. Black lines are best-fit Cepheid model light curves.

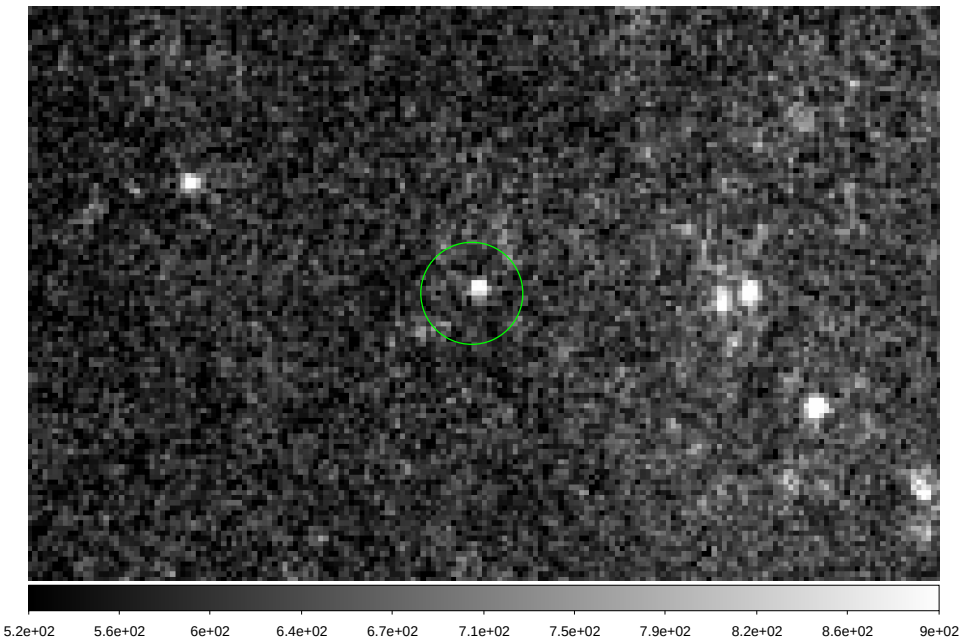

Figure A.11: Cepheid 169 image.

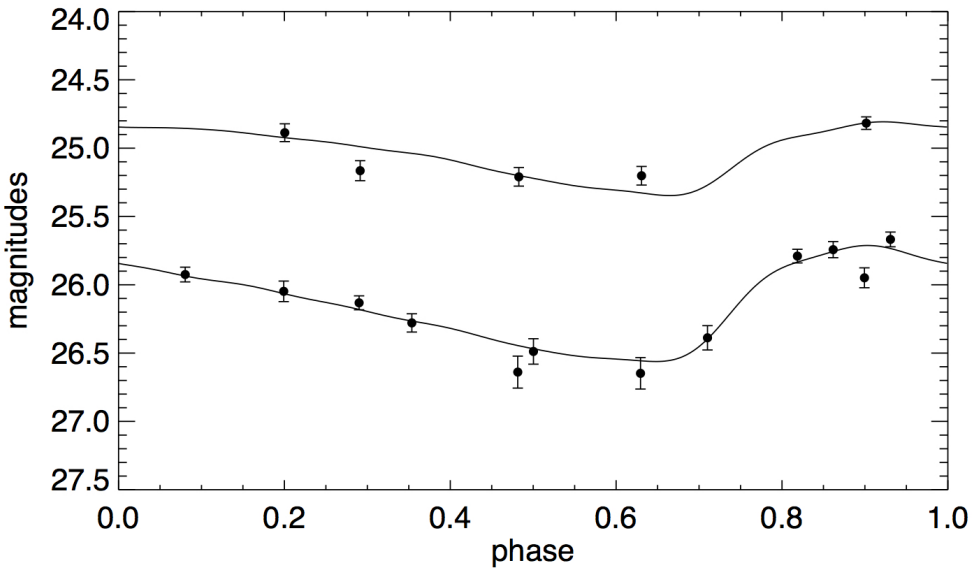

Figure A.12: Cepheid 169 light curve. I-band (top set of points) and V-band (bottom set of points) Cepheid candidate light curve. Black lines are best-fit Cepheid model light curves.

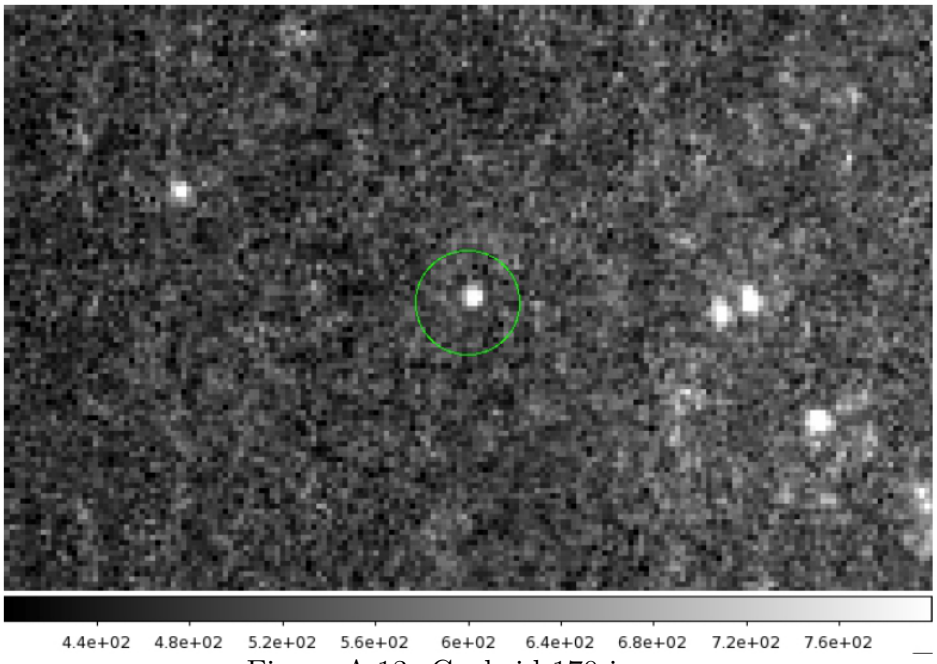

Figure A.13: Cepheid 170 image.

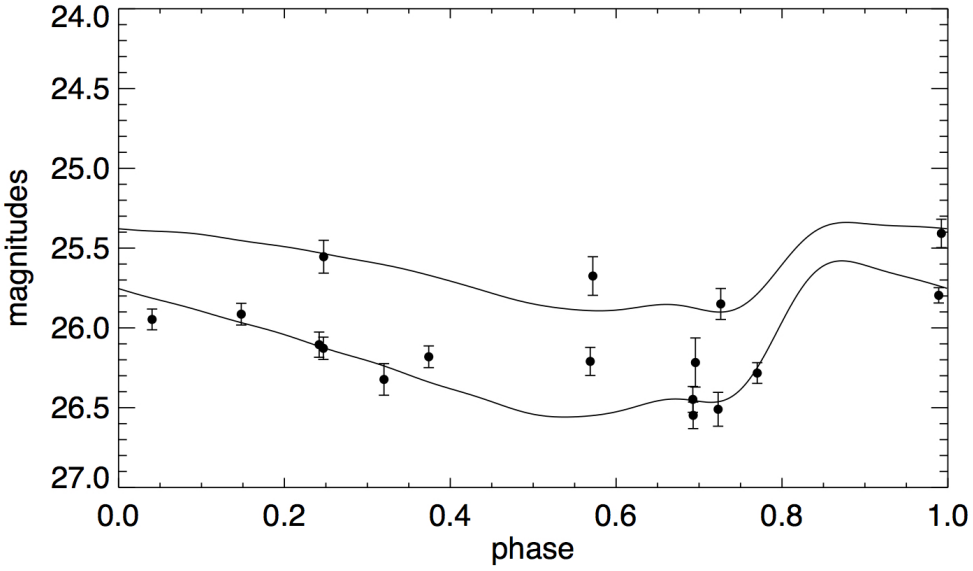

Figure A.14: Cepheid 170 light curve. I-band (top set of points) and V-band (bottom set of points) Cepheid candidate light curve. Black lines are best-fit Cepheid model light curves.

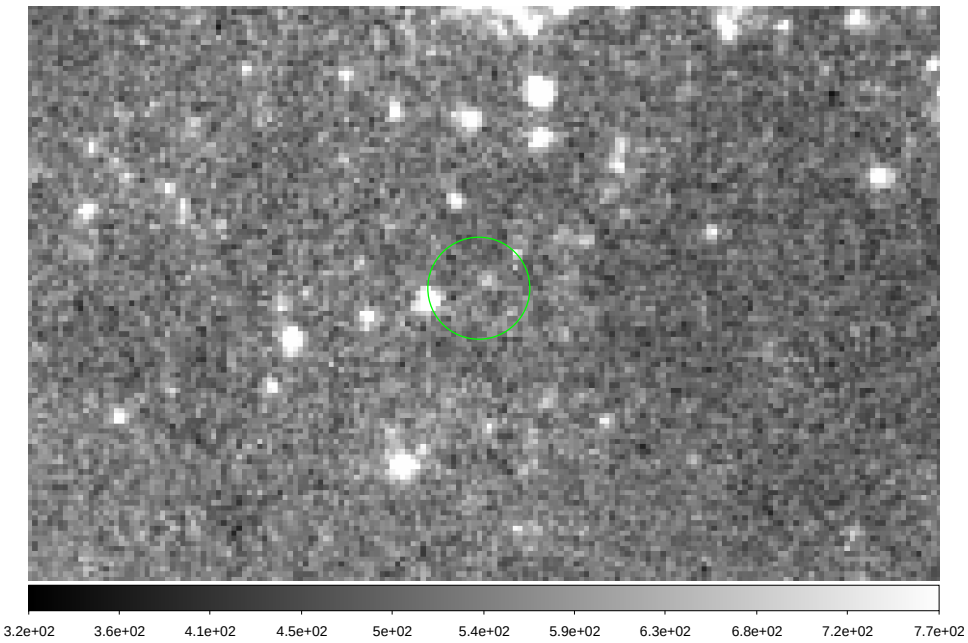

Figure A.15: Cepheid 171 image.

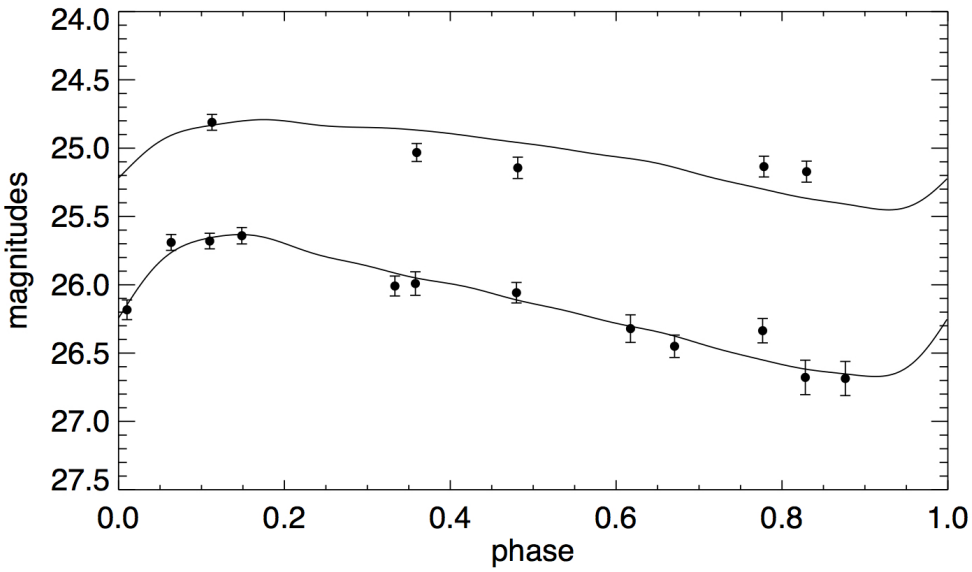

Figure A.16: Cepheid 171 light curve. I-band (top set of points) and V-band (bottom set of points) Cepheid candidate light curve. Black lines are best-fit Cepheid model light curves.

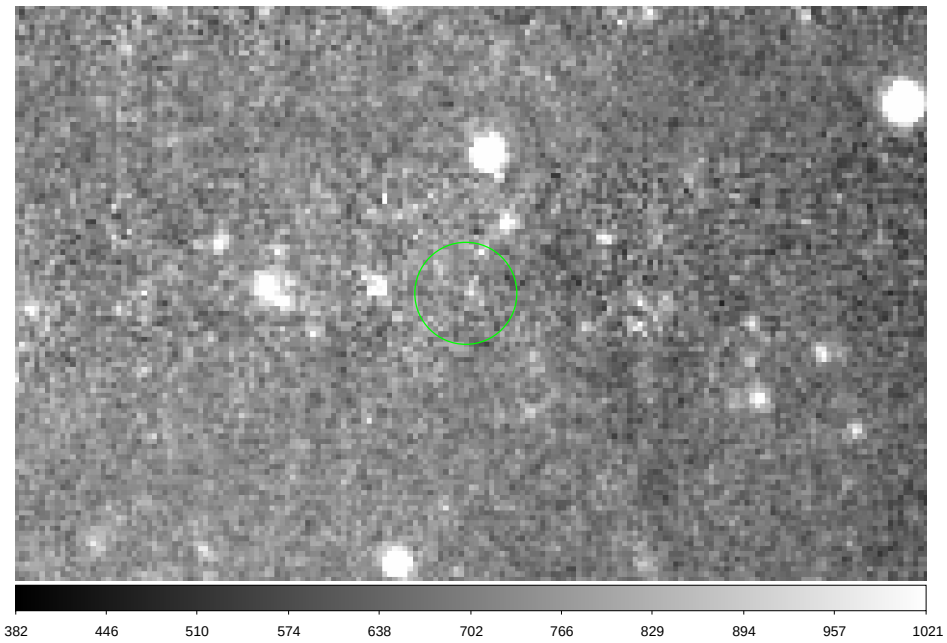

Figure A.17: Cepheid 172 image.

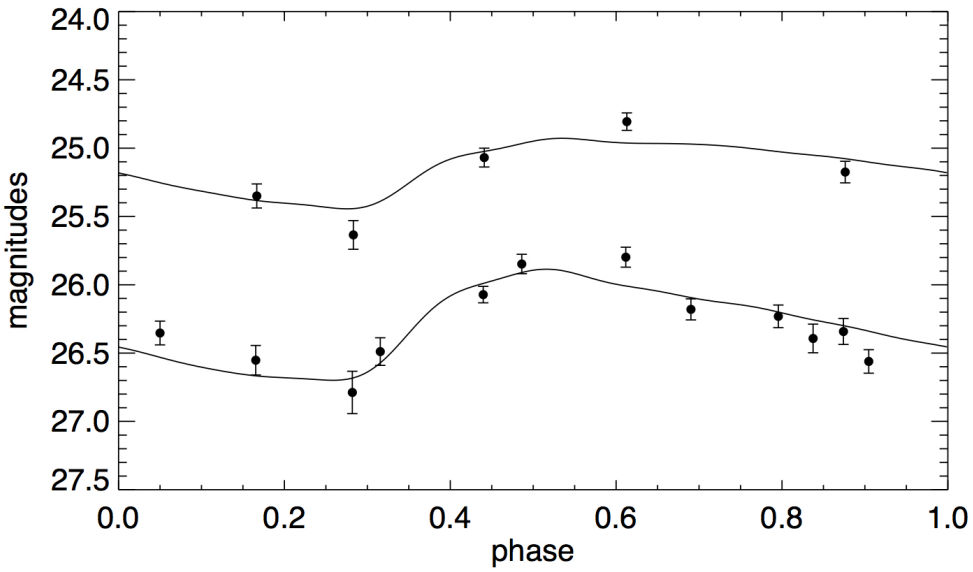

Figure A.18: Cepheid 172 light curve. I-band (top set of points) and V-band (bottom set of points) Cepheid candidate light curve. Black lines are best-fit Cepheid model light curves.

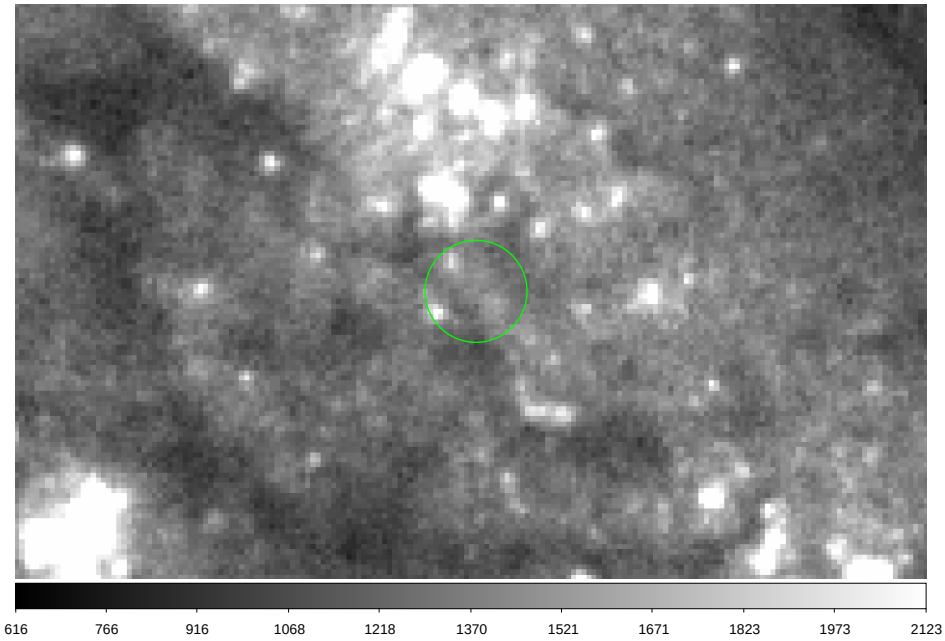

Figure A.19: Cepheid 173 image.

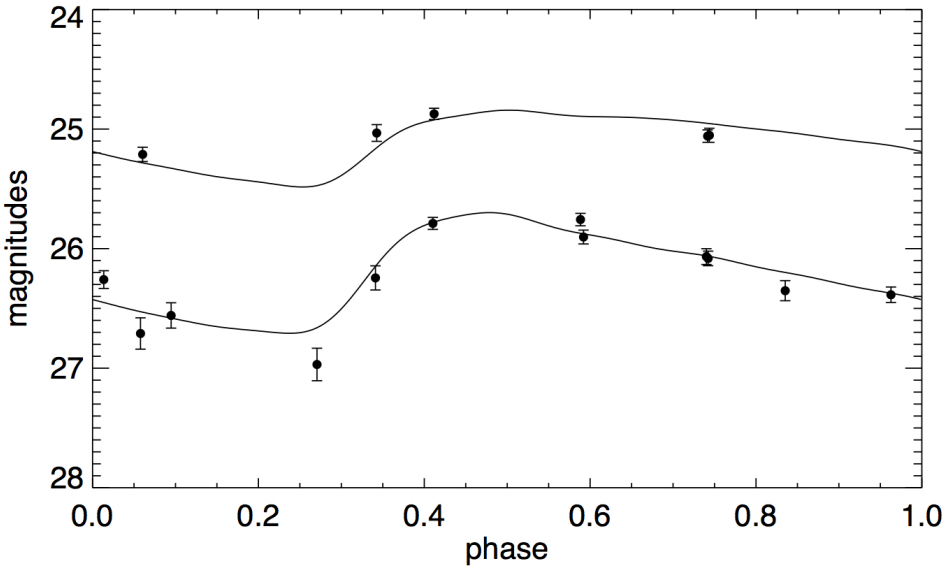

Figure A.20: Cepheid 173 light curve. I-band (top set of points) and V-band (bottom set of points) Cepheid candidate light curve. Black lines are best-fit Cepheid model light curves.

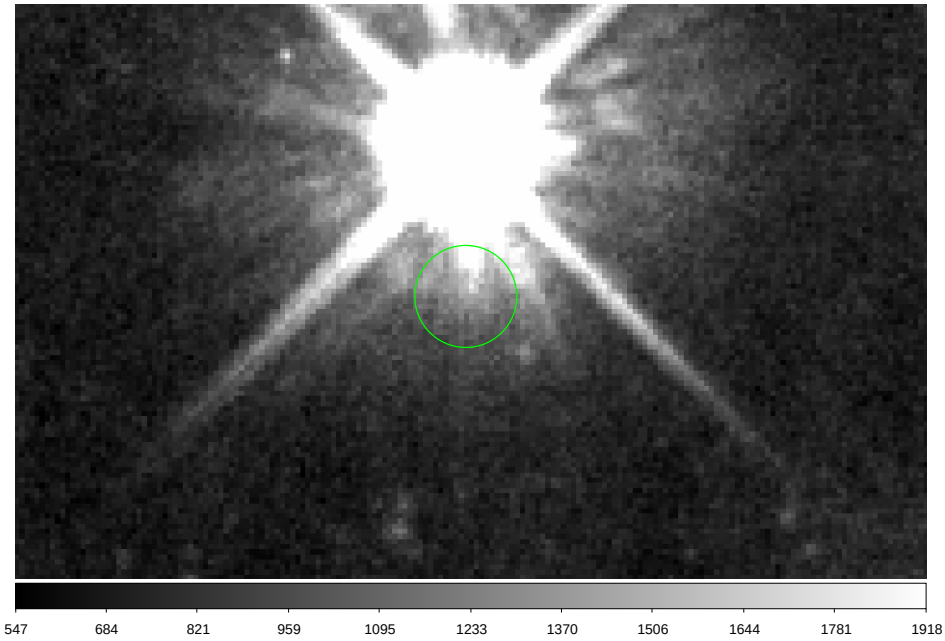

Figure A.21: Cepheid 174 image.

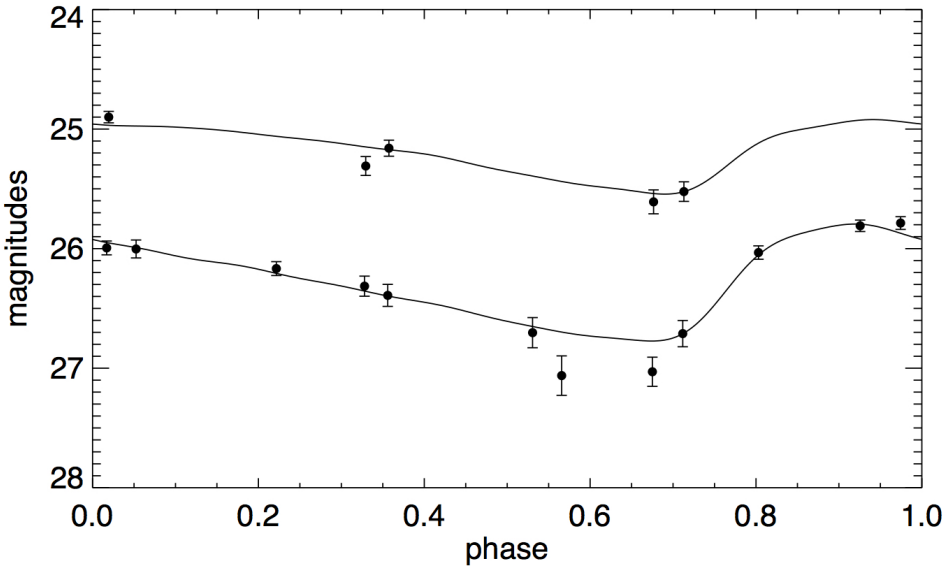

Figure A.22: Cepheid 174 light curve. I-band (top set of points) and V-band (bottom set of points) Cepheid candidate light curve. Black lines are best-fit Cepheid model light curves.

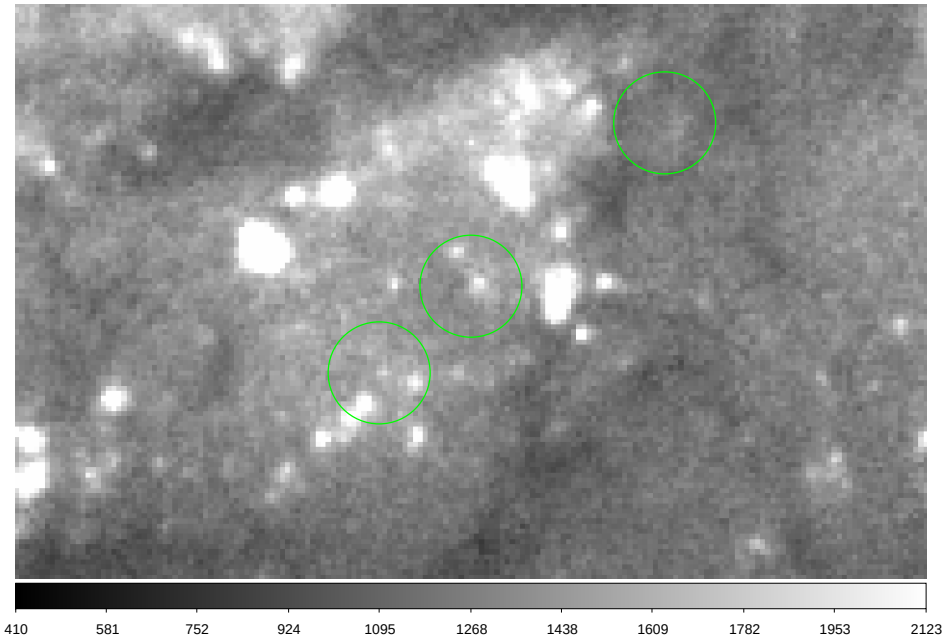

Figure A.23: Cepheid 175 image.

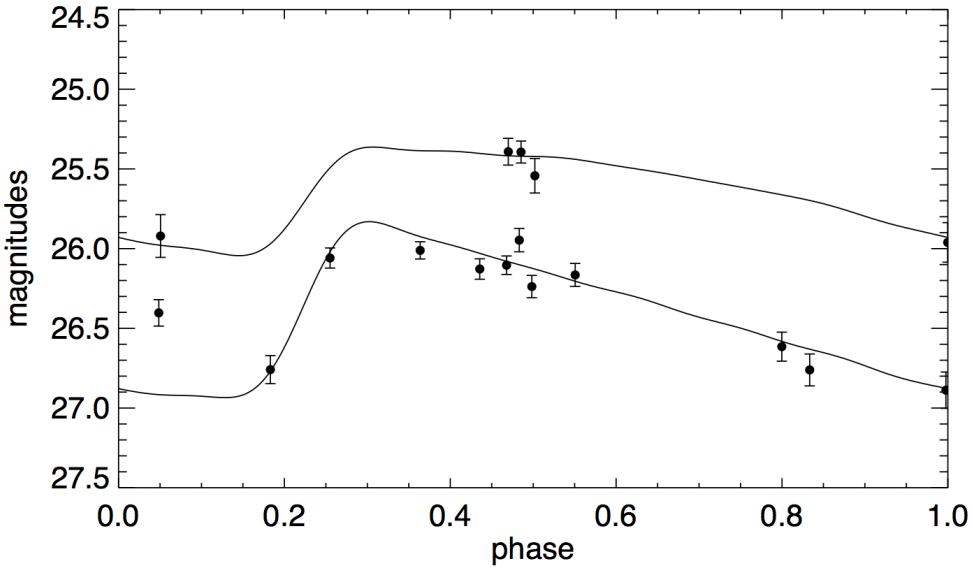

Figure A.24: Cepheid 175 light curve. I-band (top set of points) and V-band (bottom set of points) Cepheid candidate light curve. Black lines are best-fit Cepheid model light curves.

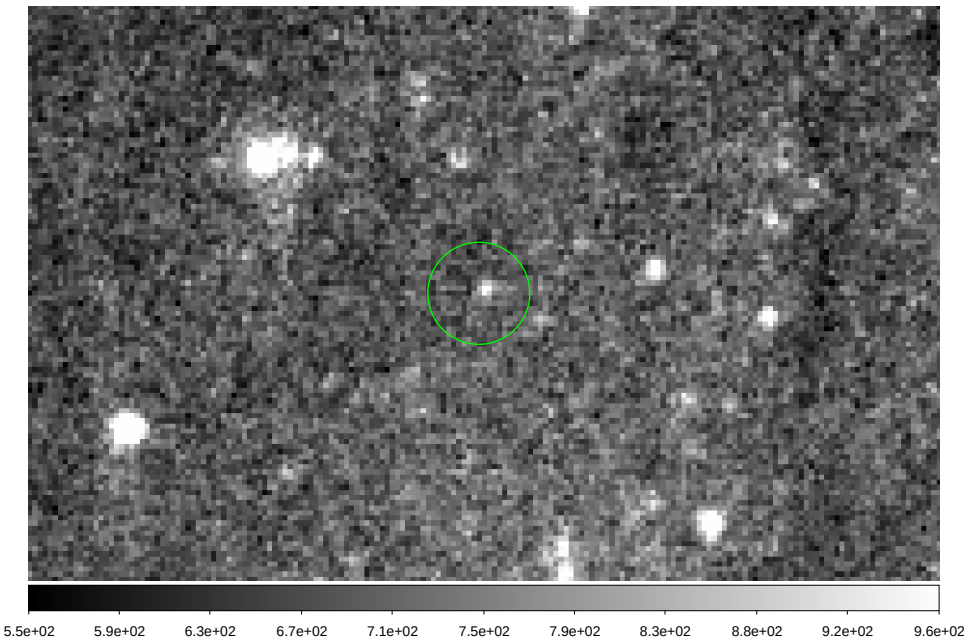

Figure A.25: Cepheid 177 image.

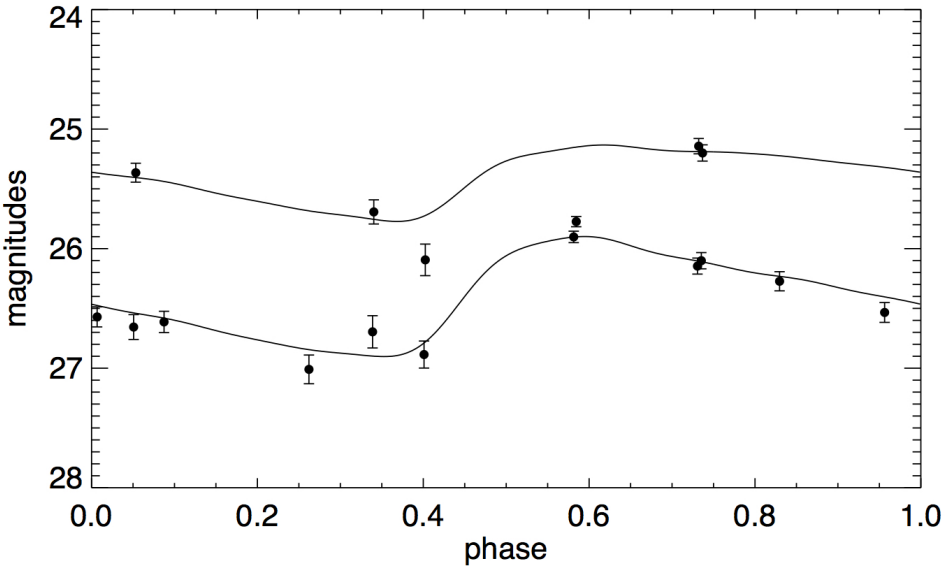

Figure A.26: Cepheid 177 light curve. I-band (top set of points) and V-band (bottom set of points) Cepheid candidate light curve. Black lines are best-fit Cepheid model light curves.

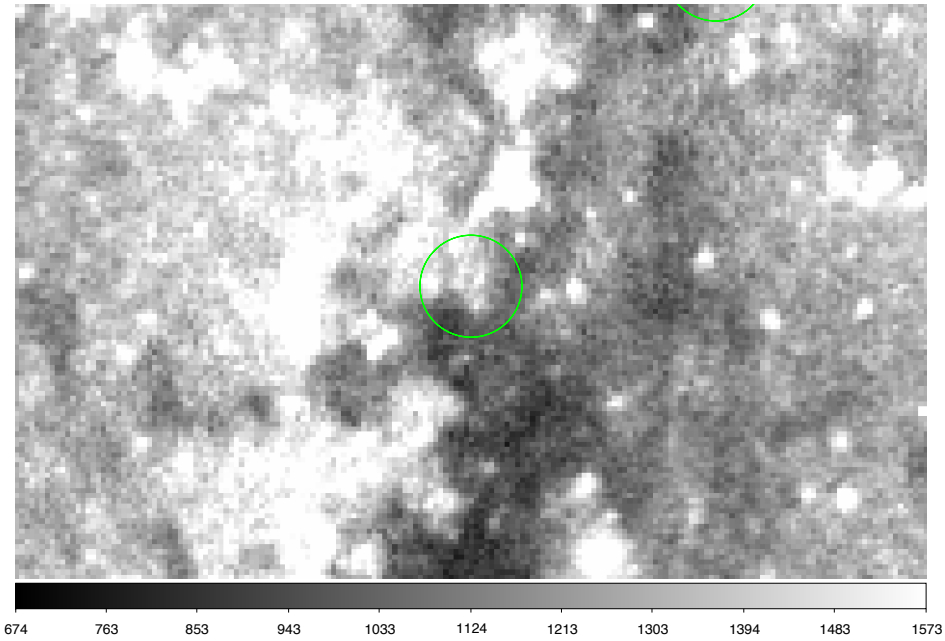

Figure A.27: Cepheid 178 image.

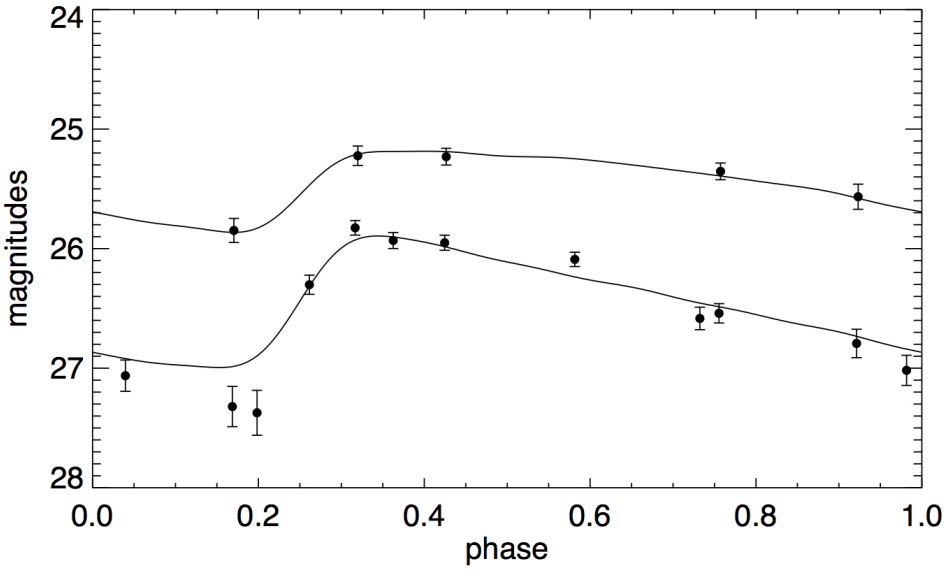

Figure A.28: Cepheid 178 light curve. I-band (top set of points) and V-band (bottom set of points) Cepheid candidate light curve. Black lines are best-fit Cepheid model light curves.

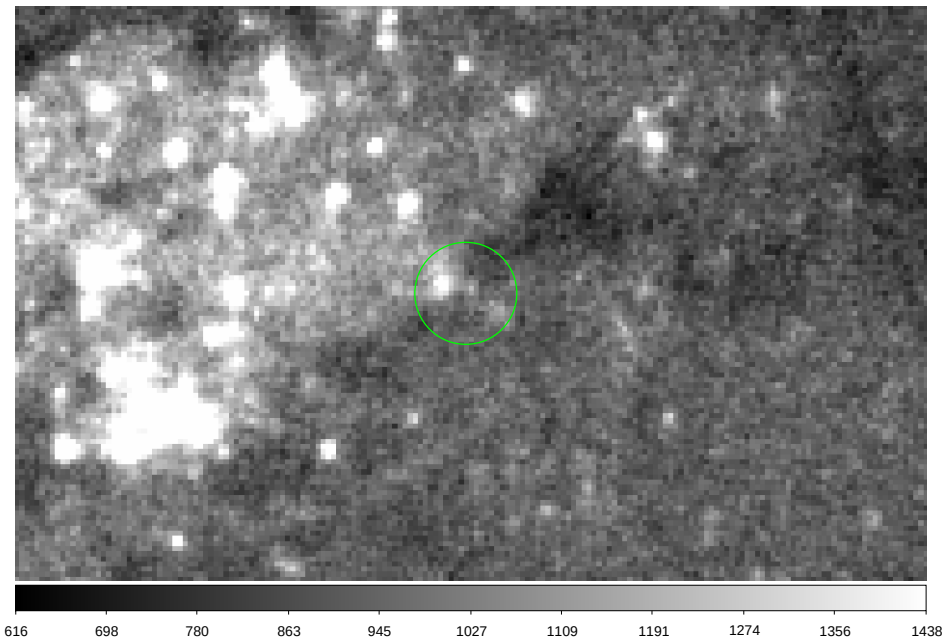

Figure A.29: Cepheid 180 image.

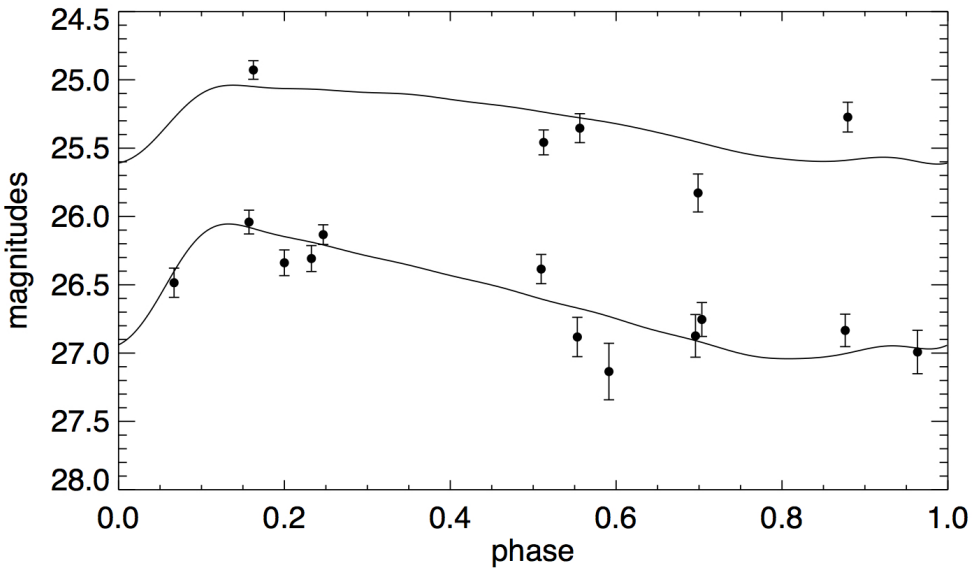

Figure A.30: Cepheid 180 light curve. I-band (top set of points) and V-band (bottom set of points) Cepheid candidate light curve. Black lines are best-fit Cepheid model light curves.

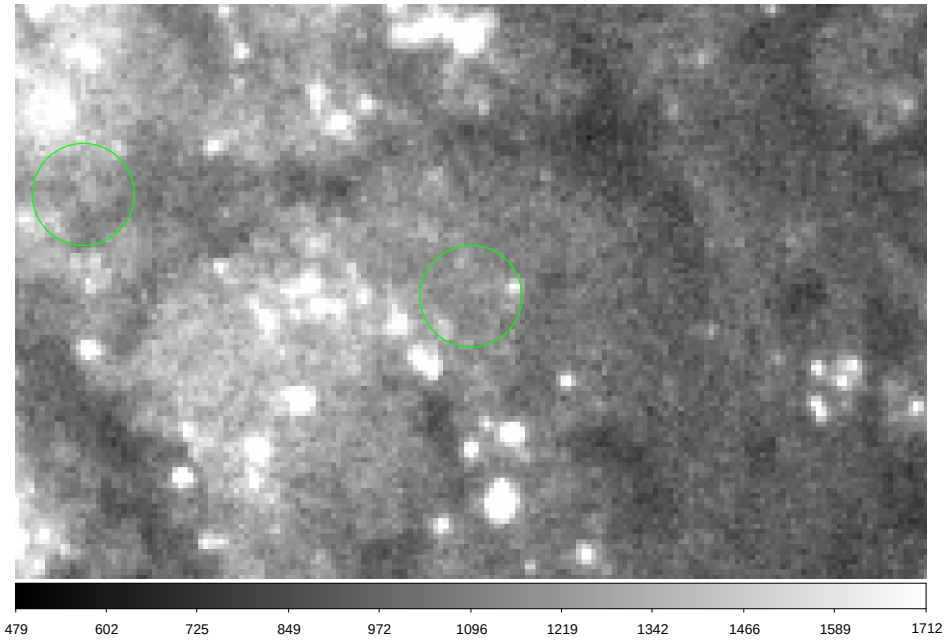

Figure A.31: Cepheid 181 image.

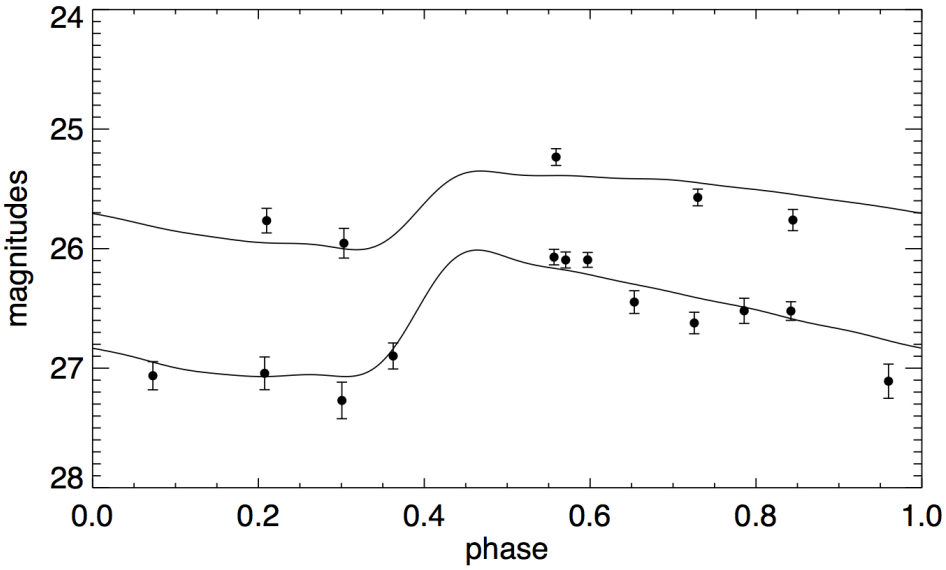

Figure A.32: Cepheid 181 light curve. I-band (top set of points) and V-band (bottom set of points) Cepheid candidate light curve. Black lines are best-fit Cepheid model light curves.

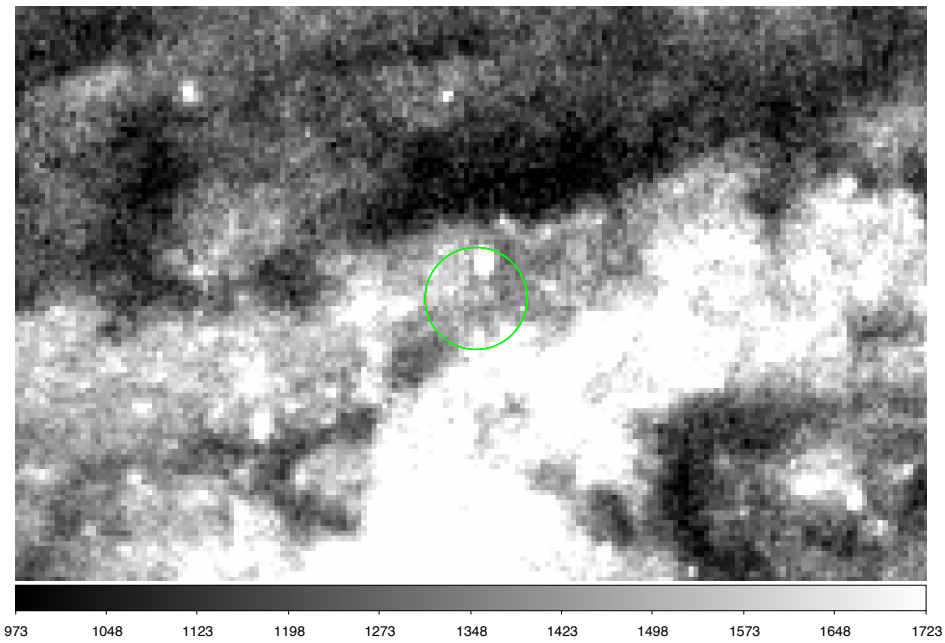

Figure A.33: Cepheid 182 image.

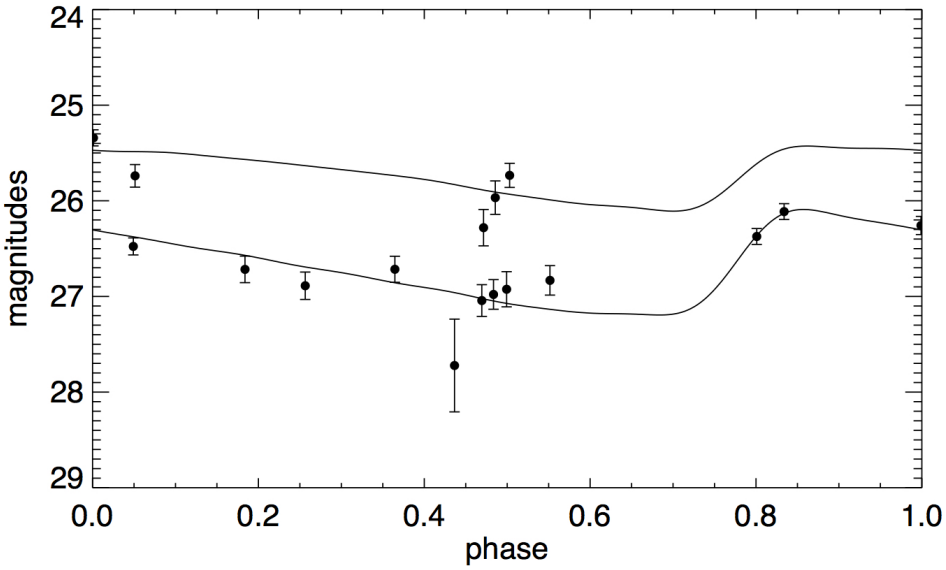

Figure A.34: Cepheid 182 light curve. I-band (top set of points) and V-band (bottom set of points) Cepheid candidate light curve. Black lines are best-fit Cepheid model light curves.

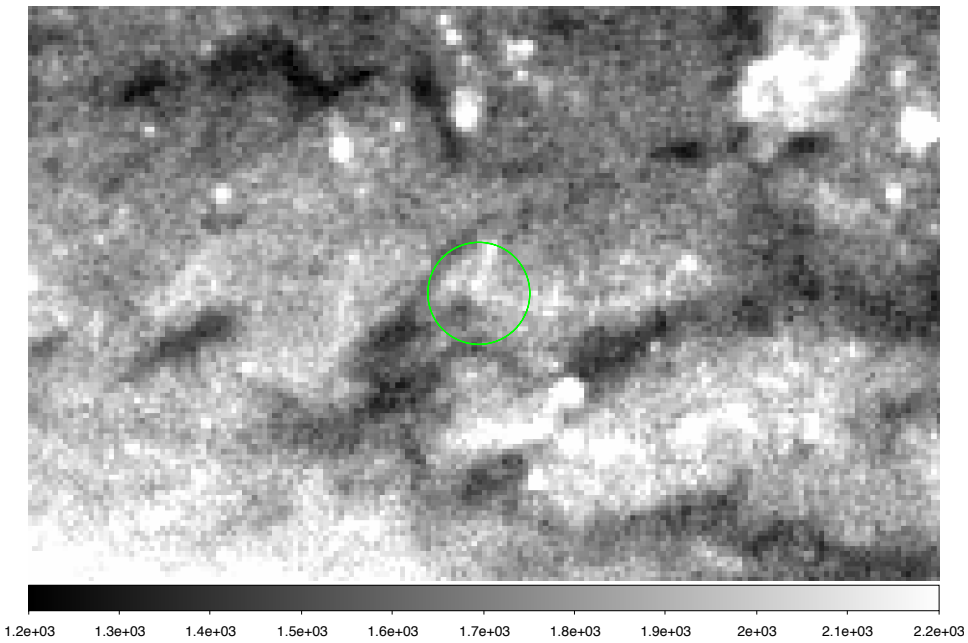

Figure A.35: Cepheid 183 image.

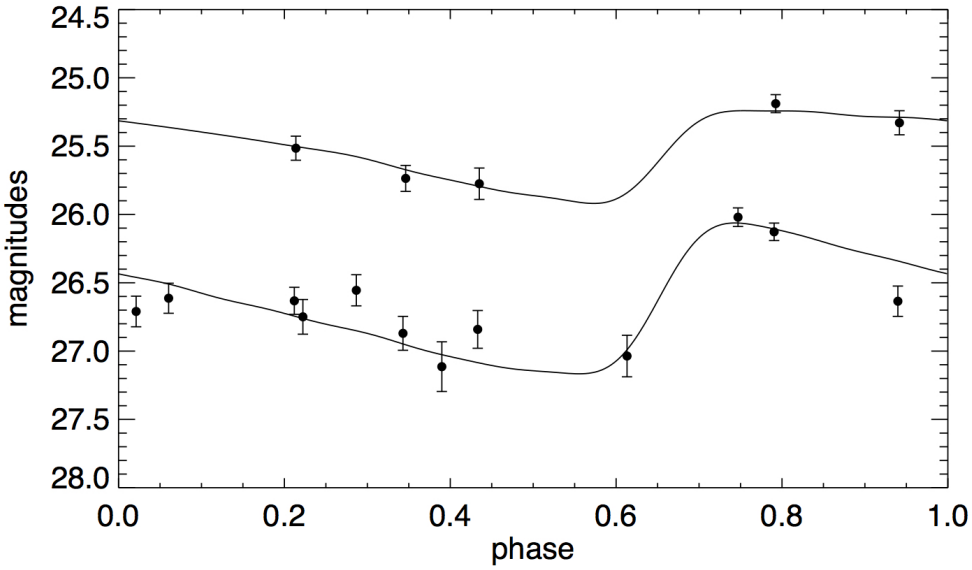

Figure A.36: Cepheid 183 light curve. I-band (top set of points) and V-band (bottom set of points) Cepheid candidate light curve. Black lines are best-fit Cepheid model light curves.

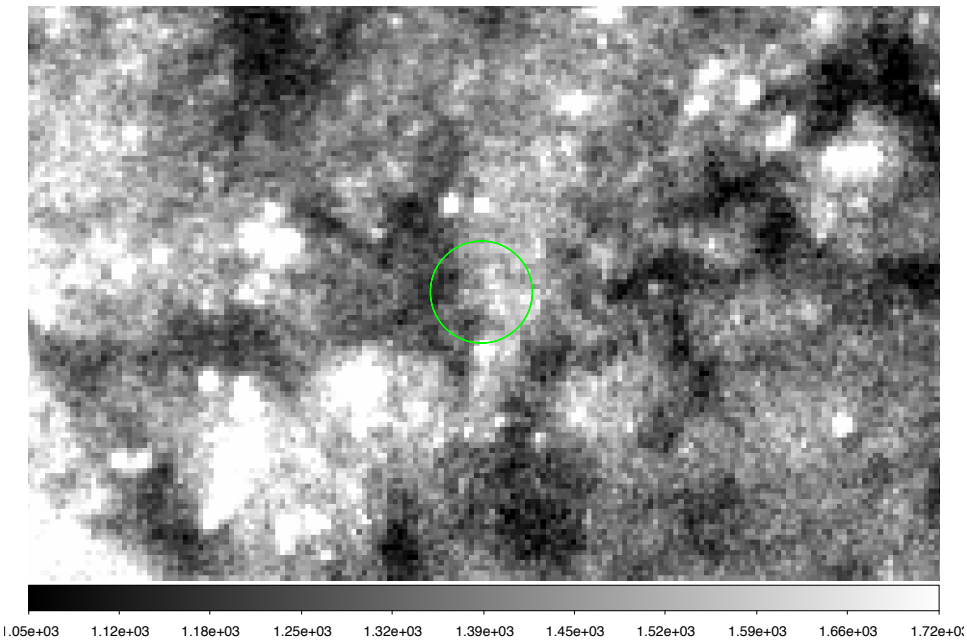

Figure A.37: Cepheid 184 image.

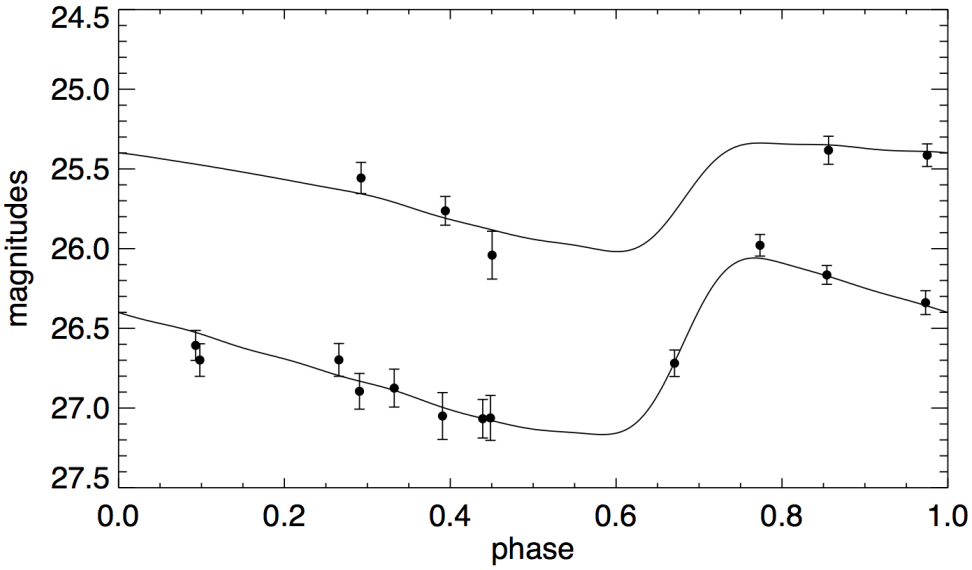

Figure A.38: Cepheid 184 light curve. I-band (top set of points) and V-band (bottom set of points) Cepheid candidate light curve. Black lines are best-fit Cepheid model light curves.

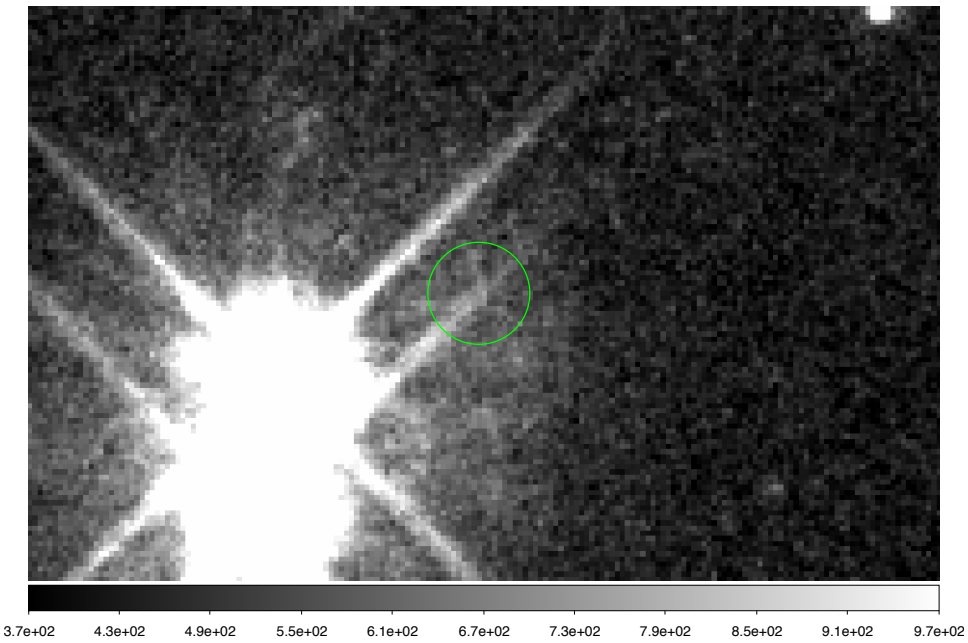

Figure A.39: Cepheid 185 image.

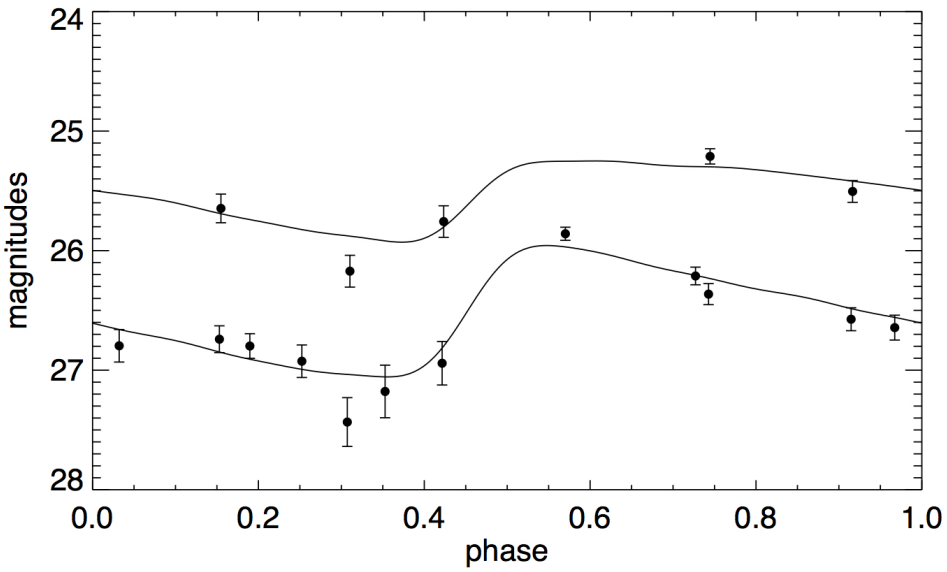

Figure A.40: Cepheid 185 light curve. I-band (top set of points) and V-band (bottom set of points) Cepheid candidate light curve. Black lines are best-fit Cepheid model light curves.

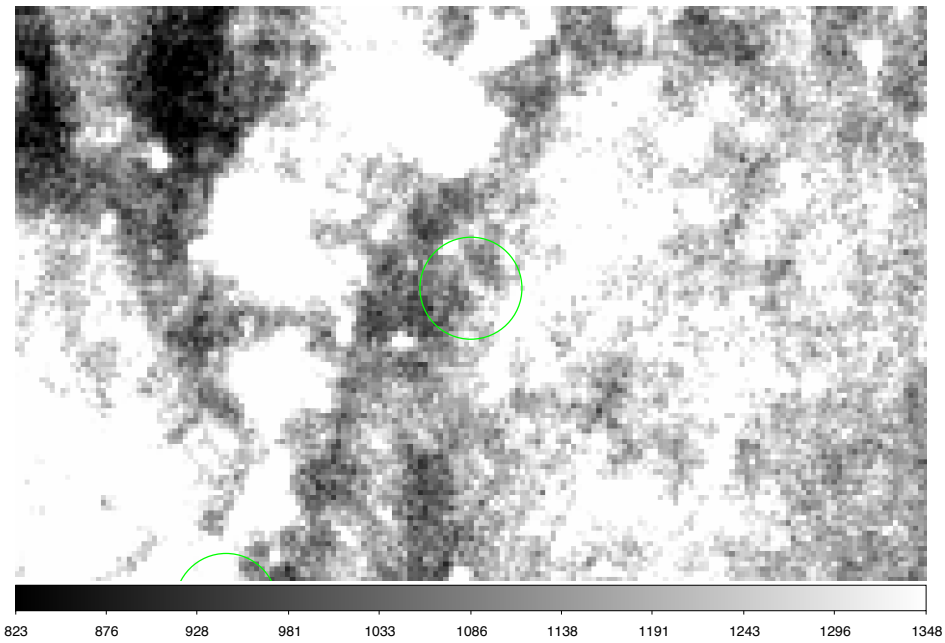

Figure A.41: Cepheid 186 image.

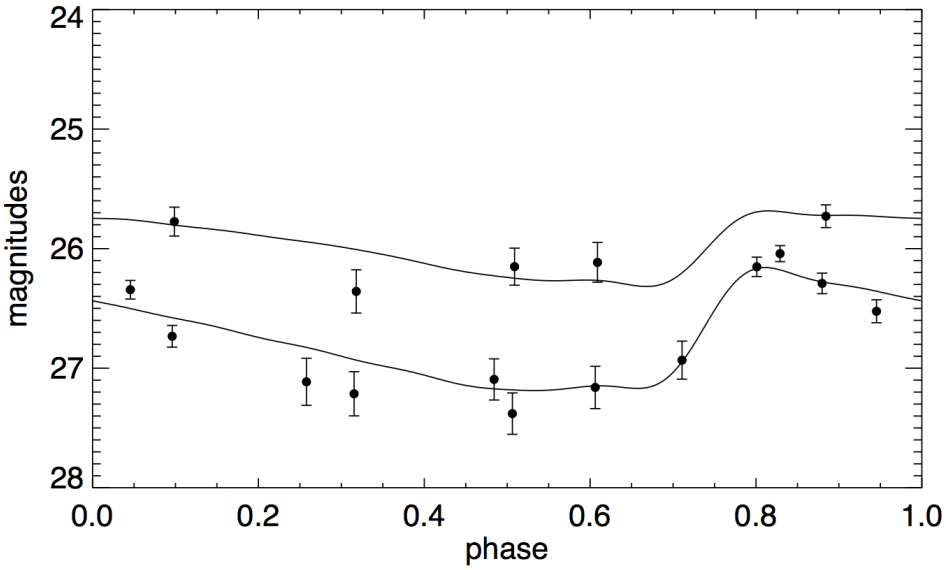

Figure A.42: Cepheid 186 light curve. I-band (top set of points) and V-band (bottom set of points) Cepheid candidate light curve. Black lines are best-fit Cepheid model light curves.

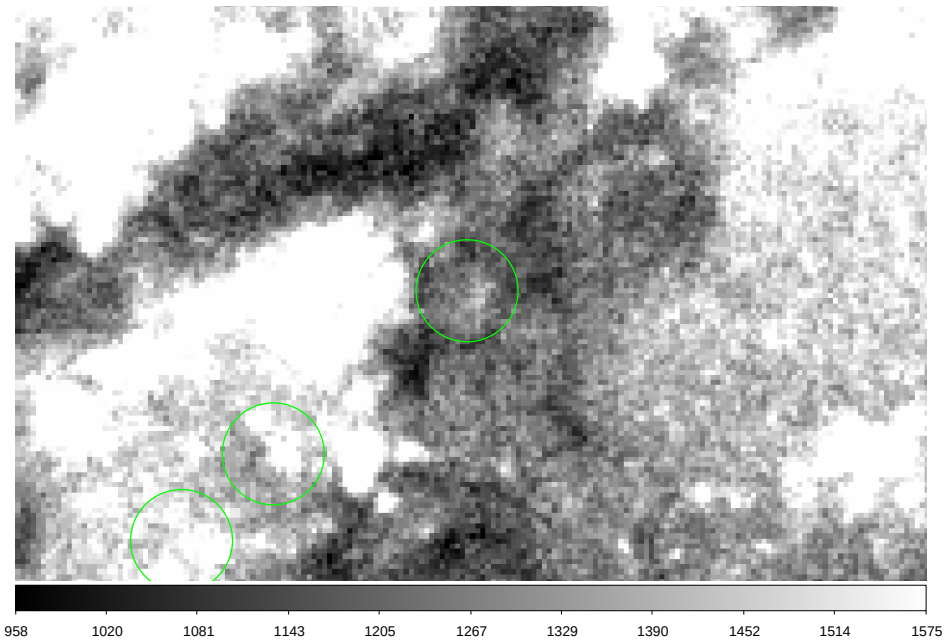

Figure A.43: Cepheid 188 image.

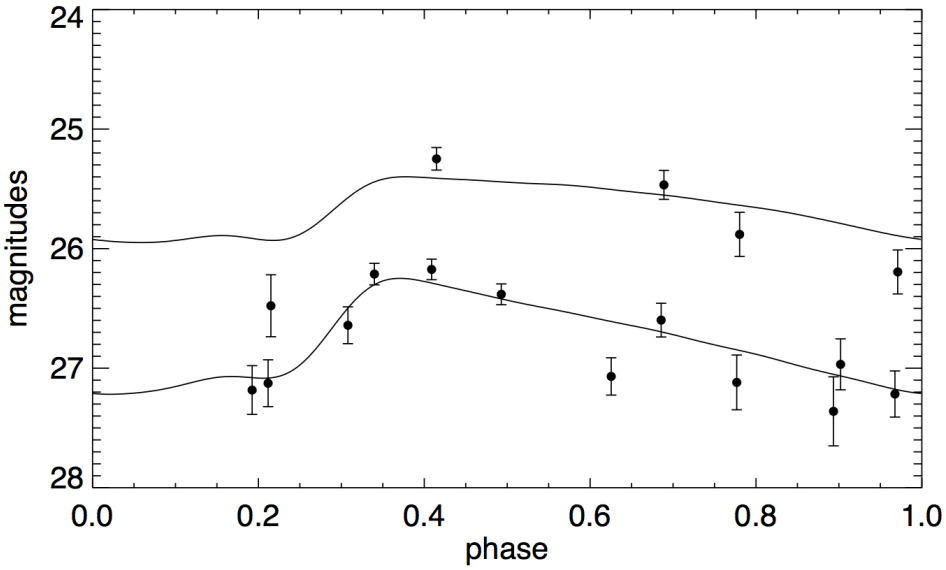

Figure A.44: Cepheid 188 light curve. I-band (top set of points) and V-band (bottom set of points) Cepheid candidate light curve. Black lines are best-fit Cepheid model light curves.

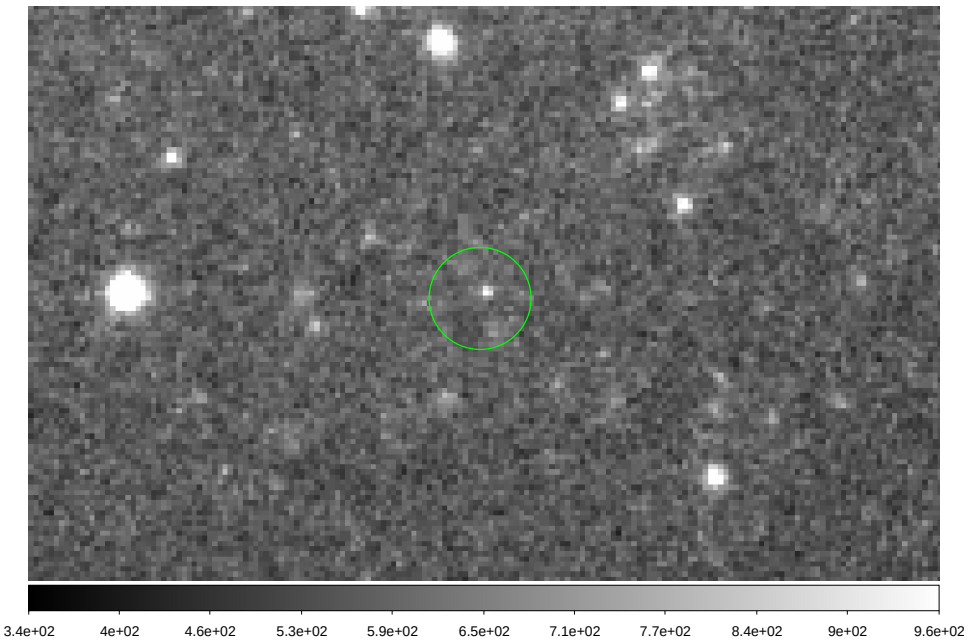

Figure A.45: Cepheid 190 image.

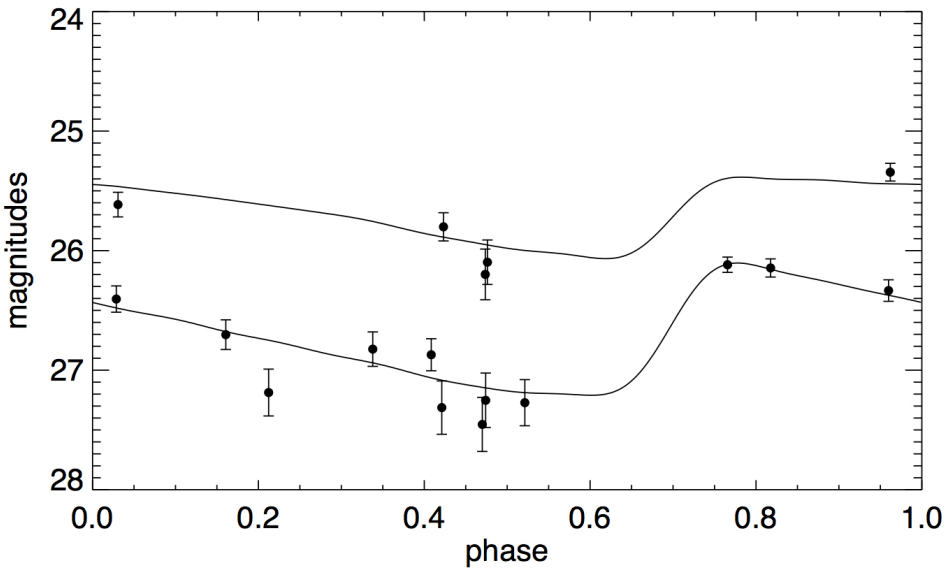

Figure A.46: Cepheid 190 light curve. I-band (top set of points) and V-band (bottom set of points) Cepheid candidate light curve. Black lines are best-fit Cepheid model light curves.

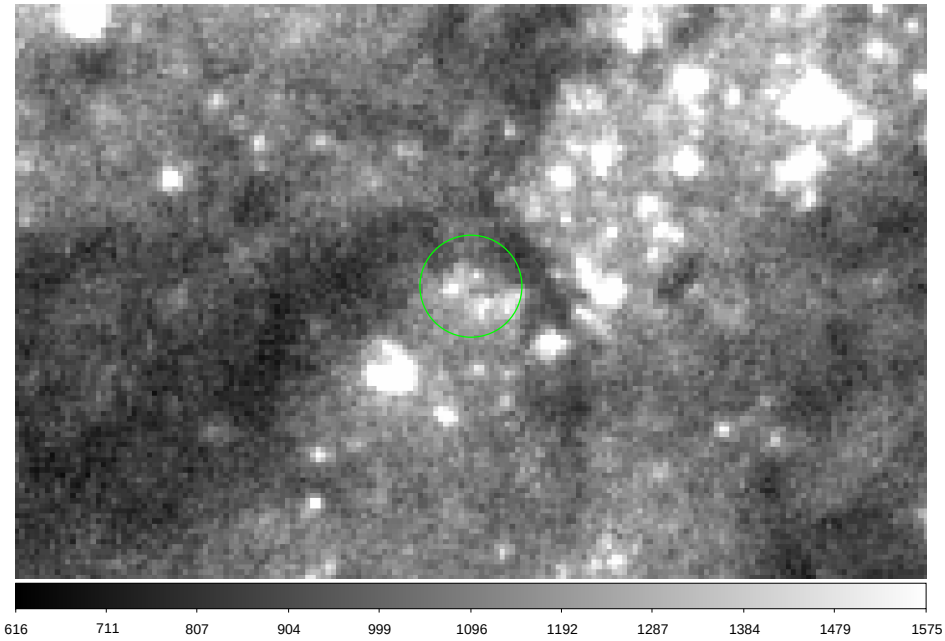

Figure A.47: Cepheid 193 image.

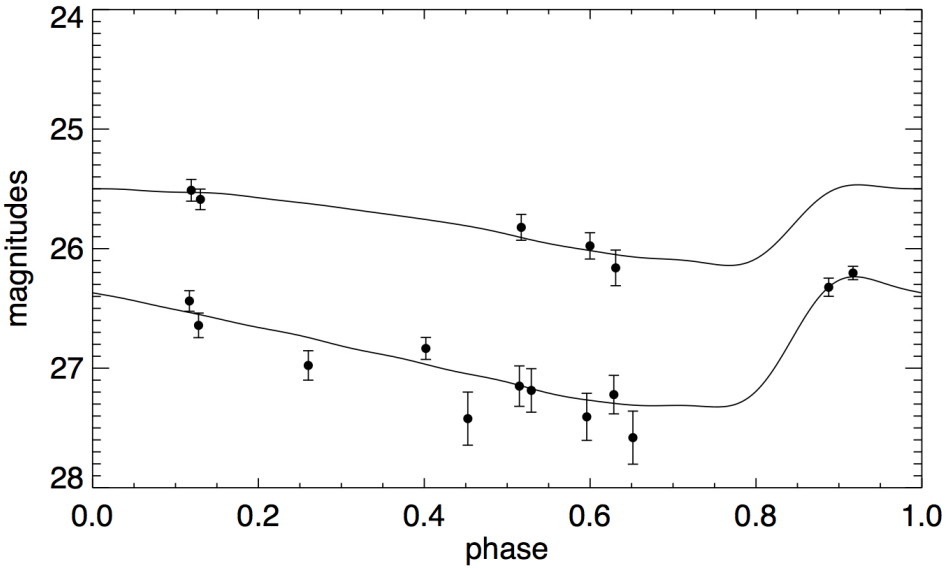

Figure A.48: Cepheid 193 light curve. I-band (top set of points) and V-band (bottom set of points) Cepheid candidate light curve. Black lines are best-fit Cepheid model light curves.

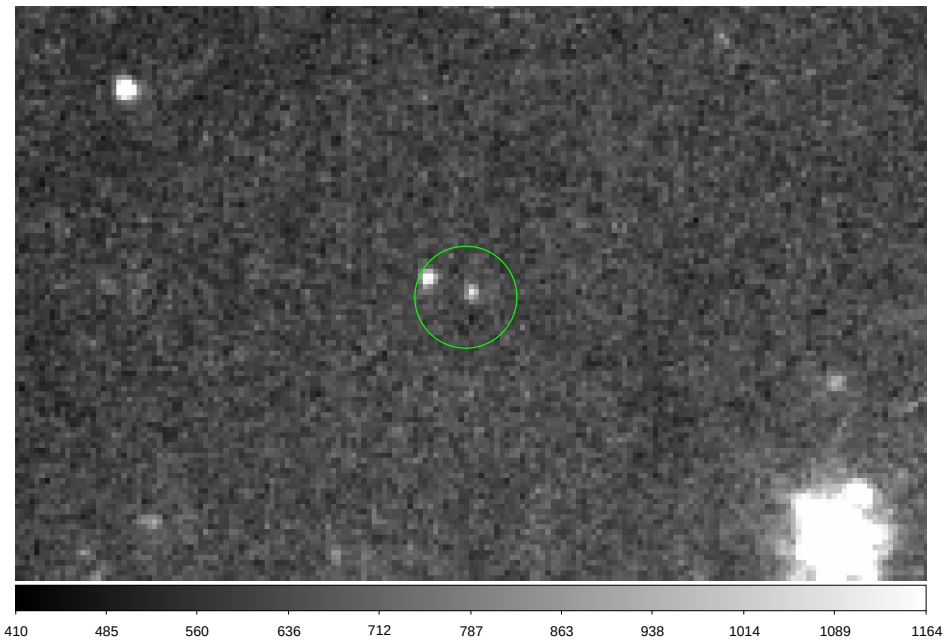

Figure A.49: Cepheid 194 image.

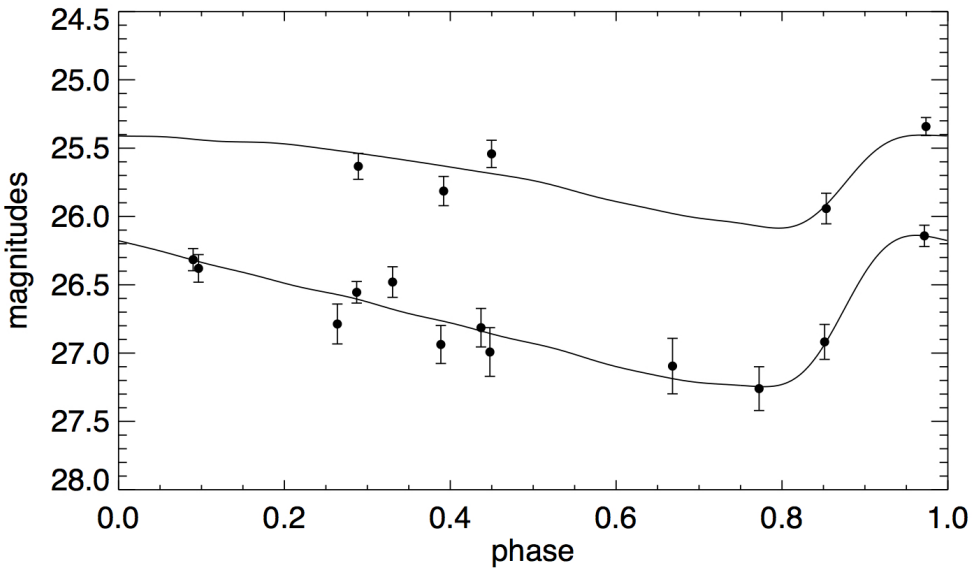

Figure A.50: Cepheid 194 light curve. I-band (top set of points) and V-band (bottom set of points) Cepheid candidate light curve. Black lines are best-fit Cepheid model light curves.

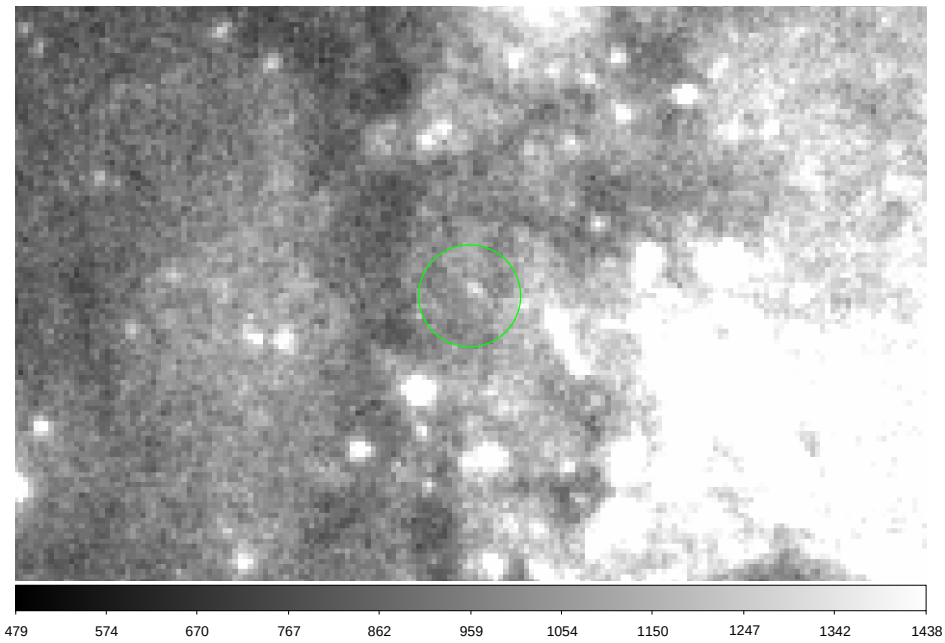

Figure A.51: Cepheid 196 image.

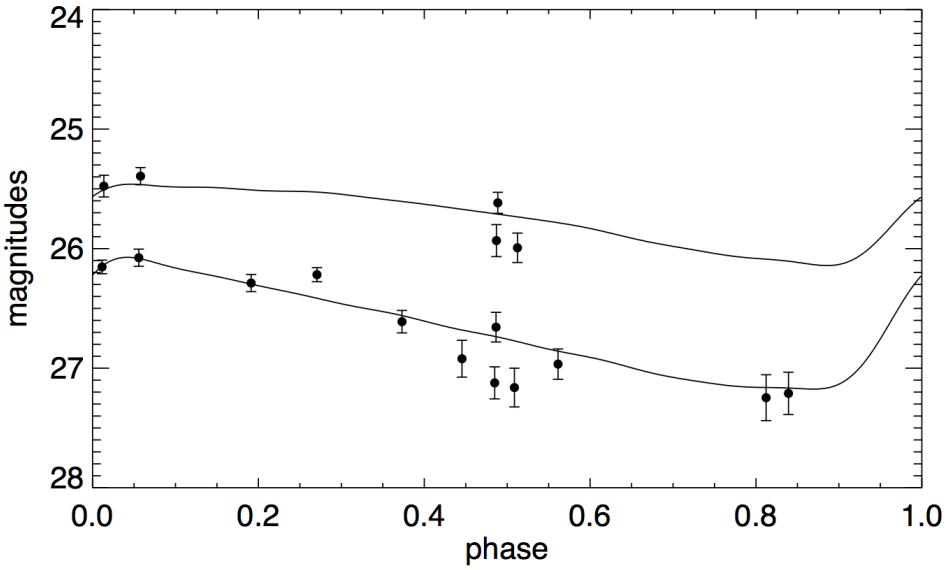

Figure A.52: Cepheid 196 light curve. I-band (top set of points) and V-band (bottom set of points) Cepheid candidate light curve. Black lines are best-fit Cepheid model light curves.

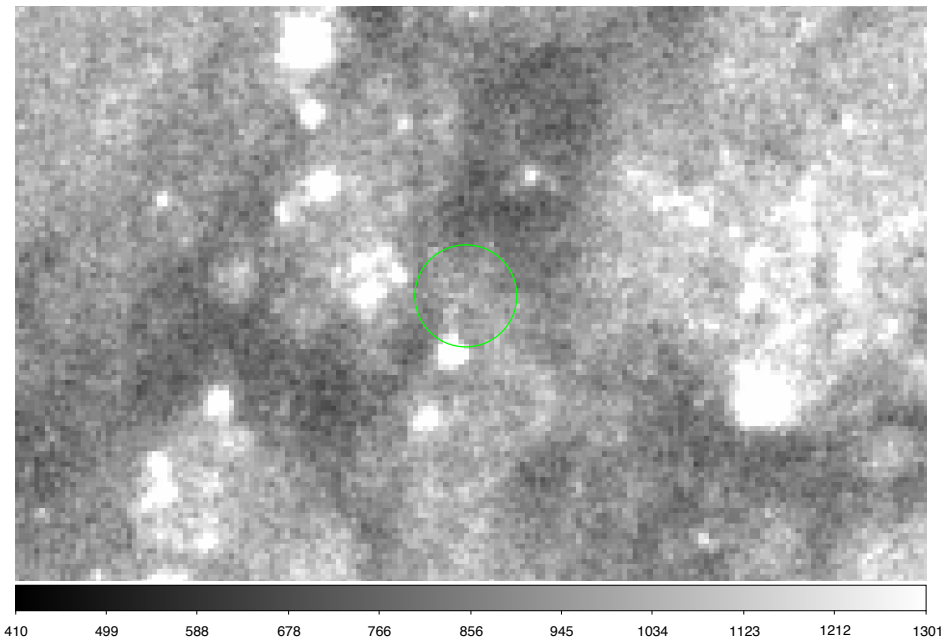

Figure A.53: Cepheid 197 image.

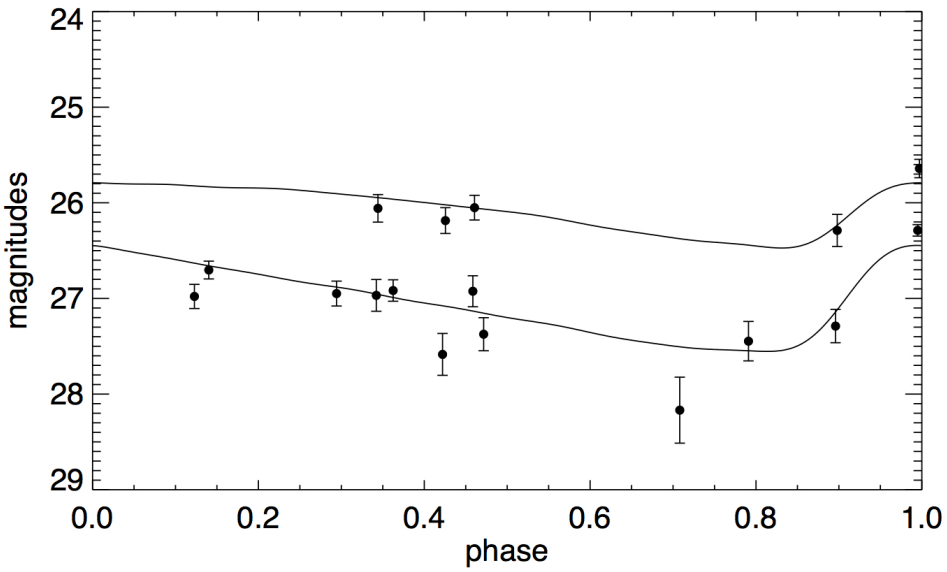

Figure A.54: Cepheid 197 light curve. I-band (top set of points) and V-band (bottom set of points) Cepheid candidate light curve. Black lines are best-fit Cepheid model light curves.

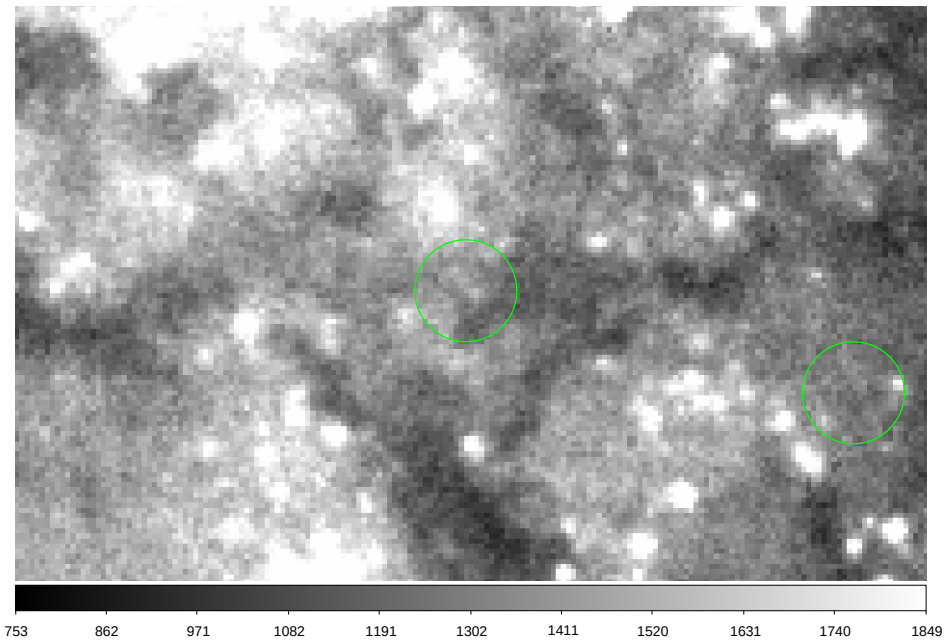

Figure A.55: Cepheid 198 image.

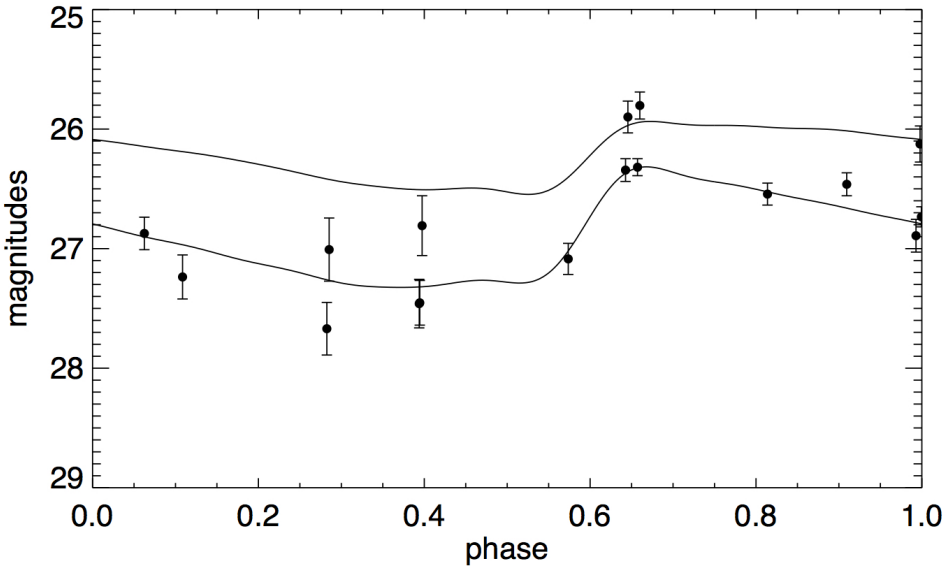

Figure A.56: Cepheid 198 light curve. I-band (top set of points) and V-band (bottom set of points) Cepheid candidate light curve. Black lines are best-fit Cepheid model light curves.

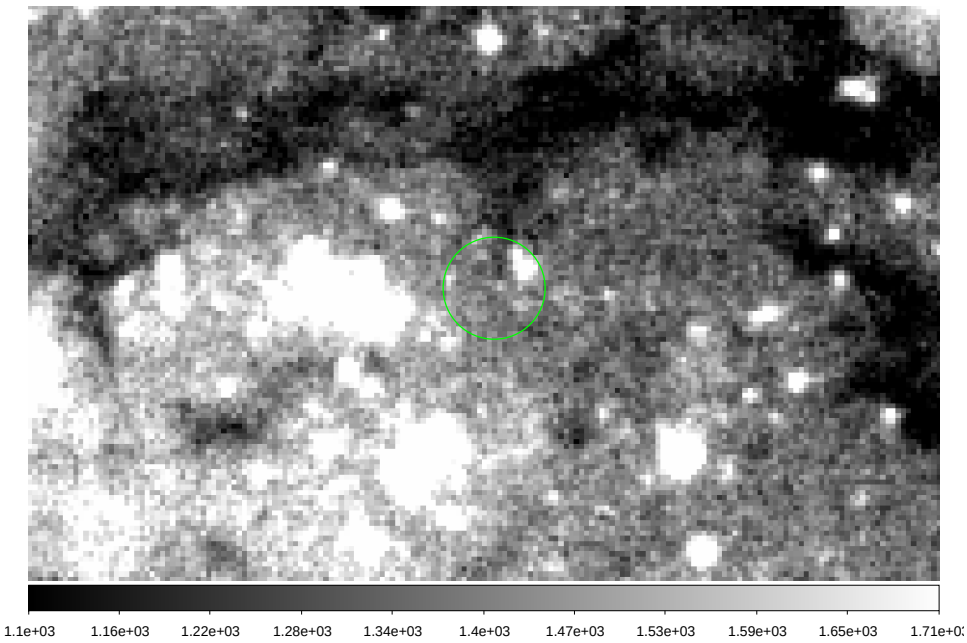

Figure A.57: Cepheid 199 image.

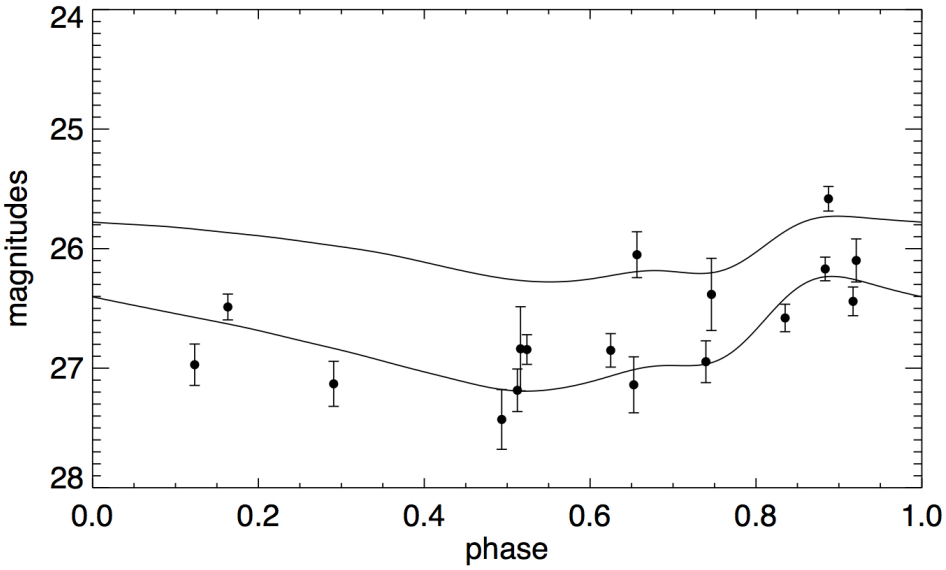

Figure A.58: Cepheid 199 light curve. I-band (top set of points) and V-band (bottom set of points) Cepheid candidate light curve. Black lines are best-fit Cepheid model light curves.

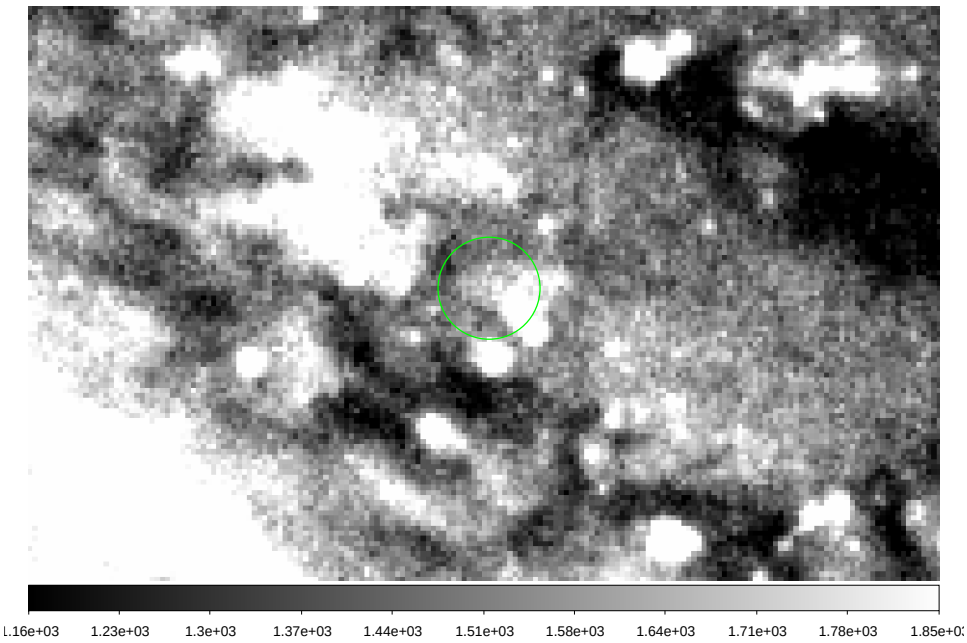

Figure A.59: Cepheid 201 image.

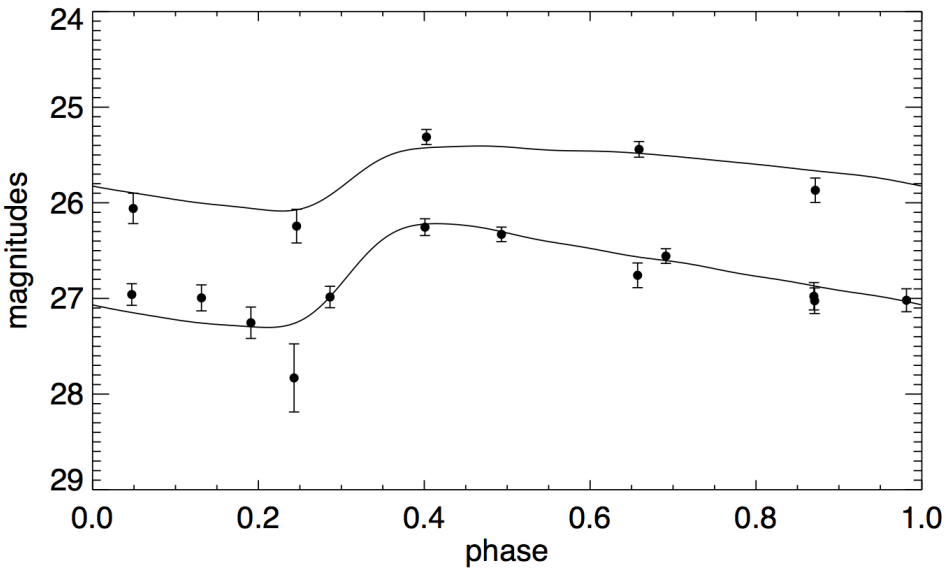

Figure A.60: Cepheid 201 light curve. I-band (top set of points) and V-band (bottom set of points) Cepheid candidate light curve. Black lines are best-fit Cepheid model light curves.

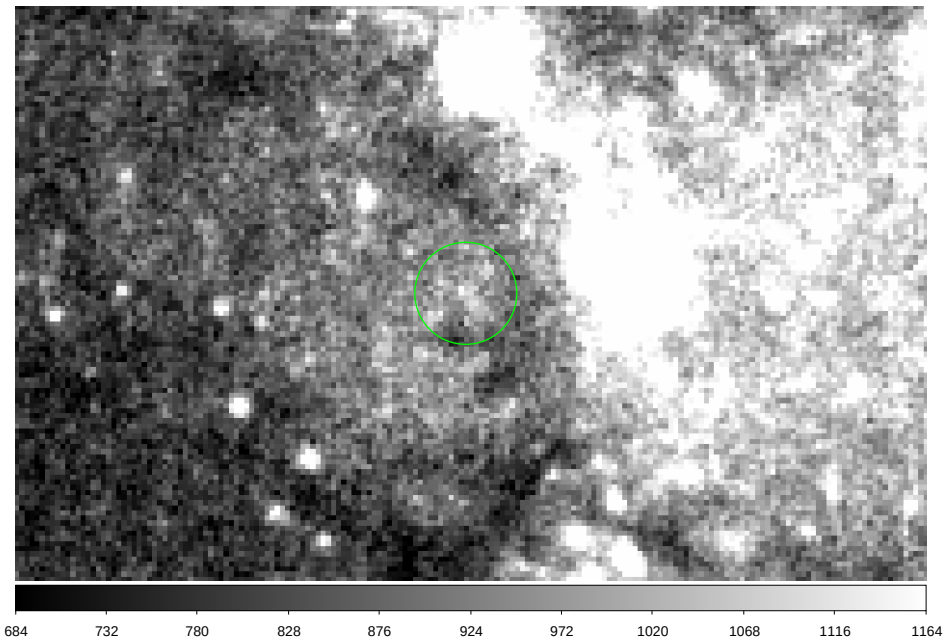

Figure A.61: Cepheid 202 image.

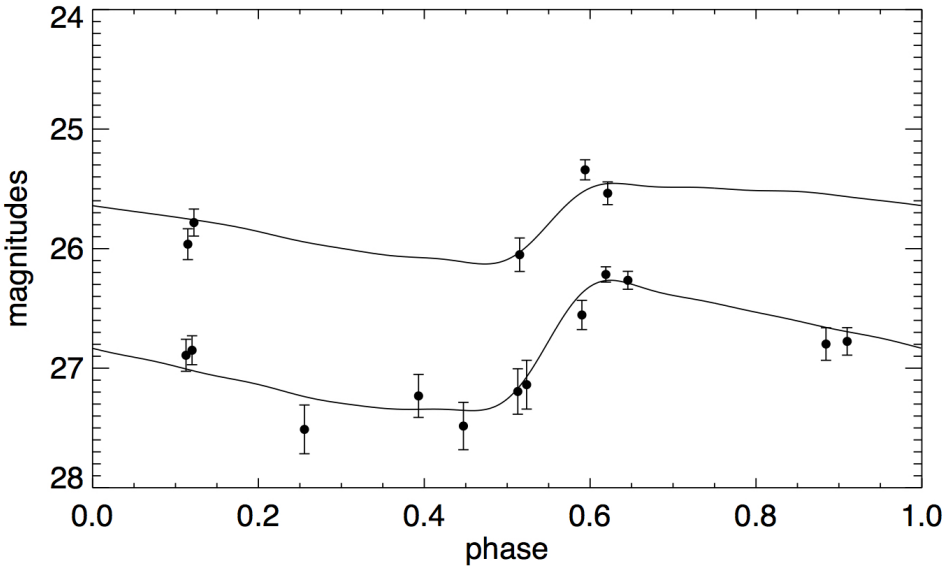

Figure A.62: Cepheid 202 light curve. I-band (top set of points) and V-band (bottom set of points) Cepheid candidate light curve. Black lines are best-fit Cepheid model light curves.

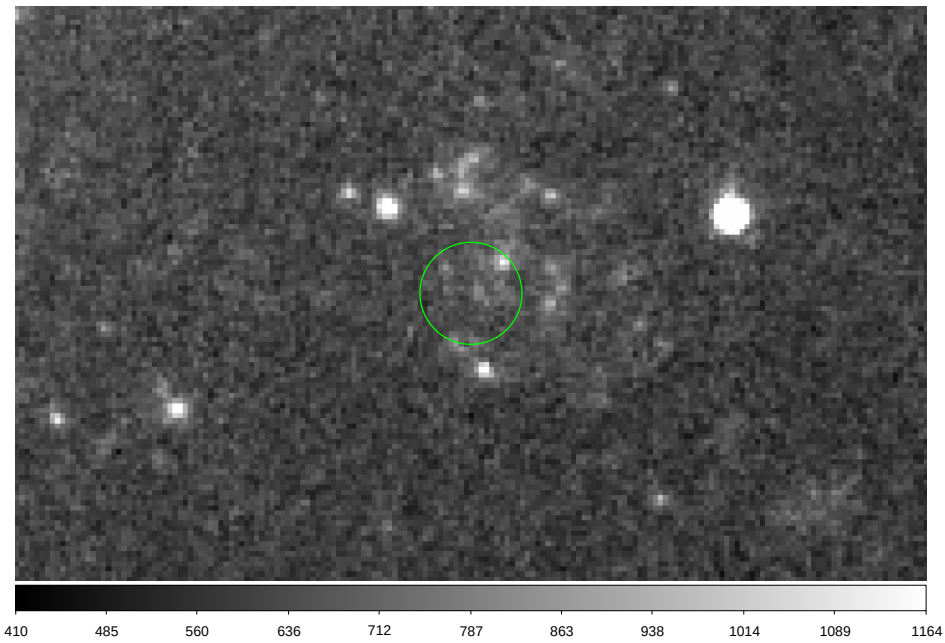

Figure A.63: Cepheid 203 image.

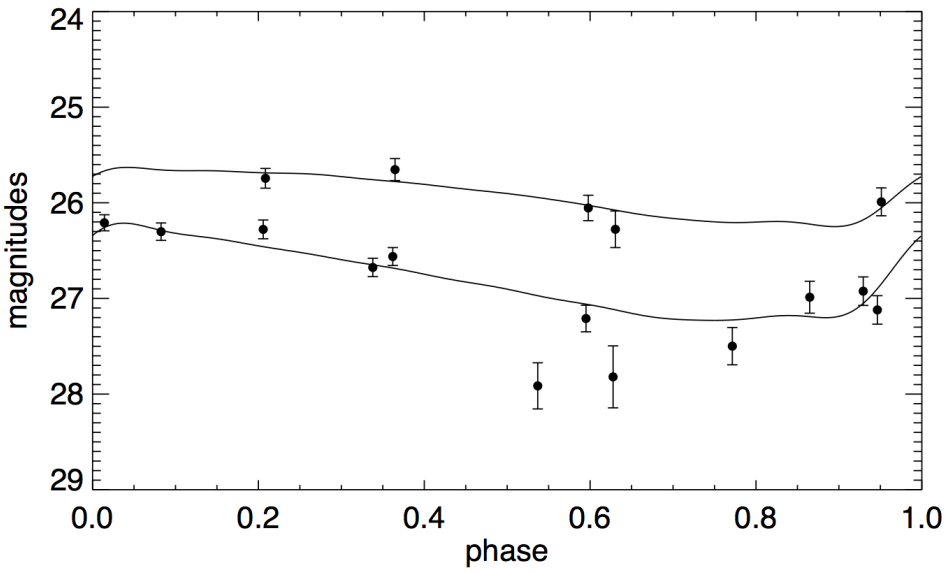

Figure A.64: Cepheid 203 light curve. I-band (top set of points) and V-band (bottom set of points) Cepheid candidate light curve. Black lines are best-fit Cepheid model light curves.

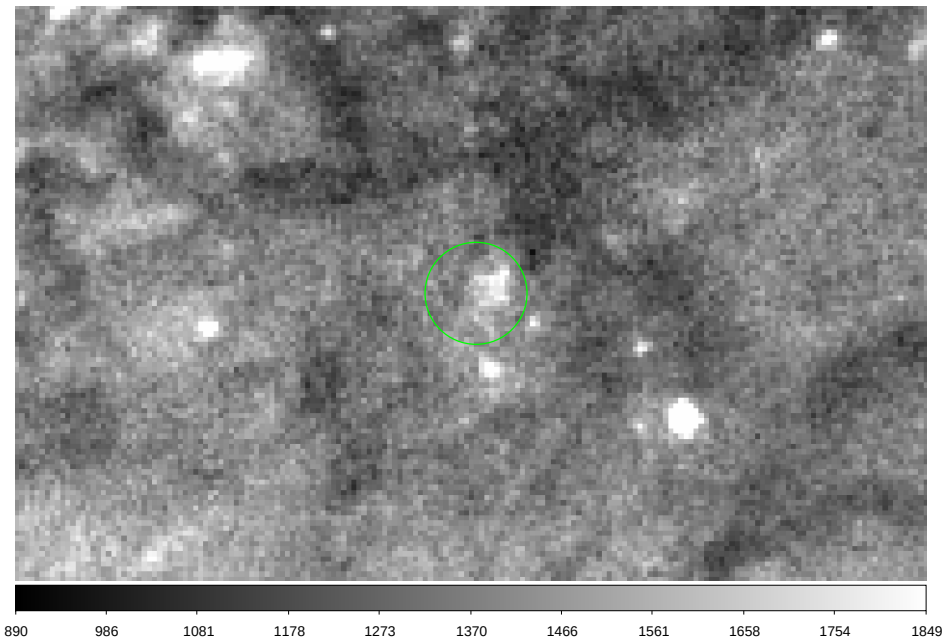

Figure A.65: Cepheid 204 image.

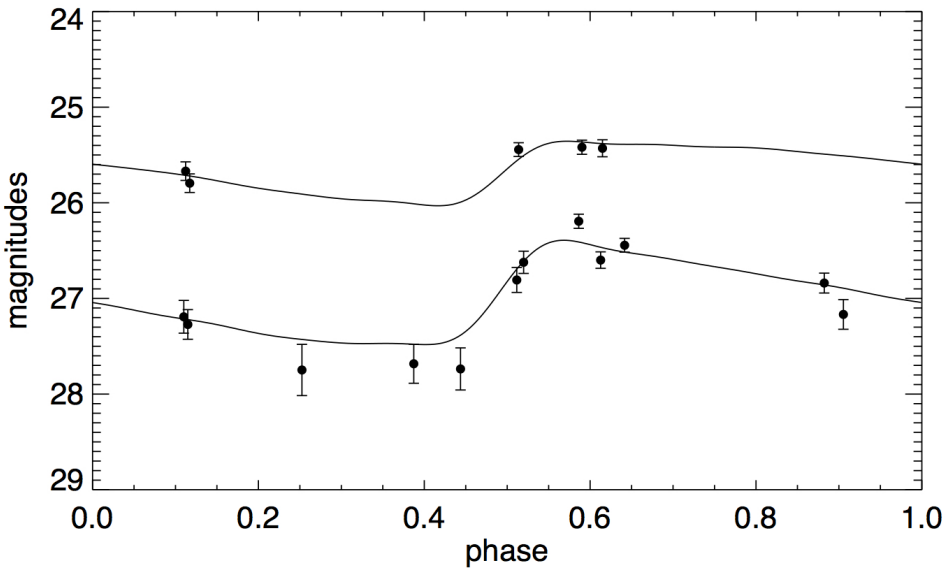

Figure A.66: Cepheid 204 light curve. I-band (top set of points) and V-band (bottom set of points) Cepheid candidate light curve. Black lines are best-fit Cepheid model light curves.

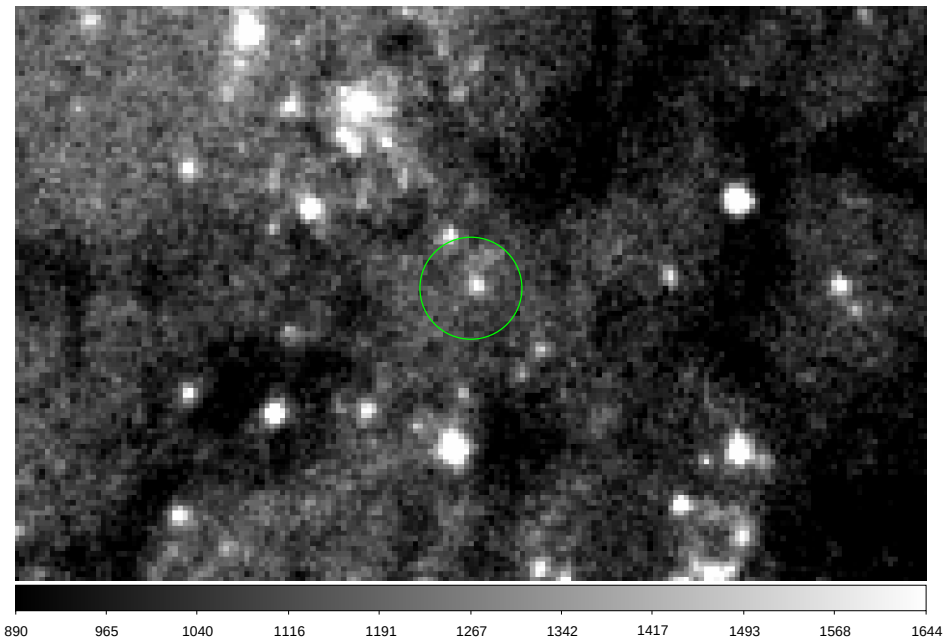

Figure A.67: Cepheid 205 image.

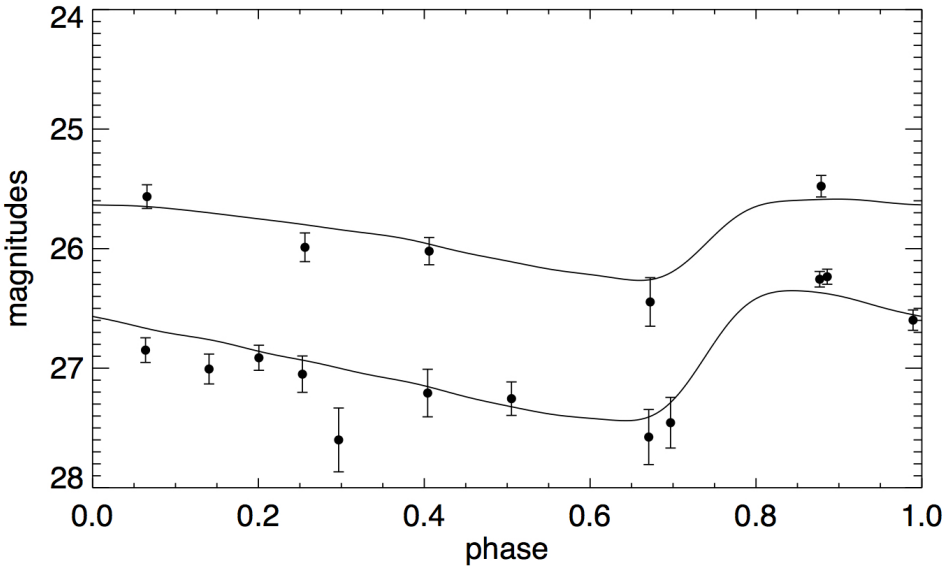

Figure A.68: Cepheid 205 light curve. I-band (top set of points) and V-band (bottom set of points) Cepheid candidate light curve. Black lines are best-fit Cepheid model light curves.

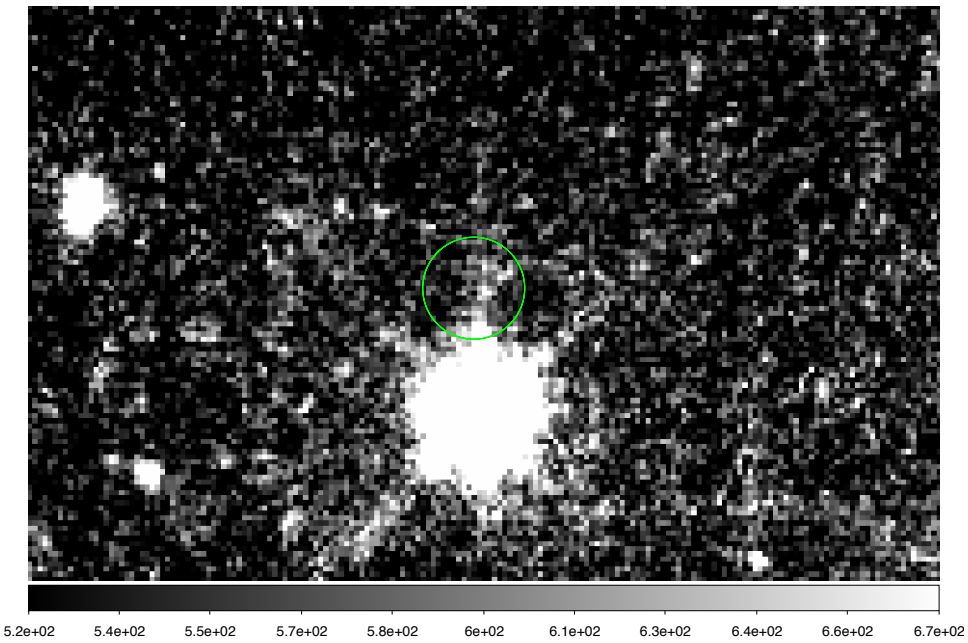

Figure A.69: Cepheid 208 image.

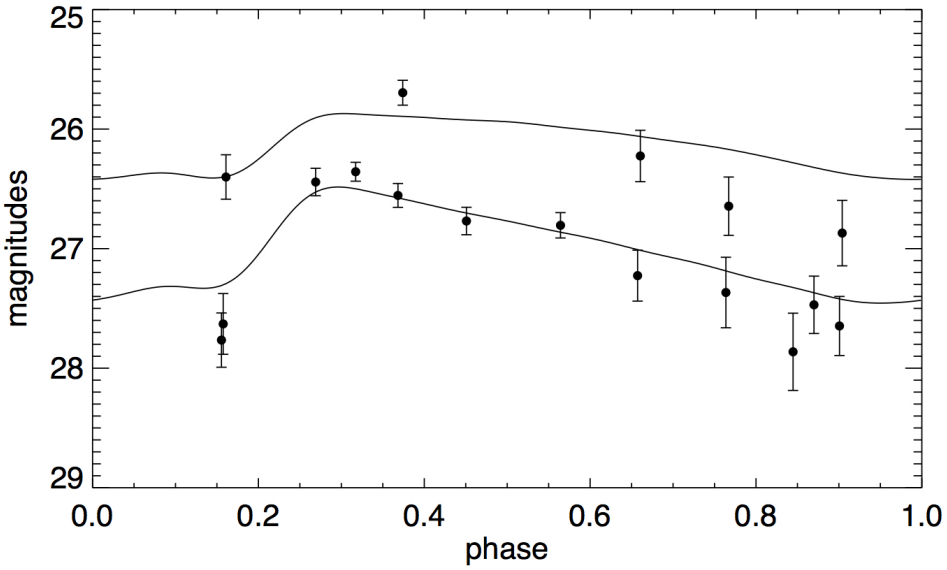

Figure A.70: Cepheid 208 light curve. I-band (top set of points) and V-band (bottom set of points) Cepheid candidate light curve. Black lines are best-fit Cepheid model light curves.

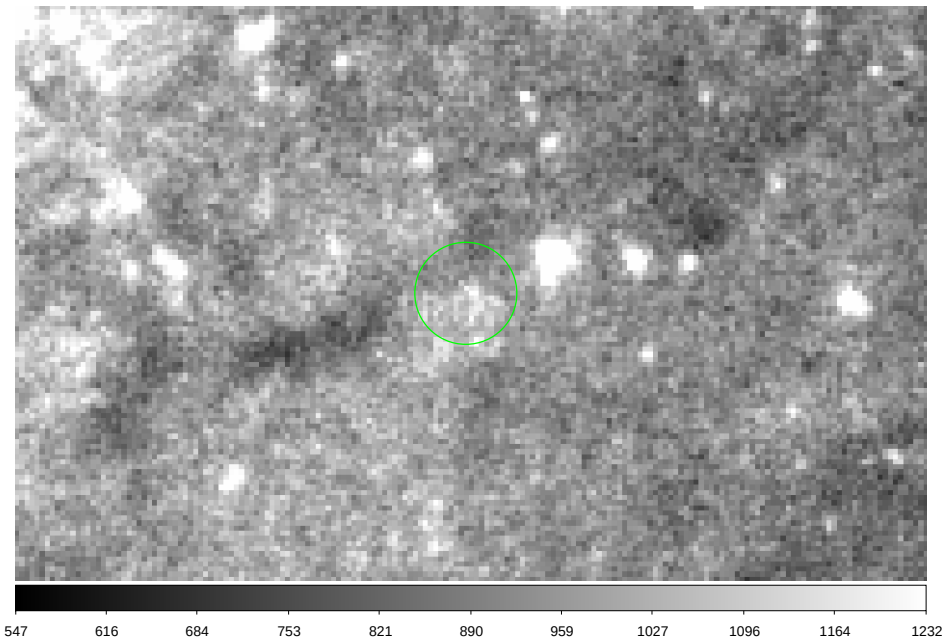

Figure A.71: Cepheid 209 image.

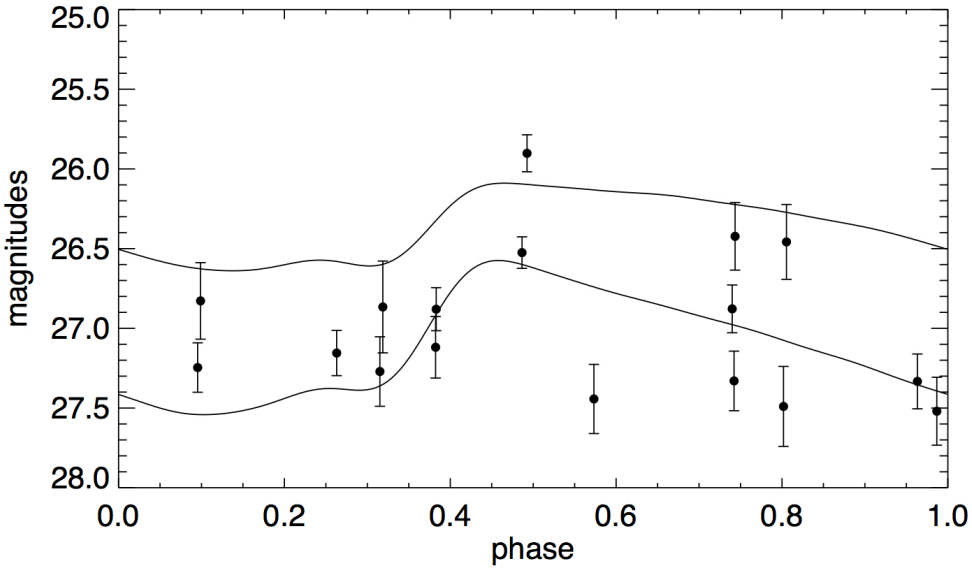

Figure A.72: Cepheid 209 light curve. I-band (top set of points) and V-band (bottom set of points) Cepheid candidate light curve. Black lines are best-fit Cepheid model light curves.

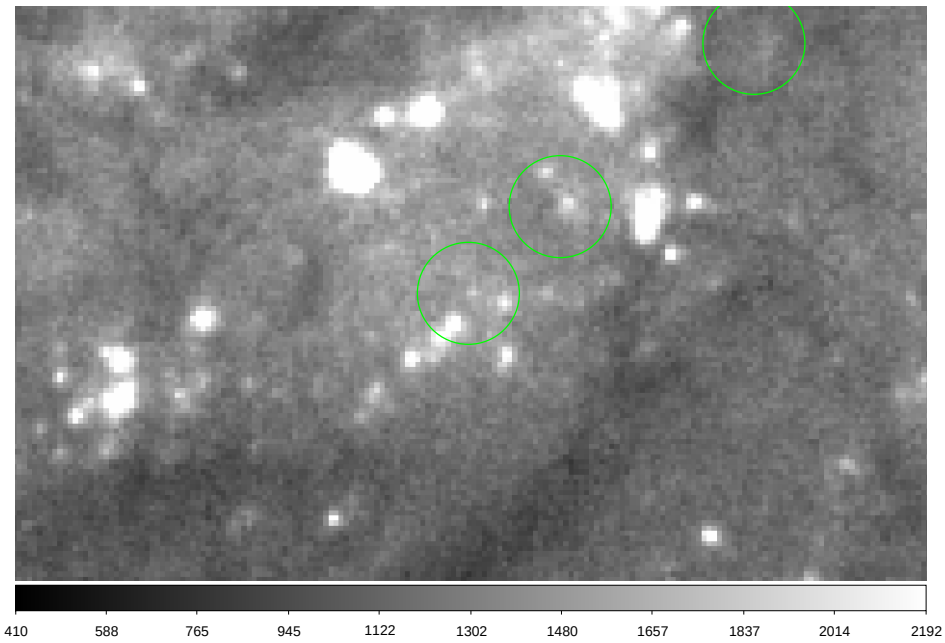

Figure A.73: Cepheid 210 image.

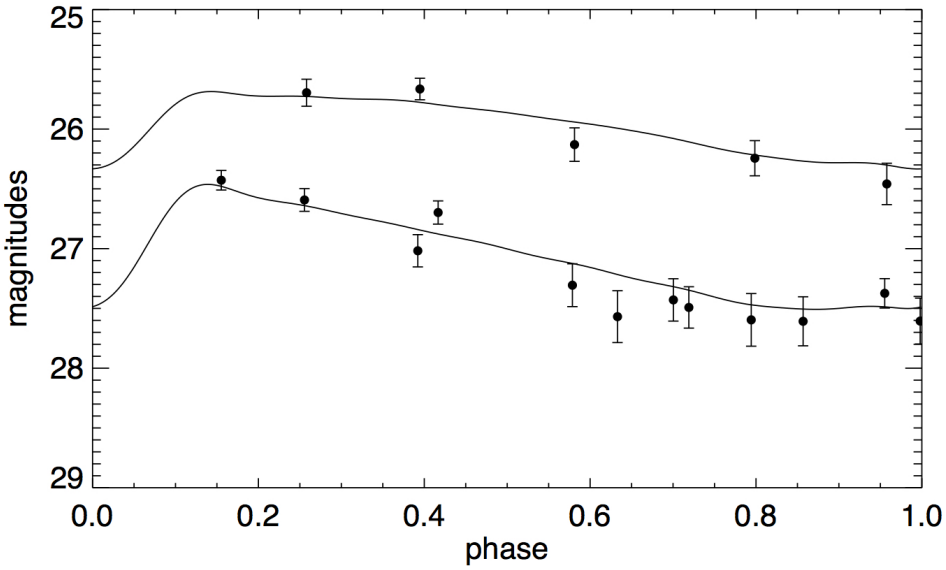

Figure A.74: Cepheid 210 light curve. I-band (top set of points) and V-band (bottom set of points) Cepheid candidate light curve. Black lines are best-fit Cepheid model light curves.

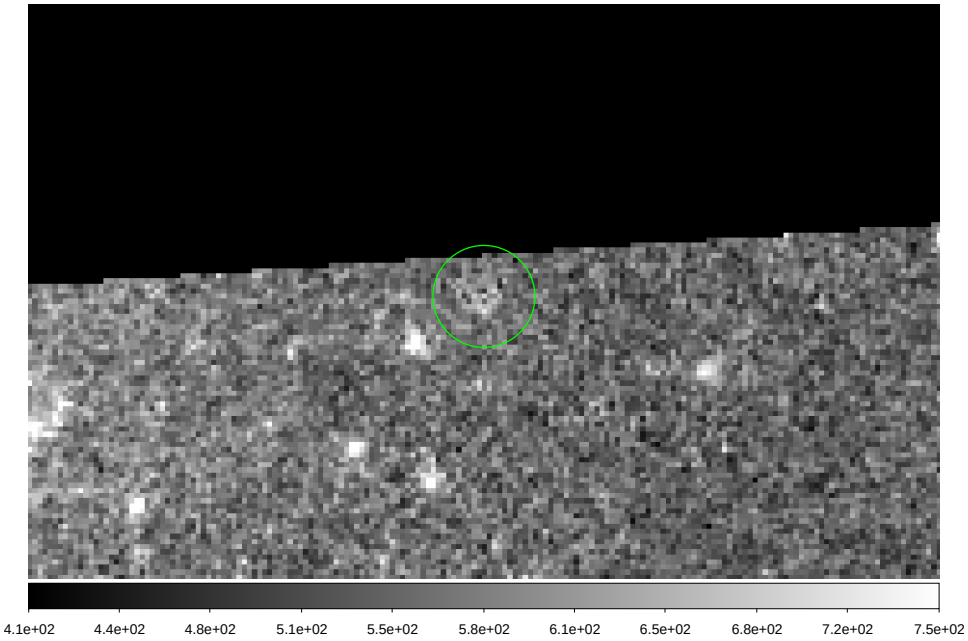

Figure A.75: Cepheid 211 image.

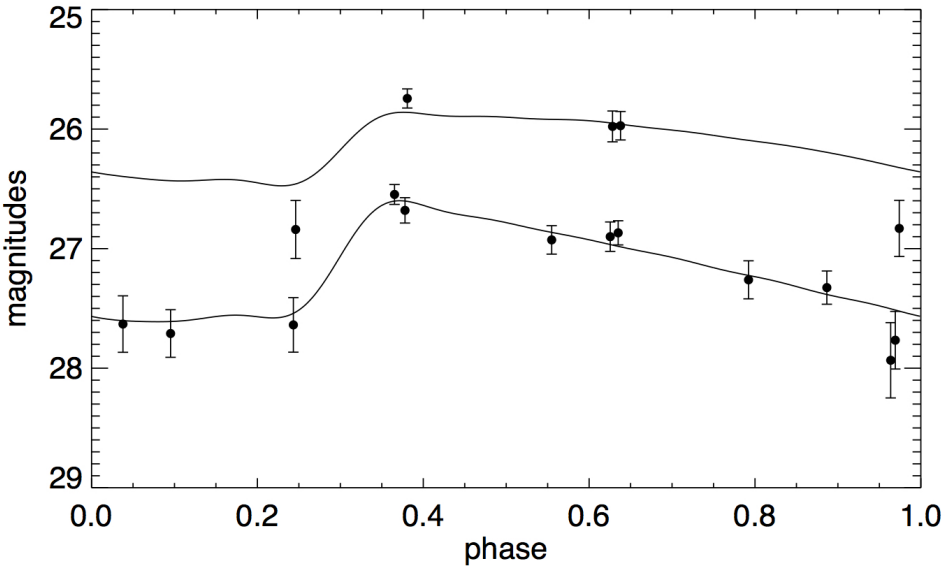

Figure A.76: Cepheid 211 light curve. I-band (top set of points) and V-band (bottom set of points) Cepheid candidate light curve. Black lines are best-fit Cepheid model light curves.

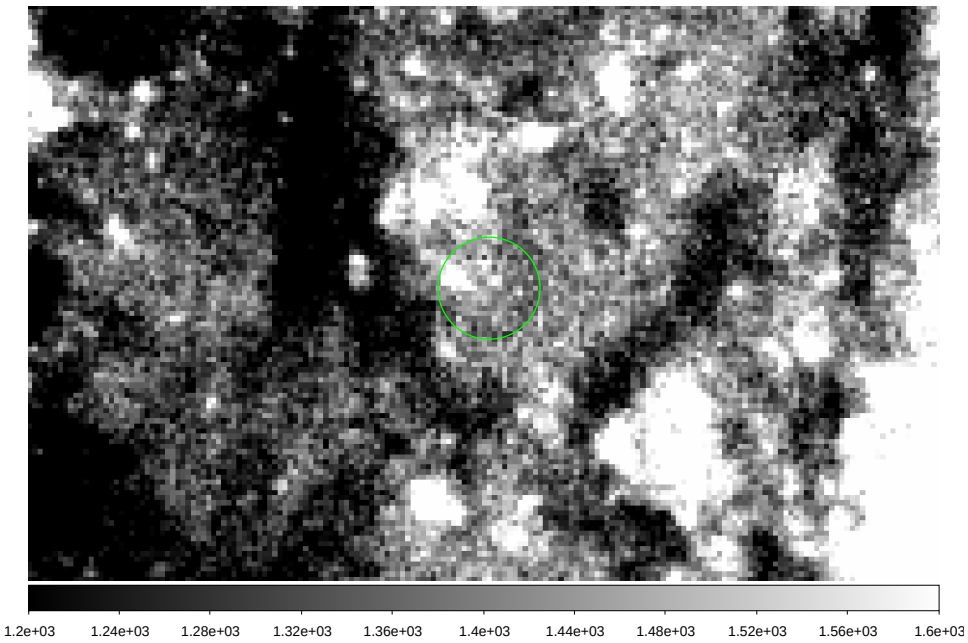

Figure A.77: Cepheid 213 image.

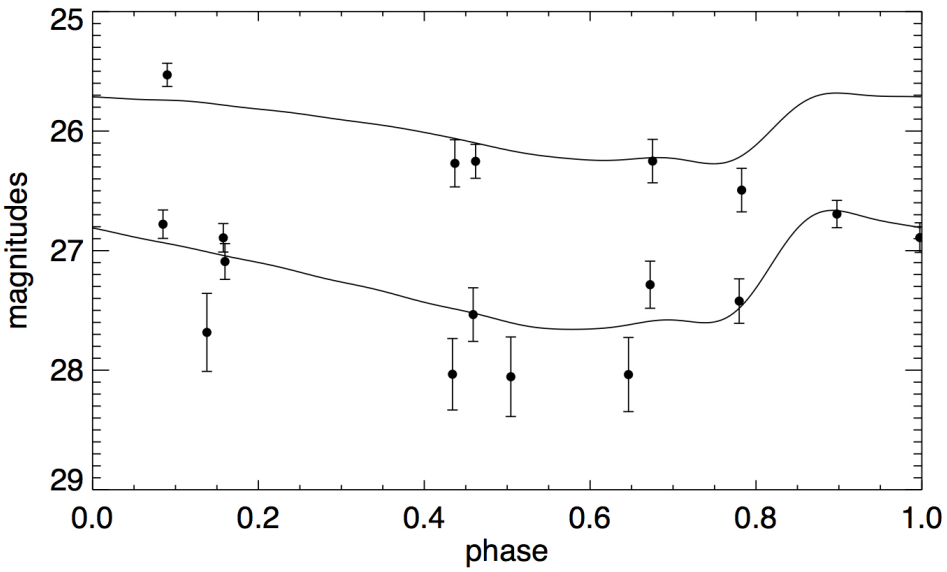

Figure A.78: Cepheid 213 light curve. I-band (top set of points) and V-band (bottom set of points) Cepheid candidate light curve. Black lines are best-fit Cepheid model light curves.

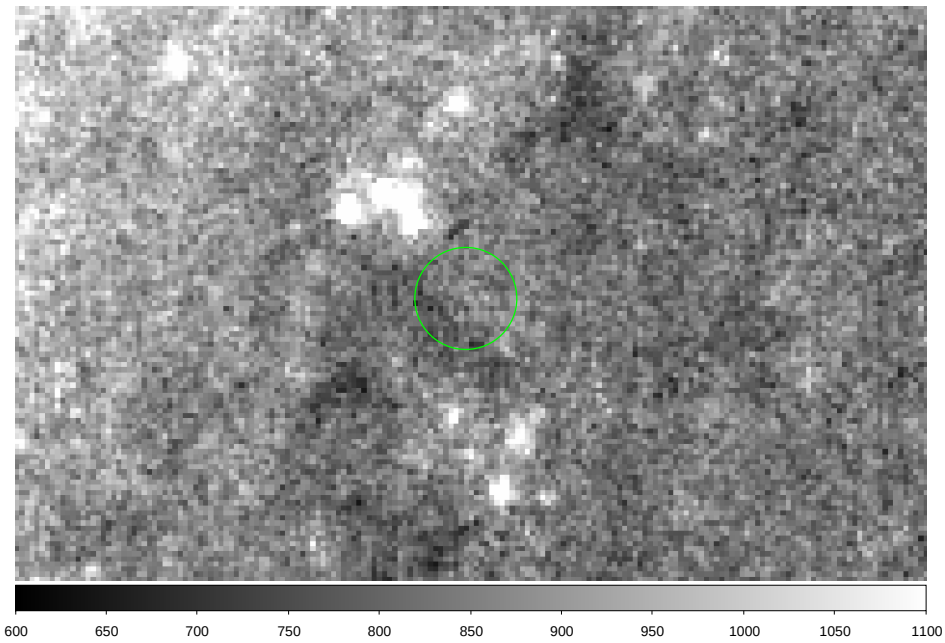

Figure A.79: Cepheid 215 image.

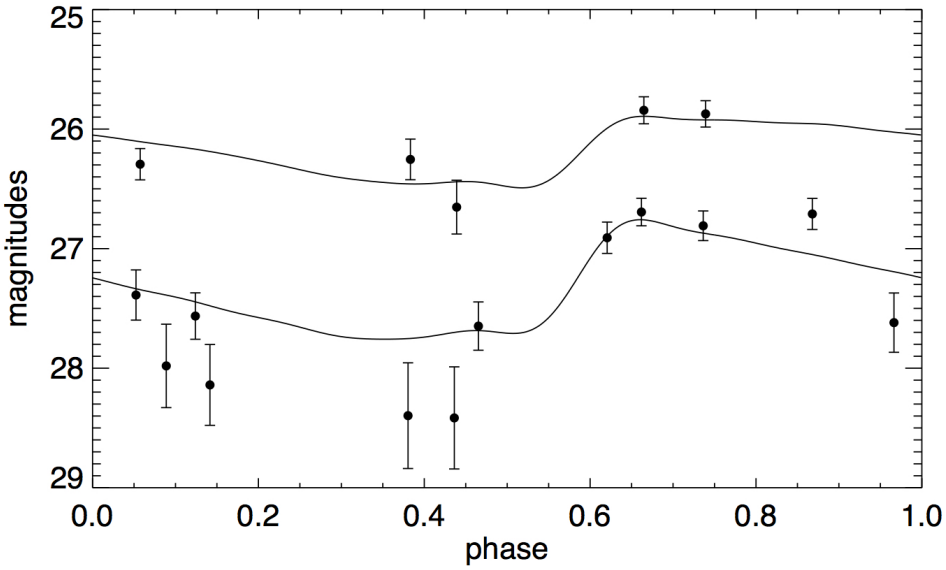

Figure A.80: Cepheid 215 light curve. I-band (top set of points) and V-band (bottom set of points) Cepheid candidate light curve. Black lines are best-fit Cepheid model light curves.

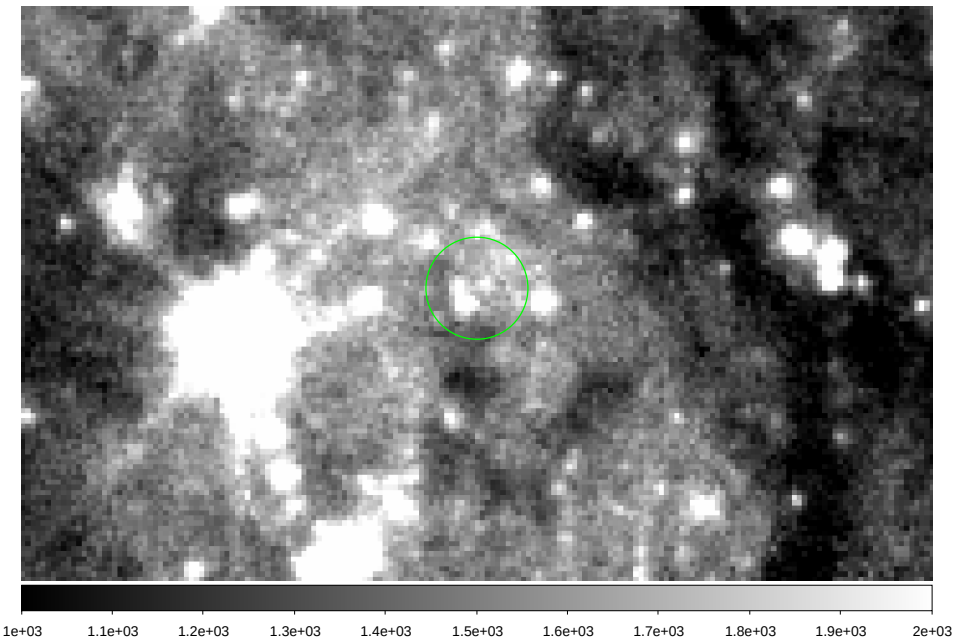

Figure A.81: Cepheid 218 image.

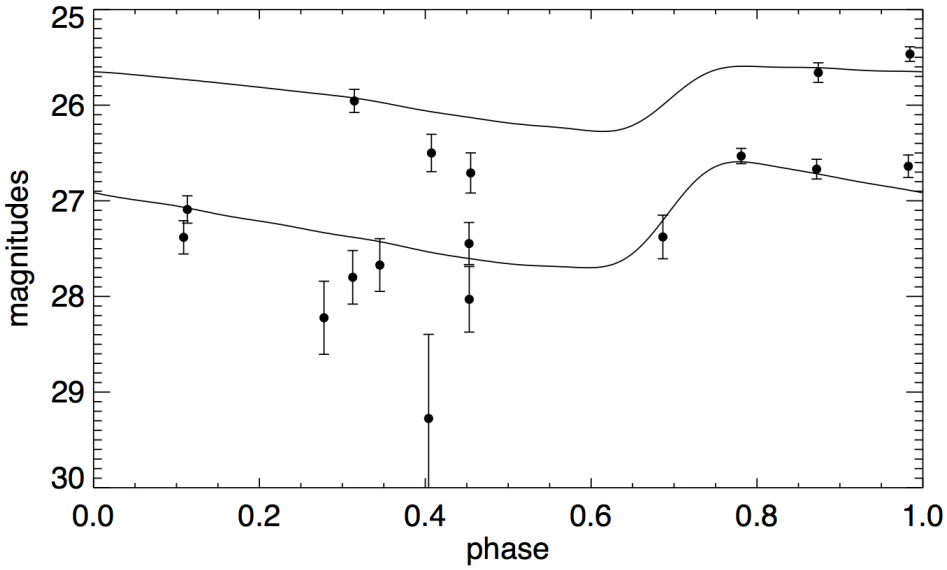

Figure A.82: Cepheid 218 light curve. I-band (top set of points) and V-band (bottom set of points) Cepheid candidate light curve. Black lines are best-fit Cepheid model light curves.

– B –

Appendix B

Table B.1: pPXF Results

x (arcsec)	y (arcsec)	v (km/s)	$\sigma_\star$ (km/s)	$h3$	$h4$
-0.75	-0.75	1580.7 ± 5.1	101.2± 2.3	0.030 ± 0.006	-0.036 ± 0.022
-0.75	-0.70	1571.7 ± 6.4	85.6 ± 9.0	-0.069 ± 0.001	-0.016 ± 0.035
-0.75	-0.65	1562.3 ± 6.9	85.6 ± 6.2	0.017 ± 0.023	0.009 ± 0.019
-0.75	-0.60	1566.1 ± 4.7	90.3 ± 1.1	0.075 ± 0.010	-0.001 ± 0.015
-0.75	-0.55	1571.1 ± 4.7	85.7 ± 4.1	0.035 ± 0.011	0.038 ± 0.009
-0.75	-0.50	1582.2 ± 6.4	92.0 ± 1.5	0.050 ± 0.007	0.023 ± 0.013
-0.75	-0.45	1572.2 ± 8.2	83.4 ± 3.0	0.069 ± 0.007	0.028 ± 0.004
-0.75	-0.40	1565.6 ± 5.8	83.0 ± 1.7	0.007 ± 0.015	0.050 ± 0.001
-0.75	-0.35	1569.3 ± 5.2	87.2 ± 0.5	-0.041 ± 0.012	0.039 ± 0.004
-0.75	-0.30	1576.6 ± 3.7	85.4 ± 2.8	-0.077 ± 0.018	0.084 ± 0.022
-0.75	-0.25	1572.6 ± 4.1	68.8 ± 2.2	-0.055 ± 0.014	0.108 ± 0.005
-0.75	-0.20	1572.1 ± 5.9	75.5 ± 1.9	-0.050 ± 0.013	0.082 ± 0.009
-0.75	-0.15	1572.7 ± 6.5	79.0 ± 3.5	-0.015 ± 0.009	0.140 ± 0.006
-0.75	-0.10	1572.6 ± 6.3	92.9 ± 2.5	0.053 ± 0.022	0.150 ± 0.022
-0.75	-0.05	1571.1 ± 7.5	82.4 ± 1.5	-0.027 ± 0.022	0.089 ± 0.009
-0.75	0.00	1565.5 ± 5.2	80.3 ± 4.4	-0.037 ± 0.019	0.091 ± 0.014
-0.75	0.05	1569.8 ± 3.7	86.3 ± 7.4	0.001 ± 0.008	0.119 ± 0.027
-0.75	0.10	1579.8 ± 4.0	92.2 ± 5.3	-0.041 ± 0.022	0.073 ± 0.026
-0.75	0.15	1575.2 ± 4.0	90.5 ± 3.5	-0.040 ± 0.020	0.137 ± 0.011
-0.75	0.20	1576.9 ± 4.9	85.8 ± 0.2	-0.067 ± 0.023	0.155 ± 0.022
-0.75	0.25	1583.1 ± 7.1	78.1 ± 2.5	-0.021 ± 0.007	0.114 ± 0.022
-0.75	0.30	1573.9 ± 6.2	79.7 ± 1.8	0.029 ± 0.007	0.097 ± 0.019
-0.75	0.35	1567.4 ± 7.4	80.2 ± 5.7	0.052 ± 0.008	0.110 ± 0.008
-0.75	0.40	1577.7 ± 7.9	78.8 ± 3.3	0.030 ± 0.007	0.083 ± 0.005
-0.75	0.45	1588.3 ± 4.1	93.3 ± 3.6	-0.014 ± 0.019	0.041 ± 0.005
-0.75	0.50	1573.2 ± 4.9	96.7 ± 3.6	0.081 ± 0.013	0.062 ± 0.013
-0.75	0.55	1578.4 ± 3.5	88.1 ± 5.3	0.056 ± 0.025	0.078 ± 0.016
-0.75	0.60	1579.1 ± 4.5	84.9 ± 5.7	0.050 ± 0.008	0.054 ± 0.004
-0.75	0.65	1576.7 ± 5.7	98.3 ± 0.9	0.021 ± 0.010	0.108 ± 0.007
-0.75	0.70	1588.7 ± 5.8	114.6 ± 4.8	-0.009 ± 0.018	0.151 ± 0.019
-0.75	0.75	1578.1 ± 3.8	96.6 ± 1.9	-0.006 ± 0.030	0.074 ± 0.005
-0.70	-0.75	1574.3 ± 5.4	112.4 ± 7.9	-0.014 ± 0.017	0.033 ± 0.022
-0.70	-0.70	1576.1 ± 5.6	101.3 ± 6.4	-0.050 ± 0.016	0.067 ± 0.008
-0.70	-0.65	1578.0 ± 5.9	92.2 ± 5.0	-0.027 ± 0.013	0.048 ± 0.008
-0.70	-0.60	1580.3 ± 6.4	107.9 ± 5.7	0.039 ± 0.017	0.071 ± 0.011
-0.70	-0.55	1581.1 ± 5.7	100.1 ± 5.1	0.049 ± 0.011	0.062 ± 0.015
-0.70	-0.50	1577.6 ± 5.2	101.2 ± 4.6	0.045 ± 0.012	0.003 ± 0.016
-0.70	-0.45	1560.3 ± 5.1	85.9 ± 3.0	0.061 ± 0.010	0.100 ± 0.009
-0.70	-0.40	1570.9 ± 4.8	86.5 ± 2.9	0.019 ± 0.012	0.093 ± 0.012
-0.70	-0.35	1572.3 ± 5.5	89.2 ± 1.8	0.022 ± 0.021	0.098 ± 0.008
-0.70	-0.30	1573.1 ± 6.3	93.2 ± 2.5	-0.039 ± 0.020	0.150 ± 0.013
-0.70	-0.25	1569.1 ± 6.2	78.4 ± 0.4	-0.036 ± 0.014	0.108 ± 0.020
-0.70	-0.20	1569.6 ± 8.2	83.9 ± 4.0	-0.042 ± 0.013	0.127 ± 0.018
-0.70	-0.15	1573.3 ± 8.2	86.4 ± 2.3	-0.008 ± 0.021	0.058 ± 0.001
-0.70	-0.10	1570.4 ± 6.6	88.8 ± 2.5	0.012 ± 0.016	0.055 ± 0.019
-0.70	-0.05	1571.2 ± 5.6	83.4 ± 2.6	0.004 ± 0.011	0.064 ± 0.013
-0.70	0.00	1566.2 ± 5.2	81.5 ± 0.2	0.006 ± 0.016	0.130 ± 0.006
-0.70	0.05	1566.8 ± 4.6	79.6 ± 3.7	0.038 ± 0.009	0.148 ± 0.013
-0.70	0.10	1572.9 ± 3.0	73.1 ± 2.9	0.000 ± 0.018	0.146 ± 0.027
-0.70	0.15	1578.4 ± 3.6	80.0 ± 2.5	-0.018 ± 0.014	0.163 ± 0.030
-0.70	0.20	1575.8 ± 3.3	77.6 ± 3.1	-0.027 ± 0.021	0.126 ± 0.020
-0.70	0.25	1569.2 ± 2.8	85.7 ± 2.7	-0.011 ± 0.021	0.145 ± 0.020
-0.70	0.30	1571.3 ± 5.1	91.1 ± 2.5	0.043 ± 0.009	0.154 ± 0.019
-0.70	0.35	1571.0 ± 5.5	86.6 ± 6.1	-0.007 ± 0.010	0.118 ± 0.006
-0.70	0.40	1569.1 ± 8.8	99.0 ± 7.2	0.008 ± 0.014	0.090 ± 0.033
-0.70	0.45	1585.3 ± 8.9	119.6 ± 5.3	0.039 ± 0.002	0.085 ± 0.003
-0.70	0.50	1574.7 ± 7.3	109.0 ± 6.0	0.051 ± 0.013	0.041 ± 0.007
-0.70	0.55	1569.2 ± 4.1	90.1 ± 3.5	0.010 ± 0.024	0.067 ± 0.006
-0.70	0.60	1564.9 ± 6.1	102.3 ± 2.8	0.051 ± 0.020	0.009 ± 0.010
-0.70	0.65	1567.4 ± 9.0	112.1 ± 3.4	0.020 ± 0.006	0.012 ± 0.005
-0.70	0.70	1573.6 ± 6.2	101.5 ± 1.4	-0.034 ± 0.016	0.026 ± 0.014
-0.70	0.75	1571.6 ± 4.9	84.9 ± 4.3	-0.010 ± 0.012	0.098 ± 0.020

x (arcsec)	y (arcsec)	v (km/s)	$\sigma_\star$ (km/s)	$h3$	$h4$
-0.65	-0.75	1565.1 ± 5.0	87.6 ± 3.4	-0.023 ± 0.020	0.046 ± 0.007
-0.65	-0.70	1573.5 ± 4.6	83.8 ± 2.9	-0.033 ± 0.004	0.031 ± 0.006
-0.65	-0.65	1584.5 ± 7.4	88.3 ± 2.2	0.017 ± 0.014	0.073 ± 0.001
-0.65	-0.60	1589.9 ± 7.4	91.2 ± 3.3	0.065 ± 0.005	0.152 ± 0.009
-0.65	-0.55	1581.9 ± 4.8	96.5 ± 2.6	0.035 ± 0.022	0.166 ± 0.017
-0.65	-0.50	1575.8 ± 6.2	101.8 ± 2.3	-0.020 ± 0.016	0.147 ± 0.012
-0.65	-0.45	1573.7 ± 6.6	94.3 ± 3.0	-0.004 ± 0.009	0.115 ± 0.028
-0.65	-0.40	1571.2 ± 7.1	71.7 ± 3.2	0.009 ± 0.010	0.095 ± 0.006
-0.65	-0.35	1577.3 ± 4.7	90.5 ± 2.0	-0.027 ± 0.013	0.058 ± 0.010
-0.65	-0.30	1572.9 ± 4.4	77.8 ± 4.6	0.000 ± 0.013	0.126 ± 0.009
-0.65	-0.25	1575.3 ± 5.6	82.5 ± 2.6	-0.011 ± 0.014	0.165 ± 0.012
-0.65	-0.20	1570.9 ± 5.3	80.8 ± 1.8	-0.051 ± 0.009	0.136 ± 0.007
-0.65	-0.15	1565.4 ± 6.2	87.9 ± 2.5	-0.020 ± 0.013	0.139 ± 0.002
-0.65	-0.10	1562.9 ± 5.1	86.3 ± 2.3	-0.018 ± 0.003	0.139 ± 0.012
-0.65	-0.05	1570.1 ± 5.5	80.1 ± 2.3	-0.032 ± 0.012	0.134 ± 0.027
-0.65	0.00	1568.3 ± 5.2	80.3 ± 3.1	0.020 ± 0.016	0.146 ± 0.012
-0.65	0.05	1572.5 ± 5.7	77.7 ± 3.7	-0.030 ± 0.012	0.154 ± 0.012
-0.65	0.10	1574.4 ± 5.8	76.8 ± 2.9	0.005 ± 0.011	0.141 ± 0.026
-0.65	0.15	1575.5 ± 5.2	69.5 ± 2.4	-0.045 ± 0.016	0.166 ± 0.013
-0.65	0.20	1570.5 ± 3.7	63.1 ± 1.5	-0.015 ± 0.024	0.152 ± 0.001
-0.65	0.25	1567.8 ± 2.9	82.2 ± 2.8	0.010 ± 0.021	0.088 ± 0.023
-0.65	0.30	1571.5 ± 3.2	86.6 ± 5.0	-0.020 ± 0.023	0.063 ± 0.008
-0.65	0.35	1578.4 ± 2.9	82.1 ± 7.0	-0.010 ± 0.009	0.098 ± 0.023
-0.65	0.40	1579.3 ± 3.7	80.6 ± 2.6	0.008 ± 0.014	0.071 ± 0.022
-0.65	0.45	1568.4 ± 5.9	95.1 ± 3.1	0.019 ± 0.015	0.095 ± 0.005
-0.65	0.50	1564.5 ± 1.2	94.1 ± 5.8	0.031 ± 0.010	0.109 ± 0.021
-0.65	0.55	1564.5 ± 4.4	86.0 ± 3.9	0.010 ± 0.022	0.068 ± 0.014
-0.65	0.60	1574.4 ± 8.1	71.6 ± 6.3	-0.008 ± 0.011	0.074 ± 0.053
-0.65	0.65	1568.7 ± 5.2	92.7 ± 2.6	0.013 ± 0.010	0.046 ± 0.017
-0.65	0.70	1565.0 ± 5.7	101.3 ± 0.9	0.033 ± 0.017	0.024 ± 0.014
-0.65	0.75	1573.2 ± 5.2	96.8 ± 2.6	0.027 ± 0.022	0.027 ± 0.018
-0.60	-0.75	1570.1 ± 8.4	88.4 ± 3.4	0.043 ± 0.005	-0.049 ± 0.019
-0.60	-0.70	1575.8 ± 5.4	82.0 ± 3.0	0.027 ± 0.025	0.071 ± 0.018
-0.60	-0.65	1580.8 ± 6.7	96.2 ± 3.8	0.024 ± 0.008	0.094 ± 0.011
-0.60	-0.60	1579.7 ± 7.1	94.1 ± 6.3	0.048 ± 0.020	0.106 ± 0.004
-0.60	-0.55	1580.8 ± 5.6	94.2 ± 1.2	0.034 ± 0.012	0.079 ± 0.025
-0.60	-0.50	1580.0 ± 5.6	90.6 ± 2.5	0.010 ± 0.015	0.136 ± 0.024
-0.60	-0.45	1581.7 ± 6.5	85.8 ± 3.5	0.031 ± 0.008	0.133 ± 0.019
-0.60	-0.40	1579.9 ± 4.6	78.4 ± 6.0	0.009 ± 0.018	0.123 ± 0.019
-0.60	-0.35	1572.0 ± 4.3	72.2 ± 6.7	-0.008 ± 0.018	0.117 ± 0.015
-0.60	-0.30	1570.8 ± 6.2	83.6 ± 5.6	-0.005 ± 0.006	0.093 ± 0.022
-0.60	-0.25	1572.9 ± 4.3	83.3 ± 2.2	-0.018 ± 0.025	0.120 ± 0.025
-0.60	-0.20	1575.8 ± 5.1	87.3 ± 2.5	-0.061 ± 0.024	0.100 ± 0.023
-0.60	-0.15	1564.7 ± 6.1	91.1 ± 5.3	-0.021 ± 0.015	0.194 ± 0.039
-0.60	-0.10	1568.1 ± 6.8	93.3 ± 0.4	0.014 ± 0.020	0.214 ± 0.010
-0.60	-0.05	1576.7 ± 5.7	81.2 ± 2.6	0.007 ± 0.011	0.152 ± 0.016
-0.60	0.00	1581.7 ± 5.6	80.0 ± 2.3	0.000 ± 0.010	0.120 ± 0.014
-0.60	0.05	1574.4 ± 5.8	78.7 ± 2.1	-0.051 ± 0.015	0.123 ± 0.022
-0.60	0.10	1573.7 ± 5.7	75.7 ± 1.8	0.010 ± 0.017	0.140 ± 0.019
-0.60	0.15	1573.4 ± 5.3	72.1 ± 1.9	-0.006 ± 0.008	0.116 ± 0.024
-0.60	0.20	1569.0 ± 5.3	83.2 ± 5.5	-0.015 ± 0.013	0.117 ± 0.020
-0.60	0.25	1566.2 ± 6.2	86.1 ± 5.3	0.025 ± 0.020	0.118 ± 0.007
-0.60	0.30	1570.5 ± 5.7	65.2 ± 2.8	0.024 ± 0.009	0.127 ± 0.003
-0.60	0.35	1573.5 ± 4.2	67.0 ± 5.3	0.027 ± 0.011	0.121 ± 0.023
-0.60	0.40	1579.0 ± 3.5	75.4 ± 2.8	-0.030 ± 0.008	0.106 ± 0.024
-0.60	0.45	1577.9 ± 4.1	94.0 ± 1.2	-0.047 ± 0.006	0.067 ± 0.008
-0.60	0.50	1564.6 ± 2.9	101.8 ± 2.2	0.014 ± 0.002	0.025 ± 0.005
-0.60	0.55	1563.7 ± 4.8	91.7 ± 3.8	0.029 ± 0.009	0.085 ± 0.001
-0.60	0.60	1573.5 ± 8.5	78.5 ± 3.9	0.000 ± 0.013	0.065 ± 0.017
-0.60	0.65	1575.9 ± 2.9	76.4 ± 2.3	-0.024 ± 0.009	0.144 ± 0.006
-0.60	0.70	1576.3 ± 5.5	80.6 ± 3.5	0.025 ± 0.001	0.119 ± 0.008
-0.60	0.75	1572.9 ± 6.1	99.8 ± 2.5	0.050 ± 0.028	0.094 ± 0.021

x (arcsec)	y (arcsec)	v (km/s)	$\sigma_\star$ (km/s)	$h3$	$h4$
-0.55	-0.75	1577.3 ± 3.6	90.7 ± 3.8	0.033 ± 0.021	-0.015 ± 0.002
-0.55	-0.70	1575.3 ± 3.3	108.2 ± 1.7	0.024 ± 0.024	-0.021 ± 0.020
-0.55	-0.65	1583.7 ± 5.7	88.2 ± 2.6	-0.015 ± 0.020	0.062 ± 0.007
-0.55	-0.60	1583.8 ± 5.9	79.7 ± 3.0	-0.032 ± 0.011	0.094 ± 0.009
-0.55	-0.55	1580.9 ± 5.6	79.7 ± 3.2	-0.053 ± 0.014	0.099 ± 0.009
-0.55	-0.50	1582.1 ± 5.1	77.3 ± 2.0	-0.062 ± 0.027	0.114 ± 0.007
-0.55	-0.45	1578.4 ± 6.0	89.5 ± 2.5	-0.087 ± 0.025	0.135 ± 0.022
-0.55	-0.40	1575.5 ± 5.5	89.4 ± 2.0	-0.096 ± 0.024	0.167 ± 0.018
-0.55	-0.35	1568.0 ± 6.8	86.6 ± 4.2	-0.026 ± 0.006	0.122 ± 0.024
-0.55	-0.30	1571.5 ± 6.3	72.8 ± 1.9	-0.048 ± 0.023	0.106 ± 0.023
-0.55	-0.25	1572.3 ± 3.6	70.3 ± 0.9	-0.048 ± 0.024	0.107 ± 0.008
-0.55	-0.20	1573.0 ± 3.9	73.2 ± 2.8	0.000 ± 0.025	0.120 ± 0.004
-0.55	-0.15	1571.3 ± 5.6	80.6 ± 3.5	0.001 ± 0.010	0.145 ± 0.005
-0.55	-0.10	1573.0 ± 5.3	75.8 ± 2.0	0.032 ± 0.006	0.161 ± 0.003
-0.55	-0.05	1579.3 ± 4.3	78.1 ± 2.2	0.071 ± 0.013	0.174 ± 0.007
-0.55	0.00	1585.2 ± 6.0	83.2 ± 3.0	0.068 ± 0.021	0.188 ± 0.005
-0.55	0.05	1575.6 ± 5.9	77.4 ± 4.6	0.040 ± 0.014	0.131 ± 0.011
-0.55	0.10	1572.7 ± 5.5	87.9 ± 6.6	0.038 ± 0.018	0.113 ± 0.032
-0.55	0.15	1574.0 ± 4.2	72.8 ± 3.9	0.024 ± 0.017	0.117 ± 0.019
-0.55	0.20	1570.5 ± 5.7	73.8 ± 3.0	-0.002 ± 0.017	0.126 ± 0.014
-0.55	0.25	1565.3 ± 5.2	74.8 ± 3.0	-0.012 ± 0.017	0.136 ± 0.016
-0.55	0.30	1575.3 ± 5.5	69.7 ± 5.8	0.002 ± 0.011	0.107 ± 0.017
-0.55	0.35	1582.2 ± 4.2	72.8 ± 3.6	-0.002 ± 0.011	0.106 ± 0.005
-0.55	0.40	1589.2 ± 4.3	76.7 ± 0.3	-0.009 ± 0.020	0.069 ± 0.015
-0.55	0.45	1587.8 ± 5.8	79.8 ± 3.0	-0.056 ± 0.018	0.081 ± 0.007
-0.55	0.50	1582.0 ± 4.4	94.7 ± 3.4	-0.049 ± 0.018	0.114 ± 0.016
-0.55	0.55	1580.9 ± 5.4	92.5 ± 3.4	-0.016 ± 0.013	0.135 ± 0.005
-0.55	0.60	1579.3 ± 5.8	74.6 ± 0.5	-0.075 ± 0.007	0.046 ± 0.021
-0.55	0.65	1576.6 ± 6.4	88.2 ± 0.6	-0.048 ± 0.020	0.047 ± 0.008
-0.55	0.70	1584.8 ± 6.1	108.0 ± 3.3	0.037 ± 0.003	0.055 ± 0.005
-0.55	0.75	1570.5 ± 4.9	98.1 ± 3.2	0.025 ± 0.010	0.147 ± 0.010
-0.50	-0.75	1580.6 ± 7.7	95.4 ± 1.7	-0.030 ± 0.019	0.103 ± 0.010
-0.50	-0.70	1580.7 ± 7.5	85.2 ± 3.0	-0.029 ± 0.017	0.081 ± 0.013
-0.50	-0.65	1582.9 ± 7.9	82.4 ± 2.1	-0.033 ± 0.017	0.009 ± 0.010
-0.50	-0.60	1582.5 ± 5.9	80.4 ± 3.7	-0.044 ± 0.021	0.020 ± 0.014
-0.50	-0.55	1580.8 ± 5.9	80.9 ± 1.9	0.000 ± 0.016	0.092 ± 0.020
-0.50	-0.50	1577.5 ± 5.9	86.0 ± 2.6	0.012 ± 0.011	0.086 ± 0.030
-0.50	-0.45	1583.1 ± 6.1	87.3 ± 0.7	-0.024 ± 0.011	0.053 ± 0.010
-0.50	-0.40	1582.8 ± 7.0	87.3 ± 2.4	-0.037 ± 0.013	0.078 ± 0.019
-0.50	-0.35	1575.4 ± 3.8	80.9 ± 0.9	-0.006 ± 0.030	0.165 ± 0.033
-0.50	-0.30	1579.0 ± 4.3	74.6 ± 1.0	-0.010 ± 0.020	0.215 ± 0.012
-0.50	-0.25	1577.5 ± 4.1	72.2 ± 2.8	-0.002 ± 0.026	0.189 ± 0.007
-0.50	-0.20	1578.4 ± 2.6	72.8 ± 1.2	-0.022 ± 0.032	0.153 ± 0.008
-0.50	-0.15	1577.5 ± 2.4	82.3 ± 2.1	-0.018 ± 0.024	0.145 ± 0.019
-0.50	-0.10	1573.7 ± 4.2	77.2 ± 2.2	-0.017 ± 0.020	0.147 ± 0.006
-0.50	-0.05	1574.9 ± 5.5	69.8 ± 4.0	0.015 ± 0.016	0.160 ± 0.003
-0.50	0.00	1576.4 ± 4.5	69.2 ± 4.2	-0.007 ± 0.025	0.173 ± 0.002
-0.50	0.05	1579.9 ± 5.5	69.2 ± 3.7	0.014 ± 0.013	0.177 ± 0.008
-0.50	0.10	1581.5 ± 3.8	71.3 ± 3.6	-0.002 ± 0.016	0.144 ± 0.021
-0.50	0.15	1578.2 ± 4.7	80.0 ± 2.0	-0.021 ± 0.012	0.145 ± 0.025
-0.50	0.20	1582.5 ± 4.5	71.8 ± 2.5	0.000 ± 0.016	0.127 ± 0.006
-0.50	0.25	1574.9 ± 4.2	73.0 ± 1.9	-0.003 ± 0.014	0.111 ± 0.005
-0.50	0.30	1576.6 ± 4.3	70.4 ± 3.4	-0.013 ± 0.018	0.142 ± 0.008
-0.50	0.35	1572.0 ± 6.1	72.4 ± 4.3	0.055 ± 0.018	0.155 ± 0.004
-0.50	0.40	1577.8 ± 5.8	79.2 ± 2.0	0.067 ± 0.010	0.122 ± 0.007
-0.50	0.45	1579.1 ± 6.0	82.5 ± 2.8	-0.006 ± 0.013	0.111 ± 0.005
-0.50	0.50	1585.5 ± 6.1	100.5 ± 1.9	-0.067 ± 0.019	0.033 ± 0.007
-0.50	0.55	1584.9 ± 3.9	93.2 ± 4.4	-0.081 ± 0.013	0.115 ± 0.010
-0.50	0.60	1583.3 ± 6.3	82.8 ± 3.6	-0.024 ± 0.013	0.098 ± 0.013
-0.50	0.65	1581.6 ± 7.2	99.5 ± 1.5	-0.003 ± 0.010	0.013 ± 0.016
-0.50	0.70	1578.0 ± 6.9	107.1 ± 6.2	-0.001 ± 0.009	0.014 ± 0.011
-0.50	0.75	1585.4 ± 7.6	104.0 ± 0.9	-0.060 ± 0.011	0.129 ± 0.009

x (arcsec)	y (arcsec)	v (km/s)	$\sigma_\star$ (km/s)	$h3$	$h4$
-0.45	-0.75	1572.5 ± 6.7	73.6 ± 1.5	-0.068 ± 0.020	0.077 ± 0.015
-0.45	-0.70	1584.1 ± 5.2	75.2 ± 3.1	-0.041 ± 0.023	0.054 ± 0.010
-0.45	-0.65	1577.8 ± 6.7	72.9 ± 1.7	-0.003 ± 0.012	-0.016 ± 0.008
-0.45	-0.60	1574.8 ± 5.7	83.1 ± 0.8	0.034 ± 0.012	0.023 ± 0.016
-0.45	-0.55	1571.1 ± 5.8	83.4 ± 6.4	0.097 ± 0.001	0.067 ± 0.019
-0.45	-0.50	1577.3 ± 7.0	85.0 ± 6.2	0.083 ± 0.005	0.098 ± 0.027
-0.45	-0.45	1578.4 ± 6.8	84.4 ± 4.7	0.045 ± 0.026	0.041 ± 0.027
-0.45	-0.40	1574.2 ± 4.5	72.4 ± 0.4	0.010 ± 0.022	0.052 ± 0.018
-0.45	-0.35	1576.3 ± 3.7	70.5 ± 4.0	-0.017 ± 0.020	0.124 ± 0.002
-0.45	-0.30	1577.6 ± 3.8	76.4 ± 4.3	-0.009 ± 0.022	0.160 ± 0.017
-0.45	-0.25	1579.1 ± 4.8	79.1 ± 3.7	0.045 ± 0.018	0.159 ± 0.028
-0.45	-0.20	1576.7 ± 4.0	78.8 ± 2.4	0.035 ± 0.016	0.149 ± 0.026
-0.45	-0.15	1580.7 ± 3.4	69.6 ± 3.2	0.017 ± 0.021	0.167 ± 0.022
-0.45	-0.10	1573.6 ± 6.2	72.5 ± 4.1	0.047 ± 0.016	0.165 ± 0.022
-0.45	-0.05	1571.2 ± 5.1	64.1 ± 2.2	0.000 ± 0.020	0.169 ± 0.001
-0.45	0.00	1577.2 ± 6.3	65.4 ± 1.3	-0.002 ± 0.018	0.141 ± 0.006
-0.45	0.05	1580.2 ± 5.3	68.4 ± 0.9	-0.050 ± 0.023	0.178 ± 0.015
-0.45	0.10	1577.1 ± 4.0	70.1 ± 1.5	-0.036 ± 0.018	0.184 ± 0.009
-0.45	0.15	1582.0 ± 2.5	77.9 ± 1.9	-0.007 ± 0.020	0.178 ± 0.022
-0.45	0.20	1576.4 ± 2.6	79.4 ± 4.0	-0.004 ± 0.017	0.136 ± 0.021
-0.45	0.25	1577.1 ± 3.7	77.5 ± 3.9	0.005 ± 0.022	0.167 ± 0.024
-0.45	0.30	1574.1 ± 5.0	80.3 ± 3.0	-0.039 ± 0.018	0.170 ± 0.027
-0.45	0.35	1581.1 ± 3.9	76.0 ± 3.5	0.007 ± 0.018	0.135 ± 0.009
-0.45	0.40	1593.8 ± 1.1	86.0 ± 2.7	-0.032 ± 0.012	0.095 ± 0.007
-0.45	0.45	1583.8 ± 6.2	91.7 ± 2.0	0.024 ± 0.014	0.056 ± 0.009
-0.45	0.50	1579.1 ± 7.3	80.1 ± 0.4	0.056 ± 0.017	0.143 ± 0.014
-0.45	0.55	1590.2 ± 7.0	95.0 ± 6.9	-0.007 ± 0.007	0.088 ± 0.028
-0.45	0.60	1584.9 ± 6.7	85.8 ± 6.1	0.039 ± 0.016	0.096 ± 0.009
-0.45	0.65	1577.5 ± 7.1	88.2 ± 3.5	0.025 ± 0.016	0.071 ± 0.010
-0.45	0.70	1579.1 ± 6.8	91.2 ± 3.5	0.030 ± 0.010	0.051 ± 0.007
-0.45	0.75	1580.0 ± 6.1	96.2 ± 4.8	-0.012 ± 0.019	0.057 ± 0.008
-0.40	-0.75	1582.7 ± 4.4	82.5 ± 0.2	-0.030 ± 0.020	0.077 ± 0.019
-0.40	-0.70	1588.6 ± 6.9	79.6 ± 2.8	-0.026 ± 0.023	0.097 ± 0.023
-0.40	-0.65	1586.1 ± 5.4	80.0 ± 3.1	0.011 ± 0.011	0.079 ± 0.036
-0.40	-0.60	1583.7 ± 5.7	61.9 ± 4.0	0.044 ± 0.014	0.149 ± 0.015
-0.40	-0.55	1587.5 ± 4.9	76.8 ± 3.2	0.043 ± 0.028	0.118 ± 0.006
-0.40	-0.50	1585.1 ± 6.8	86.3 ± 3.7	0.039 ± 0.013	0.088 ± 0.006
-0.40	-0.45	1580.4 ± 5.5	85.5 ± 4.5	0.003 ± 0.022	0.078 ± 0.007
-0.40	-0.40	1581.2 ± 4.6	83.0 ± 11.0	-0.012 ± 0.025	0.136 ± 0.015
-0.40	-0.35	1575.9 ± 4.7	88.3 ± 5.1	0.006 ± 0.021	0.130 ± 0.006
-0.40	-0.30	1578.5 ± 5.1	82.2 ± 3.3	0.032 ± 0.017	0.152 ± 0.026
-0.40	-0.25	1569.5 ± 5.5	85.6 ± 1.9	0.010 ± 0.008	0.099 ± 0.009
-0.40	-0.20	1575.4 ± 5.6	82.6 ± 4.5	0.026 ± 0.014	0.110 ± 0.009
-0.40	-0.15	1579.1 ± 5.0	73.5 ± 4.3	0.011 ± 0.009	0.129 ± 0.018
-0.40	-0.10	1576.0 ± 4.8	73.1 ± 3.9	0.018 ± 0.023	0.145 ± 0.009
-0.40	-0.05	1580.8 ± 5.1	70.6 ± 3.1	0.030 ± 0.021	0.172 ± 0.002
-0.40	0.00	1583.1 ± 5.3	68.7 ± 3.6	0.037 ± 0.022	0.138 ± 0.001
-0.40	0.05	1582.8 ± 4.3	57.7 ± 2.8	-0.009 ± 0.016	0.111 ± 0.016
-0.40	0.10	1580.3 ± 5.0	76.3 ± 1.9	-0.006 ± 0.010	0.128 ± 0.007
-0.40	0.15	1576.2 ± 5.0	69.3 ± 4.0	0.010 ± 0.011	0.117 ± 0.010
-0.40	0.20	1580.2 ± 3.8	67.5 ± 4.1	0.011 ± 0.015	0.129 ± 0.007
-0.40	0.25	1578.6 ± 4.3	67.6 ± 2.0	-0.039 ± 0.027	0.179 ± 0.004
-0.40	0.30	1577.8 ± 4.9	72.5 ± 2.6	-0.052 ± 0.020	0.160 ± 0.014
-0.40	0.35	1575.3 ± 3.0	75.4 ± 2.2	-0.001 ± 0.023	0.147 ± 0.018
-0.40	0.40	1587.2 ± 3.8	74.5 ± 5.6	-0.022 ± 0.020	0.086 ± 0.024
-0.40	0.45	1582.2 ± 3.8	82.5 ± 4.1	0.004 ± 0.008	0.116 ± 0.015
-0.40	0.50	1579.3 ± 4.7	85.5 ± 3.5	-0.016 ± 0.012	0.171 ± 0.004
-0.40	0.55	1576.9 ± 7.2	87.5 ± 5.4	-0.008 ± 0.012	0.106 ± 0.008
-0.40	0.60	1575.8 ± 5.5	80.5 ± 3.5	0.001 ± 0.009	0.047 ± 0.016
-0.40	0.65	1583.0 ± 5.7	72.7 ± 1.7	-0.030 ± 0.014	0.074 ± 0.020
-0.40	0.70	1575.6 ± 3.8	77.2 ± 2.7	0.019 ± 0.005	0.099 ± 0.019
-0.40	0.75	1583.6 ± 7.9	87.2 ± 3.1	0.023 ± 0.010	0.066 ± 0.002

x (arcsec)	y (arcsec)	v (km/s)	$\sigma_\star$ (km/s)	$h3$	$h4$
-0.35	-0.75	1588.0 ± 7.4	83.0 ± 2.0	0.019 ± 0.014	0.118 ± 0.016
-0.35	-0.70	1602.1 ± 4.7	83.9 ± 3.4	-0.031 ± 0.032	0.139 ± 0.031
-0.35	-0.65	1593.5 ± 3.7	72.4 ± 0.3	-0.003 ± 0.012	0.149 ± 0.020
-0.35	-0.60	1588.6 ± 3.9	75.8 ± 4.0	0.038 ± 0.024	0.116 ± 0.007
-0.35	-0.55	1581.1 ± 3.9	89.7 ± 2.1	0.001 ± 0.011	0.094 ± 0.019
-0.35	-0.50	1576.6 ± 3.5	81.7 ± 2.4	-0.011 ± 0.017	0.095 ± 0.003
-0.35	-0.45	1578.7 ± 4.4	75.1 ± 9.2	0.009 ± 0.020	0.197 ± 0.019
-0.35	-0.40	1577.8 ± 4.9	79.3 ± 3.5	-0.006 ± 0.024	0.173 ± 0.009
-0.35	-0.35	1580.5 ± 6.5	79.6 ± 3.0	0.036 ± 0.016	0.183 ± 0.019
-0.35	-0.30	1574.0 ± 5.1	83.9 ± 2.8	0.025 ± 0.020	0.167 ± 0.021
-0.35	-0.25	1571.5 ± 5.6	78.7 ± 1.8	0.025 ± 0.014	0.174 ± 0.008
-0.35	-0.20	1575.7 ± 5.4	74.9 ± 3.7	0.052 ± 0.012	0.124 ± 0.004
-0.35	-0.15	1572.8 ± 4.1	80.4 ± 3.8	0.040 ± 0.006	0.127 ± 0.005
-0.35	-0.10	1573.8 ± 4.7	73.1 ± 3.1	0.043 ± 0.008	0.139 ± 0.007
-0.35	-0.05	1583.9 ± 5.5	82.7 ± 2.5	0.050 ± 0.012	0.142 ± 0.009
-0.35	0.00	1589.2 ± 4.7	73.2 ± 5.7	0.057 ± 0.011	0.127 ± 0.008
-0.35	0.05	1583.5 ± 4.5	63.5 ± 5.6	0.047 ± 0.017	0.089 ± 0.015
-0.35	0.10	1577.6 ± 4.1	66.5 ± 2.6	0.040 ± 0.016	0.081 ± 0.008
-0.35	0.15	1578.5 ± 5.6	66.3 ± 2.2	0.007 ± 0.010	0.118 ± 0.007
-0.35	0.20	1581.6 ± 5.2	79.4 ± 2.1	-0.002 ± 0.014	0.166 ± 0.019
-0.35	0.25	1574.4 ± 6.6	70.0 ± 2.1	-0.043 ± 0.018	0.165 ± 0.011
-0.35	0.30	1573.5 ± 6.6	77.2 ± 2.0	-0.017 ± 0.014	0.135 ± 0.004
-0.35	0.35	1574.2 ± 4.7	73.5 ± 2.3	0.068 ± 0.010	0.152 ± 0.004
-0.35	0.40	1574.6 ± 4.1	83.4 ± 3.7	-0.019 ± 0.011	0.121 ± 0.013
-0.35	0.45	1573.8 ± 4.1	81.3 ± 2.7	-0.026 ± 0.009	0.117 ± 0.014
-0.35	0.50	1577.2 ± 6.0	84.1 ± 1.7	-0.007 ± 0.013	0.089 ± 0.014
-0.35	0.55	1573.9 ± 5.5	87.8 ± 1.1	-0.058 ± 0.018	0.038 ± 0.025
-0.35	0.60	1570.6 ± 4.8	88.2 ± 3.5	-0.011 ± 0.008	0.036 ± 0.011
-0.35	0.65	1576.7 ± 4.3	77.4 ± 2.4	-0.018 ± 0.015	0.058 ± 0.023
-0.35	0.70	1580.3 ± 5.3	80.0 ± 6.8	-0.004 ± 0.024	0.131 ± 0.013
-0.35	0.75	1584.1 ± 6.4	86.0 ± 2.5	0.008 ± 0.010	0.135 ± 0.005
-0.30	-0.75	1581.2 ± 4.9	77.5 ± 2.8	-0.060 ± 0.021	0.083 ± 0.011
-0.30	-0.70	1592.5 ± 4.4	78.1 ± 1.5	-0.059 ± 0.012	0.118 ± 0.010
-0.30	-0.65	1594.0 ± 5.2	73.3 ± 2.7	-0.002 ± 0.015	0.158 ± 0.009
-0.30	-0.60	1590.9 ± 5.5	75.2 ± 1.9	0.012 ± 0.013	0.128 ± 0.010
-0.30	-0.55	1581.3 ± 5.3	74.0 ± 0.3	0.017 ± 0.015	0.155 ± 0.016
-0.30	-0.50	1579.0 ± 5.1	70.1 ± 4.2	-0.023 ± 0.029	0.179 ± 0.008
-0.30	-0.45	1579.0 ± 7.2	97.3 ± 5.9	-0.014 ± 0.011	0.127 ± 0.006
-0.30	-0.40	1579.6 ± 6.4	76.9 ± 5.0	0.020 ± 0.013	0.158 ± 0.006
-0.30	-0.35	1579.6 ± 4.4	74.0 ± 3.7	-0.004 ± 0.014	0.140 ± 0.007
-0.30	-0.30	1577.9 ± 4.7	77.5 ± 5.1	0.035 ± 0.006	0.137 ± 0.008
-0.30	-0.25	1580.2 ± 4.9	72.1 ± 2.0	0.050 ± 0.010	0.118 ± 0.008
-0.30	-0.20	1578.9 ± 5.7	71.7 ± 2.2	0.064 ± 0.010	0.150 ± 0.005
-0.30	-0.15	1579.9 ± 4.7	70.0 ± 2.1	0.093 ± 0.011	0.135 ± 0.005
-0.30	-0.10	1577.7 ± 5.5	76.9 ± 2.6	0.094 ± 0.011	0.137 ± 0.005
-0.30	-0.05	1582.3 ± 5.6	71.1 ± 2.4	0.050 ± 0.015	0.140 ± 0.005
-0.30	0.00	1581.5 ± 4.7	65.5 ± 4.0	0.036 ± 0.022	0.125 ± 0.026
-0.30	0.05	1581.0 ± 4.8	57.2 ± 8.4	0.020 ± 0.030	0.119 ± 0.020
-0.30	0.10	1578.6 ± 4.1	63.3 ± 5.3	-0.022 ± 0.018	0.142 ± 0.021
-0.30	0.15	1577.9 ± 5.6	69.7 ± 4.2	0.001 ± 0.020	0.174 ± 0.011
-0.30	0.20	1584.7 ± 5.7	73.0 ± 4.2	-0.018 ± 0.022	0.175 ± 0.021
-0.30	0.25	1583.5 ± 6.7	72.6 ± 2.6	0.003 ± 0.010	0.159 ± 0.001
-0.30	0.30	1579.6 ± 7.4	81.5 ± 1.2	0.040 ± 0.014	0.133 ± 0.012
-0.30	0.35	1582.6 ± 5.4	80.8 ± 2.9	0.046 ± 0.016	0.142 ± 0.010
-0.30	0.40	1579.0 ± 5.2	79.9 ± 1.8	0.028 ± 0.007	0.150 ± 0.003
-0.30	0.45	1576.2 ± 4.2	89.8 ± 2.7	-0.031 ± 0.011	0.114 ± 0.008
-0.30	0.50	1577.9 ± 6.5	84.3 ± 3.6	0.005 ± 0.007	0.089 ± 0.018
-0.30	0.55	1574.3 ± 6.4	76.4 ± 2.3	0.020 ± 0.012	0.114 ± 0.004
-0.30	0.60	1582.8 ± 6.3	72.4 ± 5.8	0.053 ± 0.007	0.075 ± 0.012
-0.30	0.65	1574.0 ± 7.0	85.3 ± 3.8	0.073 ± 0.017	0.083 ± 0.019
-0.30	0.70	1574.4 ± 7.9	95.1 ± 0.3	0.076 ± 0.009	0.063 ± 0.007
-0.30	0.75	1579.3 ± 5.9	80.9 ± 1.9	0.075 ± 0.008	0.149 ± 0.006

x (arcsec)	y (arcsec)	v (km/s)	$\sigma_\star$ (km/s)	$h3$	$h4$
-0.25	-0.75	1579.2 ± 4.5	94.0 ± 3.7	-0.018 ± 0.019	0.069 ± 0.013
-0.25	-0.70	1594.1 ± 4.1	84.1 ± 1.9	-0.020 ± 0.025	0.083 ± 0.020
-0.25	-0.65	1596.5 ± 5.9	87.1 ± 3.5	0.018 ± 0.012	0.083 ± 0.011
-0.25	-0.60	1590.5 ± 5.5	85.4 ± 2.4	0.028 ± 0.010	0.125 ± 0.018
-0.25	-0.55	1582.8 ± 6.1	93.9 ± 2.8	-0.004 ± 0.003	0.073 ± 0.013
-0.25	-0.50	1583.3 ± 4.4	72.0 ± 9.1	-0.031 ± 0.027	0.177 ± 0.059
-0.25	-0.45	1583.6 ± 4.3	70.4 ± 3.6	-0.011 ± 0.025	0.152 ± 0.003
-0.25	-0.40	1581.7 ± 6.9	71.0 ± 2.2	0.016 ± 0.002	0.126 ± 0.007
-0.25	-0.35	1583.3 ± 6.8	75.5 ± 2.5	0.009 ± 0.010	0.074 ± 0.007
-0.25	-0.30	1585.8 ± 7.1	78.6 ± 3.0	0.024 ± 0.011	0.116 ± 0.007
-0.25	-0.25	1587.0 ± 5.4	64.7 ± 1.8	0.029 ± 0.014	0.126 ± 0.006
-0.25	-0.20	1582.3 ± 3.7	64.5 ± 2.7	0.025 ± 0.019	0.154 ± 0.005
-0.25	-0.15	1582.2 ± 5.4	63.9 ± 4.0	0.080 ± 0.017	0.136 ± 0.002
-0.25	-0.10	1586.1 ± 5.6	65.2 ± 3.8	0.074 ± 0.017	0.108 ± 0.003
-0.25	-0.05	1588.5 ± 4.6	57.1 ± 4.3	0.063 ± 0.009	0.119 ± 0.004
-0.25	0.00	1582.5 ± 3.4	51.5 ± 2.2	0.004 ± 0.020	0.058 ± 0.003
-0.25	0.05	1580.8 ± 3.3	53.6 ± 3.9	-0.029 ± 0.025	0.071 ± 0.009
-0.25	0.10	1577.6 ± 3.2	55.0 ± 4.8	-0.031 ± 0.021	0.114 ± 0.018
-0.25	0.15	1582.6 ± 4.4	66.5 ± 2.8	-0.033 ± 0.016	0.166 ± 0.020
-0.25	0.20	1581.6 ± 5.7	72.6 ± 4.4	0.002 ± 0.017	0.194 ± 0.013
-0.25	0.25	1581.3 ± 5.3	78.1 ± 2.7	0.056 ± 0.012	0.163 ± 0.013
-0.25	0.30	1576.3 ± 5.3	64.0 ± 4.6	0.035 ± 0.014	0.146 ± 0.003
-0.25	0.35	1579.3 ± 4.9	67.2 ± 2.4	0.017 ± 0.013	0.133 ± 0.006
-0.25	0.40	1576.5 ± 5.8	74.4 ± 5.0	0.032 ± 0.001	0.169 ± 0.005
-0.25	0.45	1583.0 ± 5.7	86.0 ± 5.3	0.096 ± 0.013	0.152 ± 0.005
-0.25	0.50	1583.9 ± 6.8	99.8 ± 1.7	-0.021 ± 0.010	0.059 ± 0.012
-0.25	0.55	1583.8 ± 7.8	94.0 ± 4.9	-0.016 ± 0.014	0.104 ± 0.005
-0.25	0.60	1585.5 ± 7.5	88.9 ± 4.5	0.021 ± 0.011	0.131 ± 0.005
-0.25	0.65	1582.3 ± 6.6	72.4 ± 3.9	0.036 ± 0.006	0.147 ± 0.005
-0.25	0.70	1582.8 ± 5.8	82.7 ± 2.1	0.010 ± 0.001	0.093 ± 0.002
-0.25	0.75	1584.3 ± 6.1	96.3 ± 0.6	0.021 ± 0.006	0.039 ± 0.018
-0.20	-0.75	1585.7 ± 7.5	89.1 ± 2.1	-0.014 ± 0.015	0.089 ± 0.013
-0.20	-0.70	1583.3 ± 6.9	100.1 ± 3.4	-0.019 ± 0.008	0.031 ± 0.012
-0.20	-0.65	1584.9 ± 6.1	89.3 ± 2.1	0.000 ± 0.009	0.060 ± 0.014
-0.20	-0.60	1585.1 ± 7.1	86.0 ± 1.3	0.022 ± 0.007	0.044 ± 0.011
-0.20	-0.55	1580.1 ± 6.3	87.0 ± 3.0	0.003 ± 0.008	0.100 ± 0.018
-0.20	-0.50	1579.4 ± 5.0	79.2 ± 7.2	-0.019 ± 0.017	0.133 ± 0.012
-0.20	-0.45	1581.6 ± 5.3	68.3 ± 4.5	-0.039 ± 0.023	0.160 ± 0.012
-0.20	-0.40	1584.3 ± 6.8	76.0 ± 3.1	0.029 ± 0.013	0.128 ± 0.014
-0.20	-0.35	1592.5 ± 8.6	89.7 ± 2.5	0.024 ± 0.013	0.152 ± 0.018
-0.20	-0.30	1592.9 ± 7.6	77.0 ± 4.0	0.043 ± 0.013	0.148 ± 0.016
-0.20	-0.25	1591.6 ± 6.2	68.1 ± 2.4	0.031 ± 0.011	0.160 ± 0.021
-0.20	-0.20	1585.6 ± 5.9	62.4 ± 0.8	0.039 ± 0.009	0.124 ± 0.006
-0.20	-0.15	1587.2 ± 5.4	60.1 ± 1.8	0.085 ± 0.007	0.116 ± 0.006
-0.20	-0.10	1587.8 ± 4.7	60.2 ± 3.4	0.070 ± 0.001	0.112 ± 0.004
-0.20	-0.05	1599.2 ± 4.0	62.8 ± 5.2	0.069 ± 0.017	0.085 ± 0.006
-0.20	0.00	1600.1 ± 4.2	59.6 ± 4.1	0.027 ± 0.009	0.045 ± 0.008
-0.20	0.05	1583.9 ± 5.6	61.7 ± 3.2	0.054 ± 0.012	0.024 ± 0.016
-0.20	0.10	1585.8 ± 6.0	64.9 ± 3.2	0.033 ± 0.002	0.128 ± 0.017
-0.20	0.15	1585.9 ± 3.8	73.3 ± 0.7	0.051 ± 0.014	0.126 ± 0.010
-0.20	0.20	1589.0 ± 3.1	71.4 ± 3.8	0.013 ± 0.017	0.162 ± 0.041
-0.20	0.25	1579.8 ± 4.1	77.5 ± 2.4	-0.008 ± 0.004	0.181 ± 0.023
-0.20	0.30	1578.9 ± 3.6	69.1 ± 2.1	-0.008 ± 0.011	0.145 ± 0.009
-0.20	0.35	1580.6 ± 5.4	67.5 ± 1.9	-0.020 ± 0.009	0.133 ± 0.004
-0.20	0.40	1574.2 ± 5.9	77.5 ± 3.0	-0.024 ± 0.018	0.149 ± 0.007
-0.20	0.45	1580.3 ± 5.2	82.1 ± 4.1	0.004 ± 0.017	0.145 ± 0.006
-0.20	0.50	1576.0 ± 5.7	95.2 ± 3.3	0.021 ± 0.010	0.158 ± 0.007
-0.20	0.55	1573.4 ± 5.2	88.6 ± 6.3	-0.003 ± 0.017	0.082 ± 0.013
-0.20	0.60	1578.0 ± 4.9	70.7 ± 1.6	0.015 ± 0.016	0.087 ± 0.008
-0.20	0.65	1581.1 ± 6.7	84.6 ± 2.4	0.000 ± 0.015	0.097 ± 0.005
-0.20	0.70	1569.8 ± 6.1	93.3 ± 2.8	0.001 ± 0.009	0.086 ± 0.007
-0.20	0.75	1577.3 ± 4.9	101.0 ± 6.3	0.091 ± 0.022	0.102 ± 0.004

x (arcsec)	y (arcsec)	v (km/s)	$\sigma_\star$ (km/s)	$h3$	$h4$
-0.15	-0.75	1572.2 ± 4.5	100.7 ± 4.1	0.007 ± 0.001	0.036 ± 0.002
-0.15	-0.70	1583.3 ± 6.6	76.3 ± 4.1	-0.017 ± 0.004	0.102 ± 0.012
-0.15	-0.65	1585.6 ± 6.2	81.0 ± 2.1	-0.031 ± 0.004	0.107 ± 0.018
-0.15	-0.60	1587.9 ± 5.4	87.4 ± 3.8	0.011 ± 0.016	0.101 ± 0.012
-0.15	-0.55	1587.8 ± 5.6	87.0 ± 5.4	0.004 ± 0.014	0.136 ± 0.008
-0.15	-0.50	1580.5 ± 6.0	74.8 ± 4.4	-0.033 ± 0.024	0.110 ± 0.015
-0.15	-0.45	1575.8 ± 5.8	73.2 ± 1.9	-0.013 ± 0.001	0.114 ± 0.006
-0.15	-0.40	1589.0 ± 5.8	74.6 ± 2.7	0.005 ± 0.011	0.130 ± 0.004
-0.15	-0.35	1595.0 ± 5.4	76.3 ± 2.5	0.028 ± 0.019	0.143 ± 0.008
-0.15	-0.30	1599.7 ± 5.0	78.6 ± 2.7	0.041 ± 0.016	0.139 ± 0.025
-0.15	-0.25	1601.2 ± 5.7	70.2 ± 2.8	0.094 ± 0.015	0.086 ± 0.024
-0.15	-0.20	1597.5 ± 5.1	66.3 ± 3.7	0.077 ± 0.012	0.041 ± 0.012
-0.15	-0.15	1592.2 ± 6.6	66.6 ± 4.5	0.032 ± 0.007	0.042 ± 0.018
-0.15	-0.10	1591.1 ± 3.7	71.6 ± 2.6	0.023 ± 0.018	0.029 ± 0.008
-0.15	-0.05	1591.4 ± 4.4	28.6 ± 37.7	0.003 ± 0.045	-0.008 ± 0.051
-0.15	0.00	1612.7 ± 15.9	125.7 ± 40.9	0.047 ± 0.012	0.063 ± 0.037
-0.15	0.05	1587.1 ± 7.5	28.6 ± 29.8	-0.006 ± 0.001	0.003 ± 0.040
-0.15	0.10	1579.7 ± 4.8	56.5 ± 5.8	-0.003 ± 0.013	0.064 ± 0.017
-0.15	0.15	1578.7 ± 4.1	82.0 ± 4.4	0.006 ± 0.003	0.111 ± 0.018
-0.15	0.20	1582.5 ± 3.3	77.2 ± 2.1	0.009 ± 0.010	0.179 ± 0.007
-0.15	0.25	1572.6 ± 4.9	74.5 ± 1.7	0.004 ± 0.012	0.155 ± 0.018
-0.15	0.30	1580.5 ± 4.3	73.5 ± 2.1	-0.020 ± 0.016	0.171 ± 0.007
-0.15	0.35	1578.0 ± 4.0	83.8 ± 1.3	-0.060 ± 0.021	0.148 ± 0.008
-0.15	0.40	1581.5 ± 4.5	70.6 ± 3.3	-0.069 ± 0.030	0.110 ± 0.016
-0.15	0.45	1588.1 ± 4.4	75.0 ± 2.2	-0.105 ± 0.022	0.118 ± 0.028
-0.15	0.50	1584.0 ± 4.0	92.2 ± 2.4	-0.115 ± 0.017	0.134 ± 0.032
-0.15	0.55	1582.7 ± 3.7	102.1 ± 5.6	-0.031 ± 0.015	0.128 ± 0.028
-0.15	0.60	1586.4 ± 4.8	96.7 ± 6.7	0.013 ± 0.010	0.113 ± 0.013
-0.15	0.65	1568.4 ± 7.7	100.3 ± 3.1	0.030 ± 0.005	0.077 ± 0.014
-0.15	0.70	1566.1 ± 8.7	101.1 ± 2.9	-0.027 ± 0.010	0.026 ± 0.007
-0.15	0.75	1572.3 ± 5.3	101.4 ± 2.0	-0.029 ± 0.003	0.017 ± 0.009
-0.10	-0.75	1588.5 ± 4.1	73.2 ± 1.4	-0.059 ± 0.020	0.081 ± 0.009
-0.10	-0.70	1592.5 ± 5.2	76.7 ± 3.1	-0.022 ± 0.014	0.122 ± 0.006
-0.10	-0.65	1593.7 ± 7.8	82.3 ± 8.1	0.038 ± 0.013	0.104 ± 0.008
-0.10	-0.60	1588.3 ± 5.3	78.2 ± 5.0	0.004 ± 0.016	0.109 ± 0.019
-0.10	-0.55	1584.9 ± 4.1	81.8 ± 5.9	-0.011 ± 0.017	0.120 ± 0.005
-0.10	-0.50	1581.3 ± 3.3	84.1 ± 2.8	-0.054 ± 0.021	0.124 ± 0.011
-0.10	-0.45	1588.5 ± 4.8	76.3 ± 1.6	-0.016 ± 0.024	0.123 ± 0.008
-0.10	-0.40	1592.2 ± 5.1	83.6 ± 1.6	-0.037 ± 0.016	0.136 ± 0.017
-0.10	-0.35	1593.2 ± 6.2	80.8 ± 2.5	-0.042 ± 0.021	0.139 ± 0.013
-0.10	-0.30	1596.6 ± 6.0	78.4 ± 2.5	0.068 ± 0.018	0.166 ± 0.028
-0.10	-0.25	1598.6 ± 4.6	73.6 ± 3.6	0.046 ± 0.008	0.090 ± 0.008
-0.10	-0.20	1601.5 ± 7.0	71.8 ± 1.8	0.024 ± 0.011	0.066 ± 0.007
-0.10	-0.15	1607.8 ± 6.7	52.8 ± 4.0	-0.002 ± 0.008	0.023 ± 0.016
-0.10	-0.10	1601.6 ± 6.6	48.5 ± 13.3	-0.030 ± 0.011	0.020 ± 0.005
-0.10	-0.05	1608.0 ± 6.9	13.2 ± 10.3	-0.008 ± 0.009	-0.009 ± 0.002
-0.10	0.00	1593.3 ± 6.8	15.2 ± 7.5	0.002 ± 0.009	-0.004 ± 0.005
-0.10	0.05	1583.2 ± 1.5	9.4 ± 11.1	0.000 ± 0.013	-0.002 ± 0.006
-0.10	0.10	1586.3 ± 5.1	13.5 ± 10.3	0.006 ± 0.007	-0.004 ± 0.006
-0.10	0.15	1569.6 ± 2.2	57.7 ± 13.2	-0.046 ± 0.013	0.039 ± 0.017
-0.10	0.20	1592.1 ± 4.1	76.1 ± 2.3	0.047 ± 0.024	0.159 ± 0.002
-0.10	0.25	1577.8 ± 5.0	74.8 ± 3.2	0.011 ± 0.010	0.149 ± 0.016
-0.10	0.30	1584.3 ± 3.7	69.7 ± 1.6	-0.012 ± 0.010	0.173 ± 0.021
-0.10	0.35	1582.9 ± 4.5	65.0 ± 2.4	-0.006 ± 0.017	0.156 ± 0.008
-0.10	0.40	1584.1 ± 3.9	70.2 ± 2.7	-0.015 ± 0.019	0.183 ± 0.009
-0.10	0.45	1581.4 ± 3.3	72.0 ± 1.4	-0.087 ± 0.027	0.157 ± 0.009
-0.10	0.50	1581.3 ± 3.3	82.3 ± 4.0	-0.041 ± 0.020	0.162 ± 0.008
-0.10	0.55	1582.7 ± 6.6	88.1 ± 5.4	0.030 ± 0.010	0.151 ± 0.007
-0.10	0.60	1582.6 ± 8.9	95.7 ± 7.7	0.029 ± 0.014	0.131 ± 0.006
-0.10	0.65	1575.2 ± 6.5	105.8 ± 3.2	0.007 ± 0.013	0.075 ± 0.001
-0.10	0.70	1574.1 ± 7.3	101.4 ± 4.0	0.047 ± 0.018	0.058 ± 0.009
-0.10	0.75	1586.4 ± 5.8	80.9 ± 5.3	0.002 ± 0.013	0.065 ± 0.003

x (arcsec)	y (arcsec)	v (km/s)	$\sigma_\star$ (km/s)	$h3$	$h4$
-0.05	-0.75	1596.1 ± 4.5	70.6 ± 2.7	-0.047 ± 0.009	0.092 ± 0.020
-0.05	-0.70	1595.4 ± 5.5	84.9 ± 4.1	0.001 ± 0.014	0.142 ± 0.005
-0.05	-0.65	1588.8 ± 6.5	91.6 ± 5.4	-0.008 ± 0.014	0.132 ± 0.016
-0.05	-0.60	1581.5 ± 7.4	82.6 ± 3.8	-0.020 ± 0.014	0.089 ± 0.013
-0.05	-0.55	1580.4 ± 5.3	85.0 ± 4.9	-0.057 ± 0.016	0.084 ± 0.018
-0.05	-0.50	1584.5 ± 4.5	84.4 ± 3.5	-0.033 ± 0.012	0.083 ± 0.019
-0.05	-0.45	1588.4 ± 5.6	85.4 ± 3.3	0.021 ± 0.011	0.116 ± 0.021
-0.05	-0.40	1590.5 ± 5.9	79.3 ± 3.6	-0.026 ± 0.017	0.111 ± 0.011
-0.05	-0.35	1589.5 ± 6.9	78.6 ± 4.2	-0.050 ± 0.014	0.138 ± 0.012
-0.05	-0.30	1602.3 ± 7.7	86.3 ± 2.1	0.062 ± 0.019	0.079 ± 0.021
-0.05	-0.25	1596.3 ± 6.3	72.7 ± 1.4	0.027 ± 0.016	0.087 ± 0.001
-0.05	-0.20	1597.5 ± 7.5	83.8 ± 3.5	-0.021 ± 0.008	0.099 ± 0.018
-0.05	-0.15	1602.7 ± 10.1	89.5 ± 12.6	-0.059 ± 0.015	0.071 ± 0.012
-0.05	-0.10	1543.6 ± 27.5	164.4 ± 16.6	-0.017 ± 0.012	0.005 ± 0.008
-0.05	-0.05	1631.2 ± 23.5	279.1 ± 22.8	-0.014 ± 0.017	-0.012 ± 0.000
-0.05	0.00	1555.4 ± 1.2	348.6 ± 25.9	0.034 ± 0.009	-0.014 ± 0.004
-0.05	0.05	1608.7 ± 15.5	108.5 ± 16.6	0.008 ± 0.001	0.028 ± 0.006
-0.05	0.10	1567.1 ± 19.4	145.6 ± 2.4	-0.003 ± 0.010	0.009 ± 0.004
-0.05	0.15	1589.3 ± 7.8	156.7 ± 16.0	-0.020 ± 0.003	0.030 ± 0.005
-0.05	0.20	1599.1 ± 3.5	74.7 ± 3.3	0.073 ± 0.006	0.152 ± 0.018
-0.05	0.25	1582.8 ± 4.6	74.4 ± 3.4	0.007 ± 0.010	0.122 ± 0.015
-0.05	0.30	1590.2 ± 3.8	77.7 ± 0.6	-0.021 ± 0.023	0.171 ± 0.016
-0.05	0.35	1588.9 ± 4.5	94.0 ± 8.0	0.001 ± 0.005	0.120 ± 0.008
-0.05	0.40	1582.4 ± 2.3	78.7 ± 5.6	-0.027 ± 0.027	0.167 ± 0.021
-0.05	0.45	1571.7 ± 4.1	85.1 ± 4.8	-0.012 ± 0.017	0.150 ± 0.022
-0.05	0.50	1571.5 ± 6.1	84.3 ± 9.7	0.008 ± 0.010	0.140 ± 0.021
-0.05	0.55	1581.7 ± 7.0	78.0 ± 3.1	0.017 ± 0.014	0.187 ± 0.008
-0.05	0.60	1584.7 ± 6.9	79.8 ± 2.3	0.033 ± 0.021	0.195 ± 0.007
-0.05	0.65	1576.9 ± 4.9	82.1 ± 6.5	-0.044 ± 0.018	0.137 ± 0.002
-0.05	0.70	1584.0 ± 4.1	93.0 ± 6.4	-0.006 ± 0.025	0.074 ± 0.013
-0.05	0.75	1587.0 ± 3.8	85.3 ± 2.5	0.001 ± 0.024	0.112 ± 0.013
0.00	-0.75	1600.2 ± 5.3	69.8 ± 1.6	-0.023 ± 0.016	0.182 ± 0.019
0.00	-0.70	1601.5 ± 4.6	76.0 ± 1.5	-0.014 ± 0.016	0.141 ± 0.002
0.00	-0.65	1592.8 ± 4.4	82.2 ± 2.1	-0.064 ± 0.022	0.096 ± 0.018
0.00	-0.60	1580.5 ± 6.6	81.3 ± 2.9	-0.033 ± 0.005	0.091 ± 0.009
0.00	-0.55	1582.7 ± 6.7	85.8 ± 4.3	-0.058 ± 0.009	0.109 ± 0.009
0.00	-0.50	1589.9 ± 4.1	85.8 ± 3.1	-0.035 ± 0.017	0.095 ± 0.016
0.00	-0.45	1584.4 ± 4.1	82.3 ± 2.4	0.035 ± 0.015	0.070 ± 0.001
0.00	-0.40	1588.7 ± 4.9	78.8 ± 2.7	0.024 ± 0.018	0.103 ± 0.011
0.00	-0.35	1595.6 ± 5.6	90.9 ± 1.9	0.001 ± 0.001	0.175 ± 0.028
0.00	-0.30	1597.3 ± 6.7	83.8 ± 2.9	-0.013 ± 0.012	0.108 ± 0.018
0.00	-0.25	1590.8 ± 7.5	85.7 ± 3.5	-0.027 ± 0.014	0.096 ± 0.014
0.00	-0.20	1593.0 ± 7.8	83.0 ± 4.1	-0.068 ± 0.015	0.086 ± 0.013
0.00	-0.15	1598.2 ± 9.9	104.9 ± 12.9	-0.002 ± 0.022	0.110 ± 0.003
0.00	-0.10	1606.2 ± 5.9	235.8 ± 7.9	-0.003 ± 0.004	0.015 ± 0.004
0.00	-0.05	1652.1 ± 10.9	249.7 ± 18.7	-0.039 ± 0.006	-0.008 ± 0.003
0.00	0.00	1690.8 ± 11.7	102.5 ± 15.8	0.018 ± 0.005	-0.005 ± 0.005
0.00	0.05	1649.1 ± 13.0	176.4 ± 13.6	-0.048 ± 0.012	0.015 ± 0.005
0.00	0.10	1555.7 ± 18.3	278.2 ± 92.1	0.015 ± 0.027	0.004 ± 0.022
0.00	0.15	1616.1 ± 7.6	222.8 ± 4.1	-0.002 ± 0.011	-0.016 ± 0.002
0.00	0.20	1633.9 ± 0.2	105.8 ± 7.6	0.036 ± 0.032	0.021 ± 0.007
0.00	0.25	1598.5 ± 4.5	103.7 ± 4.5	0.033 ± 0.003	0.091 ± 0.016
0.00	0.30	1609.1 ± 4.0	103.3 ± 6.7	-0.021 ± 0.023	0.042 ± 0.004
0.00	0.35	1593.3 ± 5.7	81.9 ± 4.4	0.028 ± 0.006	0.100 ± 0.016
0.00	0.40	1589.9 ± 5.8	83.0 ± 4.6	0.014 ± 0.008	0.109 ± 0.007
0.00	0.45	1580.2 ± 6.2	87.2 ± 5.8	-0.015 ± 0.008	0.116 ± 0.009
0.00	0.50	1578.4 ± 5.5	85.0 ± 5.2	-0.037 ± 0.007	0.099 ± 0.011
0.00	0.55	1580.8 ± 7.5	88.2 ± 3.7	-0.046 ± 0.011	0.073 ± 0.013
0.00	0.60	1584.9 ± 5.4	84.3 ± 0.1	-0.070 ± 0.013	0.082 ± 0.009
0.00	0.65	1583.6 ± 4.9	72.3 ± 2.6	-0.070 ± 0.012	0.099 ± 0.001
0.00	0.70	1582.6 ± 5.9	88.0 ± 2.9	-0.023 ± 0.016	0.100 ± 0.005
0.00	0.75	1577.8 ± 4.1	112.0 ± 4.0	-0.007 ± 0.011	0.004 ± 0.010

x (arcsec)	y (arcsec)	v (km/s)	$\sigma_\star$ (km/s)	$h3$	$h4$
0.05	-0.75	1591.1 ± 3.6	81.1 ± 4.3	-0.039 ± 0.013	0.057 ± 0.021
0.05	-0.70	1596.0 ± 6.7	75.9 ± 1.3	-0.055 ± 0.012	0.095 ± 0.018
0.05	-0.65	1589.1 ± 7.7	75.2 ± 7.4	-0.017 ± 0.004	0.095 ± 0.005
0.05	-0.60	1587.6 ± 6.3	78.2 ± 4.5	-0.047 ± 0.005	0.118 ± 0.008
0.05	-0.55	1585.1 ± 7.4	84.9 ± 3.9	-0.050 ± 0.013	0.125 ± 0.016
0.05	-0.50	1589.0 ± 6.3	97.8 ± 4.1	-0.049 ± 0.016	0.100 ± 0.008
0.05	-0.45	1589.7 ± 6.2	86.6 ± 1.8	0.004 ± 0.013	0.152 ± 0.021
0.05	-0.40	1589.8 ± 4.9	76.9 ± 2.4	0.005 ± 0.018	0.118 ± 0.018
0.05	-0.35	1587.3 ± 6.4	75.6 ± 4.3	0.018 ± 0.012	0.116 ± 0.017
0.05	-0.30	1585.3 ± 5.6	93.9 ± 3.5	0.007 ± 0.019	0.175 ± 0.024
0.05	-0.25	1588.5 ± 5.8	77.6 ± 2.3	-0.009 ± 0.016	0.117 ± 0.019
0.05	-0.20	1591.4 ± 6.8	76.7 ± 4.8	-0.032 ± 0.015	0.121 ± 0.019
0.05	-0.15	1586.4 ± 6.6	76.6 ± 5.5	-0.092 ± 0.014	0.088 ± 0.029
0.05	-0.10	1613.2 ± 6.3	37.4 ± 5.9	-0.025 ± 0.007	-0.007 ± 0.004
0.05	-0.05	1609.0 ± 1.7	109.9 ± 14.4	-0.009 ± 0.016	0.047 ± 0.006
0.05	0.00	1638.2 ± 8.3	30.3 ± 1.8	-0.018 ± 0.016	-0.015 ± 0.027
0.05	0.05	1629.6 ± 0.1	50.3 ± 3.6	-0.006 ± 0.001	-0.016 ± 0.002
0.05	0.10	1638.4 ± 1.2	89.9 ± 20.4	0.010 ± 0.012	0.014 ± 0.014
0.05	0.15	1635.5 ± 4.3	121.7 ± 18.5	-0.017 ± 0.021	0.034 ± 0.008
0.05	0.20	1608.2 ± 7.9	79.8 ± 12.7	0.116 ± 0.019	0.111 ± 0.032
0.05	0.25	1599.1 ± 8.4	86.7 ± 7.6	0.060 ± 0.016	0.112 ± 0.009
0.05	0.30	1595.2 ± 7.3	74.6 ± 10.0	0.090 ± 0.001	0.163 ± 0.029
0.05	0.35	1592.2 ± 7.3	81.7 ± 5.1	0.026 ± 0.004	0.148 ± 0.016
0.05	0.40	1590.1 ± 6.7	85.5 ± 5.1	0.048 ± 0.012	0.137 ± 0.009
0.05	0.45	1585.7 ± 6.9	94.1 ± 4.4	0.023 ± 0.006	0.077 ± 0.004
0.05	0.50	1583.7 ± 5.4	86.3 ± 2.8	-0.051 ± 0.013	0.086 ± 0.017
0.05	0.55	1583.7 ± 5.5	86.5 ± 3.4	-0.032 ± 0.003	0.046 ± 0.025
0.05	0.60	1588.4 ± 4.1	92.3 ± 4.8	-0.055 ± 0.015	0.075 ± 0.012
0.05	0.65	1576.1 ± 5.6	83.3 ± 3.1	-0.043 ± 0.009	0.117 ± 0.026
0.05	0.70	1573.1 ± 5.9	97.6 ± 3.8	0.014 ± 0.015	0.098 ± 0.022
0.05	0.75	1578.3 ± 5.8	98.4 ± 2.5	0.014 ± 0.015	0.065 ± 0.017
0.10	-0.75	1591.1 ± 6.3	83.6 ± 3.0	-0.031 ± 0.010	0.112 ± 0.001
0.10	-0.70	1583.3 ± 6.1	91.7 ± 7.3	-0.009 ± 0.009	0.080 ± 0.013
0.10	-0.65	1584.8 ± 7.3	84.9 ± 3.9	-0.063 ± 0.012	0.140 ± 0.013
0.10	-0.60	1589.9 ± 6.9	84.8 ± 3.6	-0.049 ± 0.012	0.133 ± 0.024
0.10	-0.55	1591.2 ± 3.9	78.1 ± 3.5	-0.052 ± 0.018	0.131 ± 0.019
0.10	-0.50	1593.0 ± 3.8	97.9 ± 3.2	-0.015 ± 0.019	0.153 ± 0.019
0.10	-0.45	1593.3 ± 4.9	83.8 ± 1.3	0.024 ± 0.018	0.131 ± 0.011
0.10	-0.40	1591.1 ± 5.7	84.7 ± 2.3	0.018 ± 0.015	0.103 ± 0.001
0.10	-0.35	1590.7 ± 6.5	73.5 ± 3.3	-0.027 ± 0.008	0.147 ± 0.009
0.10	-0.30	1592.3 ± 4.6	79.1 ± 2.7	-0.043 ± 0.017	0.140 ± 0.003
0.10	-0.25	1592.8 ± 5.3	82.1 ± 2.0	-0.046 ± 0.018	0.173 ± 0.021
0.10	-0.20	1586.0 ± 5.2	78.6 ± 2.2	-0.042 ± 0.016	0.155 ± 0.023
0.10	-0.15	1594.1 ± 4.6	69.8 ± 5.2	-0.023 ± 0.015	0.146 ± 0.037
0.10	-0.10	1589.7 ± 6.6	89.9 ± 2.5	-0.038 ± 0.009	0.149 ± 0.008
0.10	-0.05	1571.4 ± 13.7	107.1 ± 22.7	-0.089 ± 0.001	0.035 ± 0.008
0.10	0.00	1639.6 ± 14.2	71.5 ± 9.2	0.022 ± 0.006	-0.006 ± 0.011
0.10	0.05	1644.7 ± 9.3	80.2 ± 14.7	0.016 ± 0.027	-0.020 ± 0.003
0.10	0.10	1620.9 ± 6.1	129.0 ± 8.1	-0.008 ± 0.007	-0.014 ± 0.004
0.10	0.15	1655.0 ± 6.4	94.9 ± 0.8	0.038 ± 0.010	-0.018 ± 0.008
0.10	0.20	1626.7 ± 1.0	109.7 ± 5.1	0.072 ± 0.025	0.049 ± 0.007
0.10	0.25	1616.5 ± 5.5	95.9 ± 3.4	0.107 ± 0.018	0.098 ± 0.009
0.10	0.30	1600.4 ± 6.4	87.3 ± 6.0	0.044 ± 0.026	0.119 ± 0.009
0.10	0.35	1590.2 ± 5.8	85.2 ± 4.7	0.013 ± 0.012	0.157 ± 0.007
0.10	0.40	1582.4 ± 4.2	77.1 ± 3.3	-0.018 ± 0.020	0.164 ± 0.003
0.10	0.45	1579.6 ± 4.4	83.3 ± 2.2	0.029 ± 0.003	0.115 ± 0.013
0.10	0.50	1584.5 ± 5.3	79.9 ± 2.6	-0.021 ± 0.016	0.131 ± 0.006
0.10	0.55	1588.3 ± 3.5	75.0 ± 3.1	0.017 ± 0.012	0.138 ± 0.006
0.10	0.60	1586.1 ± 4.9	71.7 ± 4.0	0.057 ± 0.022	0.130 ± 0.004
0.10	0.65	1584.8 ± 4.8	92.4 ± 2.4	-0.042 ± 0.021	0.119 ± 0.013
0.10	0.70	1582.4 ± 7.0	120.7 ± 3.6	-0.029 ± 0.014	0.073 ± 0.010
0.10	0.75	1587.3 ± 6.8	95.8 ± 2.2	-0.044 ± 0.021	0.096 ± 0.022

x (arcsec)	y (arcsec)	v (km/s)	$\sigma_\star$ (km/s)	$h3$	$h4$
0.15	-0.75	1585.5 ± 5.1	101.3 ± 4.1	-0.028 ± 0.011	0.076 ± 0.006
0.15	-0.70	1577.9 ± 5.3	87.4 ± 3.7	0.013 ± 0.012	0.113 ± 0.010
0.15	-0.65	1579.4 ± 6.5	86.5 ± 2.1	-0.070 ± 0.017	0.137 ± 0.003
0.15	-0.60	1581.2 ± 6.9	86.5 ± 5.6	-0.039 ± 0.007	0.134 ± 0.011
0.15	-0.55	1589.6 ± 4.9	76.5 ± 3.6	0.023 ± 0.009	0.113 ± 0.014
0.15	-0.50	1592.4 ± 4.2	78.8 ± 4.2	0.020 ± 0.016	0.097 ± 0.007
0.15	-0.45	1593.5 ± 5.6	79.4 ± 1.8	-0.025 ± 0.008	0.093 ± 0.027
0.15	-0.40	1592.7 ± 4.2	82.1 ± 1.1	-0.052 ± 0.001	0.108 ± 0.014
0.15	-0.35	1588.7 ± 5.7	73.9 ± 1.6	0.013 ± 0.016	0.119 ± 0.004
0.15	-0.30	1587.9 ± 5.0	74.9 ± 4.1	0.018 ± 0.005	0.123 ± 0.006
0.15	-0.25	1594.9 ± 4.3	78.6 ± 2.5	-0.040 ± 0.018	0.118 ± 0.003
0.15	-0.20	1588.2 ± 5.3	76.4 ± 2.2	0.000 ± 0.016	0.171 ± 0.021
0.15	-0.15	1589.0 ± 5.6	79.0 ± 3.4	0.002 ± 0.012	0.160 ± 0.021
0.15	-0.10	1596.2 ± 4.2	79.1 ± 3.6	0.006 ± 0.014	0.101 ± 0.013
0.15	-0.05	1604.3 ± 4.9	69.7 ± 4.0	0.003 ± 0.007	0.114 ± 0.009
0.15	0.00	1614.2 ± 0.6	65.3 ± 8.8	0.044 ± 0.004	0.081 ± 0.001
0.15	0.05	1619.9 ± 3.6	72.3 ± 3.7	0.073 ± 0.003	0.091 ± 0.004
0.15	0.10	1618.5 ± 7.6	108.1 ± 6.3	0.032 ± 0.011	0.080 ± 0.008
0.15	0.15	1627.9 ± 4.8	137.9 ± 1.4	0.009 ± 0.008	0.016 ± 0.007
0.15	0.20	1618.7 ± 8.9	110.6 ± 9.4	0.048 ± 0.028	0.081 ± 0.005
0.15	0.25	1601.9 ± 7.1	89.9 ± 9.4	0.051 ± 0.019	0.202 ± 0.013
0.15	0.30	1599.8 ± 6.7	92.0 ± 4.3	0.020 ± 0.003	0.141 ± 0.004
0.15	0.35	1598.8 ± 4.5	92.1 ± 2.5	-0.002 ± 0.002	0.131 ± 0.005
0.15	0.40	1588.5 ± 4.6	81.0 ± 2.2	-0.020 ± 0.019	0.216 ± 0.007
0.15	0.45	1582.1 ± 5.5	80.2 ± 3.9	-0.035 ± 0.012	0.167 ± 0.007
0.15	0.50	1577.2 ± 3.8	75.9 ± 1.6	-0.026 ± 0.014	0.205 ± 0.008
0.15	0.55	1580.2 ± 4.5	69.4 ± 1.9	0.027 ± 0.014	0.181 ± 0.011
0.15	0.60	1577.5 ± 4.6	69.4 ± 2.6	0.057 ± 0.016	0.097 ± 0.005
0.15	0.65	1583.0 ± 5.0	85.8 ± 1.8	-0.042 ± 0.013	0.061 ± 0.017
0.15	0.70	1591.5 ± 6.0	107.0 ± 3.8	-0.029 ± 0.014	0.050 ± 0.018
0.15	0.75	1594.1 ± 4.3	110.4 ± 2.9	0.025 ± 0.010	0.044 ± 0.007
0.20	-0.75	1585.7 ± 6.0	82.9 ± 3.5	-0.013 ± 0.009	0.061 ± 0.015
0.20	-0.70	1579.5 ± 5.1	87.2 ± 3.3	0.007 ± 0.001	0.078 ± 0.020
0.20	-0.65	1583.0 ± 5.8	92.4 ± 2.3	-0.085 ± 0.008	0.096 ± 0.031
0.20	-0.60	1593.7 ± 6.8	94.5 ± 4.2	-0.035 ± 0.014	0.121 ± 0.014
0.20	-0.55	1591.7 ± 6.0	91.9 ± 4.1	-0.040 ± 0.013	0.116 ± 0.026
0.20	-0.50	1594.6 ± 6.9	80.4 ± 3.6	-0.040 ± 0.015	0.120 ± 0.027
0.20	-0.45	1593.1 ± 6.7	74.1 ± 3.8	-0.031 ± 0.015	0.117 ± 0.021
0.20	-0.40	1591.5 ± 6.4	78.2 ± 2.6	-0.024 ± 0.013	0.113 ± 0.024
0.20	-0.35	1586.9 ± 4.6	95.4 ± 4.4	-0.044 ± 0.018	0.117 ± 0.010
0.20	-0.30	1585.0 ± 7.3	88.6 ± 4.1	0.010 ± 0.013	0.105 ± 0.017
0.20	-0.25	1590.4 ± 3.9	74.8 ± 1.7	-0.050 ± 0.017	0.122 ± 0.024
0.20	-0.20	1594.0 ± 3.4	72.6 ± 2.4	-0.052 ± 0.020	0.142 ± 0.009
0.20	-0.15	1594.7 ± 5.4	69.0 ± 0.8	-0.045 ± 0.018	0.139 ± 0.009
0.20	-0.10	1594.2 ± 5.5	82.5 ± 1.9	-0.014 ± 0.021	0.149 ± 0.023
0.20	-0.05	1595.7 ± 6.8	87.8 ± 2.4	0.069 ± 0.007	0.159 ± 0.006
0.20	0.00	1597.3 ± 5.6	89.9 ± 2.8	0.025 ± 0.015	0.203 ± 0.003
0.20	0.05	1601.7 ± 4.8	84.2 ± 5.5	0.044 ± 0.017	0.207 ± 0.001
0.20	0.10	1613.0 ± 4.8	112.0 ± 9.7	0.047 ± 0.005	0.036 ± 0.024
0.20	0.15	1615.5 ± 3.8	117.3 ± 4.2	0.012 ± 0.016	0.035 ± 0.008
0.20	0.20	1613.2 ± 4.4	118.7 ± 5.5	0.020 ± 0.011	0.050 ± 0.004
0.20	0.25	1598.2 ± 6.6	81.4 ± 2.5	0.034 ± 0.011	0.177 ± 0.006
0.20	0.30	1605.0 ± 6.2	85.9 ± 3.8	0.030 ± 0.008	0.143 ± 0.004
0.20	0.35	1598.5 ± 3.8	76.1 ± 4.5	0.046 ± 0.002	0.174 ± 0.006
0.20	0.40	1592.3 ± 3.8	76.5 ± 2.6	0.027 ± 0.017	0.181 ± 0.004
0.20	0.45	1586.1 ± 5.5	82.2 ± 2.2	0.040 ± 0.012	0.109 ± 0.002
0.20	0.50	1582.0 ± 5.0	81.5 ± 2.3	0.058 ± 0.020	0.165 ± 0.009
0.20	0.55	1587.8 ± 3.8	76.4 ± 3.0	0.034 ± 0.002	0.146 ± 0.005
0.20	0.60	1587.0 ± 4.4	72.2 ± 3.7	-0.001 ± 0.002	0.149 ± 0.001
0.20	0.65	1582.2 ± 4.9	77.7 ± 4.0	-0.020 ± 0.010	0.134 ± 0.027
0.20	0.70	1582.1 ± 5.7	103.7 ± 2.8	-0.030 ± 0.004	0.054 ± 0.015
0.20	0.75	1580.3 ± 6.8	97.9 ± 3.1	-0.024 ± 0.008	0.061 ± 0.039

x (arcsec)	y (arcsec)	v (km/s)	$\sigma_\star$ (km/s)	$h3$	$h4$
0.25	-0.75	1593.9 ± 4.2	76.0 ± 1.0	-0.050 ± 0.024	0.066 ± 0.010
0.25	-0.70	1590.2 ± 5.1	72.1 ± 3.5	-0.043 ± 0.012	0.092 ± 0.011
0.25	-0.65	1585.3 ± 5.2	84.2 ± 2.4	-0.046 ± 0.021	0.083 ± 0.018
0.25	-0.60	1580.3 ± 5.8	79.6 ± 1.4	-0.021 ± 0.016	0.049 ± 0.012
0.25	-0.55	1588.0 ± 6.1	80.8 ± 4.8	0.003 ± 0.009	0.059 ± 0.021
0.25	-0.50	1594.6 ± 5.0	79.5 ± 4.7	-0.008 ± 0.012	0.080 ± 0.004
0.25	-0.45	1591.4 ± 5.8	75.3 ± 3.5	-0.027 ± 0.017	0.127 ± 0.019
0.25	-0.40	1590.4 ± 4.6	74.3 ± 2.3	-0.074 ± 0.031	0.115 ± 0.015
0.25	-0.35	1590.4 ± 5.4	89.7 ± 2.2	-0.034 ± 0.020	0.092 ± 0.022
0.25	-0.30	1595.0 ± 6.4	87.8 ± 4.9	-0.024 ± 0.013	0.132 ± 0.026
0.25	-0.25	1591.6 ± 7.5	80.9 ± 1.1	0.029 ± 0.016	0.074 ± 0.015
0.25	-0.20	1593.0 ± 5.0	74.5 ± 6.6	0.019 ± 0.030	0.106 ± 0.026
0.25	-0.15	1591.8 ± 3.3	74.6 ± 2.8	-0.029 ± 0.028	0.142 ± 0.004
0.25	-0.10	1594.5 ± 4.5	74.9 ± 2.6	-0.003 ± 0.017	0.139 ± 0.006
0.25	-0.05	1599.0 ± 4.7	85.7 ± 2.4	0.003 ± 0.014	0.171 ± 0.005
0.25	0.00	1597.7 ± 3.5	80.3 ± 3.0	-0.001 ± 0.023	0.155 ± 0.002
0.25	0.05	1593.4 ± 6.1	96.5 ± 3.0	0.066 ± 0.009	0.093 ± 0.010
0.25	0.10	1600.3 ± 5.9	111.4 ± 5.3	0.069 ± 0.006	0.022 ± 0.016
0.25	0.15	1605.4 ± 3.4	99.7 ± 5.6	0.053 ± 0.012	0.104 ± 0.023
0.25	0.20	1606.2 ± 6.6	94.3 ± 4.4	0.043 ± 0.007	0.122 ± 0.009
0.25	0.25	1601.6 ± 6.1	73.9 ± 1.4	0.003 ± 0.019	0.181 ± 0.022
0.25	0.30	1599.4 ± 6.0	76.0 ± 6.2	0.040 ± 0.009	0.163 ± 0.025
0.25	0.35	1605.0 ± 4.5	78.6 ± 0.2	0.052 ± 0.012	0.188 ± 0.007
0.25	0.40	1589.8 ± 3.9	77.3 ± 3.1	0.004 ± 0.019	0.173 ± 0.004
0.25	0.45	1586.8 ± 4.7	81.7 ± 0.2	0.014 ± 0.001	0.090 ± 0.009
0.25	0.50	1592.0 ± 4.0	92.3 ± 2.0	-0.036 ± 0.014	0.049 ± 0.024
0.25	0.55	1590.4 ± 1.4	96.6 ± 4.0	-0.041 ± 0.025	0.063 ± 0.014
0.25	0.60	1581.8 ± 4.9	99.6 ± 5.5	0.004 ± 0.017	0.063 ± 0.010
0.25	0.65	1571.8 ± 6.2	98.5 ± 4.3	0.006 ± 0.012	0.068 ± 0.012
0.25	0.70	1586.9 ± 6.0	91.1 ± 7.5	-0.030 ± 0.018	0.118 ± 0.001
0.25	0.75	1586.5 ± 8.7	108.4 ± 3.2	0.025 ± 0.022	0.013 ± 0.006
0.30	-0.75	1586.6 ± 6.0	79.2 ± 0.1	-0.050 ± 0.009	0.004 ± 0.009
0.30	-0.70	1587.8 ± 6.2	80.7 ± 5.0	0.009 ± 0.016	0.079 ± 0.000
0.30	-0.65	1582.6 ± 4.9	86.8 ± 3.6	-0.010 ± 0.015	0.043 ± 0.009
0.30	-0.60	1580.8 ± 4.4	78.7 ± 2.1	0.003 ± 0.014	0.034 ± 0.019
0.30	-0.55	1592.0 ± 4.7	83.2 ± 5.4	-0.060 ± 0.006	0.073 ± 0.010
0.30	-0.50	1594.1 ± 6.3	83.8 ± 3.9	0.010 ± 0.009	0.135 ± 0.009
0.30	-0.45	1590.3 ± 7.3	71.1 ± 4.8	0.058 ± 0.026	0.150 ± 0.000
0.30	-0.40	1589.7 ± 6.1	82.6 ± 3.3	-0.025 ± 0.013	0.081 ± 0.025
0.30	-0.35	1587.0 ± 4.5	78.6 ± 4.2	-0.063 ± 0.026	0.142 ± 0.010
0.30	-0.30	1589.8 ± 3.3	74.8 ± 4.1	-0.064 ± 0.034	0.130 ± 0.009
0.30	-0.25	1590.1 ± 3.4	74.6 ± 2.4	-0.018 ± 0.030	0.118 ± 0.007
0.30	-0.20	1591.0 ± 4.6	77.8 ± 2.8	-0.003 ± 0.016	0.145 ± 0.012
0.30	-0.15	1591.3 ± 4.8	87.1 ± 5.5	0.034 ± 0.011	0.129 ± 0.015
0.30	-0.10	1599.7 ± 6.2	82.3 ± 5.0	0.029 ± 0.008	0.179 ± 0.007
0.30	-0.05	1598.3 ± 5.1	70.7 ± 4.4	0.045 ± 0.014	0.201 ± 0.007
0.30	0.00	1595.9 ± 4.9	69.4 ± 2.6	0.027 ± 0.017	0.201 ± 0.018
0.30	0.05	1596.6 ± 4.8	79.8 ± 4.2	0.021 ± 0.020	0.206 ± 0.008
0.30	0.10	1603.7 ± 5.1	87.1 ± 6.8	0.033 ± 0.012	0.151 ± 0.046
0.30	0.15	1604.7 ± 5.5	93.4 ± 3.6	0.045 ± 0.011	0.099 ± 0.012
0.30	0.20	1603.3 ± 5.4	91.2 ± 5.8	-0.008 ± 0.020	0.104 ± 0.007
0.30	0.25	1598.8 ± 4.0	82.3 ± 6.5	-0.023 ± 0.015	0.166 ± 0.002
0.30	0.30	1599.0 ± 4.4	71.0 ± 4.7	-0.008 ± 0.001	0.186 ± 0.008
0.30	0.35	1605.7 ± 4.0	88.7 ± 5.6	0.008 ± 0.008	0.181 ± 0.003
0.30	0.40	1605.9 ± 4.0	91.0 ± 7.2	-0.012 ± 0.021	0.137 ± 0.003
0.30	0.45	1599.7 ± 4.8	100.1 ± 3.3	-0.048 ± 0.013	0.128 ± 0.006
0.30	0.50	1587.4 ± 3.0	100.8 ± 4.4	-0.082 ± 0.022	0.130 ± 0.014
0.30	0.55	1582.1 ± 3.0	90.4 ± 2.5	-0.058 ± 0.019	0.069 ± 0.017
0.30	0.60	1589.3 ± 5.0	94.7 ± 2.0	0.018 ± 0.016	0.079 ± 0.019
0.30	0.65	1591.8 ± 4.3	95.1 ± 3.6	-0.036 ± 0.017	0.078 ± 0.016
0.30	0.70	1593.5 ± 4.3	90.0 ± 0.2	-0.027 ± 0.012	0.038 ± 0.006
0.30	0.75	1592.6 ± 5.0	83.6 ± 5.8	-0.001 ± 0.021	0.034 ± 0.017

x (arcsec)	y (arcsec)	v (km/s)	$\sigma_\star$ (km/s)	$h3$	$h4$
0.35	-0.75	1591.8 ± 4.2	81.2 ± 4.6	-0.006 ± 0.011	0.042 ± 0.007
0.35	-0.70	1590.2 ± 6.9	80.8 ± 4.3	-0.015 ± 0.018	0.034 ± 0.009
0.35	-0.65	1588.4 ± 6.1	78.8 ± 2.7	-0.018 ± 0.017	0.051 ± 0.009
0.35	-0.60	1598.0 ± 4.9	71.1 ± 4.8	-0.054 ± 0.007	0.092 ± 0.020
0.35	-0.55	1598.0 ± 5.7	69.6 ± 1.6	-0.084 ± 0.019	0.073 ± 0.017
0.35	-0.50	1598.5 ± 5.6	76.1 ± 2.7	-0.070 ± 0.013	0.080 ± 0.008
0.35	-0.45	1594.2 ± 5.5	87.7 ± 2.3	0.011 ± 0.020	0.099 ± 0.017
0.35	-0.40	1591.6 ± 4.2	87.4 ± 3.3	-0.011 ± 0.023	0.140 ± 0.032
0.35	-0.35	1589.9 ± 4.9	89.8 ± 5.3	-0.014 ± 0.016	0.144 ± 0.024
0.35	-0.30	1586.5 ± 4.7	87.9 ± 2.8	0.002 ± 0.015	0.114 ± 0.005
0.35	-0.25	1589.0 ± 6.0	87.2 ± 2.1	0.011 ± 0.010	0.135 ± 0.010
0.35	-0.20	1592.4 ± 6.4	81.6 ± 1.7	0.015 ± 0.012	0.107 ± 0.017
0.35	-0.15	1599.2 ± 5.7	82.4 ± 1.5	-0.006 ± 0.013	0.110 ± 0.015
0.35	-0.10	1602.4 ± 4.6	73.9 ± 3.9	-0.007 ± 0.013	0.123 ± 0.006
0.35	-0.05	1600.5 ± 3.7	72.6 ± 5.2	0.025 ± 0.018	0.164 ± 0.003
0.35	0.00	1598.9 ± 4.2	67.5 ± 4.5	0.027 ± 0.015	0.180 ± 0.006
0.35	0.05	1594.1 ± 3.4	70.4 ± 3.9	0.009 ± 0.019	0.204 ± 0.009
0.35	0.10	1597.4 ± 3.3	70.9 ± 4.8	0.022 ± 0.024	0.188 ± 0.008
0.35	0.15	1604.7 ± 3.8	77.6 ± 2.6	0.004 ± 0.013	0.183 ± 0.012
0.35	0.20	1601.9 ± 4.6	77.6 ± 3.4	-0.015 ± 0.014	0.159 ± 0.023
0.35	0.25	1596.9 ± 5.1	73.6 ± 2.9	-0.011 ± 0.016	0.156 ± 0.010
0.35	0.30	1597.2 ± 3.8	73.0 ± 3.9	-0.014 ± 0.016	0.195 ± 0.005
0.35	0.35	1599.9 ± 4.5	71.8 ± 3.6	0.030 ± 0.014	0.218 ± 0.005
0.35	0.40	1604.4 ± 8.0	73.1 ± 7.7	0.022 ± 0.009	0.175 ± 0.010
0.35	0.45	1600.3 ± 6.5	81.0 ± 4.9	-0.033 ± 0.014	0.122 ± 0.011
0.35	0.50	1595.6 ± 5.9	96.0 ± 1.8	-0.072 ± 0.013	0.067 ± 0.024
0.35	0.55	1595.4 ± 6.8	79.5 ± 0.3	-0.037 ± 0.013	0.103 ± 0.012
0.35	0.60	1590.2 ± 5.2	85.0 ± 4.2	0.013 ± 0.015	0.054 ± 0.010
0.35	0.65	1594.9 ± 6.3	97.4 ± 3.0	-0.013 ± 0.015	0.099 ± 0.012
0.35	0.70	1580.4 ± 5.8	97.4 ± 2.5	-0.022 ± 0.003	0.092 ± 0.003
0.35	0.75	1574.8 ± 4.2	96.7 ± 7.0	-0.009 ± 0.001	0.055 ± 0.007
0.40	-0.75	1585.9 ± 6.2	100.2 ± 4.4	-0.081 ± 0.004	0.047 ± 0.005
0.40	-0.70	1590.5 ± 7.4	92.4 ± 1.5	-0.034 ± 0.013	0.023 ± 0.017
0.40	-0.65	1601.6 ± 6.6	81.3 ± 6.4	-0.029 ± 0.016	0.105 ± 0.040
0.40	-0.60	1602.4 ± 4.0	81.8 ± 2.0	-0.065 ± 0.017	0.085 ± 0.021
0.40	-0.55	1594.6 ± 4.4	79.1 ± 3.9	0.002 ± 0.007	0.107 ± 0.016
0.40	-0.50	1597.9 ± 6.3	92.0 ± 4.2	0.013 ± 0.007	0.087 ± 0.011
0.40	-0.45	1593.8 ± 7.3	98.0 ± 4.6	-0.033 ± 0.010	0.069 ± 0.014
0.40	-0.40	1595.5 ± 4.9	102.3 ± 3.1	-0.083 ± 0.025	0.043 ± 0.015
0.40	-0.35	1595.1 ± 2.1	84.6 ± 7.2	-0.049 ± 0.027	0.138 ± 0.019
0.40	-0.30	1605.0 ± 3.0	82.1 ± 5.1	-0.029 ± 0.017	0.122 ± 0.005
0.40	-0.25	1605.4 ± 5.2	76.2 ± 3.6	-0.016 ± 0.012	0.183 ± 0.010
0.40	-0.20	1602.2 ± 5.2	73.2 ± 4.4	-0.009 ± 0.014	0.137 ± 0.008
0.40	-0.15	1595.7 ± 4.8	76.2 ± 0.4	0.016 ± 0.014	0.092 ± 0.020
0.40	-0.10	1595.6 ± 3.9	69.1 ± 2.9	0.020 ± 0.015	0.201 ± 0.006
0.40	-0.05	1598.7 ± 4.3	79.8 ± 4.4	-0.023 ± 0.024	0.166 ± 0.033
0.40	0.00	1593.4 ± 5.0	84.1 ± 3.3	-0.036 ± 0.018	0.190 ± 0.015
0.40	0.05	1596.5 ± 3.4	70.4 ± 4.6	-0.055 ± 0.019	0.196 ± 0.012
0.40	0.10	1595.9 ± 3.3	67.0 ± 3.8	-0.024 ± 0.018	0.207 ± 0.017
0.40	0.15	1599.0 ± 4.6	75.6 ± 2.3	0.001 ± 0.009	0.152 ± 0.015
0.40	0.20	1599.1 ± 5.1	68.2 ± 1.8	-0.001 ± 0.012	0.145 ± 0.008
0.40	0.25	1598.2 ± 6.6	67.1 ± 0.6	0.018 ± 0.009	0.115 ± 0.017
0.40	0.30	1595.3 ± 6.5	68.3 ± 4.5	0.003 ± 0.016	0.112 ± 0.002
0.40	0.35	1595.5 ± 5.8	78.0 ± 5.4	-0.039 ± 0.013	0.144 ± 0.006
0.40	0.40	1594.9 ± 5.1	82.3 ± 4.5	0.000 ± 0.013	0.127 ± 0.007
0.40	0.45	1589.8 ± 3.9	87.6 ± 5.6	-0.033 ± 0.017	0.114 ± 0.045
0.40	0.50	1600.5 ± 4.4	103.3 ± 2.7	0.006 ± 0.016	0.056 ± 0.023
0.40	0.55	1598.2 ± 6.0	88.2 ± 2.1	0.032 ± 0.020	0.092 ± 0.007
0.40	0.60	1588.1 ± 3.5	76.0 ± 2.1	-0.007 ± 0.019	0.136 ± 0.007
0.40	0.65	1590.5 ± 4.3	82.4 ± 1.6	-0.067 ± 0.006	0.094 ± 0.014
0.40	0.70	1591.3 ± 7.3	86.0 ± 4.2	-0.051 ± 0.005	0.105 ± 0.022
0.40	0.75	1585.2 ± 7.7	86.2 ± 5.0	-0.063 ± 0.009	0.151 ± 0.020

x (arcsec)	y (arcsec)	v (km/s)	$\sigma_\star$ (km/s)	$h3$	$h4$
0.45	-0.75	1586.1 ± 2.1	84.3 ± 3.0	-0.076 ± 0.022	0.082 ± 0.008
0.45	-0.70	1597.0 ± 2.1	86.0 ± 2.1	-0.065 ± 0.035	0.078 ± 0.011
0.45	-0.65	1592.1 ± 3.5	88.7 ± 2.0	-0.022 ± 0.026	0.098 ± 0.014
0.45	-0.60	1601.3 ± 4.5	92.6 ± 1.5	-0.042 ± 0.008	0.063 ± 0.001
0.45	-0.55	1591.1 ± 4.9	85.8 ± 2.2	-0.022 ± 0.021	0.108 ± 0.009
0.45	-0.50	1599.0 ± 6.3	96.1 ± 3.1	-0.069 ± 0.008	0.070 ± 0.007
0.45	-0.45	1585.9 ± 5.7	95.1 ± 2.8	-0.036 ± 0.016	0.122 ± 0.012
0.45	-0.40	1590.6 ± 6.2	88.5 ± 4.5	-0.051 ± 0.012	0.138 ± 0.009
0.45	-0.35	1590.3 ± 4.2	87.1 ± 3.8	-0.026 ± 0.013	0.097 ± 0.008
0.45	-0.30	1596.1 ± 3.4	92.9 ± 7.9	0.002 ± 0.013	0.123 ± 0.008
0.45	-0.25	1600.2 ± 3.8	81.9 ± 8.0	-0.058 ± 0.021	0.135 ± 0.002
0.45	-0.20	1599.3 ± 1.8	78.0 ± 5.4	-0.069 ± 0.027	0.127 ± 0.008
0.45	-0.15	1595.4 ± 3.2	79.8 ± 3.5	-0.062 ± 0.023	0.108 ± 0.006
0.45	-0.10	1593.7 ± 4.6	78.2 ± 3.3	-0.015 ± 0.021	0.146 ± 0.002
0.45	-0.05	1597.1 ± 4.9	75.6 ± 2.6	0.056 ± 0.017	0.202 ± 0.005
0.45	0.00	1594.0 ± 3.8	77.3 ± 2.5	-0.028 ± 0.024	0.228 ± 0.007
0.45	0.05	1594.4 ± 2.6	79.7 ± 2.8	-0.039 ± 0.020	0.191 ± 0.012
0.45	0.10	1596.4 ± 3.5	90.4 ± 5.0	-0.009 ± 0.013	0.127 ± 0.007
0.45	0.15	1602.8 ± 4.2	84.0 ± 3.7	0.026 ± 0.012	0.154 ± 0.007
0.45	0.20	1596.6 ± 4.4	84.0 ± 4.0	0.004 ± 0.019	0.145 ± 0.022
0.45	0.25	1595.9 ± 3.9	90.7 ± 1.8	-0.011 ± 0.018	0.114 ± 0.021
0.45	0.30	1594.1 ± 5.1	84.8 ± 4.3	0.011 ± 0.016	0.124 ± 0.019
0.45	0.35	1587.2 ± 5.9	66.8 ± 3.1	-0.003 ± 0.013	0.138 ± 0.007
0.45	0.40	1591.0 ± 6.3	66.6 ± 3.4	-0.011 ± 0.017	0.111 ± 0.023
0.45	0.45	1582.9 ± 5.7	91.6 ± 4.8	0.007 ± 0.011	0.091 ± 0.001
0.45	0.50	1593.2 ± 4.7	91.6 ± 7.6	-0.001 ± 0.001	0.077 ± 0.004
0.45	0.55	1595.7 ± 6.3	83.1 ± 1.4	0.006 ± 0.010	0.072 ± 0.005
0.45	0.60	1586.2 ± 7.4	105.1 ± 4.5	-0.001 ± 0.010	0.019 ± 0.001
0.45	0.65	1589.5 ± 7.2	100.6 ± 1.6	-0.037 ± 0.001	0.074 ± 0.020
0.45	0.70	1592.4 ± 7.8	116.3 ± 3.6	0.017 ± 0.015	0.090 ± 0.023
0.45	0.75	1579.6 ± 8.3	104.2 ± 1.5	0.000 ± 0.006	0.106 ± 0.027
0.50	-0.75	1582.5 ± 6.6	94.2 ± 5.0	-0.005 ± 0.011	0.048 ± 0.014
0.50	-0.70	1589.5 ± 4.7	98.9 ± 4.1	-0.034 ± 0.016	0.062 ± 0.012
0.50	-0.65	1587.7 ± 5.6	110.6 ± 3.8	-0.013 ± 0.022	0.070 ± 0.006
0.50	-0.60	1604.0 ± 6.7	101.3 ± 4.1	-0.022 ± 0.016	0.062 ± 0.008
0.50	-0.55	1601.9 ± 7.6	92.5 ± 6.2	-0.059 ± 0.015	0.120 ± 0.028
0.50	-0.50	1593.1 ± 5.1	80.5 ± 3.9	-0.082 ± 0.013	0.126 ± 0.014
0.50	-0.45	1602.4 ± 4.9	81.2 ± 1.7	-0.070 ± 0.020	0.140 ± 0.032
0.50	-0.40	1599.7 ± 5.8	79.9 ± 2.2	-0.051 ± 0.024	0.139 ± 0.009
0.50	-0.35	1600.6 ± 4.9	78.4 ± 4.4	-0.005 ± 0.017	0.116 ± 0.000
0.50	-0.30	1597.1 ± 3.7	86.4 ± 9.2	0.001 ± 0.021	0.129 ± 0.022
0.50	-0.25	1598.1 ± 3.5	96.6 ± 10.6	-0.003 ± 0.023	0.138 ± 0.020
0.50	-0.20	1585.6 ± 3.0	88.4 ± 4.9	-0.048 ± 0.031	0.155 ± 0.007
0.50	-0.15	1590.5 ± 4.7	84.7 ± 2.3	-0.031 ± 0.020	0.149 ± 0.021
0.50	-0.10	1593.7 ± 5.7	81.8 ± 2.0	-0.031 ± 0.020	0.141 ± 0.018
0.50	-0.05	1596.3 ± 7.0	78.6 ± 2.1	0.044 ± 0.014	0.189 ± 0.005
0.50	0.00	1596.3 ± 5.1	69.3 ± 2.8	0.032 ± 0.023	0.178 ± 0.013
0.50	0.05	1595.2 ± 3.6	71.9 ± 3.9	-0.024 ± 0.023	0.199 ± 0.007
0.50	0.10	1595.6 ± 3.5	88.5 ± 7.2	-0.051 ± 0.023	0.143 ± 0.023
0.50	0.15	1600.3 ± 5.1	88.8 ± 6.1	-0.008 ± 0.005	0.127 ± 0.003
0.50	0.20	1600.7 ± 3.9	94.3 ± 6.5	-0.051 ± 0.020	0.111 ± 0.008
0.50	0.25	1598.2 ± 3.3	91.3 ± 1.5	-0.046 ± 0.030	0.107 ± 0.021
0.50	0.30	1594.8 ± 4.8	77.3 ± 2.0	0.043 ± 0.015	0.146 ± 0.020
0.50	0.35	1588.1 ± 4.3	80.0 ± 1.7	0.001 ± 0.011	0.151 ± 0.004
0.50	0.40	1592.0 ± 4.9	86.4 ± 2.2	-0.060 ± 0.024	0.093 ± 0.026
0.50	0.45	1592.4 ± 2.9	85.6 ± 2.0	-0.074 ± 0.015	0.086 ± 0.002
0.50	0.50	1596.5 ± 2.2	85.8 ± 5.0	-0.093 ± 0.023	0.083 ± 0.004
0.50	0.55	1601.2 ± 3.0	87.7 ± 1.3	-0.077 ± 0.026	-0.034 ± 0.005
0.50	0.60	1591.9 ± 6.2	108.3 ± 0.5	-0.085 ± 0.012	-0.055 ± 0.015
0.50	0.65	1590.7 ± 8.0	114.2 ± 1.1	-0.062 ± 0.010	-0.036 ± 0.016
0.50	0.70	1585.8 ± 4.0	116.9 ± 3.2	0.027 ± 0.013	-0.032 ± 0.018
0.50	0.75	1596.2 ± 9.3	90.6 ± 1.1	0.007 ± 0.021	0.086 ± 0.021

x (arcsec)	y (arcsec)	v (km/s)	$\sigma_\star$ (km/s)	$h3$	$h4$
0.55	-0.75	1576.0 ± 3.4	75.1 ± 2.2	-0.031 ± 0.024	0.129 ± 0.011
0.55	-0.70	1585.4 ± 4.9	82.7 ± 1.7	0.003 ± 0.012	0.128 ± 0.010
0.55	-0.65	1596.5 ± 6.1	100.9 ± 3.6	-0.047 ± 0.012	0.088 ± 0.010
0.55	-0.60	1595.5 ± 4.1	94.0 ± 3.2	-0.091 ± 0.022	0.081 ± 0.021
0.55	-0.55	1588.7 ± 7.0	93.8 ± 2.1	-0.078 ± 0.013	0.073 ± 0.011
0.55	-0.50	1588.4 ± 7.8	90.9 ± 2.3	-0.098 ± 0.014	0.061 ± 0.016
0.55	-0.45	1594.1 ± 6.6	80.6 ± 1.0	-0.058 ± 0.019	0.116 ± 0.014
0.55	-0.40	1594.1 ± 6.5	70.5 ± 0.8	-0.031 ± 0.016	0.124 ± 0.006
0.55	-0.35	1591.1 ± 4.7	80.5 ± 0.7	-0.044 ± 0.017	0.114 ± 0.008
0.55	-0.30	1593.1 ± 2.3	84.5 ± 4.1	-0.052 ± 0.025	0.104 ± 0.008
0.55	-0.25	1596.8 ± 2.9	88.9 ± 3.1	-0.071 ± 0.021	0.092 ± 0.016
0.55	-0.20	1591.3 ± 5.4	84.4 ± 2.1	-0.055 ± 0.016	0.106 ± 0.010
0.55	-0.15	1594.7 ± 6.5	83.7 ± 2.1	-0.049 ± 0.012	0.116 ± 0.009
0.55	-0.10	1597.2 ± 6.2	86.7 ± 2.4	0.019 ± 0.012	0.124 ± 0.018
0.55	-0.05	1599.3 ± 6.4	77.6 ± 3.7	0.040 ± 0.011	0.147 ± 0.001
0.55	0.00	1599.7 ± 6.3	71.6 ± 3.3	0.009 ± 0.012	0.163 ± 0.006
0.55	0.05	1601.6 ± 3.4	86.1 ± 3.4	-0.006 ± 0.018	0.126 ± 0.017
0.55	0.10	1603.1 ± 4.4	81.6 ± 6.3	0.025 ± 0.018	0.146 ± 0.016
0.55	0.15	1600.9 ± 7.6	91.3 ± 8.8	0.077 ± 0.015	0.139 ± 0.018
0.55	0.20	1596.6 ± 6.7	93.4 ± 8.9	0.020 ± 0.011	0.128 ± 0.020
0.55	0.25	1588.4 ± 4.4	90.3 ± 5.7	0.019 ± 0.016	0.120 ± 0.020
0.55	0.30	1592.9 ± 6.1	88.7 ± 2.5	-0.032 ± 0.010	0.095 ± 0.019
0.55	0.35	1597.7 ± 7.1	77.5 ± 0.1	-0.070 ± 0.010	0.099 ± 0.013
0.55	0.40	1593.2 ± 6.0	77.9 ± 2.8	-0.078 ± 0.012	0.048 ± 0.025
0.55	0.45	1592.7 ± 4.5	74.1 ± 2.4	-0.082 ± 0.022	0.119 ± 0.010
0.55	0.50	1595.5 ± 4.6	72.6 ± 3.7	-0.068 ± 0.010	0.075 ± 0.017
0.55	0.55	1597.8 ± 3.2	74.0 ± 2.4	-0.050 ± 0.005	0.077 ± 0.008
0.55	0.60	1595.3 ± 4.0	66.1 ± 1.2	0.002 ± 0.004	0.127 ± 0.019
0.55	0.65	1595.0 ± 7.2	74.3 ± 0.2	-0.048 ± 0.009	0.111 ± 0.007
0.55	0.70	1582.0 ± 5.9	96.9 ± 1.5	-0.084 ± 0.009	-0.008 ± 0.024
0.55	0.75	1581.6 ± 5.6	86.4 ± 2.9	-0.011 ± 0.004	0.045 ± 0.019
0.60	-0.75	1573.3 ± 4.6	89.0 ± 6.8	-0.015 ± 0.021	0.078 ± 0.023
0.60	-0.70	1587.1 ± 4.0	93.5 ± 4.7	-0.025 ± 0.026	0.025 ± 0.029
0.60	-0.65	1600.6 ± 5.8	94.9 ± 6.2	-0.029 ± 0.010	0.083 ± 0.004
0.60	-0.60	1596.0 ± 5.4	92.2 ± 2.2	0.009 ± 0.011	0.095 ± 0.018
0.60	-0.55	1586.2 ± 6.4	89.4 ± 2.1	0.004 ± 0.008	0.048 ± 0.015
0.60	-0.50	1585.0 ± 4.5	99.2 ± 2.3	-0.050 ± 0.010	0.041 ± 0.019
0.60	-0.45	1599.0 ± 5.8	84.6 ± 2.4	-0.063 ± 0.018	0.084 ± 0.012
0.60	-0.40	1597.2 ± 4.9	85.9 ± 3.3	-0.064 ± 0.012	0.139 ± 0.014
0.60	-0.35	1597.7 ± 4.3	85.8 ± 2.0	-0.030 ± 0.013	0.086 ± 0.012
0.60	-0.30	1592.6 ± 4.9	96.3 ± 1.5	-0.076 ± 0.016	0.020 ± 0.011
0.60	-0.25	1589.8 ± 5.7	82.5 ± 2.0	-0.046 ± 0.020	0.132 ± 0.009
0.60	-0.20	1592.1 ± 6.5	83.1 ± 4.8	-0.053 ± 0.015	0.137 ± 0.009
0.60	-0.15	1592.3 ± 5.6	86.1 ± 3.3	-0.014 ± 0.006	0.139 ± 0.003
0.60	-0.10	1599.2 ± 6.5	93.0 ± 4.2	0.010 ± 0.016	0.114 ± 0.025
0.60	-0.05	1601.0 ± 6.4	89.7 ± 2.4	-0.036 ± 0.015	0.118 ± 0.013
0.60	0.00	1593.4 ± 5.9	80.6 ± 4.3	-0.037 ± 0.011	0.128 ± 0.013
0.60	0.05	1596.9 ± 2.5	75.4 ± 3.4	-0.048 ± 0.015	0.140 ± 0.013
0.60	0.10	1594.4 ± 4.4	78.3 ± 2.8	0.001 ± 0.019	0.139 ± 0.013
0.60	0.15	1593.4 ± 5.6	78.3 ± 1.6	0.019 ± 0.017	0.131 ± 0.006
0.60	0.20	1594.2 ± 5.2	72.2 ± 5.2	0.041 ± 0.010	0.127 ± 0.017
0.60	0.25	1597.1 ± 3.3	73.4 ± 0.3	0.003 ± 0.013	0.093 ± 0.014
0.60	0.30	1602.1 ± 4.9	78.8 ± 2.1	0.009 ± 0.019	0.084 ± 0.005
0.60	0.35	1596.0 ± 3.7	87.0 ± 2.6	0.004 ± 0.015	0.047 ± 0.013
0.60	0.40	1593.1 ± 3.4	90.1 ± 2.0	-0.011 ± 0.018	0.080 ± 0.013
0.60	0.45	1596.7 ± 6.1	92.6 ± 1.8	-0.047 ± 0.017	0.118 ± 0.014
0.60	0.50	1595.0 ± 4.3	91.6 ± 2.7	-0.069 ± 0.018	0.065 ± 0.018
0.60	0.55	1594.2 ± 4.0	92.3 ± 3.6	-0.055 ± 0.000	0.083 ± 0.017
0.60	0.60	1589.7 ± 4.9	83.9 ± 5.3	0.030 ± 0.011	0.165 ± 0.019
0.60	0.65	1595.5 ± 5.9	82.2 ± 1.5	0.007 ± 0.007	0.144 ± 0.018
0.60	0.70	1583.7 ± 7.6	90.6 ± 4.7	0.007 ± 0.009	0.075 ± 0.009
0.60	0.75	1588.8 ± 5.6	94.9 ± 5.7	0.034 ± 0.012	0.049 ± 0.005

x (arcsec)	y (arcsec)	v (km/s)	$\sigma_\star$ (km/s)	$h3$	$h4$
0.65	-0.75	1594.1 ± 0.5	101.8 ± 4.3	-0.059 ± 0.021	0.040 ± 0.005
0.65	-0.70	1604.5 ± 3.6	97.6 ± 2.8	-0.110 ± 0.020	0.056 ± 0.011
0.65	-0.65	1606.5 ± 4.2	96.7 ± 2.4	-0.020 ± 0.025	0.105 ± 0.019
0.65	-0.60	1589.3 ± 6.8	98.0 ± 3.7	0.075 ± 0.024	0.114 ± 0.009
0.65	-0.55	1581.9 ± 5.9	82.0 ± 2.2	0.025 ± 0.012	0.079 ± 0.006
0.65	-0.50	1591.5 ± 5.3	81.5 ± 4.3	0.005 ± 0.007	0.093 ± 0.008
0.65	-0.45	1596.6 ± 5.5	76.8 ± 7.0	0.036 ± 0.010	0.137 ± 0.019
0.65	-0.40	1595.3 ± 4.2	82.0 ± 4.8	-0.018 ± 0.019	0.172 ± 0.010
0.65	-0.35	1590.9 ± 4.5	104.3 ± 4.4	-0.001 ± 0.013	0.115 ± 0.021
0.65	-0.30	1590.7 ± 4.1	113.4 ± 2.2	-0.027 ± 0.013	0.045 ± 0.010
0.65	-0.25	1588.7 ± 4.6	88.8 ± 2.3	-0.059 ± 0.018	0.112 ± 0.003
0.65	-0.20	1589.5 ± 3.2	86.2 ± 4.3	-0.093 ± 0.016	0.115 ± 0.007
0.65	-0.15	1591.8 ± 1.0	93.4 ± 7.9	-0.030 ± 0.014	0.122 ± 0.006
0.65	-0.10	1595.4 ± 3.3	91.0 ± 2.1	0.000 ± 0.016	0.087 ± 0.015
0.65	-0.05	1596.7 ± 5.0	84.0 ± 0.2	0.011 ± 0.007	0.064 ± 0.016
0.65	0.00	1595.8 ± 6.5	77.2 ± 1.1	0.012 ± 0.013	0.094 ± 0.015
0.65	0.05	1595.3 ± 5.7	80.8 ± 3.6	0.006 ± 0.016	0.151 ± 0.002
0.65	0.10	1599.9 ± 7.5	95.2 ± 3.2	-0.010 ± 0.011	0.077 ± 0.010
0.65	0.15	1592.0 ± 6.3	86.9 ± 2.2	0.019 ± 0.006	0.140 ± 0.005
0.65	0.20	1588.5 ± 5.6	89.1 ± 2.1	-0.010 ± 0.009	0.123 ± 0.028
0.65	0.25	1595.9 ± 5.9	99.5 ± 5.5	0.049 ± 0.003	0.054 ± 0.019
0.65	0.30	1590.0 ± 7.0	101.2 ± 5.8	0.055 ± 0.014	0.040 ± 0.008
0.65	0.35	1593.9 ± 5.0	100.7 ± 10.1	0.054 ± 0.010	0.060 ± 0.010
0.65	0.40	1594.5 ± 3.4	108.3 ± 4.4	0.009 ± 0.020	0.132 ± 0.007
0.65	0.45	1592.7 ± 5.6	101.3 ± 4.0	-0.043 ± 0.012	0.099 ± 0.014
0.65	0.50	1595.7 ± 5.3	105.2 ± 4.1	-0.018 ± 0.003	0.143 ± 0.008
0.65	0.55	1583.8 ± 7.9	134.6 ± 6.5	-0.008 ± 0.016	0.020 ± 0.012
0.65	0.60	1584.4 ± 8.6	116.8 ± 6.3	-0.006 ± 0.005	0.063 ± 0.009
0.65	0.65	1595.0 ± 6.8	94.2 ± 5.2	0.057 ± 0.009	0.135 ± 0.006
0.65	0.70	1594.1 ± 3.7	112.9 ± 5.2	-0.014 ± 0.012	0.126 ± 0.027
0.65	0.75	1587.5 ± 5.8	107.5 ± 2.6	0.006 ± 0.015	0.126 ± 0.025
0.70	-0.75	1587.6 ± 3.3	111.8 ± 1.2	-0.080 ± 0.020	0.103 ± 0.001
0.70	-0.70	1602.0 ± 2.8	90.7 ± 11.2	-0.060 ± 0.023	0.130 ± 0.017
0.70	-0.65	1596.6 ± 6.3	98.7 ± 11.7	-0.015 ± 0.017	0.146 ± 0.008
0.70	-0.60	1593.4 ± 6.4	100.9 ± 4.7	0.025 ± 0.014	0.022 ± 0.009
0.70	-0.55	1588.4 ± 5.2	73.5 ± 1.1	-0.064 ± 0.012	0.011 ± 0.016
0.70	-0.50	1580.8 ± 7.8	86.4 ± 2.7	-0.040 ± 0.009	0.053 ± 0.006
0.70	-0.45	1593.1 ± 6.5	79.7 ± 2.2	-0.064 ± 0.018	0.132 ± 0.012
0.70	-0.40	1591.2 ± 5.5	83.9 ± 2.8	-0.021 ± 0.017	0.143 ± 0.008
0.70	-0.35	1591.1 ± 3.9	90.1 ± 2.8	0.008 ± 0.012	0.096 ± 0.003
0.70	-0.30	1589.8 ± 5.0	98.8 ± 7.4	0.001 ± 0.014	0.110 ± 0.014
0.70	-0.25	1588.1 ± 3.1	95.9 ± 3.3	-0.018 ± 0.018	0.098 ± 0.016
0.70	-0.20	1590.1 ± 3.1	89.0 ± 3.1	-0.020 ± 0.018	0.128 ± 0.008
0.70	-0.15	1583.1 ± 3.7	84.5 ± 1.7	-0.046 ± 0.018	0.134 ± 0.023
0.70	-0.10	1586.9 ± 4.4	72.5 ± 3.0	-0.028 ± 0.018	0.102 ± 0.008
0.70	-0.05	1585.8 ± 4.4	76.0 ± 2.1	0.018 ± 0.029	0.137 ± 0.001
0.70	0.00	1594.9 ± 3.5	65.7 ± 3.0	0.038 ± 0.020	0.124 ± 0.008
0.70	0.05	1598.5 ± 7.2	80.4 ± 4.8	0.016 ± 0.007	0.158 ± 0.007
0.70	0.10	1604.2 ± 7.4	81.3 ± 4.7	-0.019 ± 0.007	0.146 ± 0.007
0.70	0.15	1595.9 ± 7.3	93.7 ± 2.7	0.000 ± 0.012	0.116 ± 0.006
0.70	0.20	1588.4 ± 6.1	97.8 ± 2.2	0.019 ± 0.012	0.108 ± 0.014
0.70	0.25	1590.6 ± 5.7	86.9 ± 5.1	0.027 ± 0.016	0.144 ± 0.014
0.70	0.30	1589.0 ± 6.6	98.9 ± 4.9	0.023 ± 0.020	0.074 ± 0.011
0.70	0.35	1593.6 ± 3.7	90.7 ± 7.6	-0.015 ± 0.023	0.099 ± 0.003
0.70	0.40	1592.3 ± 4.0	93.0 ± 2.5	-0.035 ± 0.024	0.135 ± 0.007
0.70	0.45	1578.3 ± 4.9	92.6 ± 1.2	-0.034 ± 0.014	0.125 ± 0.006
0.70	0.50	1582.1 ± 6.0	94.5 ± 3.7	0.006 ± 0.011	0.138 ± 0.005
0.70	0.55	1589.2 ± 6.8	112.8 ± 10.8	0.033 ± 0.004	0.105 ± 0.019
0.70	0.60	1584.3 ± 5.4	117.7 ± 12.0	-0.010 ± 0.011	0.112 ± 0.009
0.70	0.65	1591.9 ± 4.6	117.7 ± 5.5	0.020 ± 0.011	0.099 ± 0.016
0.70	0.70	1603.6 ± 5.4	110.9 ± 10.4	0.091 ± 0.009	0.076 ± 0.005
0.70	0.75	1600.5 ± 7.6	86.1 ± 5.3	0.039 ± 0.016	0.083 ± 0.019

x (arcsec)	y (arcsec)	v (km/s)	$\sigma_\star$ (km/s)	$h3$	$h4$
0.75	-0.70	1597.5 ± 5.6	90.7 ± 8.0	-0.033 ± 0.011	0.077 ± 0.010
0.75	-0.65	1605.3 ± 8.8	105.6 ± 4.9	-0.036 ± 0.015	0.013 ± 0.024
0.75	-0.60	1607.5 ± 3.9	83.7 ± 0.9	-0.019 ± 0.026	0.016 ± 0.018
0.75	-0.55	1601.8 ± 1.8	86.0 ± 8.6	-0.065 ± 0.036	0.075 ± 0.015
0.75	-0.50	1601.8 ± 4.5	92.9 ± 6.8	-0.086 ± 0.012	0.097 ± 0.004
0.75	-0.45	1593.4 ± 5.8	87.4 ± 1.8	-0.043 ± 0.010	0.106 ± 0.010
0.75	-0.40	1597.3 ± 7.5	83.8 ± 3.4	-0.027 ± 0.014	0.106 ± 0.004
0.75	-0.35	1591.6 ± 9.6	90.1 ± 3.0	-0.019 ± 0.019	0.068 ± 0.016
0.75	-0.30	1586.6 ± 7.9	88.8 ± 5.7	-0.005 ± 0.013	0.097 ± 0.005
0.75	-0.25	1580.8 ± 5.1	90.0 ± 5.2	-0.029 ± 0.010	0.082 ± 0.006
0.75	-0.20	1594.1 ± 4.8	88.9 ± 4.9	-0.047 ± 0.021	0.105 ± 0.015
0.75	-0.15	1589.0 ± 5.9	95.3 ± 4.0	-0.067 ± 0.023	0.084 ± 0.009
0.75	-0.10	1594.0 ± 5.0	80.0 ± 3.5	-0.027 ± 0.016	0.097 ± 0.009
0.75	-0.05	1585.0 ± 6.3	95.3 ± 3.5	0.002 ± 0.017	0.080 ± 0.001
0.75	0.00	1586.1 ± 6.6	116.5 ± 4.2	0.058 ± 0.013	0.043 ± 0.008
0.75	0.05	1592.8 ± 5.0	87.0 ± 4.2	-0.003 ± 0.013	0.115 ± 0.007
0.75	0.10	1598.8 ± 4.9	75.0 ± 2.2	-0.022 ± 0.025	0.119 ± 0.007
0.75	0.15	1595.5 ± 3.6	83.8 ± 1.7	-0.034 ± 0.019	0.134 ± 0.009
0.75	0.20	1592.0 ± 5.4	76.7 ± 3.0	0.011 ± 0.017	0.103 ± 0.014
0.75	0.25	1584.2 ± 4.2	74.9 ± 1.9	-0.037 ± 0.023	0.148 ± 0.009
0.75	0.30	1597.1 ± 6.3	94.0 ± 6.7	-0.007 ± 0.012	0.099 ± 0.029
0.75	0.35	1603.4 ± 4.8	97.7 ± 2.9	-0.055 ± 0.020	0.070 ± 0.017
0.75	0.40	1594.0 ± 3.5	90.8 ± 1.8	-0.068 ± 0.007	0.051 ± 0.010
0.75	0.45	1588.6 ± 3.8	76.7 ± 3.2	0.012 ± 0.007	0.074 ± 0.007
0.75	0.50	1590.6 ± 4.8	82.1 ± 2.7	0.080 ± 0.000	0.064 ± 0.019
0.75	0.55	1588.6 ± 5.0	99.2 ± 3.3	-0.009 ± 0.005	0.118 ± 0.018
0.75	0.60	1576.3 ± 3.7	97.3 ± 3.8	-0.028 ± 0.008	0.101 ± 0.020
0.75	0.65	1582.8 ± 3.7	87.3 ± 7.8	-0.043 ± 0.005	0.080 ± 0.016
0.75	0.70	1593.6 ± 5.5	84.5 ± 3.0	-0.020 ± 0.007	0.037 ± 0.005
0.75	0.75	1583.2 ± 6.0	108.8 ± 5.1	-0.052 ± 0.004	0.042 ± 0.009